b QUARK ENRICHMENT BY LIFETIME TAGGING IN e^+e^- ANNIHILATIONS

Su Dong
Imperial College, University of London

A thesis submitted for the degree of
Doctor of Philosophy
at the University of London

March 1987

TO MY FAMILY

b QUARK ENRICHMENT BY LIFETIME TAGGING IN e^+e^- ANNIHILATIONS

Su Dong
Imperial College, University of London

ABSTRACT

The recent measurements of average B hadron lifetime consistently yielded values ~1 ps. A method of b quark enrichment in $e^+e^- \rightarrow$Hadrons annihilation events has been developed in this thesis using the secondary decay vertex structure in $b\bar{b}$ events.

The data were taken with the TASSO detector at the e^+e^- storage ring PETRA during 1983 to 1985, at an average e^+e^- centre of mass energy of 42.1 GeV. Since the method relies on the accurate tracking resolution of the TASSO vertex detector, a detailed account of the performance of the vertex detector is also given.

The b enrichment scheme includes an individual event interaction point determination. Tracks are paired in an event and weights are assigned to the pairs according to their probabilities of not coinciding with the event interaction point. A required minimum value of the sum of weights gives the enrichment of $b\bar{b}$ events relative to other flavours. The method not only allows the conventional technique of tagging one jet and studying the opposite jet free of bias, but also allows tagging using the information from the whole event. A b purity of ~60% is achieved with efficiencies of 12% and 16% for the two different modes of tagging.

The b enrichment method is used to study the fragmentation properties of b jets. Significant differences are observed compared to average jets, in charged particle inclusive momentum, rapidity and charge multiplicity distributions. The measured average charge multiplicity of b jets is 8.51±0.50±0.35 compared to 7.44±0.03±0.35 for the average jets. The flavour independence of α_s is tested using the asymmetry of the energy-energy correlation to give an upper limit of $\alpha_s(b)/\alpha_s(average) < 2.1$ at 95% confidence level.

Acknowledgements

I am indebted to my supervisor Professor David Binnie for his guidance during my postgraduate research with many helpful discussions in both general aspects of physics and the details of the analysis. I also thank Professor Binnie for the opportunity of working with the Imperial College high energy physics group.

The accomplishment of this thesis is owing greatly to the constant encouragement and support from my family.

I have greatly enjoyed the friendship and the cooperation of my fellow students in TASSO. Especially David Mellor, for his help on the Monte Carlo.

I am very grateful to Dr. John Hassard for many enthusiastic discussions about the analysis and for his careful and patient reading of the manuscript.

I thank all the members of the TASSO collaboration for their effort to support our experiment and to create an interesting environment for research. I thank the DESY directorate for their hospitality and for the superb experimental and computing facilities they provided.

I acknowledge the Science and Engineering Research Council for the financial support.

Contents

List of Figures

List of Tables

Chapter 1

Introduction

1.1 The Standard Model

The great amount of experimental effort put into probing the properties of leptons and quarks in the last half century, marked by continuous discoveries, has played an important role in understanding the fundamental constituents of nature and their interactions. The abundant sources of experimental information are accompanied by the advances in theory, with its main stream consists of various attempts of formulating gauge theories based on Yukawa's one particle exchange model [1] to explain the fundamental interactions.

The successful formulation of Quantum Electrodynamics (QED) to describe electromagnetism, was marked by the impressive accuracy with which it agreed with experimental test results [2]. Taking QED as a firm starting point, quantum field theories with non-Abelian gauge groups satisfying local gauge invariance were firstly explored by Yang and Mills [3]. This laid the foundation for the whole domain of gauge theories including the components of the standard model.

The standard model is based on the gauge group $SU(3) \times SU(2) \times U(1)$ with the group $SU(3)_{colour}$ for the strong interactions and $SU(2) \times U(1)$ for the electroweak interactions. The gauge bosons mediating the interactions are directly related to the generators of the gauge groups. There are 8 massless gluons for strong interactions, 2 massive bosons $W^{\pm}$ for charged weak currents, 1 massive Z^0 for weak neutral currents and 1 massless photon γ for electromagnetic interactions. However, gravitational interactions are not accounted for by the standard model.

The initial step toward the unification of electromagnetic interactions and weak interactions was the exploration of the group $SU(2)\times U(1)$ as proposed by Glashow [4] and also by Salam and Ward [5]. Although the weak charged currents and electromagnetic currents could be accounted for, it was realised that weak neutral currents, which were then not observed experimentally must also exist under this scheme. The specific way of incorporating the Higgs mechanism [6] to give masses to W, Z bosons, was formulated by Weinberg and Salam [7] and led to the full Glashow-Salam-Weinberg (GSW) model as part of the standard model for the the electroweak interactions. The discovery of neutral weak currents at CERN [8] and the direct observations of the W, Z bosons by experiments at CERN $Sp\bar{p}S$ collider [9] with masses in good agreement with the GSW model prediction, gave convincing experimental confirmation of the model. However, the existence of the crucial Higgs particle(s) responsible for the finite masses of particles is yet to be confirmed.

The leading theory of strong interactions is Quantum Chromodynamics (QCD) with gauge group $SU(3)_{colour}$. The choice of the group came from various experimental hints that quarks have 3 additional degrees of freedom referred to as the 'colour' quantum numbers. Unlike in the case of the electroweak sector, the $SU(3)_c$ symmetry here is assumed to be exact so that the gluons remain massless. The non-Abelian nature of the theory demands the presence of gluon self coupling as well as the gluon-quark coupling.

If the strong coupling constant α_s can be assumed to be small enough for the usual procedure of perturbation expansion to be applicable, the summation of leading log corrections to the bare coupling constant to all orders gives a 'running' effective coupling constant which can be written as [11]

$$\alpha_s(Q^2) = \frac{12\pi}{(33-2N_f)ln(Q^2/\Lambda^2)} \tag{1.1}$$

depending on the interaction momentum transfer Q^2. The scale parameter Λ has to be determined from experiments and is believed to be in the range 0.1 – 1 Gev. The parameter N_f is the number of quark flavours contributing to the virtual corrections involving fermion loops in Feynman diagrams.

It can be noticed that Equation 1.1 only makes sense when $N_f \leq 16$ which is not challenged by the presently conceived 3 generations of 6 quarks total. An important observation from Equation 1.1 is the effect of 'asymptotic freedom', referring to the continuously decreasing α_s with increasing Q^2 or with shorter probing distance. It is directly caused by the gluon self-couplings arising from this non-Abelian theory. This is consistent with the experimental fact that the constituent quarks in hadrons can only be seen when large enough Q^2 are involved e.g. in deep inelastic scattering experiments.

The physical observables in nature, such as mesons and baryons, are all distinctly colour neutral bound states. The mechanism which leads to this non-observation of free coloured objects is generally referred to as the 'confinement' mechanism. According to Equation 1.1, when $Q^2 \sim \Lambda^2$ the α_s becomes very large in contradiction with the assumption of a small α_s used to obtain Equation 1.1. Therefore at small momentum transfers compared to Λ_{QCD} the perturbation theory breaks down. However, the trend of increasing α_s with decreasing Q^2, or stronger binding force as the interaction distance increases in other words, seems to lead toward the wanted explanation for colour 'confinement'. But this is merely a hint, while the real solution lies in other non-perturbative means of calculating the low Q^2 behaviour of strong interactions.

Compared to the electroweak sector, QCD has the merit of only bringing in one free parameter Λ_{QCD}. However, its predictive power is limited by the fact that perturbation calculations are only applicable at large Q^2. The larger coupling constant also means higher order corrections may become significant under many circumstances which results in the mathematical calculations becoming more difficult.

The 'fundamental' building blocks of matter, known as quarks and leptons, are all fermions with spin 1/2. Charged leptons and quarks can participate in electromagnetic interactions. Only quarks can participate in strong interactions while all leptons and quarks can participate in weak interactions but with variable coupling strengths. The presently known 3 generations of leptons and quarks can be listed in the weak isospin $SU(2)_L$ doublet format as

$$\begin{array}{llll} \textit{Leptons} & \begin{pmatrix} \nu_e \\ e \end{pmatrix}_L & \begin{pmatrix} \nu_\mu \\ \mu \end{pmatrix}_L & \begin{pmatrix} \nu_\tau \\ \tau \end{pmatrix}_L \\ & & & \\ \textit{Quarks} & \begin{pmatrix} u \\ d' \end{pmatrix}_L & \begin{pmatrix} c \\ s' \end{pmatrix}_L & \begin{pmatrix} t \\ b' \end{pmatrix}_L \end{array} \tag{1.2}$$

where the existence of the top quark t is strongly believed but no direct evidence has so far been obtained and the evidence for the existence of the neutrino ν_τ is also somewhat indirect.

The subscript L on each doublet stresses that this format is only relevant to the *Left-handed* charged weak currents due to the well known effect of parity non-conservation in weak interactions. Each fermion with finite mass also forms a right-hand singlet which can participate in weak neutral current interactions. All fermions carrying electric charge can participate in electromagnetic interactions. Only the quarks which are coloured, can participate in strong interactions while leptons do not. The primes on d, s, b quarks indicate the fact that these are weak interaction eigenstates which are different from the mass eigenstates which appear in the strong interactions.

Particles	Electric Charge	Mass
e	-1	0.5110 Mev
ν_e	0	$<$ 46 ev
μ	-1	105.66 Mev
ν_μ	0	$<$ 250 ev
τ	-1	1.7842 Gev
ν_τ	0	$<$ 70 Mev
d	$-1/3$	$\sim$ 8 Mev
u	$+2/3$	$\sim$ 5 Mev
s	$-1/3$	$\sim$ 155 Mev
c	$+2/3$	$\sim$ 1.6 Gev
b	$-1/3$	$\sim$ 4.9 Gev
t	$+2/3$	? ($>$23 Gev)

Table 1.1: Electric Charges and Masses of Leptons and Quarks.

The non-observation of right handed neutrinos and the more direct experimental measurements of neutrino masses all indicated that they must be very light or even exactly massless. Because the quarks have not been observed as free particles but only as constituents of hadrons, they are always in 'dressed' states surrounded by soft gluons. This leads to the notion of 'running' quark masses depending on the probing momentum transfer Q^2. The electric charges and masses of the quarks and leptons are listed in Table 1.1. The masses of charged leptons and upper limits of neutrino masses are from the Particle Data Group [13]. Because the quark masses have to be estimated from dressed states, there are some uncertainties in the mass values as different methods gave somewhat different results [12]. The estimated masses of the light u, d, s quarks as appeared in Table 1.1 are taken from a particular set of values in [12] and are relevant to momentum transfer Q^2 at 1 Gev^2. The estimated masses of the heavy quarks c, b are from [14] and are relevant at average momentum transfers in semileptonic D, B decays respectively.

1.2 Quark Mixing

The fact that quark mass eigenstates are different from the weak interaction eigenstates requires the transformation relating the two different sets of eigenstates. It is exactly these mixings that allow the s, b quarks to decay into the lower generations. Because there is some arbitrariness in parametrising this fact, the two eigenstates of a Q=+2/3 quark are commonly chosen to be identical while the eigenstates for the Q=–1/3 quarks are related by

$$\begin{pmatrix} d' \\ s' \\ b' \end{pmatrix} = \begin{pmatrix} U_{ud} & U_{us} & U_{ub} \\ U_{cd} & U_{cs} & U_{cb} \\ U_{td} & U_{ts} & U_{tb} \end{pmatrix} \begin{pmatrix} d \\ s \\ b \end{pmatrix} \tag{1.3}$$

in the present 3 generation picture. The primed states (d', s', b') are the weak interaction eigenstates. The original parametrisation by Kobayashi and Maskawa [15] is

$$U = \begin{pmatrix} C_1 & -S_1C_3 & -S_1S_3 \\ S_1C_2 & C_1C_2C_3 - S_2S_3e^{i\delta} & C_1C_2S_3 + S_2C_3e^{i\delta} \\ S_1S_2 & C_1S_2C_3 + C_2S_3e^{i\delta} & C_1S_2S_3 - C_2C_3e^{i\delta} \end{pmatrix} \tag{1.4}$$

where $C_i = cos\theta_i$, $S_i = sin\theta_i$; i =1,2,3 with $\theta_{1,2,3}$ being equivalent to 3 Euler angles. It was pointed out by Kobayashi and Maskawa that a non-zero phase δ could naturally account for CP violation effect.

Because the mixing parameters are not predicted by the standard model, they have to be measured experimentally. A comprehensive review of the various measurements related to the determinations of the K-M matrix elements can be found in [16]. Experimentally, only the *magnitudes* of the various K-M matrix elements $|U_{ij}|$ are measured. The unitarity constraint that the squared sum of elements in each row and each column must be 1, not only allows the estimations of $|U_{td}|, |U_{ts}|, |U_{tb}|$ without measurements, but some other elements can also be estimated with smaller errors. The results obtained as in [13] are

$$|U| = \begin{pmatrix} 0.9742 - 0.9756 & 0.219 - 0.225 & < 0.008 \\ 0.219 - 0.225 & 0.973 - 0.975 & 0.037 - 0.053 \\ 0.002 - 0.018 & 0.036 - 0.052 & 0.9988 - 0.9993 \end{pmatrix} \tag{1.5}$$

The information from the experiments leading to the above matrix elements magnitudes can give a fairly accurate value only for θ_1, but the ranges of values θ_2, θ_3 and δ can take are still rather wide.

1.3 The Generation Puzzle

The repetitive pattern of quark and lepton families is one of the most interesting puzzle left unexplained by the standard model. The discoveries of the leptons and quarks in the second and third generations were historically associated with surprises and confusion [2].

When the muon appeared as the first signal of the rich generation pattern, it immediately caused problem as it was initially welcomed as the then expected Yukawa pion. The presence of the s quark through the discovery of the hyperons, was greeted with the name '*strange*'. Although still somewhat surprising, the discovery of charm was very much welcomed as it confirmed the GIM [17] mechanism and made the nice picture of 2 complete generations of leptons and quarks. However, this was immediately followed by the emergence of the τ lepton and the story went on further with the discovery of the b quark. All these inevitably lead to questions like 'Are there any more generations ? If so, how many ?' They cannot be answered with any theory at the present.

Concerning the standard model, the mass of each fermion enters as a free parameter proportional to its coupling to the Higgs field. The quark mixing parameters are also free parameters not predicted by the model. Possible new generations of fermions may invoke yet more free parameters. However, this many free parameters contains a rich source of information which may be important clues to physics beyond the standard model. By studying the properties of different flavours separately, possible effects beyond the simple mass differences may also lead to much more insight into this puzzle.

1.4 Heavy Flavour Decays

The basic principle of weak decays can be perceived from the simplest of all weak decays $\mu \to e\bar{\nu}_e\nu_\mu$. The lowest order electroweak Feynman diagram for this decay process is diagramatically shown in Fig. 1.1. The muon decay

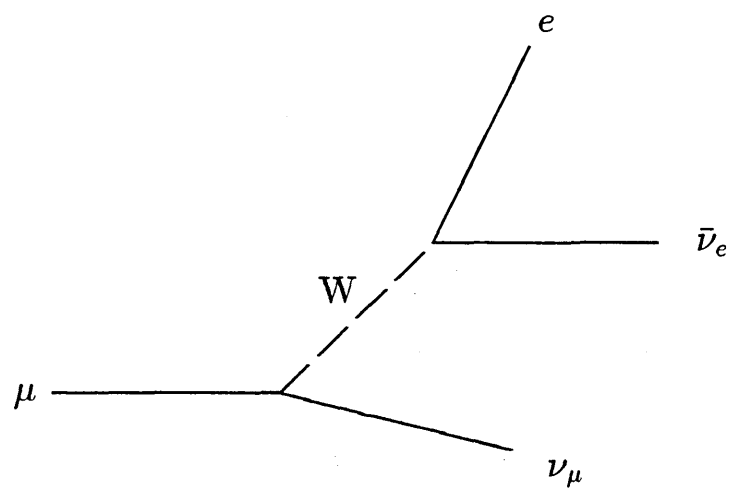

Figure 1.1: Lowest Order Feynman Diagram of $\mu \to e\bar{\nu}_e\nu_\mu$ decay.

width evaluated from this graph, neglecting the electron mass, yields

$$\frac{\hbar}{\tau_\mu} = \Gamma_\mu = \frac{G_F^2 m_\mu^5}{192\pi^3} \tag{1.6}$$

where τ_μ is the muon decay lifetime. The semi-leptonic decay width of a heavier lepton can also be obtained from Equation 1.6 by simply replacing the muon mass with the appropriate heavy lepton mass. However, this relies on lepton universality since the same constant G_F, related to the coupling of charged lepton current and W, has been assumed.

To test the above proposition, the decay lifetime of the τ lepton can be predicted using Equation 1.6 and the measured branching ratio $Br(\tau \to e\bar{\nu}_e\nu_\tau)$ of 17.69$\pm$0.47% [18] averaged over experiments. The QED corrections and and phase space corrections are small compared to experimental errors and thus ignored. Quoting only the dominant error due to $Br(\tau \to e\bar{\nu}_e\nu_\tau)$, the theoretical prediction of τ lifetime is

$$\tau_{\tau}\ (Theory) \ = \ 2.82 \ \pm \ 0.07 \ \times 10^{-13}\ s \tag{1.7}$$

The present world average of experimental measurements [18] is

$$\tau_{\tau}\ (Experiment) \ = \ 2.94 \ \pm \ 0.12 \ \times 10^{-13}\ s \tag{1.8}$$

The good agreement between the theory and the experiments indeed confirms the lepton universality within the present experimental accuracy.

To proceed along the same line for the heavy quarks, the situation becomes somewhat more complicated. The heavy quark decays cannot be studied in isolation but always as constituents of heavy hadrons. The quark mixing parameters as appearing in the K-M matrix also have to be invoked for the couplings of charged weak currents to the W in this case. By only considering the relatively simple case of semileptonic heavy meson decays, other complications can be avoided to a large extent.

In a heavy meson containing a heavy quark and light antiquark partner, the heavy quark mass results in large momentum transfers involved in the decays. This implies that the interference on the heavy quark decay from the light antiquark will be smaller as the heavy quark mass becomes larger, which is expected from the asymptotic free behaviour of the strong interactions. This leads to the popular 'spectator model' which assumes the lighter anti-quark accompanying the heavy quark in a heavy meson does not play an active part so that the heavy meson decay is essentially a free heavy quark decay. This is illustrated in Fig. 1.2 for the spectator decays of a B meson as an example. Concentrating on the semileptonic mode under the spectator model,

$$\begin{aligned}\Gamma_b(b \ \rightarrow \ e\bar{\nu}_e + X) \ &= \ \frac{G_F^2 m_b^5}{192\pi^3}\left(g(z_u)C(z_u)\left|U_{ub}\right|^2 \ + \ g(z_c)C(z_c)\left|U_{cb}\right|^2\right) \\ &= \ \hbar \cdot Br(B \rightarrow e\bar{\nu}_e + X)/\tau_B \end{aligned}\tag{1.9}$$

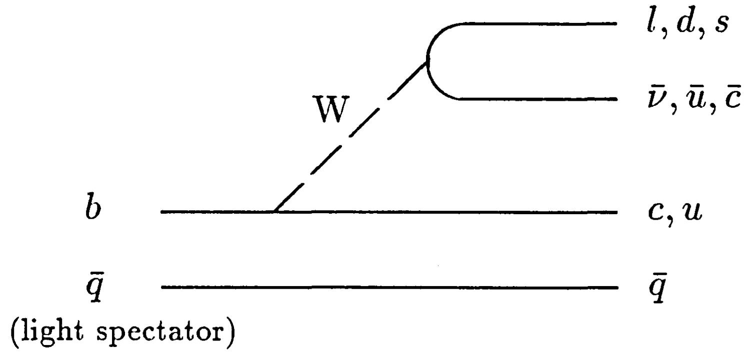

Figure 1.2: Illustration of B Decay Spectator Model.

where U_{ub} and U_{cb} are quark mixing K-M matrix elements as in Equations 1.3 and 1.4. The mass ratio variables $z_u = m_u/m_b$, $z_c = m_c/m_b$ are used as inputs to the phase space correction function $g(z)$ and QCD correction function $C(z)$. The phase space correction, neglecting the insignificant electron mass, is given by [19]

$$g(z) \; = \; 1 \; - \; 8z^2 \; + \; 8z^6 \; - \; z^8 \; - \; 24z^4 \, ln \; z \qquad (1.10)$$

In case of $b \to u$, the phase space correction is very small, thus $g(z_u) \sim 1$. In the case of $b \to c$, taking the values of $m_c = 1.6$ Gev and $m_b = 4.9$ Gev as in Table 1.1, the value of $g(z_c)$ is 0.46. The QCD correction to $O(\alpha_s)$ is given as

$$C(z) \; = \; 1 \; - \; \frac{2\pi}{3} f(z) \qquad (1.11)$$

where $f(z)$ can be read from the numerical evaluation in [20] which turns out to be $f(z_u)$ ~3.5 and $f(z_c)$ ~2.5. Taking Λ_{QCD} as 200 Mev to give an α_s of 0.28 at energy $\sim m_b$, the QCD correction factors can be obtained as $C(z_u) \sim 0.79$ and $C(z_c) \sim 0.85$. Combining the numerical factors, the formula in Equation 1.9 becomes

$$\begin{aligned} \Gamma_b(b \; \to \; e\nu_e + X) \; &= \; \frac{G_F^2 m_b^5}{192\pi^3}(0.79\,|U_{ub}|^2 \; + \; 0.39\,|U_{cb}|^2) \\ &= \; \hbar \cdot Br(B \to e\bar{\nu}_e + X)/\tau_B \qquad (1.12) \end{aligned}$$

Unlike the case for the τ lepton, this formula is not used to test the standard model but rather to measure $|U_{cb}|$ incorporating the measured B lifetime, B decay semileptonic branching ratio and an upper limit on $\Gamma(b \to u)/\Gamma(b \to c)$. The recurring difficulty in choosing the b quark mass has an important effect here because of the sensitive dependence on m_b^5. The unfortunate lack of theoretical guidance on the matter leads to an uncertainty of $\sim 20\%$ [14], which is larger than the experimental errors on B lifetime and B decay semileptonic branching ratio.

The more complicated hadronic decays of the heavy mesons are frequently discussed in the present literature inspired by the rich information which came from the MARK III D meson decay measurements. The first indication of the departure from the naive spectator model came from the original MARK I measurement of the rather different D^0 and D^+ semileptonic decay branching ratios [21]. The more recent values from MARK III [22] stand at

$$\begin{aligned}
Br(D^0 \to e^+ + X) &= 0.075 \pm 0.011 \pm 0.004 \\
Br(D^+ \to e^+ + X) &= 0.170 \pm 0.019 \pm 0.007 \\
\frac{Br(D^+ \to e^+ + X)}{Br(D^0 \to e^+ + X)} &= 2.3 \pm^{0.5}_{0.4} \pm^{0.1}_{0.1}
\end{aligned} \tag{1.13}$$

This is followed by measurement results of very different lifetimes of the D^+ and D^0. A recent review [18] gave the following world average values:

$$\begin{aligned}
\tau_{D^0} &= 4.30 \pm^{0.20}_{0.19} \times 10^{-13}\ s \\
\tau_{D^+} &= 10.31 \pm^{0.52}_{0.44} \times 10^{-13}\ s \\
\frac{\tau_{D^+}}{\tau_{D^0}} &= 2.40 \pm 0.16
\end{aligned} \tag{1.14}$$

The fact that the two ratios of the lifetimes and semileptonic branching fractions are roughly equal seems to indicate that the semileptonic decay widths are the same for D^+ and D^0 but the hadronic widths are very different.

The QCD corrections with gluons connecting the quarks from different ends of the propagating virtual W in hadronic spectator decays are referred to as 'short distance enhancement'. These corrections can raise the D decay hadronic width by as large as a factor of 2 in the simple spectator picture [23]. Further inclusion of QCD radiative corrections and phase space corrections together give an expected D decay semileptonic branching ratio of 13–16%. However all these corrections are within the spectator decay framework, and thus still cannot produce different lifetimes for D^0 and D^+.

To examine the non-spectator effect, some Cabbibo allowed 2 body D decay diagrams are drawn in Fig. 1.3. It was noted in [24] that the modes a) and b) in Fig. 1.3 give identical final states for D^+ while different final states for D^0. Therefore possible destructive interference between the 2 modes may reduce the D^+ decay hadronic width. The W exchange modes c) and d) are only available to D^0 but not D^+ which may be a source of enhancing the D^0 hadronic width. However, these types of decays are suppressed by helicity for the spin 0 D analogous to the well known $\Gamma(\pi^- \to e\bar{\nu}_e)/\Gamma(\pi^- \to \mu\bar{\nu}_\mu)$ suppression. Two distinct mechanisms have been proposed to remove the helicity suppression. The first possible mechanism [25] is the effect that soft gluon radiation before the W exchange can give a temporary spin 1 component to the $c\bar{u}$ system in D^0. The second possible mechanism [26] is the effect of the gluons involved in quark-gluon fluctuations in the D^0 meson wavefunction which can also produce a temporary spin 1 component. The quantitative contributions of the various mechanisms which reduce the D^+ width or enhance the D^0 width are still rather uncertain.

Owing to the heavier b quark mass, not only is the spectator model expected to be a better description for B decay, but some strong interaction effects within the spectator frame should also be less significant compared to the D decays. As can be noted, many of the effects are QCD corrections with magnitudes follow the running α_s. The larger momentum transfers involved in B decays compared to D decays imply a smaller α_s. Using Equation 1.1 and assuming Λ_{QCD} to be 200 Mev, the ratio of the values of α_s is

$$\frac{\alpha_s(B)}{\alpha_s(D)} = \frac{ln(m_c/\Lambda)}{ln(m_b/\Lambda)} = 0.65$$

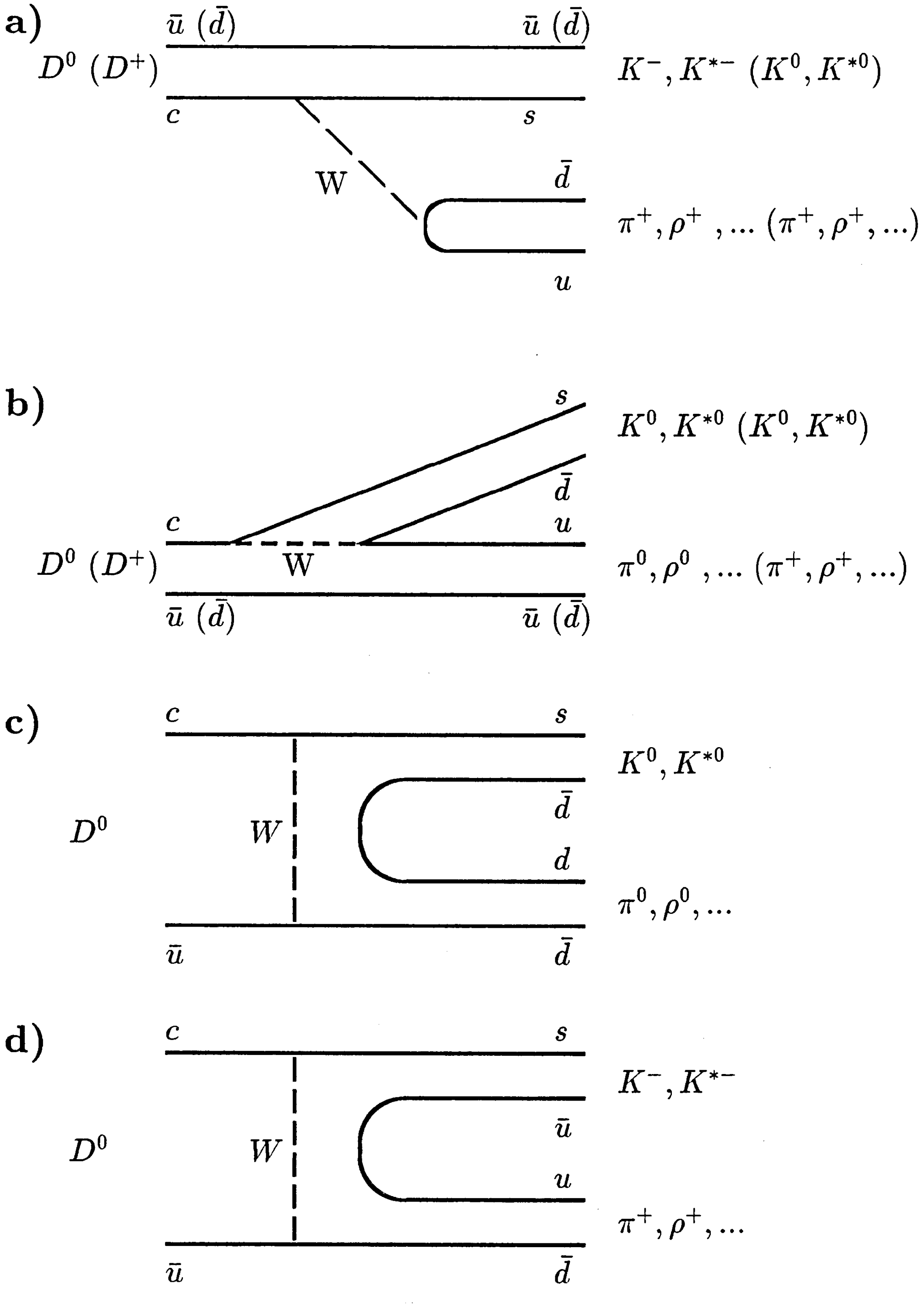

Figure 1.3: Some Cabbibo Allowed Hadronic 2-body D Decays.

which is not very sensitive to the choice of Λ_{QCD}.

The present available data on B decays are still insufficient for making separate studies of different species of B mesons in detail like in the case for the D mesons. However, the data coming from CLEO at CESR and ARGUS at DORIS running on Υ(4S) have produced a good deal of information on unseparated mixtures of $B_u^+ B_u^-$ and $B_d^0 \bar{B}_d^0$ events. This will be discussed in some detail together with a description of Monte Carlo modelling in chapter 4.

The only property of the B mesons to be discussed here is the B lifetime which has a very important role in this analysis. The measurements have so far come exclusively from experiments at high energy e^+e^- machines running well above the $b\bar{b}$ threshold. Because the proportions of different species of B hadrons is unknown, the measurements can only be quoted as an average B hadron lifetime.

Based on the knowledge that meson production dominates over baryons and the creation of $q\bar{q}$ pairs is more suppressed as the quark masses increase, the B hadrons produced at PETRA/PEP energies can be expected to still mainly consist of B_u, B_d mesons and smaller fractions of B_s mesons and B baryons. The large expected fractions of B_u and B_d mesons encourage the modelling of B decays according to the results of Υ(4S) experiments. However, a difference which should be noted is that the two B hadrons produced in the same $b\bar{b}$ event at PETRA/PEP energies may not, for example, be always a B_d^+ and B_d^- together as in the Υ(4S) experiments. This means that the correlations in, for example, B lifetimes between 2 sides of an $e^+e^- \rightarrow b\bar{b}$ event at high energies should be small.

The measurement results of the average B hadron lifetime, updated to the end of 1986 are shown in Fig. 1.4 together with the references. The last reference for each experiment indicates the source of the measurement value used

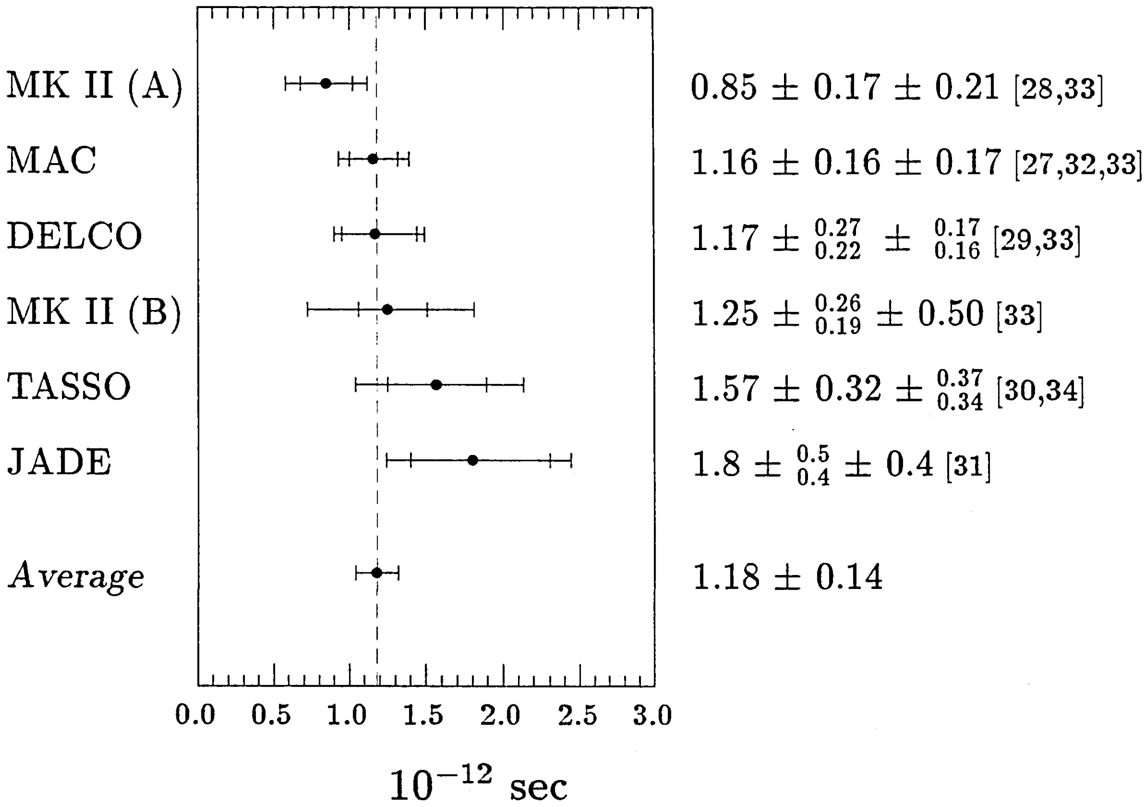

Figure 1.4: Measurements of Average B Hadron Lifetime.

in the table, which are mostly updates from the original publications. The measurements from MARK II(A),DELCO and JADE used the most popular method of selecting leptons with high jet P_T and measuring their average impact parameters. The MAC measurement is a combination of impact parameters of high P_T leptons and impact parameters of all good hadronic tracks in event samples enriched with high P_T leptons. The MARK II(B) measurement also used a b-enriched event sample with high P_T leptons but also measured the flight paths of the best 3 track vertices. The TASSO measurement used event shape to enrich the fraction of $b\bar{b}$ events and measured the impact parameters of all good hadronic tracks.

The rather long B lifetime compared to the D mesons, despite the heavier b quark mass, came as a surprise. However, this can be accommodated within the standard model by translating this long lifetime to a small quark mixing parameter $|U_{cb}|$ according to equation 1.12. The error on the combined average value should not be taken too seriously considering the possibility of different lifetimes for different species of B hadrons. Although rather different methods were used by different experiments, the measurement results showed no obvious inconsistency with each other within the present experimental errors, bearing in mind the correlation of semileptonic branching ratio and lifetime as in the D meson case. Another useful fact is that the measurements of average B decay semileptonic branching ratios at higher energies agree with $\Upsilon(4S)$ experiments (references are given in chapter 4) despite the rather different mixtures. These facts support the view that there is probably no dramatic spread of lifetimes among different species of B hadrons. The measurement result from CLEO [35] based on the rates of dilepton and single lepton production in B decay events, gave, at 90% confidence level, a rather mild bound of

$$0.44 < \frac{\tau_{B^-}}{\tau_{B^0}} < 2.05 \tag{1.15}$$

Some theoretical calculations based on the study from the D meson decays resulted a possible scenario [36] of

$$\frac{\tau_{B^-}}{\tau_{B^0}} \sim 1.6 \tag{1.16}$$

which still cannot be excluded experimentally at the present.

To investigate the effect of possible different B lifetimes very briefly, a simple model of a mixture consisting of just 2 species with equal populations but different lifetimes can be considered. The decay time spectra go according to the functions

$$\begin{aligned} F_1(t) &= \frac{2}{\tau_1 + \tau_2} e^{-\frac{2t}{\tau_1+\tau_2}} \\ F_2(t) &= \frac{1}{2\tau_1} e^{-\frac{t}{\tau_1}} + \frac{1}{2\tau_2} e^{-\frac{t}{\tau_2}} \end{aligned} \tag{1.17}$$

which can be compared, for example, at $\tau_1 \sim 0.9$ and $\tau_2 \sim 1.5$ as shown in Fig. 1.5. It can be seen that the case with 2 different lifetimes is very

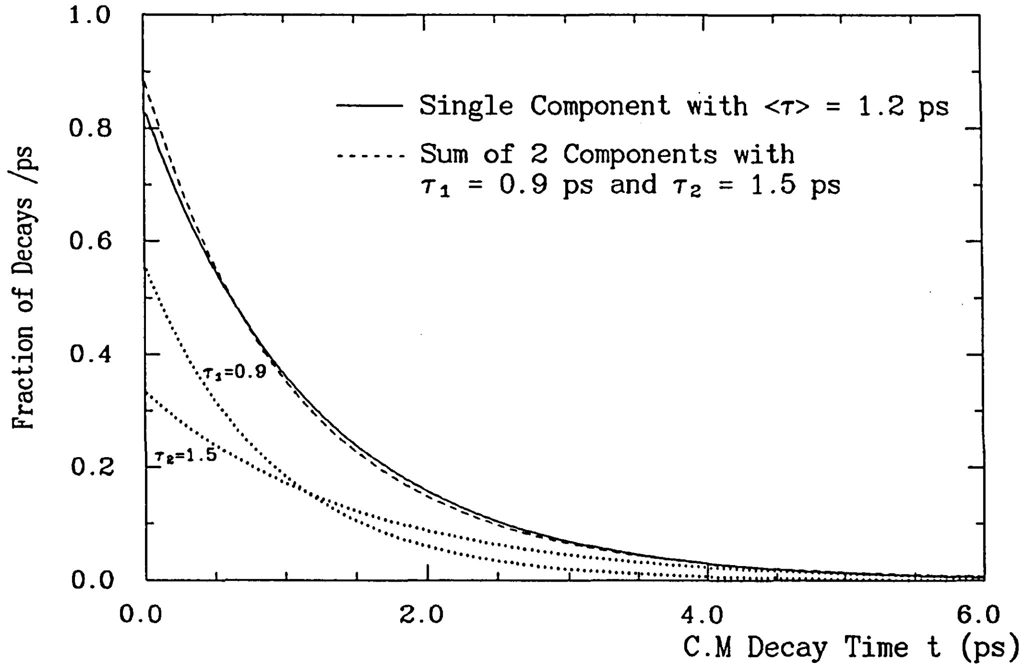

Figure 1.5: Single and Double Component Decay Lifetime Exponentials.

difficult to distinguish from a single lifetime if we are only considering the overall centre of mass decay time distribution or similar distributions like the impact parameters and decay distances.

1.5 High Energy e^+e^- Interactions

Because of the well defined simple initial states and much cleaner final states, e^+e^- colliding experiment is a very favourable technique in high energy particle physics. The full annihilation of the electron and positron with the centre of mass frame stationary in the laboratory gives the maximum energy transfer for final state particle production. Apart from the historical achievements of providing the most prolific studies of heavy flavours near the various $c\bar{c}$ and $b\bar{b}$ resonances, the machines at higher energies, above the $b\bar{b}$ threshold, have opened up yet more opportunities for new physics.

The basic annihilation processes to the lowest order of QED are shown diagramatically in Fig. 1.6. The fermion pair $f\bar{f}$ can be a charged lepton pair

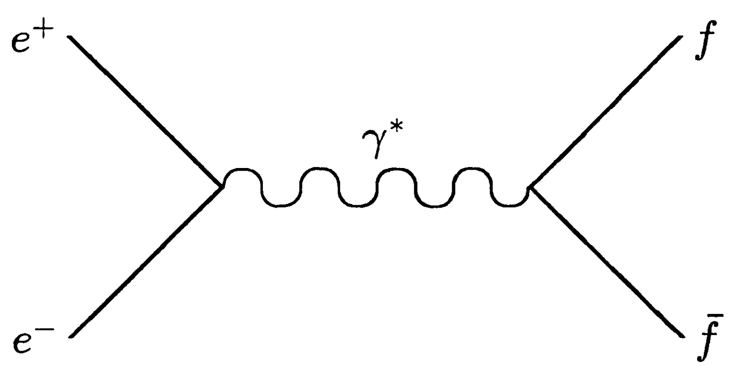

Figure 1.6: Lowest Order QED $e^+e^- \rightarrow f\bar{f}$ Annihilation Diagram.

l^+l^- or a quark-antiquark pair $q\bar{q}$ once the energy is above the pair production threshold. The QED differential cross section for the above process is

$$\frac{d\sigma}{d\Omega}(e^+e^- \rightarrow f\bar{f}) \;=\; \frac{\alpha^2}{4s}Q_f^2\beta\left[\,1 + \;cos^2\theta \;+\; (1-\beta^2)sin^2\theta\,\right] \tag{1.18}$$

where

$$\begin{aligned} s &= e^+e^-\ Centre\ of\ mass\ energy\ squared \\ \alpha &= Fine\ structure\ constant \\ Q_f &= Final\ state\ fermion\ electric\ charge \\ \beta &= Final\ state\ fermion\ velocity \\ \theta &= Angle\ of\ f\bar{f}\ flight\ direction\ w.r.t.\ e^+e^-\ beam\ direction \end{aligned}$$

For high energy machines, the limiting case of $\beta \rightarrow 1$ can be safely taken as a good approximation. In case of the μ-pair production, this gives the total cross section of

$$\sigma_0 \;=\; \sigma(e^+e^- \rightarrow \mu^+\mu^-)_{QED} \;=\; \frac{4\pi\alpha^2}{3s} \;=\; \frac{86.8}{s\ (Gev^2)}\,nb \tag{1.19}$$

Unlike the lepton pair production, the final state of the process $e^+e^- \rightarrow q\bar{q}$ does not just contain the coloured free quark and antiquark as stable objects but rather the colour neutral hadrons as fragments from them. The observation at the high energy e^+e^- storage rings, that many hadronic events appeared as two back to back 'jets' of hadrons, indirectly hinted at the need of initial $q\bar{q}$ production. One of the major landmarks of high energy e^+e^- machine was the observation of events with three distinct hadronic jets, initially seen by experiments at PETRA. This was interpreted as an indirect evidence supporting QCD, corresponding to the process shown in Fig. 1.7 in analogy to QED bremsstrahlung process. The 'hard' gluon emission processes are calculable

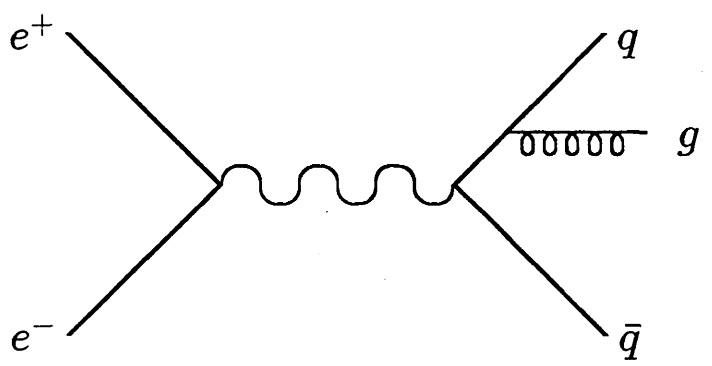

Figure 1.7: Example of a Feynman Diagram for QCD Gluon Bremsstrahlung Process $e^+e^-\rightarrow q\bar{q}g$.

using QCD, but the hadronisation (or fragmentation) processes turning quarks or gluons into hadron jets are mainly low Q^2 phenomena where perturbative QCD is not possible.

Together with QCD corrections up to the order $O(\alpha_s^2)$ in $\overline{MS}$ scheme, the total cross section for the annihilation of $e^+e^-\rightarrow$Hadrons is given by [37]

$$\sigma(e^+e^- \rightarrow Hadrons) \;=\; \frac{4\pi\alpha^2}{3s}\sum_i^{N_f} 3Q_i^2\left[1+\frac{\alpha_s}{\pi}+(1.986-0.115N_f)(\frac{\alpha_s}{\pi})^2\right] \tag{1.20}$$

where N_f is the number of quark flavours below the production threshold. The factor 3 in front of the quark charge Q_i is due to the fact that quarks can come in 3 different colours.

A further contribution comes from the annihilation channel mediated by the heavy Z^0 boson in a similar role to that of the photon as diagramatically

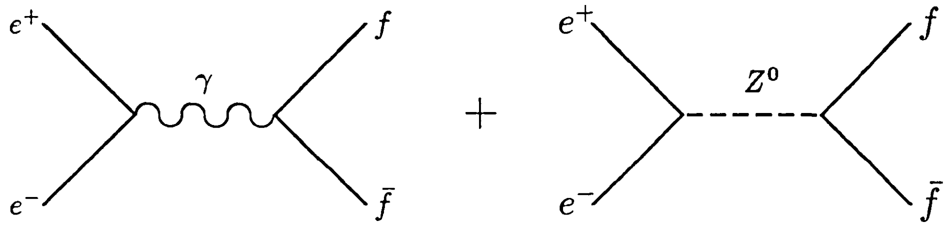

Figure 1.8: Lowest Order Electroweak Contributions to e^+e^- Annihilations.

shown in Fig. 1.8. The contribution from the Z^0 channel becomes increasingly important as the e^+e^- centre of mass energy $\sqrt{s}$ increases towards the Z^0 mass energy of $\sim$ 93 Gev. The interference between the two diagrams causes asymmetric θ distributions for the $f\bar{f}$ production. Reviews of the various experimental measurements of the electroweak forward-backward asymmetries in confirmation of the standard model can be found in [38,39]. With less significance, the Z^0 also contributes to the total hadronic cross section, which is so far only relevant for the highest energy runnings with $\sqrt{s}$ >40 Gev at PETRA.

The important cross section ratio parameter R is defined as

$$R = \frac{\sigma(e^+e- \rightarrow Hadrons)}{\sigma(e^+e^- \rightarrow \mu^+\mu^-)} \tag{1.21}$$

where the $\sigma(e^+e^- \rightarrow \mu^+\mu^-)$ is the lowest QED cross section as defined in Equation 1.19. Because the sum $\sum Q_i^2$ as in Equation 1.20, measurements of R have been used to monitor possible surpass of a threshold of new $q\bar{q}$ production. The measurements of R at various e^+e^- centre of mass energies are shown in Fig. 1.9 [13]. The R value of $\sim$ 4 at high energies can be used as evidence to support the QCD assumption that quarks can have 3 different colours. Using the QCD and the GSW model for the electroweak effect together and combining measurements at various energies, an interesting plot of the R values obtained in [38] is shown in Fig. 1.10.

Apart from the annihilation channel, Bhabha scatterings with the t-channel contribution included, and the two photon processes $e^+e^- \rightarrow e^+e^- + X$ are also

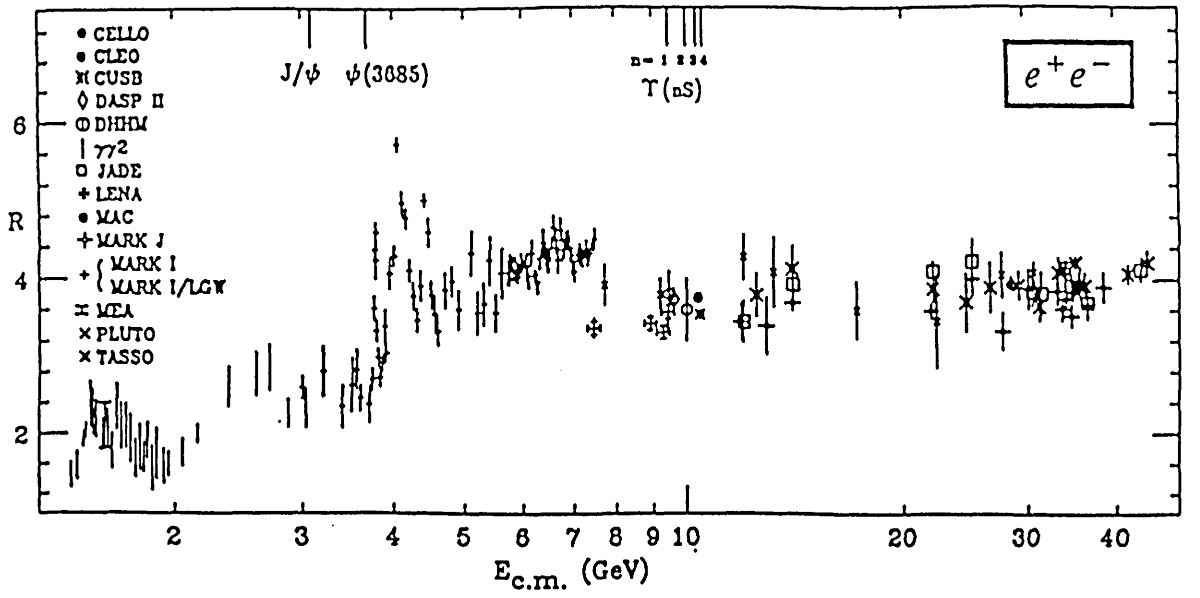

Figure 1.9: e^+e^- R Measurements at Various Energies.

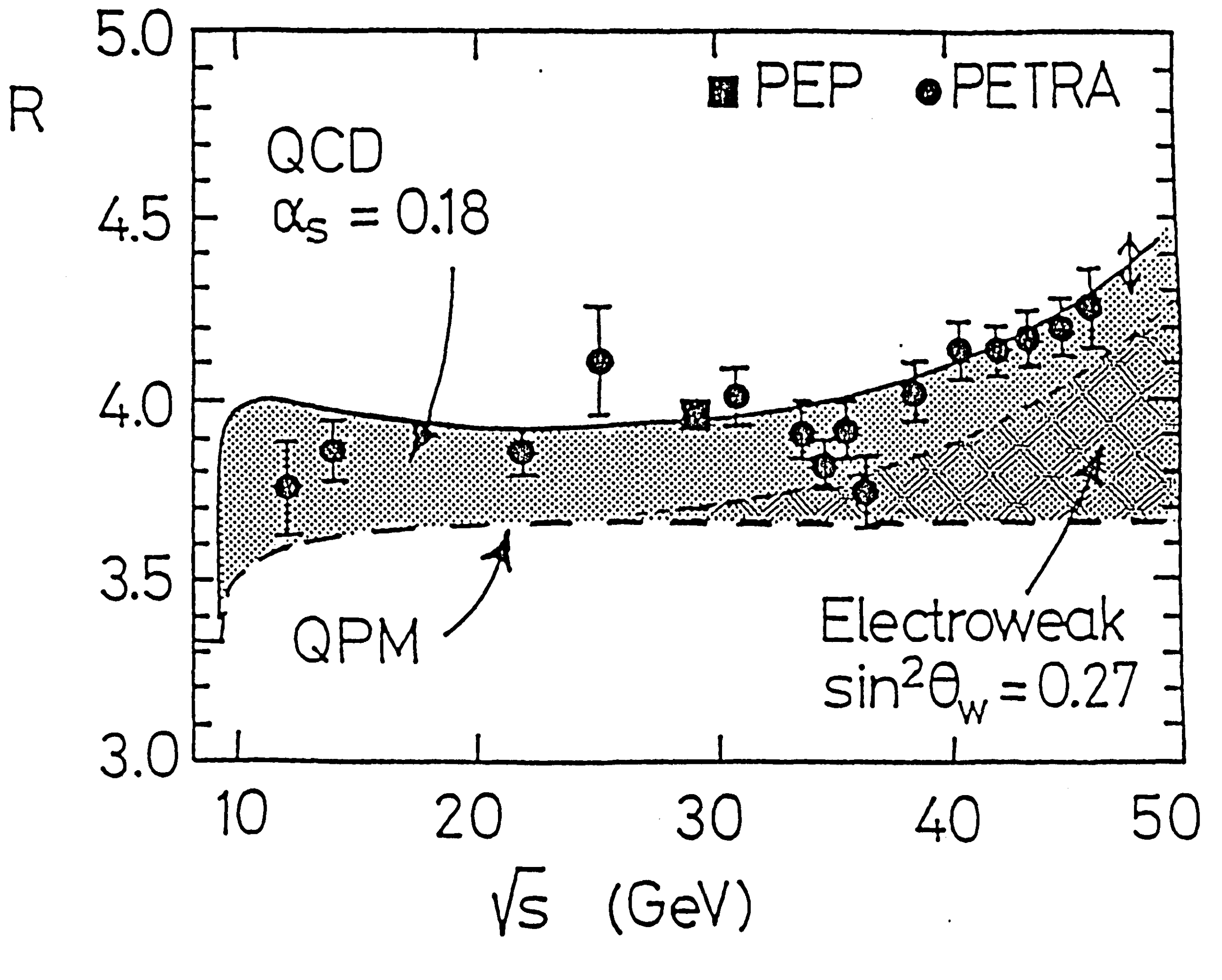

Figure 1.10: Separate Contributions from the Simple Coloured Quark Parton Model (QPM), QCD Corrections and Electroweak Effect are shown.

sources of interesting measurements. Because of the clean environment, high energy e^+e^- experiments also hold a leading role in the searches for new particles both within and beyond the standard model [41]. A detailed discussion of various physics results from different processes in high energy e^+e^- interactions can be found in [40] for the PETRA experiments.

1.6 Motivation of Analysis

The process relevant to the analysis in this thesis is the $e^+e^- \rightarrow$Hadrons production via the annihilation channel. For the experiments at PETRA and PEP, the primary production of different quark flavours in the hadronic events are roughly given by

$$u\bar{u} \;:\; d\bar{d} \;:\; s\bar{s} \;:\; c\bar{c} \;:\; b\bar{b} \;\sim\; 4 \;:\; 1 \;:\; 1 \;:\; 4 \;:\; 1$$

proportional to the squares of quark electric charges. Since there is no extra suppression for heavy quark production once beyond threshold, the relative proportions of heavy flavours are comparable to light flavours.

The measurement results shown in Fig. 1.4 reveal that the average B hadron lifetime is even longer than the D meson lifetimes as seen in Equation 1.14. This gives the possibility of enriching the proportion of $b\bar{b}$ events by selecting events with long decay vertices. The analysis presented in this thesis is an investigation of such a method which is made plausible by the installation of a vertex detector in TASSO leading to a considerable improvement in track resolution.

There are many measurements on hard QCD processes such as multijet production as well as the softer processes of hadronisations of partons using the high energy $e^+e^- \rightarrow$Hadrons events. However, they are averaged effects over different quark flavours. While the electroweak sector of the standard model has many free parameters, the QCD covering the strong interactions is somewhat more restrictive since it has only one free parameter Λ_{QCD}. An important assumption in QCD is that the characteristics of strong interactions are independent of the quark flavours apart from the effect of the masses.

While much progress has been made in studying the weak decay properties of heavy flavours as discussed in section 1.4, the tests of strong interaction properties for different flavours are so far still very brief. A general study of event shape variables sensitive to hard gluon emissions and jet properties relating to the soft fragmentation processes, after flavour separation, should be an interesting test of the flavour independence of strong interactions assumed by QCD. Therefore the b-enrichment scheme to be presented in this thesis is mainly aiming at this direction. However, the development of the method of flavour tagging using their lifetimes is also an initial investigation for providing a possible general tool with a broad range of applications in future experiments.

Chapter 2

Experimental Environment

2.1 PETRA

The e^+e^- storage ring accelerator PETRA [42] (Positron–Elektron Tandem Ring Anlage), was located in the DESY (Deutsches–Elektronen SYnchrotron) laboratory in Hamburg, Germany. It had been the highest energy e^+e^- machine with e^+e^- centre of mass energies from ~14 GeV up to over 46 GeV, during its 8 years of history from September 1978 to November 1986.

The layout of PETRA is shown in Fig. 2.1. The experiments CELLO, JADE, MARK J and TASSO situated in the four short straight sections along the 2.3 km circumference of PETRA. The eight curved sections consisted of quadrupole, sextapole and bending magnets and the four long straight sections which were used to accommodate accelerating RF (Radio Frequency) cavities.

The rate at which the interesting events take place during particle beam interactions is given by the product $\sigma \cdot L$, where σ is the cross section of the physics process concerned and L is the *Luminosity*, which depends on the beam density and intensity. In case of e^+e^- colliders, the differential luminosity at each interaction region can be written as

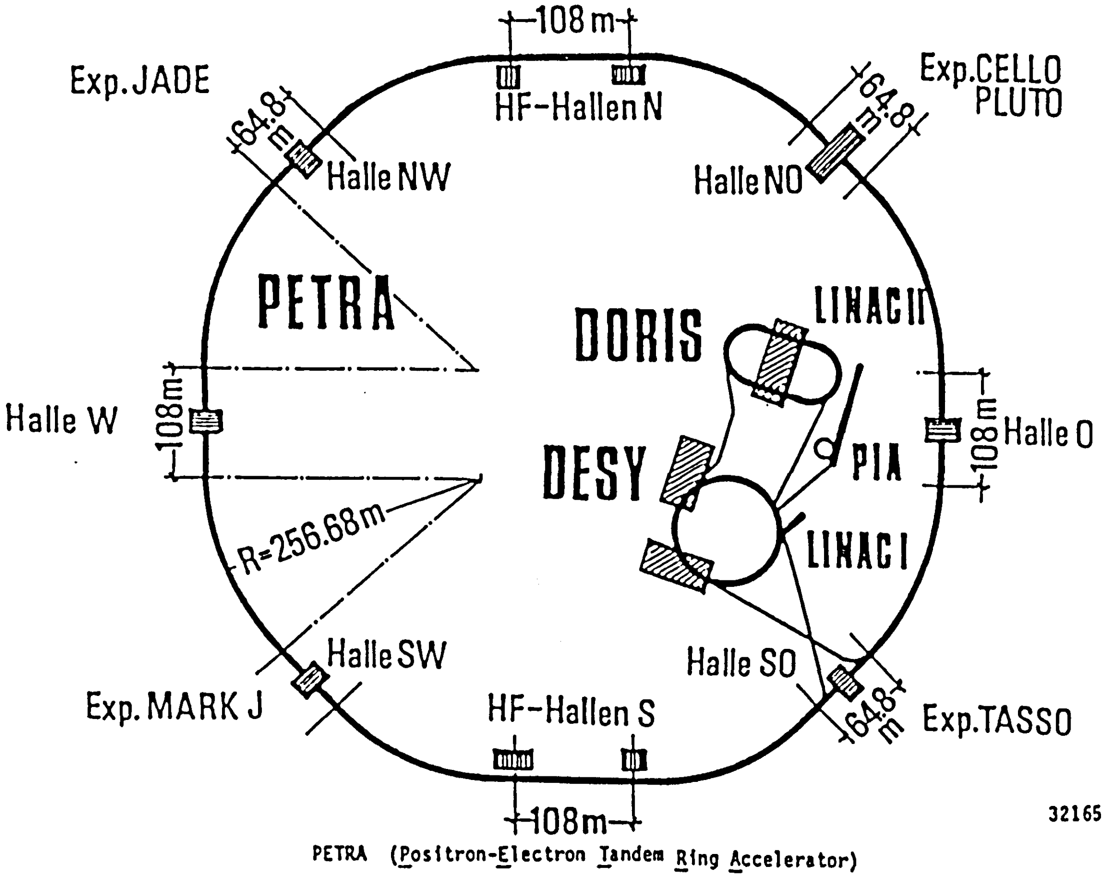

Figure 2.1: PETRA Storage Ring

$$L = \frac{n^+ n^- f}{4\pi\sigma_x\sigma_y} \quad (2.1)$$

where

$$\begin{aligned} n^{\pm} &= \textit{Number of } e^{\pm} \textit{ per bunch} \\ f &= \textit{Beam collision frequency} \\ \sigma_x, \sigma_y &= \textit{R.M.S. beam widths in horizontal and vertical directions} \end{aligned}$$

The normal operating mode of PETRA was with 2 bunches of positrons against 2 bunches of electrons with roughly the same currents in electron and positron beams. This gave a beam crossing time of every 3.8 μs for each experiment. The installations of mini-beta quadrupoles [43] in 1983 for all PETRA experiments, to provide beam focusing closer to the beam collision points, lead to an improvement of the luminosity by a factor 2.5 to 3. After this upgrade, the peak luminosity at a beam energy of 22 GeV was $\sim 6\times10^{30}$ cm^{-2}s^{-1} for each experiment, with a maximum beam current of typically 6 mA per beam. The peak luminosity at a beam energy of 17 GeV was $\sim 1.7\times10^{31}$ cm^{-2}s^{-1}, with a maximum beam current of typically 11 mA per beam. The beam lifetime was typically $\sim$ 6 hours so that new beams were injected $\sim$ every 4 hours in smooth running conditions.

Since the analysis in this thesis will be dependent on the beam dimensions, some of the factors affecting these quantities will be briefly summarised here. The beam dimensions at the interaction point are related to the emittances ϵ_x, ϵ_y and the amplitude functions at the interaction point β^*_x, β^*_y, by [44]

$$\sigma_{x,y} = \sqrt{\epsilon_{x,y} \cdot \beta^*_{x,y}} \quad (2.2)$$

where x and y are the horizontal and vertical directions transverse to the beam. The amplitude functions after the mini beta insertions were β_x = 120 cm and

$\beta_y = 8$ cm. By rearranging Equation 2.2, the emittance ratio K can be written as

$$K = \frac{\epsilon_y}{\epsilon_x} = \frac{\beta_x^*}{\beta_y^*} \cdot \frac{\sigma_y^2}{\sigma_x^2} \tag{2.3}$$

The machine orbit calculations [44] indicated that for beam energies $\geq$17 GeV the horizontal emittance was typically 2×10^{-7} radm corresponding to a horizontal beam size of $\sigma_x \sim$500μm. The minimum K value was limited by beam-beam interactions as beam energy decreased below 17 GeV. At high energies, however, K could be minimised by careful orbital corrections during machine operation for maximum luminosity. Taking $K = 1.3\%$ for 17 GeV beams as in [44] and $\sigma_x = 500\mu$m for Equation 2.3, the vertical beam size σ_y would then be 15μm. Using these beam sizes and a beam current of 11 mA per beam, the peak luminosity as obtained from Equation 2.1 would be 1.9×10^{31} cm^{-2}s^{-1}, consistent with the experimental record.

Because the beam-beam interaction was expected to be smaller at a higher beam energy of 22 GeV and lower beam current, the achievable K value could only be smaller. A comparison of the beam currents and the peak luminosity at 17 GeV and 22 GeV also seemed to support this view. Therefore, a useful conclusion which could be made was that if the beam horizontal size was $\sigma_x \sim 530\mu$m then σ_y should be $< 20\mu$m for beam energy above 17 GeV, based on the luminosity achieved.

The detailed performance of PETRA can be seen from the monthly integrated luminosity collected by TASSO as shown in Fig. 2.2 together with the PETRA e^+e^- centre of mass energies in Fig. 2.3 under the same time scale. The actual luminosity delivered by PETRA was probably $\sim$ 20% more taking into account the experimental deadtimes.

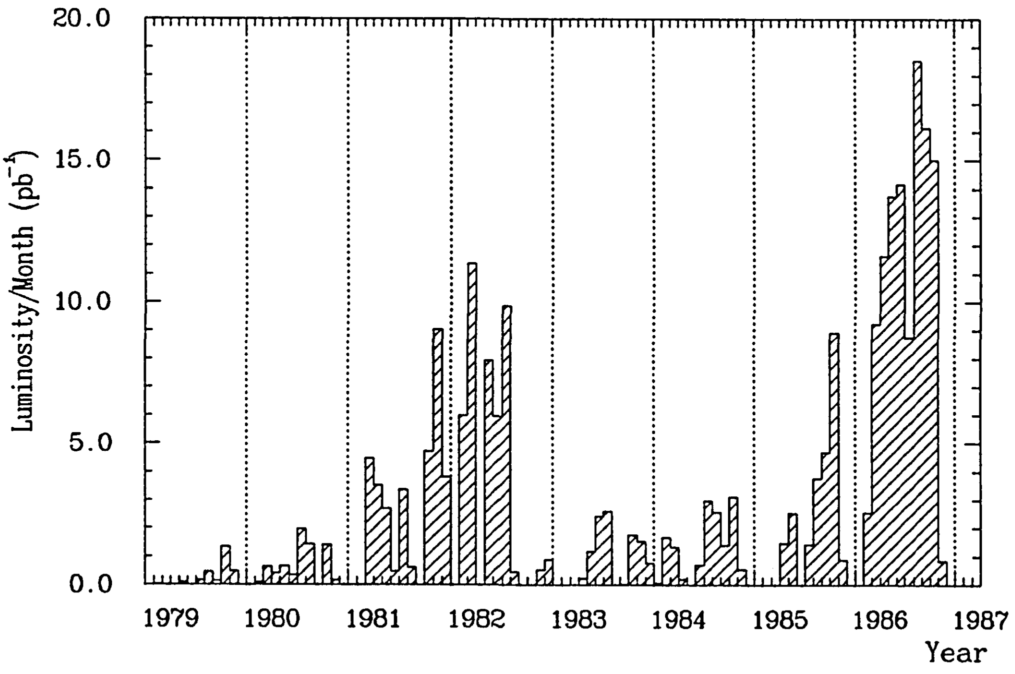

Figure 2.2: Monthly Integrated Luminosity Collected by TASSO.

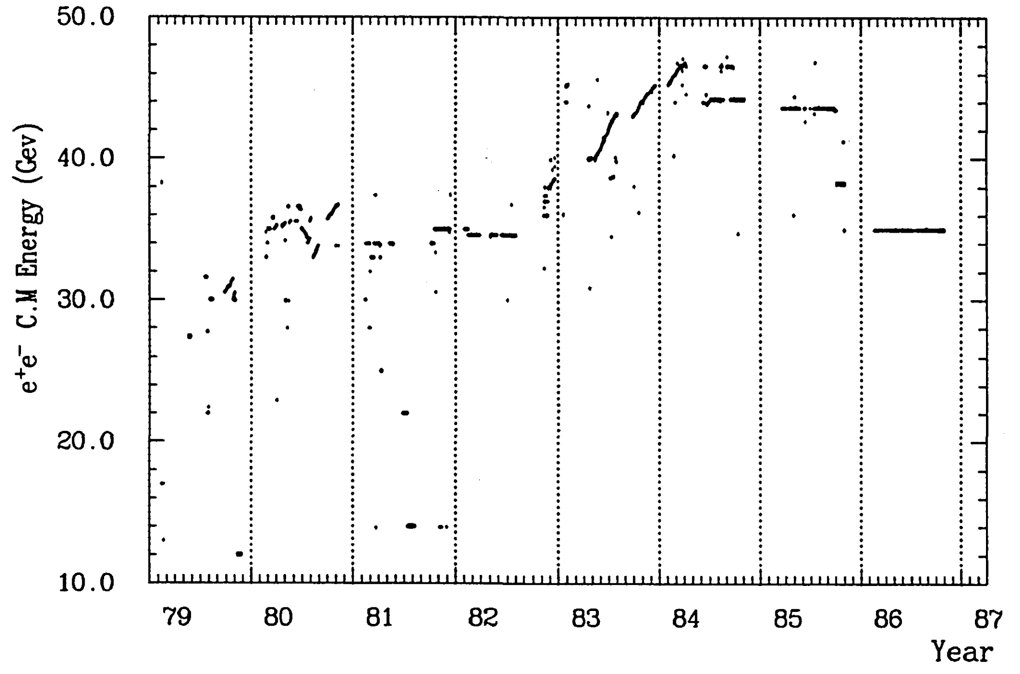

Figure 2.3: History of PETRA e^+e^- Centre of Mass Energies.

2.2 The TASSO Detector

The analysis to be presented in this thesis was based on 48 pb^{-1} of data taken with the TASSO (Two Arm Spectrometer SOlenoid) detector during the highest energy PETRA runs between 1983 and 1985, after the installation of the TASSO vertex detector. The more abundant data taken in 1986 were not used because the data processing was still in progress when most of the analysis in this thesis had been completed.

The TASSO detector viewed from different directions is shown in Fig. 2.4–2.6. The coordinate conventions which will be adopted from here on are shown in Appendix A. The z axis is defined as the direction of the positron beam. The $r - \phi$ plane refers to the plane perpendicular to the beam direction. The origin of the coordinate system is defined as the centre of the main central drift chamber. The following descriptions of the various components are mainly for the updated detector configuration since 1983.

Coil

The TASSO solenoid magnet [45,46] was a normal-conducting water cooled coil with a length of 440 cm and an inner radius of 137 cm. The conductor was a 2.94×3.64 cm^2 rectangular aluminium bar with a central bore of 1.17 cm in diameter used for cooling. The coil was wound in 4 layers with a total of 336 windings.

The coil was normally operating at the maximum current 5200 A with a DC voltage supply of 550 Volts which amounted to a power consumption $\sim$ 2.85 MW. The maximum field strength was 0.494 Tesla and the maximum field inhomogeneity along a track within the normal tracking volume was $\sim$4%. The B-field has been along the electron beam direction since 1983.

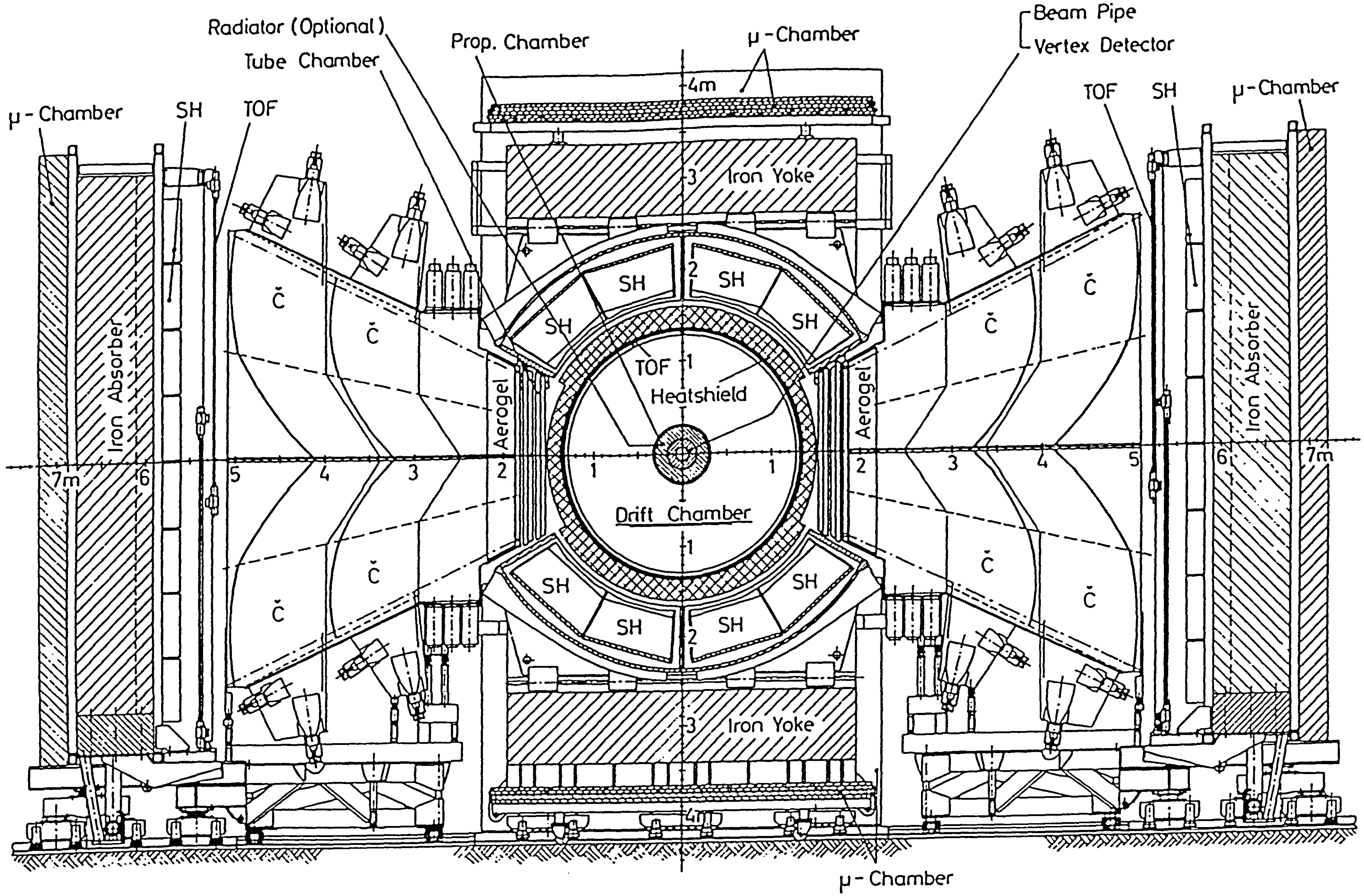

Figure 2.4: TASSO Detector Viewed along the Beam Direction

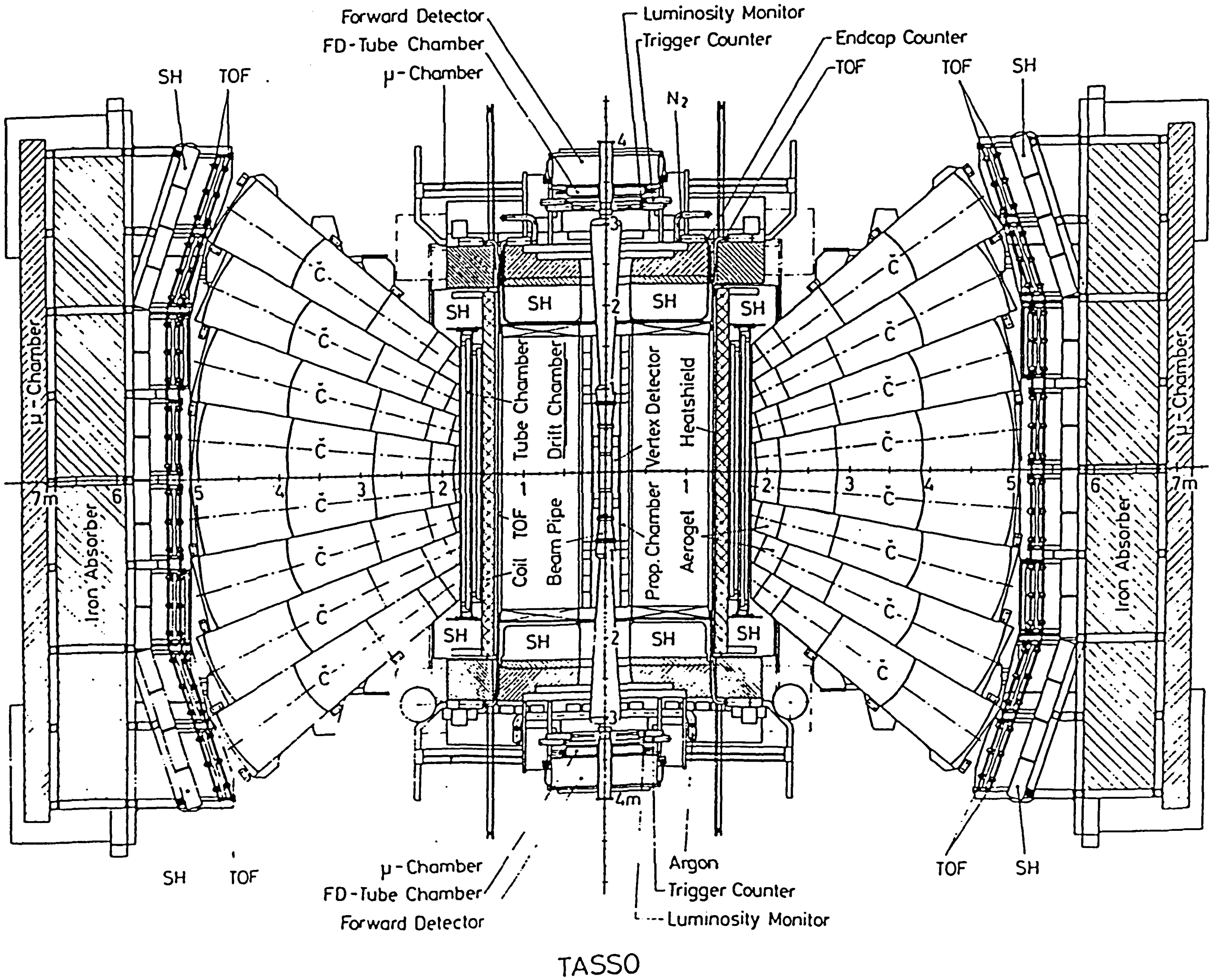

Figure 2.5: TASSO Detector Viewed Downward from Top

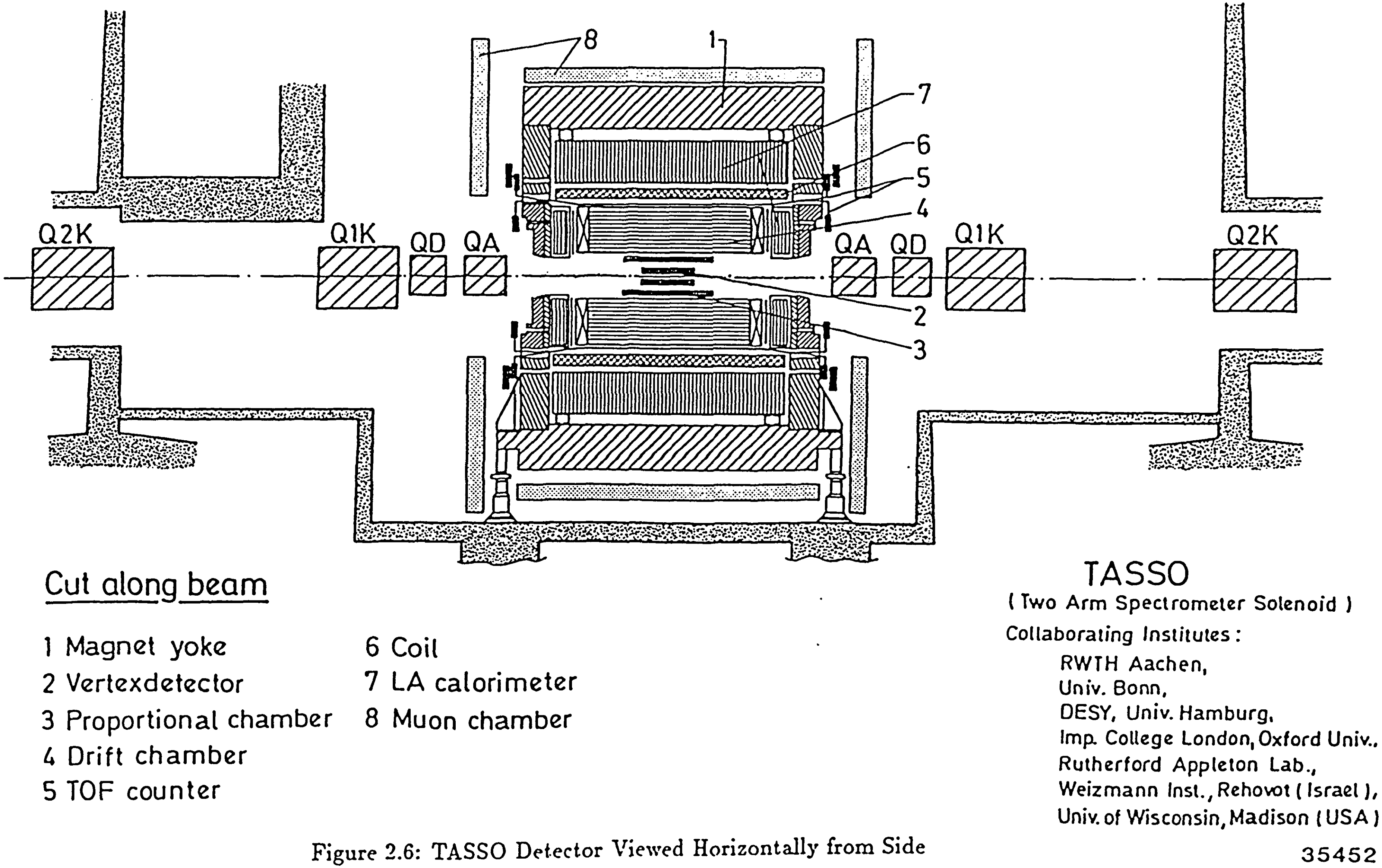

Figure 2.6: TASSO Detector Viewed Horizontally from Side

Central Drift Chamber (DC)

The large cylindrical drift chamber [45,47] occupying the radii from 32 cm to 128 cm and ± 173 cm in z was the major component of TASSO. There were nine 0° layers parallel to the beam direction and six stereo layers sandwiched between the 0° layers with α angles of $\sim 4^\circ$. The number of cells per layer were arranged so that the cells in all layers had approximately the same half width of $\sim$ 16 mm.

The original gas mixture of Ar/Methane (90/10) as described in [47] had been replaced with Ar/Ethane (50/50) at atmospheric pressure since July 1980. This solved the previous problem of rather large signal crosstalk near the cathode wires with the Ar/Methane mixture. After more careful calibration procedures including various nonlinear effects in the space–drift time relations, an improved spatial resolution [48,49] compared to the original published values in [47] was obtained. The average spatial resolution across a cell, found for the new gas mixture as in [48], was 195μm.

The fit to main drift chamber hits from a curved track in the magnetic field was the basic means of obtaining momentum measurements for the charged particles. With further assistance from the CPC and VXD hits extending the span of measuring lengths, the momentum resolution was found to be [30]

$$\frac{\sigma_P}{P} = 0.0095\sqrt{0.5 + P^2}$$

where of the slope of 0.0095 was determined from studying the achieved momentum resolution for high momentum muons from $e^+e^- \to \mu^+\mu^-$ events and the constant term of 0.5 was the estimated contribution from pion multiple scattering on the detector material.

Cylindrical Proportional Chamber (CPC)

The CPC [50,51] was a multiwire proportional chamber with 4 sense layers at radii between 18.72 and 27.88 cm with 480 sense wires per layer parallel to the beam direction. There were 120 inner and 120 outer helix cathode strips situated at 7 mm inside and 7 mm outside each sense layer. The inner and outer cathode strips were wound in opposite senses with $+36°$ and $-36°$ of pitch angles respectively. The active length of the chamber was 140 cm.

The chamber operated with the 'Magic Gas' mixture of Ar/Isobutane/Freon ($\sim$75/25/0.25) at atmospheric pressure. The anode sense wire efficiencies were typically 97% and the cathode hit efficiencies were typically 90%. For the standard tracking, only anode hits were used in the $r - \phi$ track fits.

The most important role of the CPC was to provide trigger information to reject background events in the data taking. This was performed by the CPC trigger processor [52] with masks accepting possible anode hit combinations from track segments pointing toward the beam. Because the CPC was shorter in z compared to the main drift chamber and closer to the beam, it provided a good rejection of background events not occuring at the beam colliding point e.g. events due to cosmic rays and beam pipe interactions. This was essential to reduce the data taking rate to a tolerable level. The cathode strips were also used to form an independent trigger to reject events occuring at $|z| >\sim 30$ cm together with a low charge multiplicity trigger to serve the special purposes of two photon physics.

Vertex Detector (VXD)

The vertex detector was a precision drift chamber installed in late 1982 to give accurate track hits near the interaction point. Because of the importance of the VXD in this analysis, a more detailed description of the VXD together with an evaluation of its performance will be given in chapter 3.

Inner Time of Flight Counters (ITOF)

The barrel inner time of flight counters [53,54] were situated between the main drift chamber and the coil at a radius of 132 cm from the beam. It consisted of 48 scintillator slabs parallel to the beam direction, covering 82% of 4π solid angle. An average time resolution of 0.38ns was obtained, allowing π–K separation up to a momentum of 0.6 GeV/c and (π/K)–P separation up to a momentum of 1.0 GeV/c when used in conjunction with the tracking information from main DC. The hit efficiency was typically $\sim$98%.

Liquid Argon Calorimeters

The barrel liquid argon shower counters (LABC) [55] immediately outside the coil occupied the regions

$$42^\circ < \theta < 138^\circ \quad ; \quad 30^\circ < \phi < 150^\circ$$

above the coil and

$$42^\circ < \theta < 138^\circ \quad ; \quad 210^\circ < \phi < 330^\circ$$

below the coil. By restricting the use to the fiducial volumes away from the edges of the individual modules, the effective total solid angle coverage of the LABC was limited to 36%.

The modules consisted of 35 layers of 2 mm thick lead plates separated by 5 mm thick gaps filled with liquid argon, which amounted to a total thickness of 45 cm. The modules were segmented into stacks of 7×7 cm^2 front towers with 6.1 radiation lengths and followed by 14×14 cm^2 back towers with 7.6

radiation lengths. There were also 2 cm wide strips in directions parallel and orthogonal to the beam direction (z and ϕ strips) with 2 layers of each every 1.6 radiation lengths. The charges collected on towers gave energy measurements and the signals on the strips gave accurate position and ionisation loss dE/dx measurements.

The energy resolution achieved including the effect of other detector materials and the liquid argon tank wall (1.6 radiation lengths) before the first sampling, was

$$\frac{\sigma_E}{E} = \left[0.11 + (\frac{0.02}{E - 0.5}) \right] / \sqrt{E}$$

for normal incident photons with E >1 GeV. The angular resolutions were $\sigma_\phi = \sigma_\theta = 2$ mrad for E>1 GeV photons. The efficiencies of identifying isolated high momentum electrons with P>2 GeV/c was found to be ~ 83% which degraded to 73% for P>1 GeV/c electrons inside hadron jets [56].

The endcap liquid argon shower counters (LAEC) [57] covered the regions

$$12^\circ < \theta < 30^\circ \qquad \& \qquad 150^\circ < \theta < 168^\circ$$

for all ϕ angles. The structures of the calorimeter stacks were similar to the barrel except there was a thinner liquid argon gap of 3 mm.

Hadron Arm Components

The hadron arm detectors covered the regions

$$50^\circ < \theta < 130^\circ \qquad ; \qquad -26^\circ < \phi < 26^\circ$$

and

$$50^\circ < \theta < 130^\circ \qquad ; \qquad 154^\circ < \phi < 206^\circ$$

with arrays of components dedicated to particle identification.

The 8 layers of planar drift tube chambers (PTC) immediately outside the coil were used to provide position measurements for charged particles emerging from the coil. They were followed by 3 different types of threshold Čerenkov counters [58], namely the Aerogel counters, then Freon gas and CO_2 gas counters. The refractive indices of the different radiators and the momentum thresholds of different particles can be seen from the following table.

Radiating Medium	Refractive Index	Momentum Threshold (GeV/c) π	K	P
Aerogel	1.025	0.6	2.2	4.2
Freon 114	1.0014	2.7	9.4	17.8
CO_2	1.00043	4.8	16.9	32.0

The detection efficiencies for particles above the thresholds were found to be $> 95\%$ for the Aerogel counters and $\sim 99.9\%$ for the gas counters.

The hadron arm time of flight counters (HTOF) [59,53] behind the Čerenkov counters consisted of 48 scintillators for each arm at 5.5 m from the beam. The time resolution achieved was σ=0.45ns, allowing π–K separation up to 1.1 GeV/c and (π/K)–P separation up to 2.2 GeV/c. This gave the particle identification in the low momentum range complementary to the Čerenkov counters.

The hadron arm shower counters (HASH) [60] situated behind the HTOF consisted of lead-scintillator sandwiches with a total thickness of 7.4 radiation lengths at each arm. The energy resolution was found to be $\sigma_E/E = 17\%$ independent of energy.

Iron Structures and Muon Chambers

The 4 metre wide rectangular main iron structure surrounding the central part of the detector from above and below and both endcap regions was the magnet flux return yoke for the coil. The thickness of the upper and lower parts of the iron yoke was 80 cm and the thickness of the endcap part was 50 cm.

The muon chambers [61] were stacks of proportional tubes behind various iron structures, with two staggered double layers along orthogonal directions. The muon chambers situated above and below the yoke covered 17% of 4π. The endcap muon chambers covered 13% of 4π. In addition, there were muon chambers at both hadron arms following 87 cm thick iron walls behind the HASH counters, covering 13% of 4π.

The minimum muon momentum needed to penetrate the iron yoke was 1.2 GeV/c. By requiring at least 3 chambers out of 4 fired for a good muon hit, the efficiency of accepting high momentum muons within the muon chamber coverage was found to be >95%.

Foward Detectors

The forward detectors [62] upgraded since 1983 were two sets of identical scintillator and shower counter telescopes situated symmetrically in z covering the low θ angle regions. Each side had 4 small overlapping pairs of scintillators, 7×4 cm^2 (A counter) and 9×6 cm^2 (C counter), in size, distributed every 90° around a circle at $|\theta| \sim 45$ mrad. These small scintillators starting at $|z|$=3.3m on each side, were followed by an array of scintillators, proportional chambers and lead scintillator shower counters covering a larger angular region of 28 mrad $< |\theta| <$ 118 mrad aound all ϕ angles.

The luminosity measurement used the large cross section of the well understood Bhabha scattering $e^+e^-\to e^+e^-$ at low angles. A 'Fine Luminosity Trigger' was defined by a coincidence of scintillator and shower counter hit combinations simultaneously at both $+z$ and $-z$ sides in regions diagonally opposite to each other with respect to the beam interaction point. The accuracy of luminosity measurement was $\sim \pm 4\%$ with the errors mainly systematic in origin. The information from the array of large scintillators, proportional chambers and shower counters were used for fine calibrations of luminosity measurement and low angle electron tagging for two photon physics.

2.3 Event Trigger and Data Acquisation

The experiment strobes were obtained from induced pulses on a beam pickup electrode placed at 7.1m from the beam colliding point. The gate timing and resets for various electronic equipment were all derived from the strobe for each crossing. The data from most of the electronic channels were fed into various fast 'trigger processors' synchronised to the beam crossings. An event partially reconstructed by trigger processors satisfying at least one of many possible acceptance topology conditions would give a valid 'trigger'.

The configuration of the TASSO data acquisation system in the last two years of running since the beginning of 1985, is shown in Fig. 2.7. When the main trigger supervising equipment SIGH (Strobe Interupt Gate Handler) obtained a valid trigger from the combined information of various trigger processors, an immediate communication with the online control microprocessor (Front-End Processor) was then made. If the data flow was not busy, the replied Front-End Processor interupt would pause the SIGH and disable strobes and resets to equipment for the subsequent beam crossings until all readout of relevant detector channels was complete.

After a software programmed rejection of a small proportion of events within the Front-End Processor, most of the events were then transfered to the main online computer (VAX 750). These events were passed into an emulator (370/E) to be processed briefly and then sent to the DESY computer centre

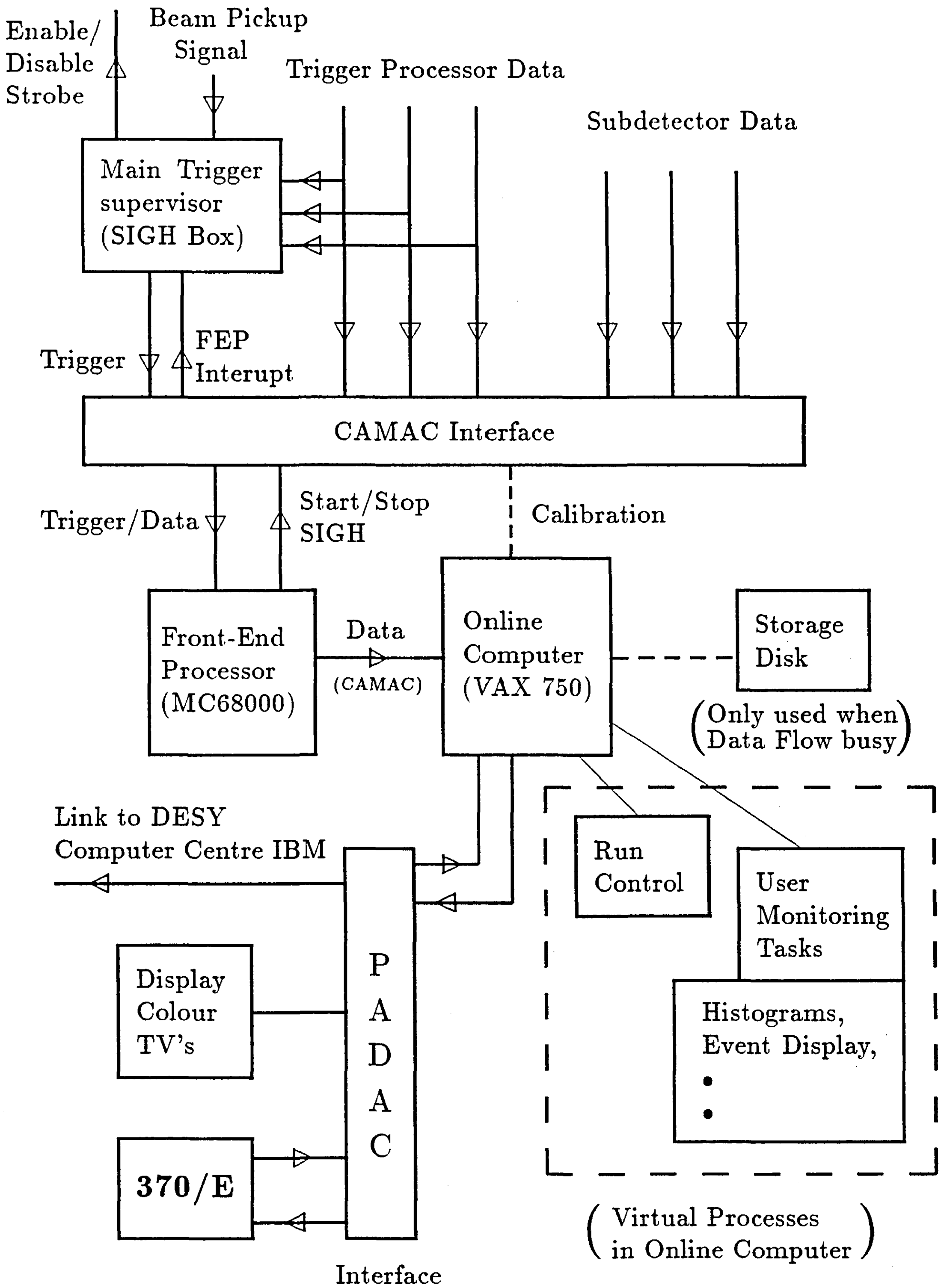

Figure 2.7: Configuration of Post-1985 TASSO Data Acquisation System.

IBM and stored. Some of the events were also copied into a user buffer to serve online monitoring purposes. A spare disk was also available to provide temporary storage when data transfer was busy or the link to the computer centre IBM was not established.

At the high energy runnings with beam energy of ~22 GeV, the total trigger rate was typically 3–6 Hz depending on the beam conditions. The average raw event length was ~12 kbytes and the average readout time per event was ~50 msec which resulted an average deadtime of ~20%. The TASSO data taking runs were normally synchronised with the PETRA filling time of ~ every 4 hours.

Among the many event triggers used in TASSO, only the multi-charged track trigger relating to the hadronic events used by this analysis will be described here. For each of the 72 wires in the first layer of the main drift chamber, a set of 15 masks consisting of various combinations of wires from 5 other pre-selected DC 0° layers were constructed. Each mask corresponded to a combination of hit wires due to charged tracks with a particular range of curvatures in the $r - \phi$ plane. By searching through all sets of masks for each wire using the PREPRO trigger processor, DC track sectors were selected demanding that at least 5 out of 6 layers in a masked combination were fired. For the high energy running, only a subgroup of masks were used so that the masks had 0% efficiency for tracks with $P_{r\phi}$ <321 MeV/c which linearly increased to 100% for tracks with $P_{r\phi}$ >~1.2 GeV/c, just taking into account the effect of the geometry of the masks.

The CPC processor also searched through sets of masks demanding 3 hits out of 4 anode layers in a masked combination to give a track candidate with $P_{r\phi}$ >220 MeV/c. The wires were grouped into 48 sectors in ϕ so that any sector contained one or more track candidates would have the sector bit set to 'ON'. A full PREPRO track required that the track sector from a particular DC mask must be in coincidence with at least one CPC bit being set at the inner ϕ region within ± 1 CPC sector. A similar requirement was that a corresponding ITOF counter must be hit at the outer ϕ region within ± 1 ITOF counter.

To eliminate spurious combinations in the same region, the full PREPRO tracks were counted only allowing an ITOF hit to be associated with one PREPRO track. The specific demand of the multi track trigger for hadronic events was that there be at least 5 full PREPRO tracks in the event. The PREPRO efficiency for a single isolated high momentum track was $\sim 95\%$ and the triggering efficiency for hadronic events satisfying the hadronic selection criteria (see next section) was $99.1 \pm 1.0\%$ [63].

2.4 Offline Data Processing

The first stage of processing (PASS1) was mostly done in the emulator as mentioned in the last section and then completed on the main IBM. The main duty of PASS1 was to run the track finding program FOREST (see section 2.5) for all events to reconstruct charged tracks using the DC and CPC hits. All events taken online were still kept after PASS1.

The PASS2 stage consisted of various selection cuts so that only event types serving specific physics topics were chosen. Tighter cuts were applied in the PASS3 stage demanding events to satisfy:

- Either ≥ 3 tracks in $r - \phi$ with $|d_0| < 2.5$ cm.
- Or ≥ 2 tracks reconstructed in 3-dimensions with $|d_0| < 2.5$ cm and $|z_0| < 8.0$ cm.

A more exhaustive track finding program MILL (see section 2.5) was then applied to the events which survived the PASS3 cuts together with some detailed analysis programs for outer detector components with the inclusion of fine calibration constants. A large reduction of background was achieved after PASS3 as only $\sim 1.5\%$ of all PASS1 events were left while nearly all 1-γ annihilation hadronic events, multi-track 2 photon events, Bhabha scattering, μ-pair and τ-pair events were still in the sample.

The PASS4 stage was the detailed selection of the hadronic events from the annihilation channel. First of all, only tracks passing the following quality cuts were counted:

- Track Reconstructed in 3-dimensions
- Track fit quality: $\chi^2_{r\phi}/\mathrm{NDF} < 10$ and $\chi^2_{sz}/\mathrm{NDF} < 20$
- Track closest approach to origin in $r-\phi$ plane: $|d_0| < 5$ cm
- Track Momentum in $r-\phi$ plane: $\mathrm{P}_{r\phi} > 0.1$ GeV/c
- Track polar angle: $|cos\theta| < 0.87$ (equivalent to passing at least 6 DC 0° layers)
- Track closet approach in z to event vertex: $|z_0 - <z_v>| < 20$ cm where $<z_v>$ was the average z_0 of all tracks in the same event satisfying the previous 5 cuts.

The hadronic event selection criteria were:

(a) ≥ 5 charged tracks passed the track quality cuts.

(b) When events divided into two hemispheres by the plane perpendicular to the event sphericity axis (see section 4.6.1) and contained 3 charged tracks in each hemisphere, the invariant mass (assume pion mass for each track) of the 3 prongs must be $\geq \tau$ mass for at least one hemisphere.

(c) The event z vertex averaged over tracks $|< z_v >| < 6$ cm.

(d) The sum of track momenta $\sum |P| > 0.265 \cdot$W where W was the total e^+e^- centre of mass energy.

The cut (a) was an effective cut against various low prong background including $\gamma\gamma$ events and τ pairs. The cut (b) was clearly used to reject τ pair events. The cut (c) was mainly used to reduce the beam gas and beam pipe events in the sample. The cut (d) gave a further reduction on high multiplicity $\gamma\gamma$ events.

About 2.5% of PASS3 events satisfied the hadronic selection criteria. The events passing the above selection were subject to visual scans mainly to reject Bhabha scattering events containing converted photons. This gave a small reduction of ~3%. The estimated background contamination in the final hadronic sample were of the types [62]:

- Beam gas and beam pipe scatterings: $1.5 \pm 0.7\%$
- $\gamma\gamma$ processes: $1.0 \pm 0.5\%$
- τ pair production: $0.5 \pm 0.4\%$

The contamination of beam gas and beampipe scattering events were mostly rejected when demanding a minimum polar angle cut of the event thrust axis (see section 4.6.1) with respect to the beam direction.

2.5 Track Finding and Fitting Routines

There were three different types of track finders employed for different purposes. The track finders FOREST/MILL only used the hits from the main DC and CPC while PASS5 and FELIX also used the hits from VXD. An additional track and vertex fitting package with special treatment for multiple scattering was also used in many analysis procedures.

FOREST/MILL

The track finders FOREST and MILL were both based on the link-and-tree algorithm [64] but FOREST served as a fast filter in hadronic event selection as it was inclined to find fast tracks from the origin while MILL was employed to give a more thorough search of tracks with looser restrictions and thus better efficiency.

Both methods initiated the track finding in the $r - \phi$ plane first using the DC $0°$ layer hits and then the associatable hits on the DC α layers were gathered around each $r - \phi$ track so that the same track finding algorithm could be applied for a straight line track search in $s - z$ leading to a full 3-dimensional track. The CPC hits were also included by projecting the track from the DC into the CPC and the CPC hits within a road leading to the best fit were associated with the MILL track.

The basic idea of the link-and-tree algorithm was to use links between hits on adjacent layers at the same ϕ region as the fundamental objects. A link combined with the origin could immediately give a curvature associated to it and spurious links were rejected early on with a minimum curvature cut. The neighbouring links with similar curvatures were combined into trees until long enough to be considered as a track candidate. As this did not require many intermediate fits, the method was relatively fast. The hits within a road near a long chain were then all considered with various permutations so that the combination which gave the best fit was taken as the final track. In the case of MILL, when the above procedure gave the fast track candidates with many of the associated hits masked out, additional searches with relaxed restrictions were carried out so that tracks not from the origin could be found from the rest of the hits.

PASS5

The track finder PASS5 [65] was a simple extension of MILL. The MILL tracks with DC and CPC hits were projected into the VXD to define a road and then various combinations of the VXD hits were considered. The curvature of a track was fixed to the same as that of a MILL track and then fitted to the VXD hits only. The set of VXD hits with a compromised combination of maximum hit association and best fit gave the final form of a track. There was a minimum VXD hit cut so that a final track must have at least 4 VXD hits associated to it.

FELIX

The link-and-tree method would work best if all links had been similar objects, which was not true when the three rather different chambers in TASSO, with rather different resolutions and layer separations, had to be combined together. So the track finder FELIX [51,67] was developed to provide a uniform trackfinding method through all 3 chambers.

The same approach of starting with $r-\phi$ track reconstruction first was also used by FELIX compared to MILL. The basic track finding algorithm was the back track method [66]. The fundamental objects considered in FELIX were the hits themselves.

The procedure started from hits at the outer most layer of the DC and partial tracks were gradually built toward the centre of the detector, by adding hits from neighbouring layers inside. The partial tracks were then extended by adding new hits which would give the the best circle fit. If the number of hits on a partial track exceeded a minimum number of hits, it was then accepted as a preliminary track candidate. For track candidates with the same starting point, only the best candidate was kept and the associated hits were masked to disallow further associations with other tracks. However, most often a partial track would end at a particular hit as all further additions of hits would result in unacceptable circle fits or there could be no hits in near vicinity to add on. In this case FELIX would invoke the back track algorithm to delete the last hit and back track to the previous layer and starting toward a different direction. When possibilities with the outer most layer hits as the starting points were exhausted, the starting points would be moved inward layer by layer to find shorter tracks.

The procedure had a built-in ordering for selecting hits from the next layer so that high momentum tracks could be found earlier and faster without going through too many improbable combinations. The finding procedure was performed for several passes with gradually relaxing constraints which was economical because later passes were much faster with loose cuts when previous passes already masked out many of the hits.

The reconstructions of tracks in $s - z$ proceeded after the $r - \phi$ searches were completed with similar ways of obtaining DC α wire hits around an $r - \phi$ track as in MILL. However, the following straight line track finding in $s - z$ used the back track algorithm again.

For all track finders, the $s - z$ information in the standard tracking came purely from the DC α wires. The CPC cathodes and VXD charge division information were not used because of their limited resolutions.

The more exhaustive search carried out by FELIX compared to MILL and PASS5 gave a good efficiency for FELIX to find tracks. This was especially favourable in case of needing tracks with VXD hit associations since PASS5 efficiency was restricted to find only a subset of tracks from MILL and limited also by the requirement of 4 VXD hits for a track at minimum. This lead to the choice of using tracks found by FELIX as the standard for this analysis. However, FELIX was more time consuming and sometimes was over enthusiastic to find tracks which gave slightly more spurious tracks. This did not present very much difficulty as the spurious tracks were often easily rejected with sensible track selection cuts.

Scattering Fit

The material between the last layer of VXD and the first layer of DC amounted to 7.5% of a radiation length. This could cause significant multiple scattering especially for the low momentum tracks and subsequently degrade the track quality from a single circle fit.

A general track and vertex fitting package [68] had been developed by D. Saxon to include the effect of multiple scattering in the fit and which also allowed rejections of bad hits. When applied to the specific case of TASSO, improvement in both track geometry parameters near the beam position and track momentum resolution were obtained.

For this analysis, only the relatively simple option of refitting tracks in $r - \phi$ plane without any vertex or beam constraint was used. The hits as found by FELIX were used and $r - \phi$ geometry parameters for a track were refitted allowing a kink located at a radius of 16 cm and the kink angle θ was an additional free parameter in fit. An extra contribution of θ^2/θ_0^2 was added in the χ^2 sum, with the scattering weighting given by

$$\theta_0 = \frac{0.15}{P}\sqrt{l}$$

where P was the starting value of the track momentum and the material radiation length l was empirically chosen to be 6%.

The option of bad hit deletion was used to avoid hits falsely assigned by the track finder pulling the track fit result. If a track fit χ^2/NDF exceeded 2, the hit deletion process would be attempted starting with the removal of the hit with the largest contribution in the χ^2 sum until the χ^2/NDF fell below 2 or the maximum number of allowed deletions were reached. The maximum hit deletion was set to 2 for most of this analysis.

Chapter 3

The Vertex Detector

The installation of the TASSO vertex detector [69] in 1982 was a major improvement in track resolutions and allowed precision measurements of lifetimes of the short lived heavy flavour particles. Also because of this improvement, the analysis of b enrichment by decay vertex tagging became possible. Therefore, a detailed account of the performance of the vertex detector (VXD) will be given in this chapter.

3.1 Chamber Geometry & Operation Setup

The TASSO VXD had 8 sense layers with 72 sense wires per layer for the inner 4 layers and 108 sense wires per layer for the outer 4 layers. There were a pair of cathode wires separated by 1.2 mm radially situated between 2 neighbouring sense wires in a layer to define the cells. The wires were staggered by half a cell between neighbouring layers to minimise the effect of hit left-right ambiguities. The active length of the chamber was 57.2 cm. The various views of the VXD are shown in Fig. 3.1. The detailed geometry parameters are listed in Table 3.1.

The sense wires were 20 μm in diameter and made of gold plated tungsten-rhenium alloy. The cathode wires were 100 μm in diameter and made of silver

Layer	Radius (cm)	No. of Wire Cells	1/2 Cell Width (mm)
Inner Equipotential	7.50	—	—
1	8.12	72	3.54
2	8.82	72	3.85
3	9.52	72	4.15
4	10.22	72	4.46
Guard Wires	11.52	72	—
5	12.82	108	3.73
6	13.52	108	3.93
7	14.22	108	4.14
8	14.92	108	4.34
Outer Equipotential	15.40	—	—

Table 3.1: VXD Geometry Specifications.

Material	Inner Radius (cm)	Thickness (cm)	X (%)
Cu Coating	6.67	0.0015	0.10
Be Beam Pipe	6.67	0.18	0.51
'Xenon Chamber'			
(95/5 Ar/CO_2 3 bar)	6.85	0.64	0.002
Kapton Inner Wall	7.50	0.0125	0.04
Al Inner Equipotential	7.50	0.0050	0.06
Chamber gas			
(95/5 Ar/CO_2 3 bar)	7.50	7.90	0.21
Cu Outer Equipotential	15.40	0.0030	0.20
Kapton Outer Wall	15.40	0.0125	0.04
Al Pressure Vessel	15.95	0.15	1.69

Table 3.2: Material Specifications of Beam pipe and VXD Assembly.

plated beryllium-copper alloy. The accuracy of the sense wire alignment was $\sim 15\ \mu m$ in the azimuthal direction. The materials in the beam pipe and VXD assembly are listed in Table 3.1 with X being the material thickness in percentage of a radiation length.

The gas mixture used was 95/5 Ar/CO_2 at 3 atmospheric pressure with argon bubbling through water and CO_2 bubbling through ethanol. The 'Xenon chamber' was originally designed to reduce currents due to synchrotron radiations but was normally only filled with the same gas mixture as in the main VXD chamber.

The arrangement of the electronics and high voltage supplies are shown in Fig. 3.2. The characteristic impedance of the wire system was 380 Ω as seen by the signals on the sense wires. Only layers 3,4,7,8 were terminated and

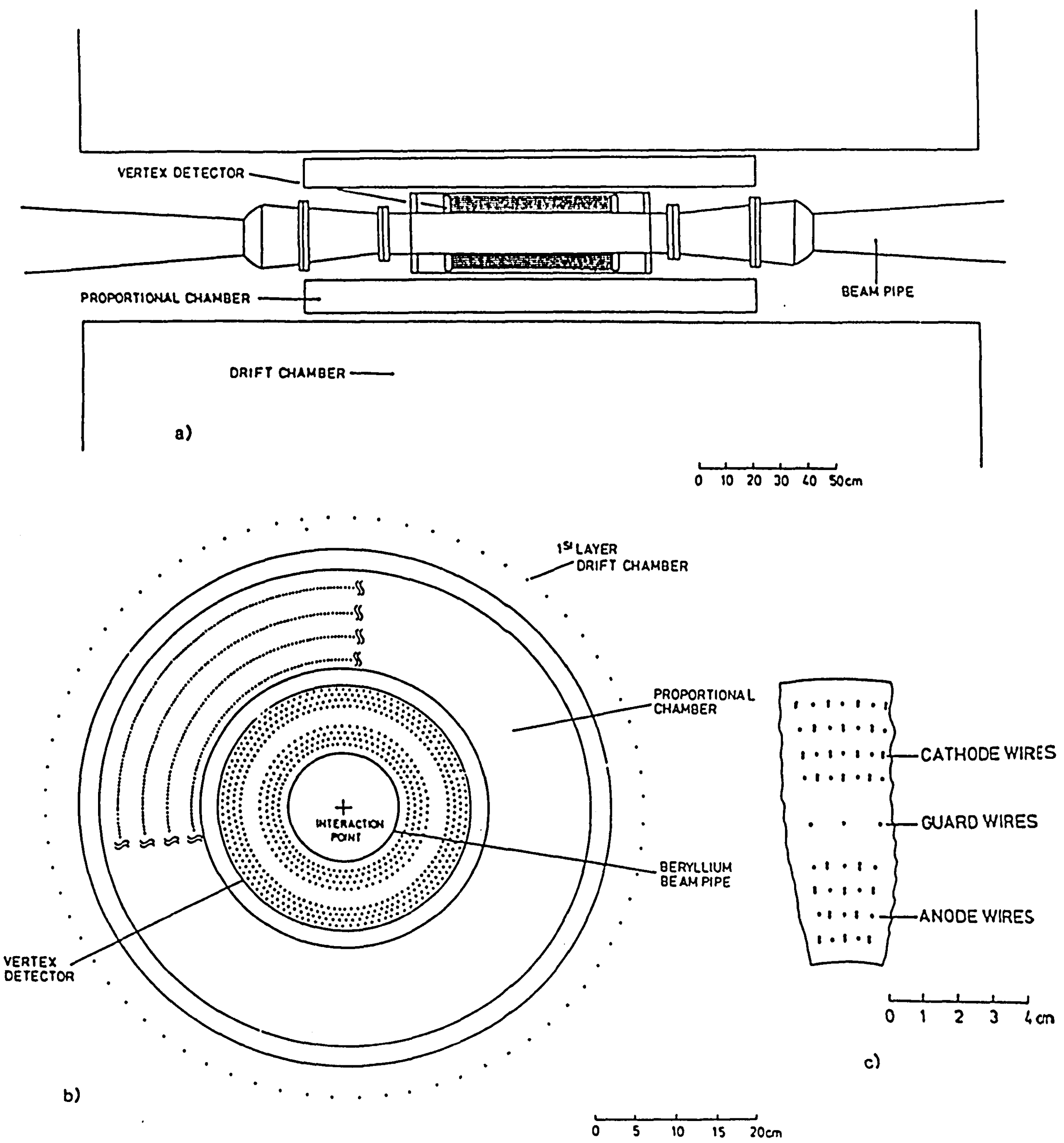

Figure 3.1: a) VXD viewed horizontally from side. b) VXD viewed along the direction of the beams. c) An expanded view of the VXD end flange to illustrate the the cell geometry.

instrumented at both ends of the chamber while the east ends of layers 1,2,5,6 were open circuits.

The signals at the west end from all wires were digitised at the discriminators and subsequently fed into the 0.5 ns per channel Lecroy 4290 TDC system to provide the crucial drift time measurements. The system operated in 'COMMON STOP' mode with the TDC channels started by the hits on individual wires separately and then all stopped at the same time by a delayed pulse derived from the beam pick-up strobe. The online calibration to line up the channels in time was done by means of an external autotrim at the beginning of every data taking run.

The wire signals were split after amplification and before digitising in the discriminators so that the analogue signals from all west end wires were fed into an $r-\phi$ trigger processor which acted as part of the integrated main system of charge track triggers in 1986. Owing to the short length of the VXD, this gave a large rejection of events which took place away from the interaction point in the z direction. The analogue signals from layers 3,4,7,8 were also fed into an ADC system at both ends to provide a charge division measurement for the hit z coordinates. However, due to the limited accuracy obtainable from this charge division system, only the main drift chamber stereo layers were used to provide the track hit z coordinate measurements in the standard tracking.

The discriminator cards used were constant-fraction discriminators designed by D. J. White at the Rutherford Appleton Laboratory. The operational principle of this discriminator system is shown schematically in Fig 3.3. A threshold level was also built in to accept only pulses with sufficiently large pulse heights so that the electronic noise were suppressed. The aim of the design was to reduce the time 'slewing' due to a simple threshold time readout on pulses with different pulse heights.

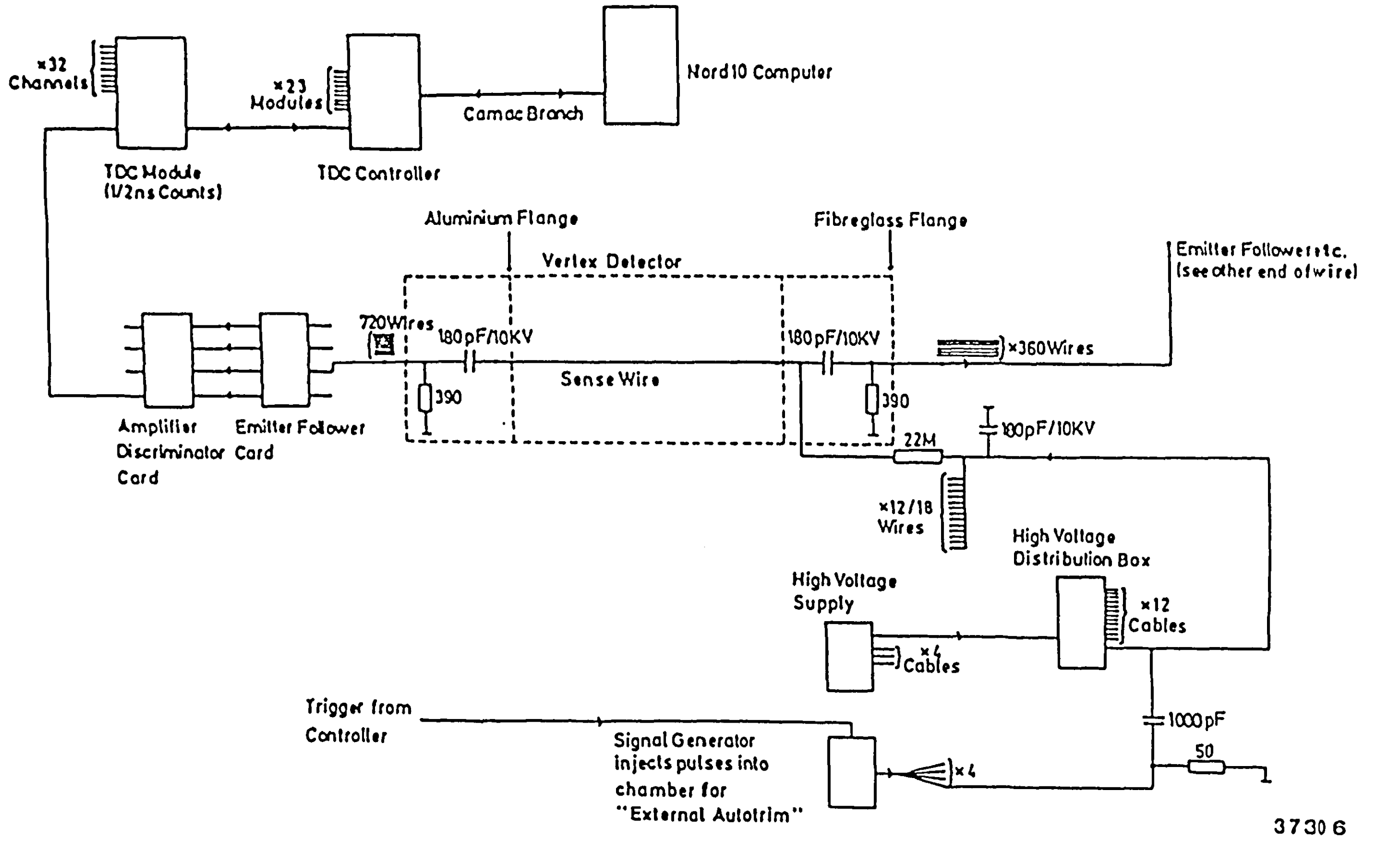

Figure 3.2: The VXD Electronics Chain

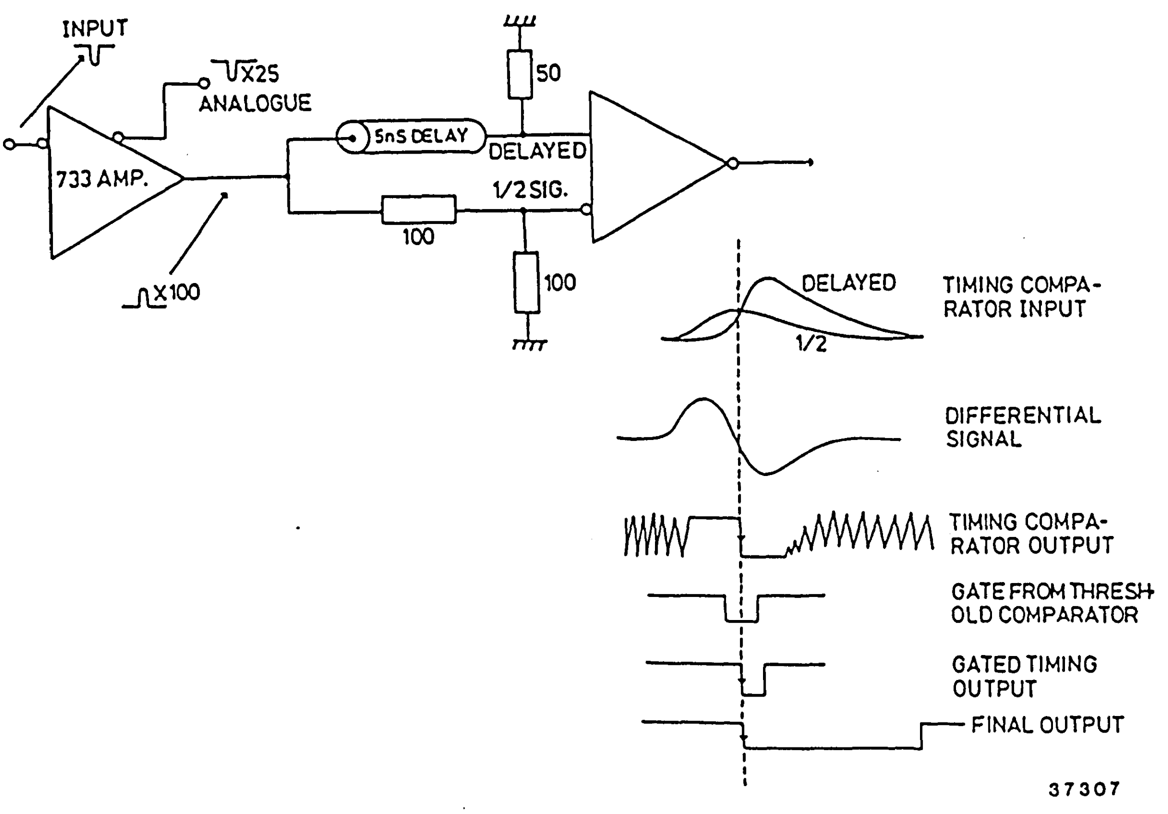

Figure 3.3: The Operational Principle of Constant Fraction Discriminator

However, the constant-fraction discriminator setup (abbr. C/F setup) was only designed to work on pulses with regular shapes and a constant pulse rise time. Because of the concern of possible irregularities of pulse shapes, only the discriminators for the outer layers 5,6,7,8 were in C/F setup while the inner layers 1,2,3,4 were in a simple high-low discriminator setup (abbr. H/L setup). This later setup had the high threshold equal to the C/F setup threshold for cutting out pulses with very small pulse heights. The front edge time of the digital output of this H/L setup was simply defined by the time a pulse took to rise to a constant low threshold $\sim 1/3$ of the high threshold.

The high voltages were supplied to groups of wires separately. There were in total 24 H.V. sectors, with each inner sector contained 6×2 wires from 2 adjacent inner layers and each outer sector contained 9×2 wires from 2 adjacent outer layers. This allowed sectors with high currents or broken wires to be turned off individually. The actual applied H.V. settings will be discussed in sections dealing with hit efficiencies and chamber gain.

3.2 VXD Offline Calibrations

3.2.1 Space - Drift time Relations

The determination of Space-Drift time relation was required to translate the TDC drift time values into accurate spatial coordinates of hits. This was performed several times a year depending on the luminosity collected. A few thousands of clean back to back 2-prong events, mostly Bhabha scattering events, were selected each time for this procedure using the MILL tracks from main drift chamber and CPC hits. A set of starting values of space - drift time relations were taken from the previous period and then the track finder PASS5 was performed to associate VXD hits with the MILL tracks.

The actual TDC values of the hits associated with tracks were then plotted and the TDC value corresponding to half the maximum point on the early time rise edge was taken as a common start time T_0. The actual drift time t for a particular TDC value of T was then simply

$$t = s \cdot (T_0 - T) \tag{3.1}$$

where s is the TDC slope of 0.5 ns per TDC count in this case.

Although for most parts of a cell the electron drift velocity should be fairly constant, non-linear corrections were needed to describe more accurately the space-drift time relations for the whole range of a cell. The paths followed by the drift electrons were also influenced by the effect of the magnetic field which could give non-linear corrections as well. Judging from the sizes of the cells, a cubic polynomial was assumed for each layer separately in the determination procedure *i.e.* the distance x of a hit from the hit wire was given by

$$x = C_0 + C_1 t + C_2 t^2 + C_3 t^3 \tag{3.2}$$

Because the VXD was small in size and very close to the beam, effects due to particle time of flight, z coordinates of hits and inclined track entrance directions to wire layers etc. had a much smaller significance compared to that for the main drift chamber. Therefore, only one set of coefficients were determined for each layer. It should be noted that the presence of the constant term C_0 gave a fine calibration of the t_0 for each layer which ensured that the initially obtained common T_0 did not have to be very accurate.

The PASS5 tracks were refitted with a set of old space-drift time relation constants using the VXD hits alone and all track parameters and hit coordinates were in the *VXD coordinate system.* The hit to track residual distance

$$d_i = x_{i(hit)} - x_{i(track)} \tag{3.3}$$

was recorded for each track hit together with the corresponding drift time t_i. The required changes of the space-drift time relation coefficients were then obtained from the solutions of the 4 simultaneous equations for each layer

$$
\begin{aligned}
-\sum_i^{Hits} d_i t_i^n &= (\sum_i t_i^n)\delta C_0 + (\sum_i t_i^{n+1})\,\delta C_1 \\
&+ (\sum_i t_i^{n+2})\,\delta C_2 + (\sum_i t_i^{n+3})\,\delta C_3
\end{aligned} \tag{3.4}
$$

with n = 0,1,2,3 and all the sums were calculated constants from hits. A new set of space-drift time relation coefficients from

$$
C'_j = C_j + \delta C_j \qquad j = 0,1,2,3 \tag{3.5}
$$

were then used to iterate again until all values converged.

As expected from an approximately linear relationship, all other coefficients were generally small compared to C_1. The significance of the non-linear corrections are shown in Fig. 3.4 for a particular running period. The constant

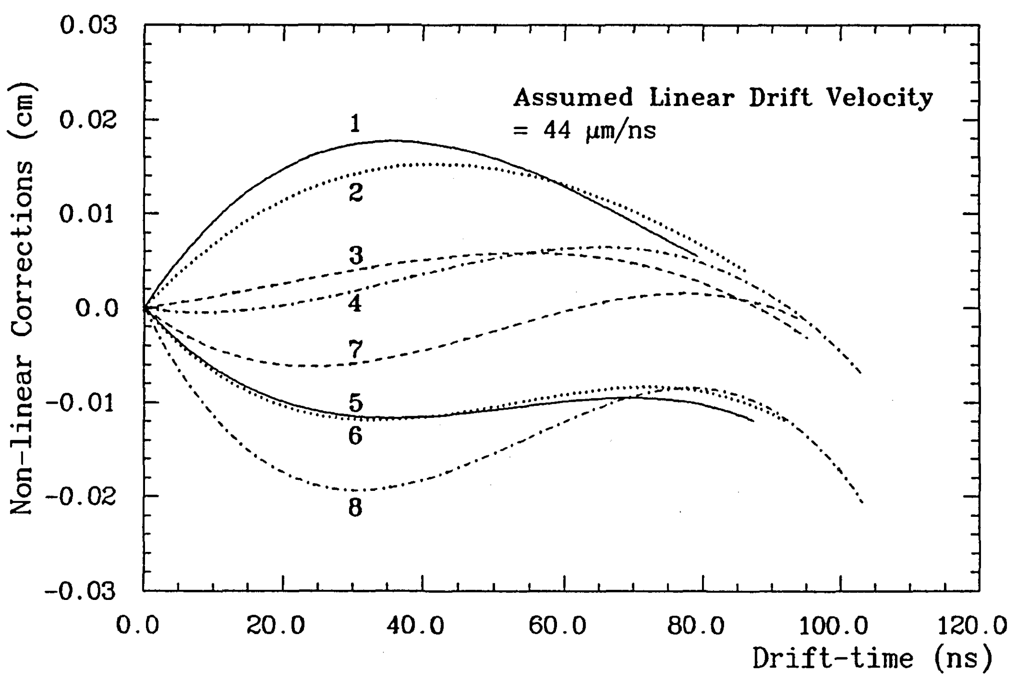

Figure 3.4: Non-linear Corrections to VXD Space-Drift Time Relations.

terms were ignored and a same linear part was subtracted out for all layers. It can be seen that the maximum corrections was $\sim 200\ \mu$m and a rough estimate of the average drift velocity gave $\sim$44 μm/ns. For the operational E field of $\sim$800 kv/cm/atm this was in reasonable agreement with the expectation from such a gas mixture [70,71].

3.2.2 VXD Alignment

To obtain the desired resolutions of track geometry parameters, the combination of accurate spatial points close to the beam from the VXD and the long lever arm of the main drift chamber was crucial. To enable such a combination to be made, an accurate determination of the relative position of the VXD with respect to the main DC was necessary.

The standard coordinate centre was defined as the centre of the main drift chamber. The position of the VXD was defined by 3 translational shifts x_v, y_v, z_v and 3 Euler angles $\alpha_{1,2,3}$. The transformation of coordinates in the VXD frame to the DC frame was an *inverse* Euler transformation as defined in Appendix A. Owing to the poor track resolutions in z, and also the rather insignificant use of the track z_0 in the analysis, the value of z_v had no particular importance.

The determination of the constants were performed at a frequency corresponding to a luminosity collection of $\sim$ every 10 pb^{-1}, the same as the determination of the space-drift time relations. This was again done with a few thousands of back to back high energy 2-prong events. Three different methods were employed for this procedure and the results were normally finalised only when all methods were in agreement with each other to the order of $\sim 10\mu$m.

The first method to be described here was developed together with the general study of VXD performance discussed in this chapter. A set of old position constants were used initially for track finders FELIX or PASS5 to give associated VXD hits for the tracks. The main procedure, however, used MILL tracks fitted with main DC and CPC hits only and then projected into the VXD. The position where a track was supposed to pass a VXD layer was calculated, then the residuals of the corresponding FELIX/PASS5 VXD hits to the projected MILL track were recorded as

$$\delta\phi \;=\; \phi_{hit} \;-\; \phi_{track} \tag{3.6}$$

The method determined different constants by separating events into various categories depending on the 2-prong event topology so that each category was only sensitive to 1 or 2 constants. The variables used for topology definitions were

$$\begin{array}{lll} \bar{\phi} & = \text{Average } \phi \text{ value of the 2 tracks} & (\text{-}45^\circ \leq \bar{\phi} \leq 135^\circ) \\ \bar{\theta} & = \text{Average } \theta \text{ value of the 2 tracks} & (0^\circ \leq \bar{\theta} \leq 90^\circ) \end{array}$$

The overall rotation $\Delta\phi$ from the assumed old position was obtained from the mean value of the $\delta\phi$ sum distribution as

$$\Delta\phi \;=\; \langle\; \frac{-\,(\delta\phi_1 + \delta\phi_2)}{2} \;\rangle \tag{3.7}$$

for all $\bar{\phi}$ pairs with $\bar{\theta} > 45^\circ$ to limit broadening due to tilt. The operation $\langle ... \rangle$ in the above equation meant the average value of the quantity inside the angled bracket, for all track hits in the distribution. The effect of x,y shifts and tilt should all cancel statistically leaving the mean equal purely to the rotation. Translating to the Euler angle definitions, this gave

$$\Delta(\alpha_1 + \alpha_3) \;=\; \Delta\phi \tag{3.8}$$

The y shift was obtained using large θ angle horizontal pairs with $\bar{\theta} >45^\circ$ and -45° $< \bar{\phi} <$45°. The pair of hits on the same VXD layer which were assigned the two opposite tracks respectively, were grouped together to give one entry in a distributon so that the shift from the old position was given by

$$\Delta y_v \;=\; \langle \; \frac{r \cdot (\delta\phi_{Right} - \delta\phi_{Left})}{-2cos\bar{\phi}} \; \rangle \tag{3.9}$$

where r is the radius of the chamber a hit was in. Rotation and tilt should cancel locally for each entry due to the subtraction of $\delta\phi$ from two opposite tracks. The effect of the x shift was not only small in magnitude, it should also cancel statistically due to the symmetric distribution of $+\bar{\phi}$ and -$\bar{\phi}$ events. The same technique of pairing hits was also used in the determinations of x shift and tilt as will be described soon.

Similarly the x shift was obtained using large θ angle vertical pairs with $\bar{\theta}$ >45° and 45° < $\bar{\phi}$ <135°. The shift from the old position was given by

$$\Delta x_v \;=\; \langle \; \frac{r \cdot (\delta\phi_{Up} - \delta\phi_{Down})}{2sin\bar{\phi}} \; \rangle \tag{3.10}$$

The magnitude of the tilt was given by the Euler angle α_2 while the direction of tilt was controlled by either α_1 or α_3. An extra definition of event z polarity was required to force the distributions to be symmetric to rotation and shift but anti-symmetric to tilt. The z polarity was defined by:
For events horizontal in the $r - \phi$ plane,

$S_z = +1$	if the Right track was in +z direction	
$= -1$	if the Left track was in +z direction	

For events vertical in the $r - \phi$ plane,

$S_z = +1$	if the Up	track was in +z direction
$= -1$	if the Down	track was in +z direction

In this case, only the low θ angle events with $\bar{\theta}$ <63° were used and again separated to horizontal and vertical types depending on event $\bar{\phi}$. The tilt angle x, y components $\Delta\beta_{x,y}$ were obtained from

$$\Delta\beta_y = \langle \frac{S_z \cdot (\delta\phi_{Right} + \delta\phi_{Left})}{-2cot\bar{\theta}cos\bar{\phi}} \rangle \tag{3.11}$$

using the horizontal types and

$$\Delta\beta_x = \langle \frac{S_z \cdot (\delta\phi_{Up} + \delta\phi_{Down})}{2cot\bar{\theta}sin\bar{\phi}} \rangle \tag{3.12}$$

using the vertical types.

The new set of Euler angles $\alpha'_{1,2,3}$ were then calculated from the old values $\alpha_{1,2,3}$ from

$$\alpha'_2 = \sqrt{(\alpha_2 sin\alpha_1 + \Delta\beta_x)^2 + (-\alpha_2 cos\alpha_1 + \Delta\beta_y)^2} \tag{3.13}$$

$$\alpha'_1 = tan^{-1}\left\{\frac{\alpha_2 sin\alpha_1 + \Delta\beta_x}{\alpha_2 cos\alpha_1 - \Delta\beta_y}\right\} \tag{3.14}$$

$$\alpha'_3 = -\alpha'_1 + \alpha_1 + \alpha_3 + \Delta\phi \tag{3.15}$$

The second method also used residuals of PASS5 VXD hits with respect to projected MILL tracks. The residuals of all track hits in all events were accumulated together to build a set of simultaneous equations

$$\sum_i^{Hits} f_i^{(n)}\delta\phi_i = \sum_{(k=1)}^{5}\sum_i^{Hits}(f_i^{(n)}f_i^{(k)})\cdot v^{(k)} \qquad n = 1,2,3,4,5 \tag{3.16}$$

where the unknown vector $v^{(k)}$ contained 5 independent position variables

$$v^{(1,2,3,4,5)} = (\ \Delta\phi,\ \Delta x,\ \Delta y,\ \Delta\beta_x,\ \Delta\beta_y\ ) \tag{3.17}$$

under the same definition as the previous method. The vector $f_i^{(n)}$ contained coefficients evaluated for each hit i separately so that $f_i^{(n)}v^{(n)}$ would give the contribution along $v^{(n)}$ in residual distance. These coefficients were

$$f_i^{(1,2,3,4,5)} = (\ r_i,\ sin\phi_i,\ -cos\phi_i,\ z_i sin\phi_i,\ -z_i cos\phi_i\ ) \tag{3.18}$$

The coefficients can be seen to have similar origins as the previous method. The main difference from the previous method was that the solution from simultaneous equations gave correlated values for the position constants.

The third method used the x, y shifts taken from one of the two other methods and then the tracks were refitted with different assumed Euler angles. The controlling variable was the d_0 separation of the two back to back tracks near the beam position which was found to be the most sensitive variable to the rotation and tilt. The Euler angles were obtained by iterations until the distributions of 2-prong d_0 separations at various ϕ and z regions with various polarity factors were all centred at zero. This was a direct calibration of the impact parameters and the widths of the d_0 separations also gave sensitive indications of alignment errors.

The statistical accuracy was $\sim 10\ \mu$m averaged over a whole running period for each constant. Justification of this accuracy can be taken from the good agreement between different methods. The x, y shifts were found to be less important compared to the rotation and tilt as long as the track fit and beam spot finding used the same constants. This can be understood from the fact that all tracks would move together without significant distortion in relative positions of tracks if there were a small error in translation constants.

3.2.3 Summary Comments

The three procedures of determining space-drift time relations, VXD alignment constants and run by run beam spot positions (see section 3.8) were designed to be very much independent of each other. The determination of space-drift time relation was performed in the VXD coordinate system with track fits independent of the VXD alignment constants or beam spot. Because the discrepancies in space-drift time relations could only produce shifts locally symmetric to each wire, it could not make any global effects on the alignment constants. The determination of the beam spot positions normally proceeded after the alignment had been done. However, because it was performed using PASS5 tracks with track geometry at the beam position fitted from VXD hits only, the results were always valid in the VXD coordinate system even with a wrong set of alignment constants. Thus the beam spot positions could be easily translated according to a new set of alignment constants when necessary.

3.3 Background Noise in VXD

In the normal operation of the VXD under the colliding beam environment, there were always noise hits as well as the good hits related to the tracks of interest. There were 3 distinct contributions to the background noise:

a) Discrete noise hits induced by synchrontron radiation. This was the most frequent contribution accounting for $\sim 80\%$ of all noise hits.

b) Coherent noise hit clusters due to off-momentum particle showers in the VXD. This occured for $\sim 7\%$ of all events and $\sim 20\%$ of these events had large numbers of noise hits in clusters.

c) Extra background hits in hadronic events induced by the large number of tracks. This was seen as a small but nevertheless consistent excess of extra hits in hadronic events which represented $\sim 5\%$ of all noise hits.

Categories **a)** and **b)** were studied mainly using random beam crossing events taken irrespective to the trigger condition. This was to avoid the confusion with the track hits in triggered events. It was found that clusters of noise hits were very different from the isolated ones.

3.3.1 Synchrotron Induced Noise Hits

There were adjustable collimators located at ± 4.5m from the beam colliding point along the beam just in front of the final focusing mini-beta quadrupoles. The beam pipe and collimator design ensured that most of the direct synchrotron photons would not have large enough θ displacement to reach the beam pipe. Only when these photons hit the far side collimator and scattered backward could they then hit the detector. Most of these backscattered photons with energies <50 keV were absorbed by the copper shield inside the beam pipe mainly via photoelectric processes. The ejected photoelectrons had a few keV of kinetic energy and were quickly re-absorbed before they could reach the wires. However a fraction of the de-excitation processes of the copper atoms could yield fluorescence photons with energies peaked at around 8.0 keV. This corresponded to transitions of atomic electrons from outer shells down to the K-shell of the copper atoms. The rest of the de-excitations yielded short range electrons again.

When these fluorescence photons were emitted into the chamber they could be absorbed by the argon to produce noise hits. When the argon K-shell electrons with binding energies of 3.2 keV were ejected as photoelectrons from the absorptions of 8.0 keV photons, their escape kinetic energy should peak at 4.8 keV. The de-excitation of an argon atom would either yield a fluorescence photon just below the argon K-edge absorption energy or eject another electron with kinetic energy ~ 3.2 keV via the Auger effect. In both cases, the practical ranges of the a few keV electrons should be no more than a few hundred μm in the gas mixture. So they would simply cause local ionisation energy releases equal to the kinetic energies carried by the ejected atomic electrons. However the 3 keV photons could travel further due to the low absorption cross-section so that they could be absorbed near some other wire or escape the chamber. This meant that the noise hits due to the 8.0 keV fluorescence photons should have characteristic pulse heights corresponding to energy losses of 8.0 keV, 4.8 keV and ~3.2 keV respectively in order of decreasing importance. The argon at 3 bars of pressure has a rather short absorption length of ~ 2.0 cm for 8 keV photons. This means that the multi-stage process described above should have given frequent isolated hits mainly in the first few layers.

To verify the above proposition, the various properties of the VXD hits in 'clean' beam crossing events were studied with a rejection on events which contained large hit clusters. The detailed separation criteria will be described in section 3.3.2 dealing with shower hit clusters.

The fact that most of these hits were not due to direct synchrotron radiation photons can be seen from the TDC distribution of hits in clean random beam crossing events as in Fig. 3.5 compared to track hits TDC values as in Fig. 3.6. The larger TDC values corresponded to hits recorded earlier in time and 1 TDC count was 0.5 ns. The ~ 30ns delay of the large rising edge of the random noise hits compared to the front edge time t_0 of the track hits, corresponded to the time required for a return trip of the synchrotron radiation photons from the collimators 4.5 m away from the interaction point.

A further evidence of the synchrotron induced origin of the random noise hits came from the ADC pulse heights for these hits. The VXD layer 4 ADC values of the random hit pulse heights are plotted in Fig. 3.7 together with normalised track hit ADC values for the electrons in Bhabha scattering events. The raw ADC pulse heights of the Bhabha track hits were scaled by dividing the estimated ionisation sampling length in a layer calculated from the track θ angle and the position it crossed a cell. The normalised value corresponded to ionisation energy release per cm per atm which should peak at ~ 2 keV. Taking the ADC values of the Bhabha track hits as a scale, the two peaks in the random hit ADC value distribution are consistent with one being 8 keV and the other being an unresolved mixture of 3.2 and 4.8 keV.

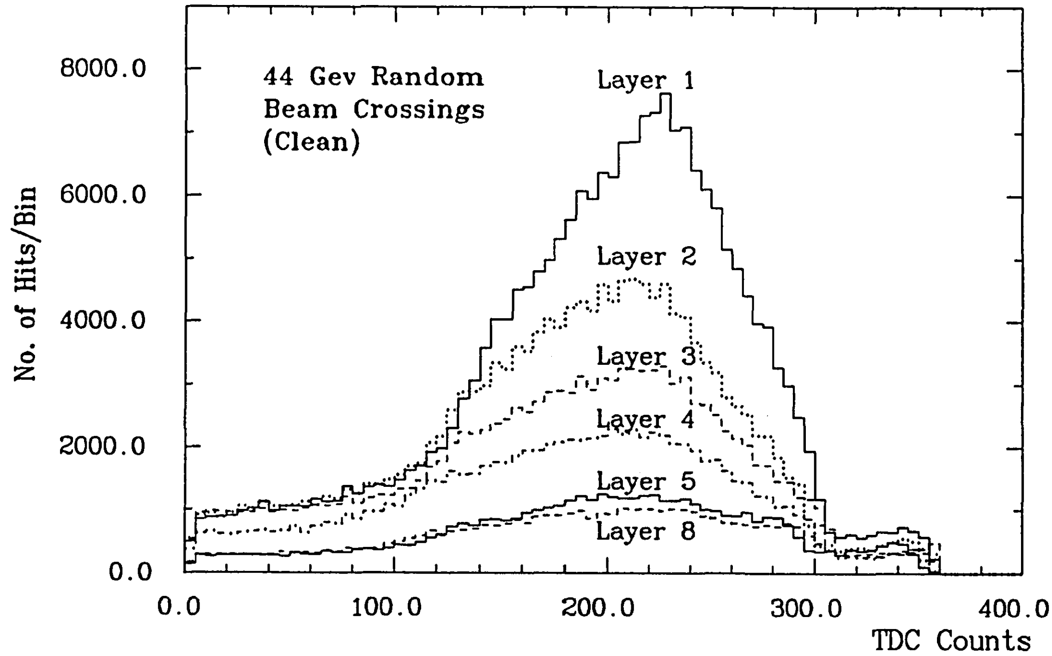

Figure 3.5: TDC Values of VXD Hits in Clean Random Beam Crossing Events.

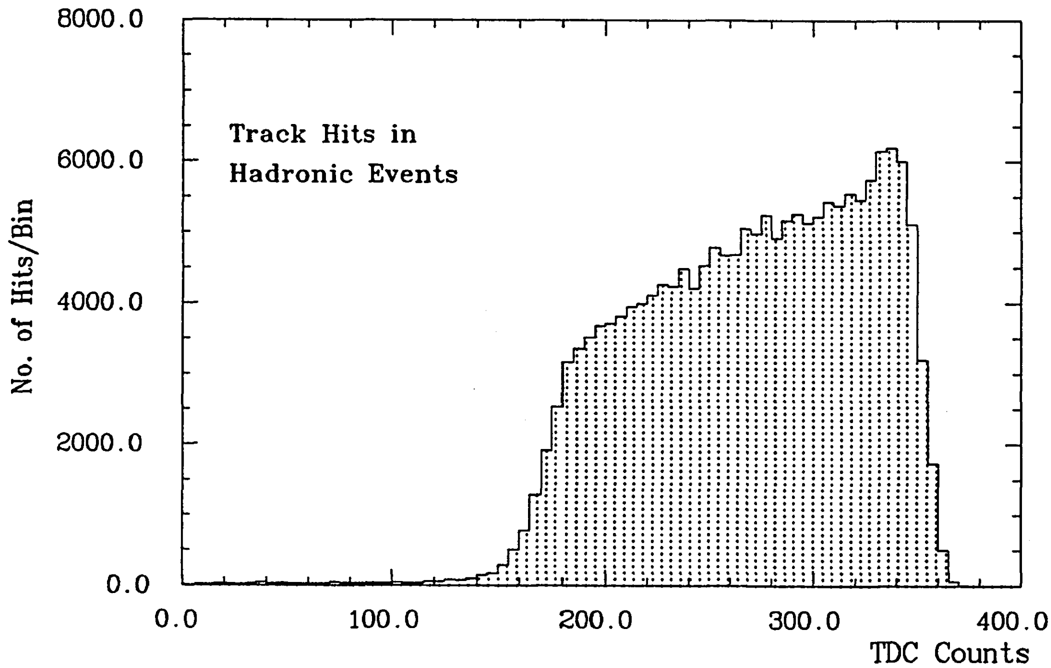

Figure 3.6: TDC Values of Track VXD Hits in Hadronic Events.

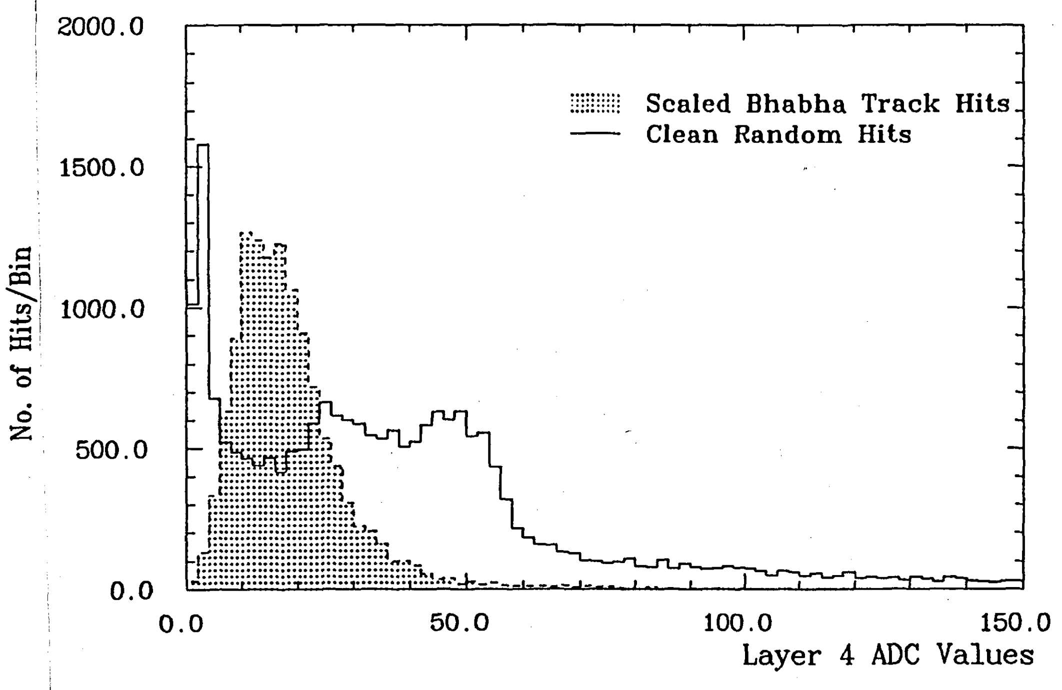

Figure 3.7: ADC Values of Isolated VXD Hits in Clean Random Beam Crossing Events Compared to Scaled ADC values of Bhabha Track Hits.

The average hit multiplicities on different layers for clean random beam crossings are listed in Table 3.3 separately for three running periods with e^+e^- centre of mass energies of 44 GeV, 38 GeV and 35 GeV respectively. Corrections were made to scale up the hits for layers with dead wire sectors.

These multiplicity values are plotted in the Fig 3.8 together with the fit results for a naive attenuation exponential function plus a constant term to allow for a small remaining unseparated contribution from shower hit clusters. The function of the form

$$f(r_i) = Ae^{-(r_i - r_0)/l} + B$$

was first fitted with 3 variable parameters A, B, l. r_i is the radius of the ith cylindrical VXD layer and r_0 was fixed to the beam pipe radius of 6.7 cm. It was found that the fitted values of l were nearly the same for 3 different energies as expected. So the value of l was then also fixed and the subsequent fitting was performed allowing only A, B to vary. The fitting results are listed in Table 3.4 and also plotted in Fig. 3.8.

VXD Layers	44 GeV	38 GeV	35 GeV
1	16.6	10.0	7.7
2	12.3	7.2	5.0
3	8.9	5.1	3.7
4	6.3	3.5	2.5
5	3.3	1.7	1.1
6	3.1	1.5	1.0
7	3.1	1.5	1.1
8	3.1	1.5	1.0

Table 3.3: Clean Random Beam Crossing Average VXD Hit Multiplicity.

Energy	A	B	r_0(cm)	l (cm)
44 GeV	34.7	2.7		
38 GeV	21.6	1.3	6.7	1.6
35 GeV	16.9	0.8		

Table 3.4: Fitted Parameters of Mean VXD Hit Multiplicity Function.

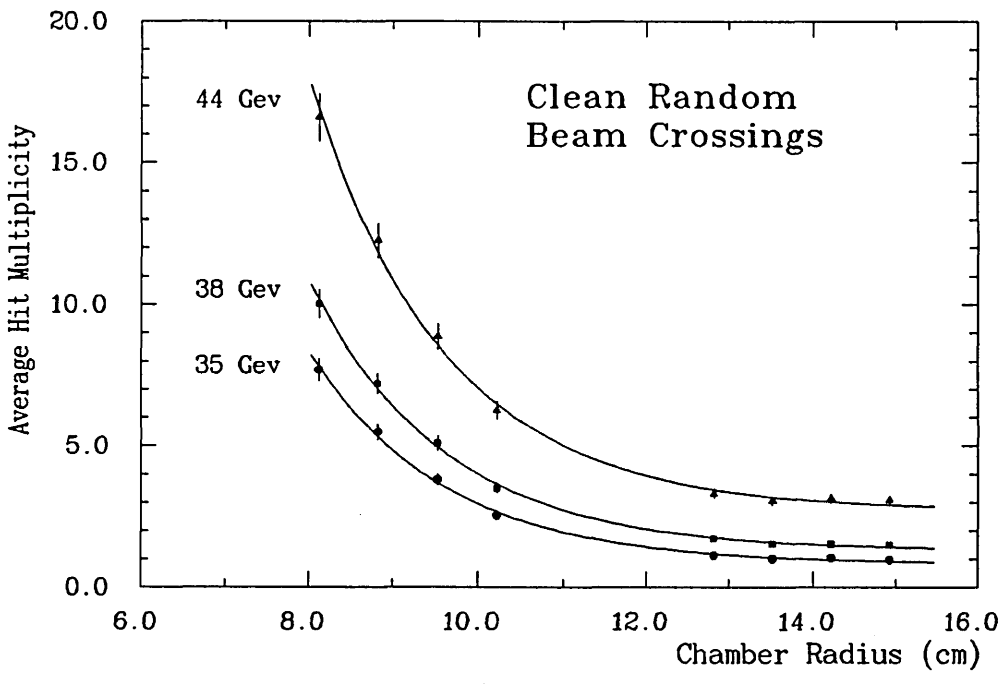

Figure 3.8: VXD Hit Multiplicities in Clean Random Beam Crossings During Different e^+e^- C.M Energy Runnings.

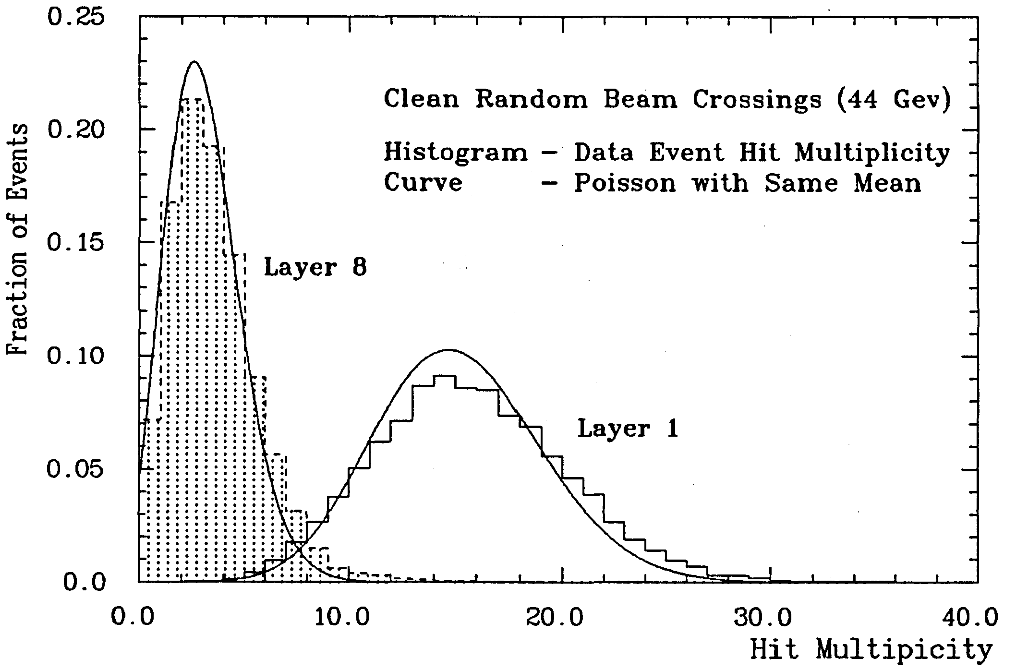

Figure 3.9: VXD Hit Multiplicities in Clean Random Beam Crossings and Simulated Poisson curves.

It should be noted from Table 3.4 that the fitted value of l was very close to the expected actual attenuation length of 8 keV photons in 3 atm argon. A clear conclusion to be made from the attenuation feature is that the 1.4 cm gap between the beam pipe and the first layer of wires was quite necessary if only the normal gas mixture was filled in that region. The dependence on beam energy should not be taken as a general result but rather under the specific machine characteristics of PETRA at different energies.

For the purpose of Monte Carlo simulation of noise hits of this type, one can simply take the average multiplicity at the relevant energy and select single hit wire randomly in ϕ. The spread of hit multiplicities around the mean can be described by Poisson distributions with the same mean values as demonstrated in Fig. 3.9

3.3.2 Coherent Noise Hit Clusters

Because the VXD was situated very close to the beam, both frequent off-momentum particle showers and some high momentum Compton scatterings in the $\sim$ 1 MeV range could result in coherent noise hit clusters of various sizes.

The random beam crossing events with such hit clusters were selected by grouping the wires into sectors with 4×9 wires in each, and counting the number of hits within each sector. This was done twice with 2 different groupings corresponding to a shift in ϕ of half a sector. An event containing ≥ 1 sector with more than half of the wires registering hits was selected as a shower cluster event.

These events occurred at a rate of $\sim 7\%$ of all random beam crossings, similar for the 3 running periods at e^+e^- centre of mass of 44, 38 and 35 GeV with quite different running conditions. The rather severe events with ≥ 3

such sectors occured at a rate of $\sim 2\%$ of all beam crossings. Events with large clusters of hits could have very serious effects on the tracking as can be seen from the example shown in Fig. 3.10 which was a back to back 2-prong event initially selected from MILL tracks.

The TDC distributions of all the hits in this type of events are shown in Fig. 3.11 for the 44 GeV running which can be compared to Fig. 3.5 for the clean random beam crossings. The obvious difference between hits in shower clusters and the 'clean' synchrotron induced hits can be seen to be the peak at early times for the hits in clusters. This could greatly increase the probability of killing a track hit in the same cell if such clusters overlapped with a track in a good event. The average hit multiplicities are shown for the two classes as functions of layers for 44 GeV running in Fig. 3.12. Subtracting the 2 curves to get a rough estimation of the pure contribution from shower clusters, it can be seen that the actual contribution from the shower clusters alone had very small attenuation across the layers. It was also found that most of these clusters occured near the horizontal plane through the centre of the detector as expected from off-momentum particle showers.

3.3.3 Track Induced Background Hits

Hadronic events with many tracks also contained additional hits due to particles with very low momenta or at very low θ angles not reconstructed by the track finder. This included contributions from hard δ-rays, γ conversion or inelastic scattering products etc. Further additional noise hits might come from crosstalk either due to the return pulses on neighbouring wires next to a hit wire or due to couplings between adjacent electronic channels.

To justify the assertion that the contributions from this category were small, the extra hits appearing in the hadronic events were counted as shown

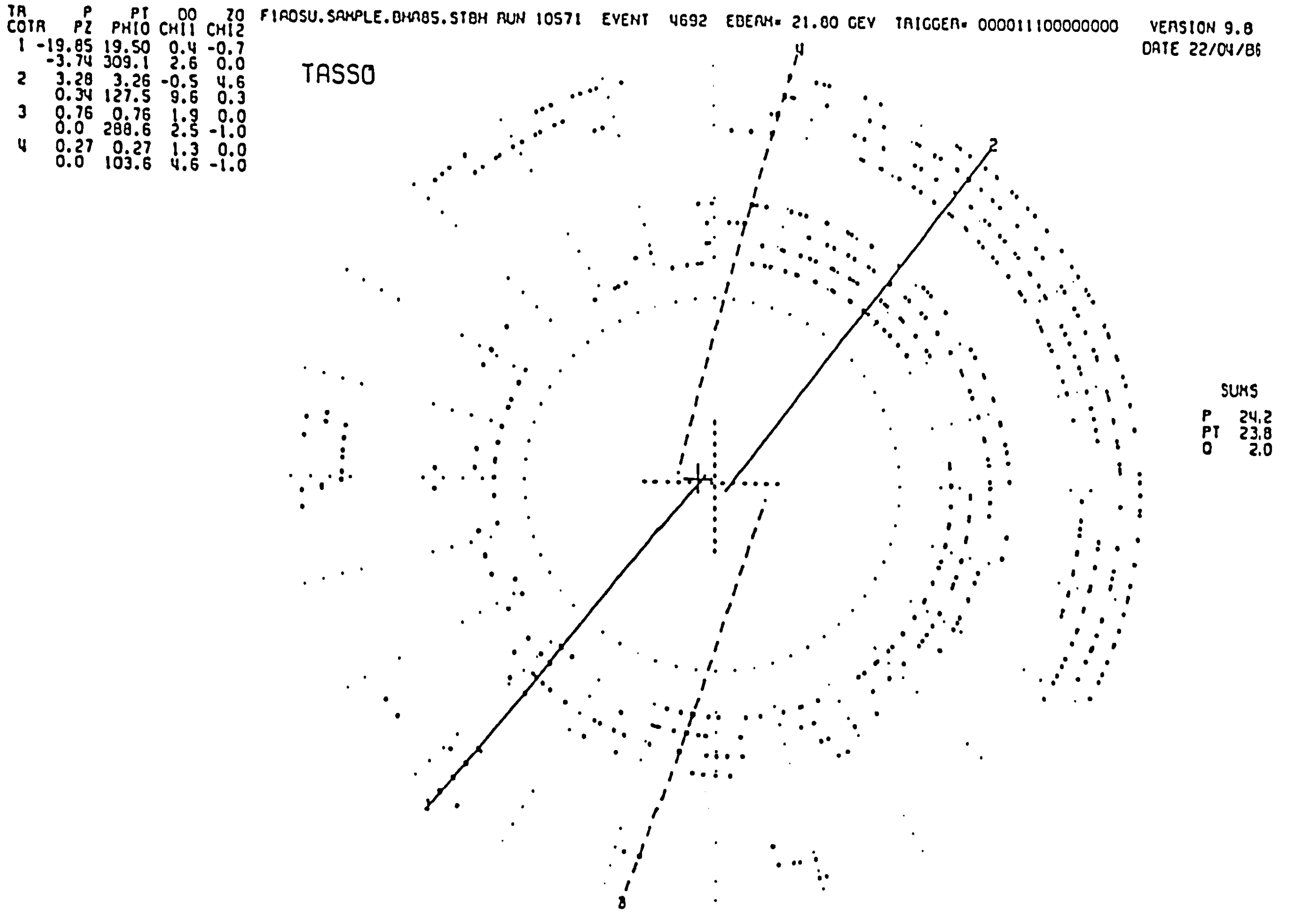

Figure 3.10: Example of a 2-prong Event with Noise Hit Clusters in VXD.

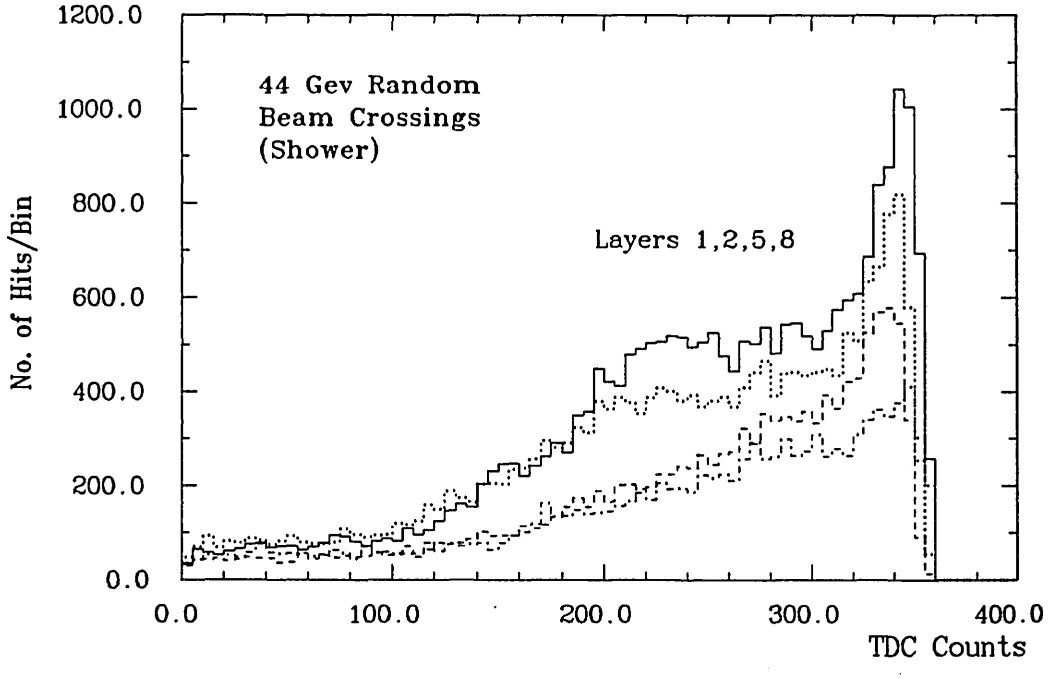

Figure 3.11: TDC Values of VXD Hits in Random Beam Crossings Contained Shower Hit Clusters.

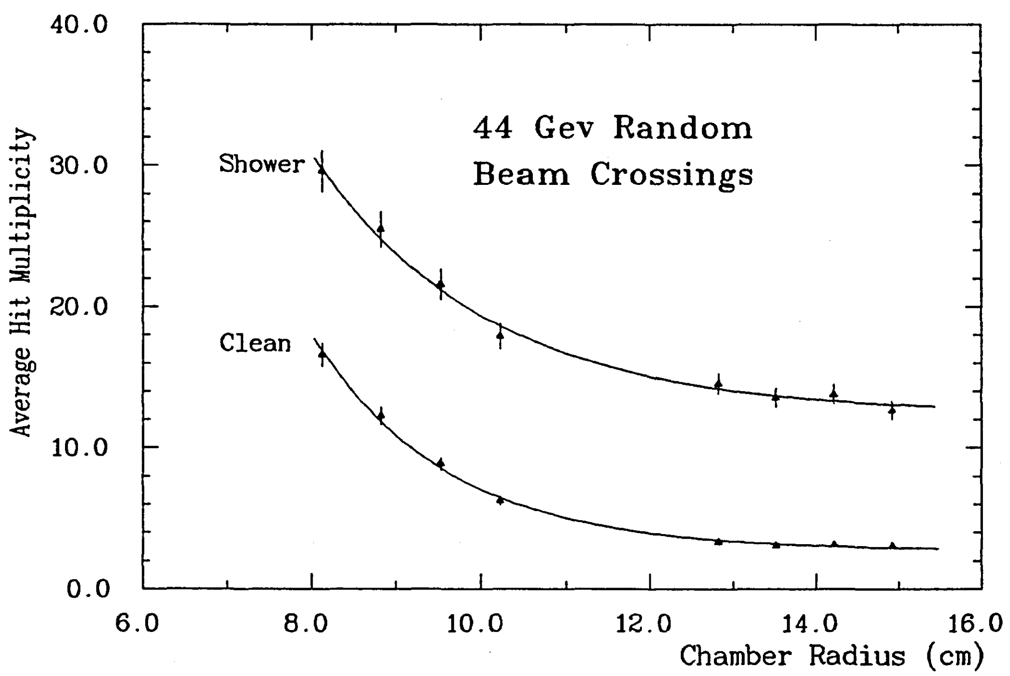

Figure 3.12: Comparison of VXD Hit Multiplicities in 'Clean' and 'Shower' Random Beam Crossings.

in Table 3.5 in comparison to the average hit multiplicities from all random beam crossing events for the same running period in 1985. The types of noise hits appearing in random beam crossings clearly explained the source for most of the total noise hits. The remaining small yet consistent excess of noise hits in the hadronic events could be attributed to the track induced background.

VXD Layers	Extra Hits in Hadronic Events	Random Beam Crossing Events	Excess in Hadronic Events
1	16.6	15.9	0.7
2	12.7	11.9	0.8
3	10.7	9.3	1.4
4	8.2	6.9	1.3
5	5.7	4.0	1.7
6	5.1	3.6	1.5
7	5.8	3.9	1.8
8	5.3	3.6	1.7

Table 3.5: Average Noise hit Multiplicities in Hadronic Events and in Random Beam Crossings.

3.4 VXD Hit Efficiency

The hit efficiencies were firstly checked using cosmic ray tracks taken when PETRA was off, with various different high voltage settings. The MILL tracks using main DC and CPC hits were projected into the VXD and the hits within $\pm$ 2 wires from the track were counted as efficient points. The resulting H.V. plateau curves are shown in the Fig. 3.13. The actual hit efficiencies at the normal operational H.V settings are listed in Table 3.6.

It can be seen from Table 3.6 that the inefficiency due to insufficient gain was very small for most of the layers except layers 4 and 8 which were slightly

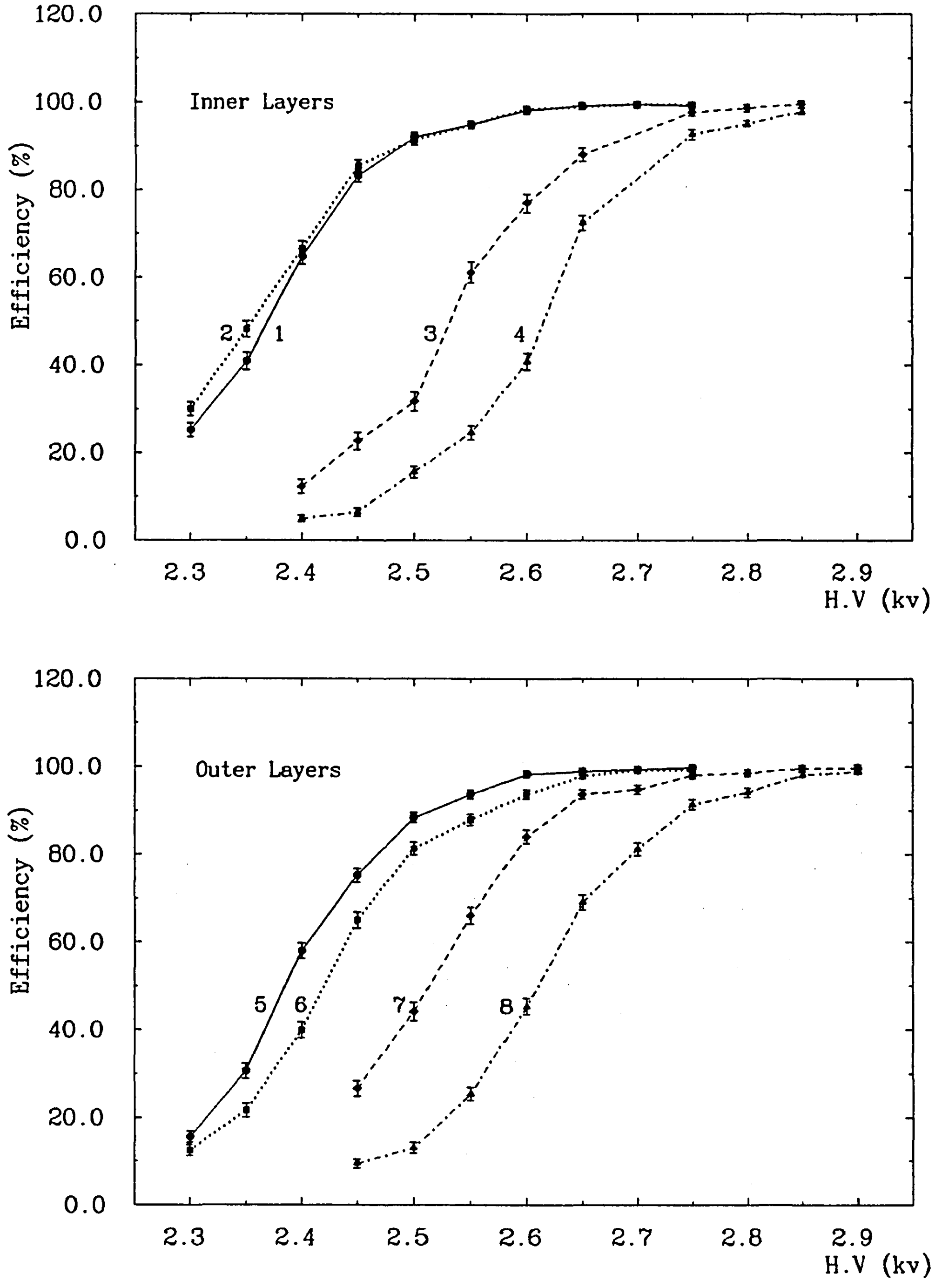

Figure 3.13: VXD H.V. Plateau Curves Obtained From Cosmics.

Layer	H.V. (kv)	Efficiency (%) (excl. dead wires)	Efficiency (%) (incl. dead wires)
1	2.70	99.4	96.6
2	2.70	99.5	98.1
3	2.80	98.6	93.0
4	2.80	95.0	93.6
5	2.70	99.3	99.3
6	2.70	99.1	96.3
7	2.85	99.6	98.7
8	2.85	98.2	97.5

Table 3.6: VXD Hit Efficiencies Obtained From Cosmics.

worse. The fact that layers 3,4,7,8 required higher voltages was because they were instrumented on both ends while the other layers had one end being open circuit. The H.V. on inner and outer equipotentials and the guard wires were set to 1 KV. The cathode wires were grounded.

The hit efficiencies in hadronic events were studied by separating the track points into different categories according to the hit-track association. There were extra reductions on useful hits due to more than one track going into the same cell, inefficiency of track finder, noise hits killing track hits, 1 dead H.V. sector etc. The relative importance of these effects is shown in Table 3.7.

The hit efficiencies were also determined directly from the hadronic events according to the hit association for each track. In the cases that a hit in the projected cell was not used by the track finder or taken by another track, the situation was rather ambiguous for efficiency calculation. So the hit efficiencies were only defined from the cases where a hit was positively assigned to the track or cell empty with inefficiencies due to dead wires included. The results for different running periods are shown in Table 3.8.

	83-84 Data (38-46 GeV)	85 data (44 GeV)	86 Data (35 GeV)
Hit assigned to track	74.1	77.7	78.3
Hit stolen by another track	11.7	10.9	10.0
Cell empty	9.2	7.3	7.9
Hit not used by track finder	5.0	4.1	3.8

Table 3.7: VXD Hit–Track Association Percentages in Hadronic Events.

Layer	83-84 Data (38-46 GeV)	85 Data (44 GeV)	86 Data (35 GeV)
1	96.0	96.9	97.2
2	94.8	95.2	95.9
3	92.8	93.7	93.0
4	91.5	95.2	92.8
5	97.6	99.5	99.4
6	95.1	96.4	96.1
7	97.1	98.5	98.5
8	94.9	98.8	97.9

Table 3.8: VXD Hit Efficiencies Obtained From Hadronic Events.

The fact that the efficiency was somewhat worse in the old data was mainly due to the bad running conditions such that some of the sectors had to be turned off to allow data taking to continue without frequent tripping. However, the results for the more recent data samples taken since 1985 with stable beam conditions, showed good agreement with the results from cosmics.

It is quite interesting to see the sources of the inefficiencies by plotting the cell position a track passed when the cell was empty. Because two layers were grouped together to form one H.V. layer, the same voltage would mean the layer with larger cell width, *i.e.* the even layer on the outside in this case would get smaller gain. Therefore these inefficient cell positions were plotted for the odd and even layers separately as seen in Fig. 3.14 where the position 0 referred

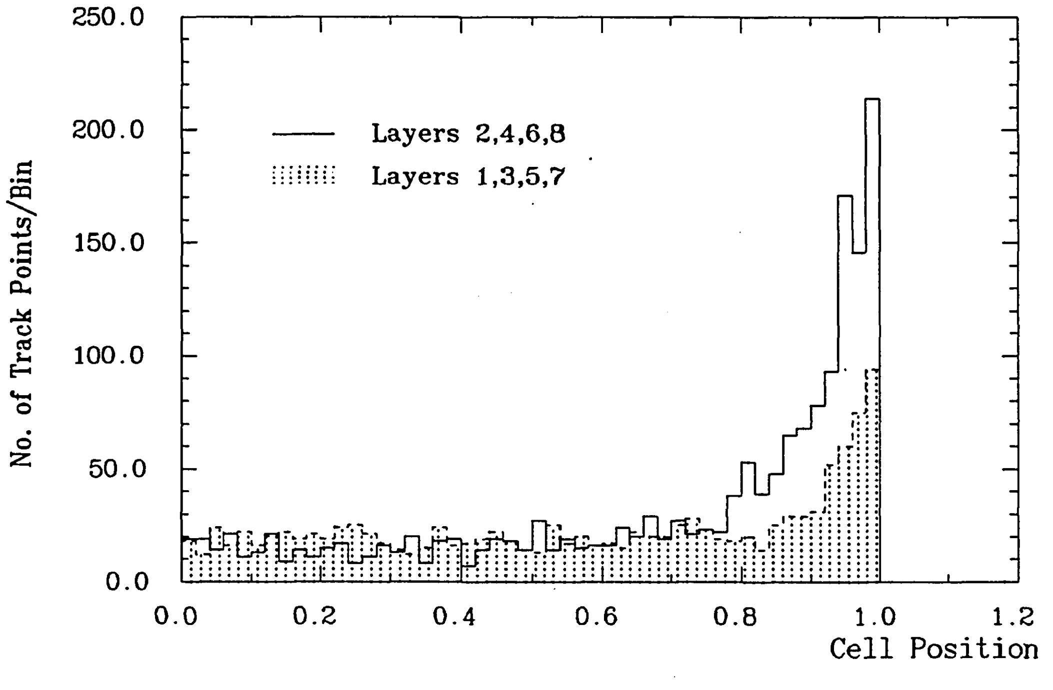

Figure 3.14: VXD Hit Inefficiency Cell Positions. (0=Sense; 1=Cathode)

to the sense wire and the position 1 was the cathode wire. The peaks at the end of cell clearly indicated the effect of insufficient ionisation collection due to the small sampling lengths near the cathode corner. Although the small errors in track geometry calculations could enhance the inefficiency near the cathode end, the difference between the odd and even layers provided the evidence independent of this error. However the integrated effect was comparable to the flat part as expected from dead wires.

3.5 Chamber Gain and Current

The main limitation of spatial resolution came from the gas amplification gain factor. A low gain condition would require a long ionisation sampling length along the track path to create a large enough pulse which resulted in the need of drift electrons with a wide spread of arrival times at the sense wire. The gain was in turn limited by the chamber current under beam induced background.

To estimate the chamber gain, the first step was to record the analogue pulse heights of 8 keV synchrotron induced hits and the slopes of pulse height variations with H.V. settings, simply using scopes. The results were checked to be consistent with the ADC values of random noise hits. A convenient unit of the chamber gain was defined with respect to the discriminator threshold so that 1/8 would correspond to the case that average pulse heights of track hits were equal to the discriminator threshold. The H.V. settings corresponding to the 1/8 gain were read from the H.V. plateau curves shown in the Fig. 3.13 at the 50% efficiency points.

It was then followed by two different ways of estimation both based on the 50% efficiency H.V. points. The gains obtained from H.V. plateau curves took the assumption of exponential dependence of gain on H.V. and used the slopes of pulse height variations with H.V. The second method took layer 4 as a normalisation point and directly scaled the gains from the pulse heights of 8 keV photon hits for different layers. The results are shown in Table 3.9. The difference between the results obtained from the two methods reflects a measure of the systematic uncertainties involved.

Layer	Operation H.V. (KV)	50% eff. H.V. (KV)	Gain (from H.V./ Pulse)
1	2.70	2.37	0.68 / 0.55
2	2.70	2.36	0.71 / 0.55
3	2.80	2.53	0.50 / 0.38
4	2.80	2.62	0.31 / 0.31
5	2.70	2.39	0.61 / 0.64
6	2.70	2.42	0.53 / 0.55
7	2.85	2.51	0.71 / 0.55
8	2.85	2.61	0.43 / 0.38

Table 3.9: The Estimated Gain Factors for Different VXD Layers.

It should be noted that actual chamber gains for layers 3,4,7,8 should be doubled since they were instrumented at both ends with only half the total pulse propagated to the west end while the other layers had the full pulse including the part reflected from the open circuit at the east end. The absolute gas gains were then estimated from the ionisation expected from 8 keV photons and the electronic amplification factors which gave an average of $\sim 2\times10^4$ with a factor of 2 between the best and the worst layers.

The actual measurements of the chamber currents due to beam induced ionisation at 44 GeV running gave on average $\sim$ 15 μA per layer for the 4 inner layers and $\sim$ 10 μA per layer for the 4 outer layers with fluctuations depending on beam conditions. At stable running condition in 1986 these currents dropped by a factor of 2 which allowed for an increase of H.V. to obtain better gain. The horizontal sectors normally had currents a factor of 2 larger than the vertical sectors and the attenuation of currents with layer radii was rather slow and which resembled the characteristics of the off-momentum particle showers. This was quite the reverse of the picture of the random noise hits where even including the larger pulse heights of the cluster hits, their relative contribution should still be smaller compared to synchrotron induced hits.

The desired chamber operation gain was 1 in the unit just defined. One of the main reasons for the lower gain obtainable was the rather large probability for drift electrons to get attached to CO_2 in the amplification region close to the sense wires. This reduced the useful drift electrons by $\sim 1/3$ [72]. The extra sampling length required to make up the loss resulted in a significant degradation of resolution naively expected from an Ar/CO_2 mixture at 3 bar.

3.6 VXD Spatial Resolution

The dependence of spatial resolution on drift electron collection geometry in a cell can be seen from Fig. 3.15 obtained from a Monte Carlo simulation [73] by D. M. Binnie. Each curve in the plot represents a trail of drift electrons from the ionisations of a straight radial track. The variable S represents the scaled distance along the wire layer arc from the track to the sense wire. S=0 means the sense wire; S=1 means the cathode wires.

The variations of resolutions can be estimated by assuming different sampling lengths along the curves to give a different time spread of the drift electron arrival times. Since the effective sampling length is directly related to the chamber gain, variations of resolution with layers can be expected. The differences between curves at different parts of a cell indicate that a fixed sampling length would correspond to different electron drift time spread at different parts of a cell. An extra contribution from diffusion should also be expected.

To extract the resolutions, the residuals between the hit positions and extrapolated track points were plotted for different layers at different cell positions. To minimise the effect of scattering and the insufficient weighting of VXD hits in whole track fits, only tracks with $P_{r\phi}$ >500 MeV/c and having 8

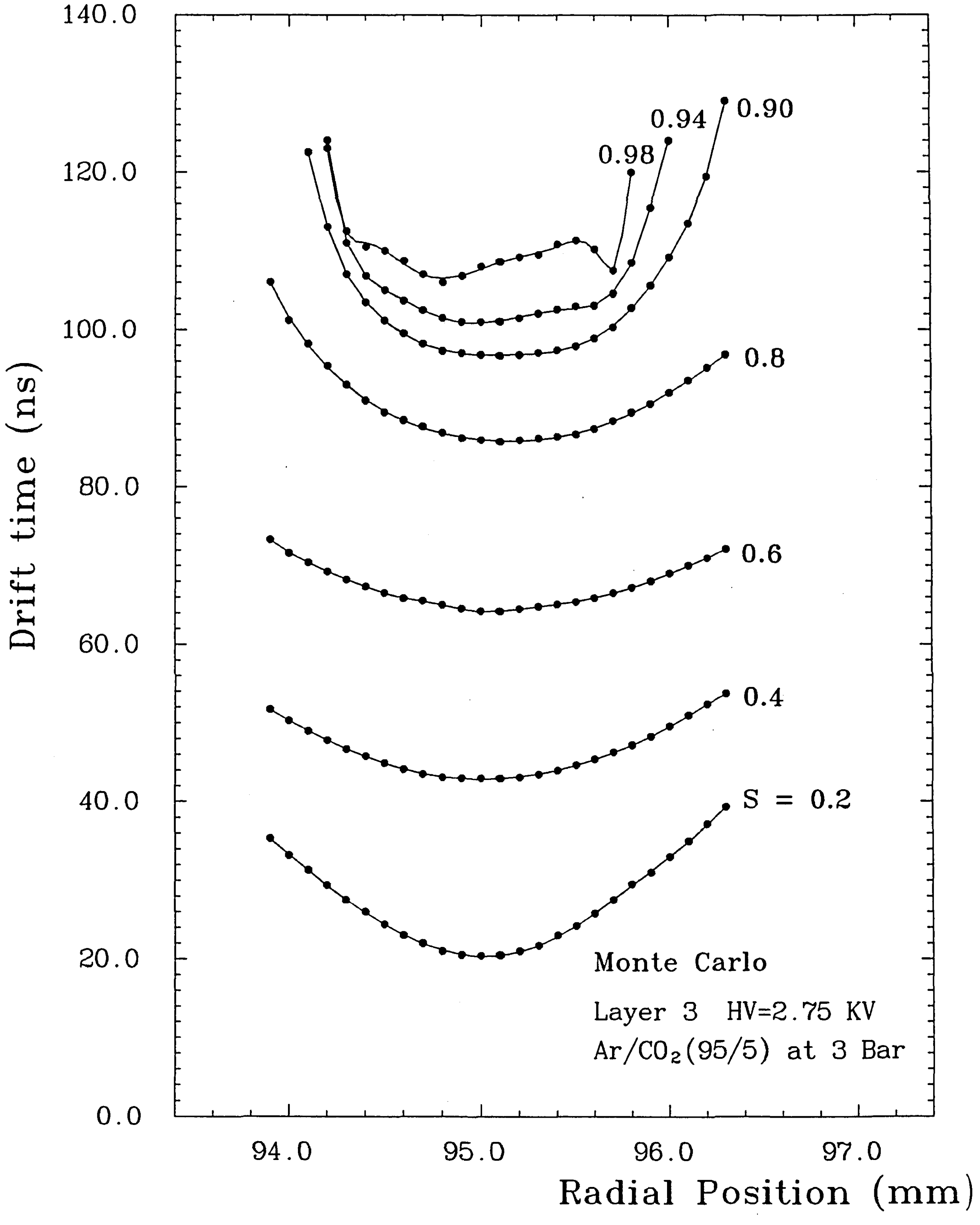

Figure 3.15: Monte Carlo Simulation of Electron Drift Time Distributions for Tracks at Different Parts of a Cell.

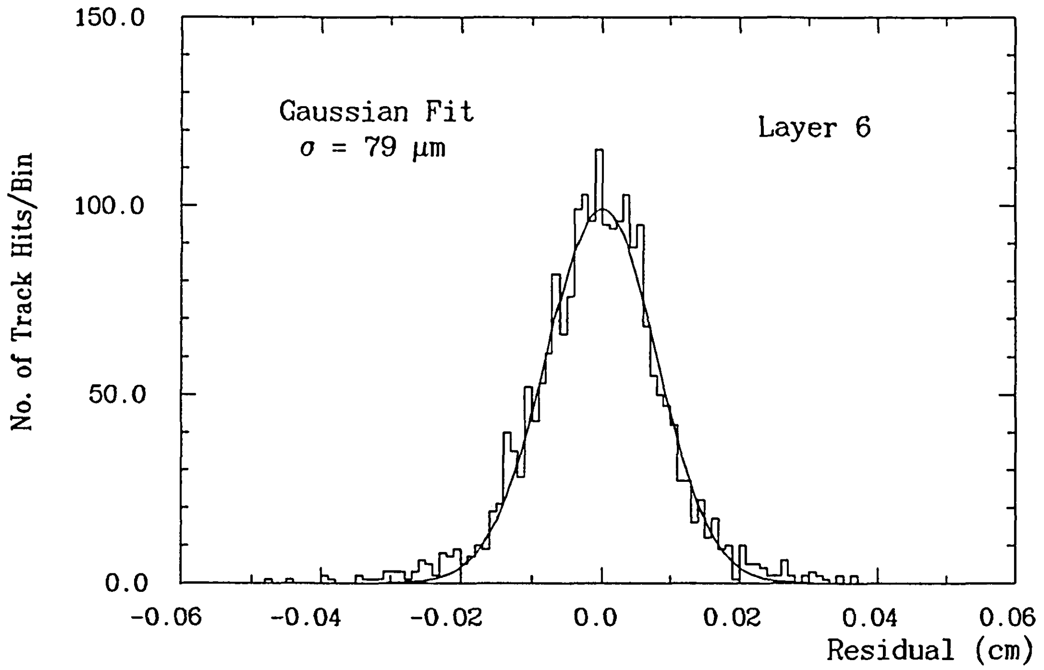

Figure 3.16: An Example of VXD Hit to Track Residual Fit.

VXD hits were used. An example of such a residual distribution is shown in Fig. 3.16 together with a Gaussian fit result.

The mid-cell position was taken as the reference point for each layer. The variations of the residual fit σ's for different layers are shown in Table 3.10 for the tracks in hadronic events. The estimated gains as in Table 3.9 are relisted together to see the direct correlation. The variation agreed with the estimated gain pattern considering the rather large systematic uncertainty involved and the different termination geometries on different layers. The fact the new data taken in 1985 and 1986 were better that the old data was partly due to the better running conditions and partly due to a re-setup of the discriminator cards.

An important observation to be made was the better resolution in the outer layers compared to the inner layers. This seemed to indicate that the constant fraction discriminator set-up was more favourable in these low gain conditions. This was tested further by fitting residuals for hits with different ADC pulse heights separately. The result is shown in Table 3.11. This indeed confirmed

Layer	83-85 Hadrons (μm)	86 Hadrons (μm)	Gain (DMB unit)
1	101	98	0.55
2	107	96	0.55
3	96	92	0.38
4	109	105	0.31
5	86	78	0.64
6	87	78	0.55
7	89	80	0.55
8	99	86	0.38

Table 3.10: Layer Variation of Mid-Cell Hit Residual σ.

ADC Values	20–40	40–60	60–90	> 90
Layer 3 σ (μm)	94	83	74	77
Layer 7 σ (μm)	79	79	85	85

Table 3.11: Residual Width Variation with Hit Pulse Heights.

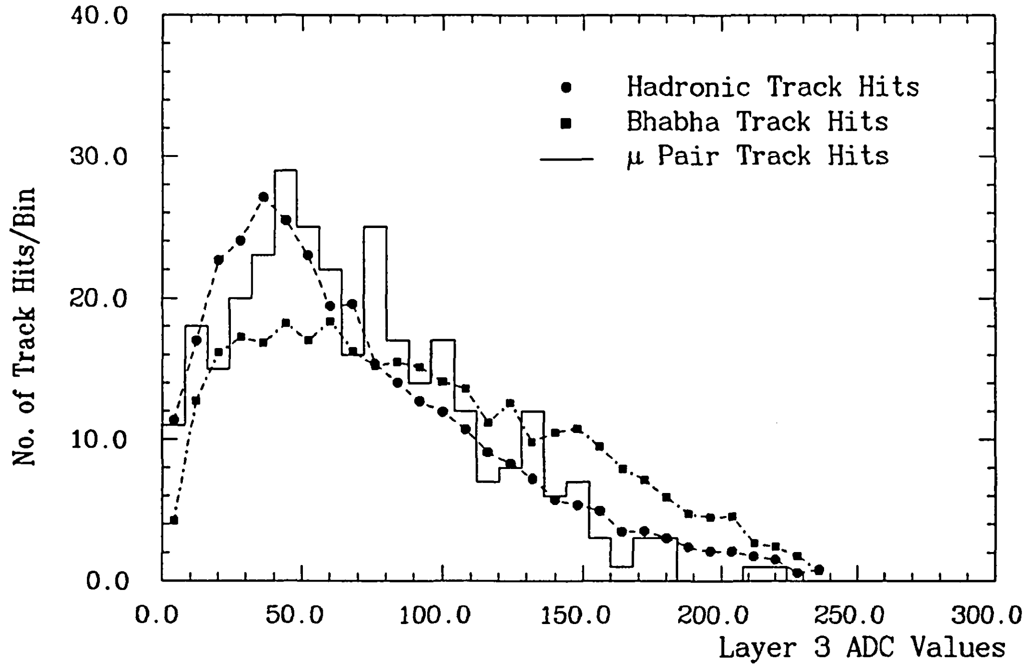

Figure 3.17: VXD Hit ADC Pulse Heights of Various Types of Tracks.

the expectation from Monte Carlo simulation [73] as the simple H/L setup continuously improved in resolution as the pulse heights increased while the C/F setup did a better job for the more abundant low pulse height hits.

The residual resolutions obtained from Bhabha scattering tracks were typically ~10% better in σ than the tracks in hadronic events. The best outer layers gave mid-cell residual σ <70μm. This was readily understood following the study of resolution variations with chamber gain since the Bhabha electrons had larger dE/dx ionisation losses once on the Fermi plateau while the hadrons below a few GeV were closer to being minimum ionising. The Bhabha scattering tracks which were mostly at low θ angles also gave an enhancement for more ionisation. This was verified by directly observing the ADC pulse height distributions of the hadron track hits and Bhabha scattering electron track hits on the same layer as seen in Fig. 3.17. This was the main reason that hadronic tracks were used directly to obtain the spatial resolutions.

Because the finite number of hit points, the statistical procedure of fitting a track would tend to give residual σ's better than the actual spatial resolution.

For the fitting procedure used in this analysis, the correction was found to be $\sim 10\%$. Another effect also due to the statistical minimisation was that a hit in a layer or a part of cell with relatively bad resolution would tend to pull the track fits to give itself a better apparent residual σ.

To overcome the above effects, Monte Carlo events were generated iteratively with variations in both layers and cell positions and were fitted in the same way as for the data until the final residuals matched between the data and Monte Carlo in all parts of VXD. The mid-cell position was taken as the normalisation point for each layer and the result of the mid-cell spatial resolutions on different layers are listed in Table 3.12. For simplicity and good

Layer	1	2	3	4	5	6	7	8
83-85 Data	113	121	103	110	92	97	103	109
86 Data	110	109	99	106	83	87	93	95

Table 3.12: Mid-Cell Spatial Resolutions of Various VXD Layers.

statistics, all layers were combined to give a common scale of spatial resolution variation within a cell. The cells were divided into 0.5 mm intervals according to the distances to the sense wires. The result is plotted in Fig. 3.18 and listed in Table 3.13. It can be seen from Table 3.13 that the apparant residual σ's for parts of a cell with worse resolutions were better than the actual resolutions by significant factors.

The worst resolution near the sense wire where the ionisation sampling spread was most pronounced, stressed the major limitation of spatial resolution for this design. Unlike in the case for large drift chambers, the contribution due to diffusion was relatively small because of the small cells. The longitudinal diffusion coefficient σ_L for a single electron in Ar/CO_2 mixtures is expected to fall to a minimum value of $\sim 200\ \mu m$ at our operating electric field of

Cell Position (mm)	83–85 Data Residual σ (μm)	Apparent Residual Scale	Generated M.C. Match Scale
0.0 – 0.5	125	1.29	1.45
0.5 – 1.0	116	1.20	1.27
1.0 – 1.5	109	1.12	1.15
1.5 – 2.0	99	1.02	1.04
2.0 – 2.5	97	1.00	1.00
2.5 – 3.0	103	1.06	1.07
3.0 – 3.5	109	1.12	1.15
3.5 – 4.0	114	1.18	1.18
4.0 – 4.5	115	1.19	1.24

Table 3.13: Cell Variation Factors of VXD Spatial Resolutions.

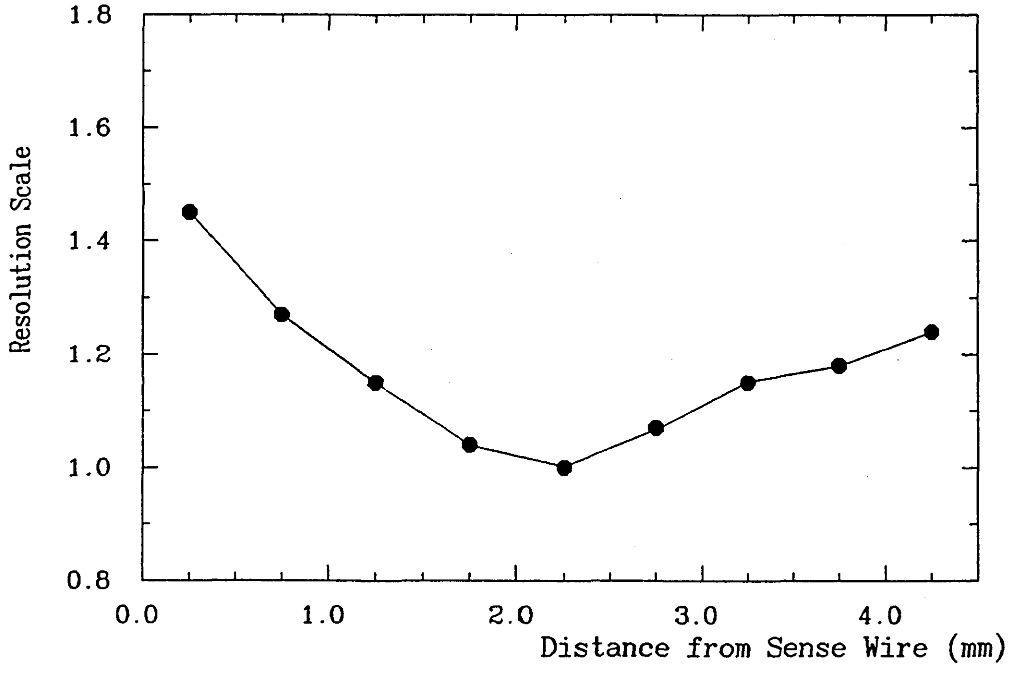

Figure 3.18: VXD Spatial Resolution Cell Variation Factors.

~800 V/cm/atm [72]. The collective effect due to diffusion with leading edge timing can be estimated statistically from [74]

$$\sigma(x) \sim \frac{0.91\sigma_L}{\sqrt{lnN}}\sqrt{\frac{x}{P}} \tag{3.19}$$

where N is number of drift electrons in the *effective* sampling length, P is the pressure of the gas and x is the distance to the sense wire. If a rough guess of the useful sampling length is taken to be 0.5 mm at a gas mixture pressure of 3 atm, the maximum contribution from diffusion would be 40 μm near the cathode wires.

The resultant resolution was approximately 20 μm worse than the intrinsic design resolution which could be explained by the extra complications of running the full system *e.g.* channel to channel calibration, mechanical construction tolerance, errors in detector position and space drift time relation determination, tracks entering the chamber off the radial direction, track finder mis-assigning hits *etc.*

3.7 Impact Parameter Resolution

The aim of the installation of the vertex detector was to improve the track resolution near the beam position. It not only depended on the spatial resolution of the detector, but also the general environment the vertex detector was in, *eg.* beam pipe size and radiation length, radial span of the VXD and link with the main DC hits. The impact parameters mentioned in this section referred to the closest approach distance of a final track to its actual starting point in reality.

The impact parameter resolutions depended sensitively on the track momenta especially for tracks below 1 GeV/c, due to multiple scattering. The

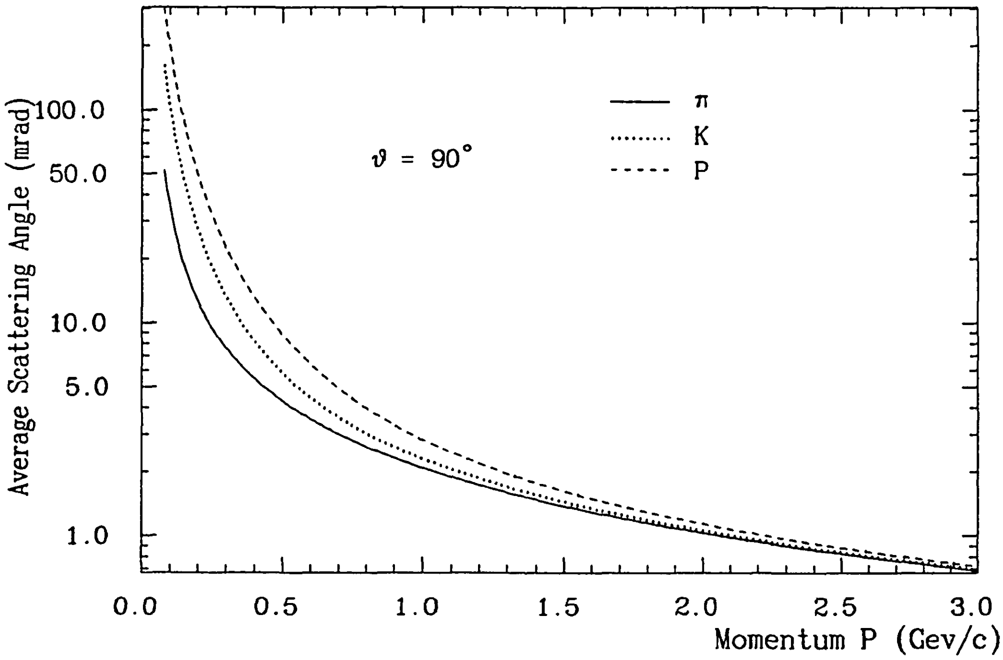

Figure 3.19: Expected Track Multiple Scattering Deflections in $r - \phi$ Plane after the Materials in front of VXD.

r.m.s angular spread of track direction in a plane, θ_0, after traversing a layer of material with thickness L and radiation length L_R, is given by [13]

$$\theta_0 \;=\; \frac{14.1\ MeV/c}{P\beta} Z_{inc}\sqrt{L/L_R}\{\ 1\ +\ \frac{1}{9}log_{10}(L/L_R)\ \} \qquad (3.20)$$

where Z_{inc} is the electric charge of the incoming particle in units of e , and P and β are the momentum and velocity of the incoming particle. Taking into account the materials before the VXD and the gas mixtures as listed in Table 3.1, the expected r.m.s. spread of track directions in the $r - \phi$ plane are shown in Fig. 3.19. A scattering of 1 mrad on the beam pipe is equivalent to an impact parameter smear of 70μm.

To observe the impact parameter resolution in the limiting case of minimum multiple scattering, the high momentum back to back 2-prong events were used. Only clean wide angle pairs with track $|\theta| > 50°$ were taken and the d_0 separation between the 2 tracks in the $r - \phi$ plane near the beam position is plotted in Fig. 3.20. This eliminated the uncertainty in actual event spot

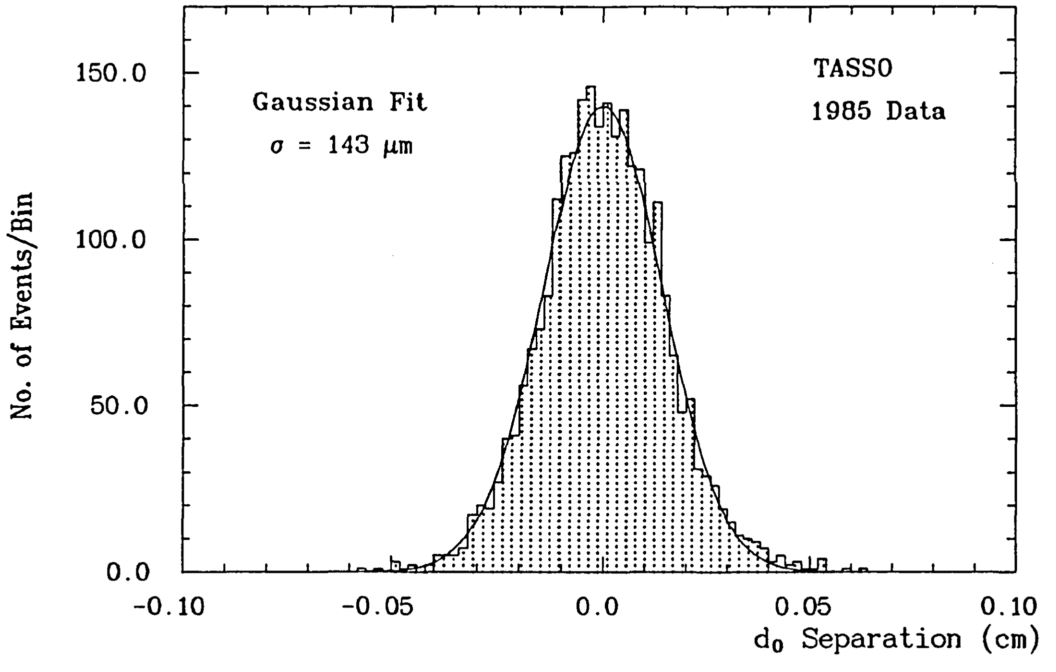

Figure 3.20: Clean Wide Angle 2-Prong d_0 Separations with FELIX Fit.

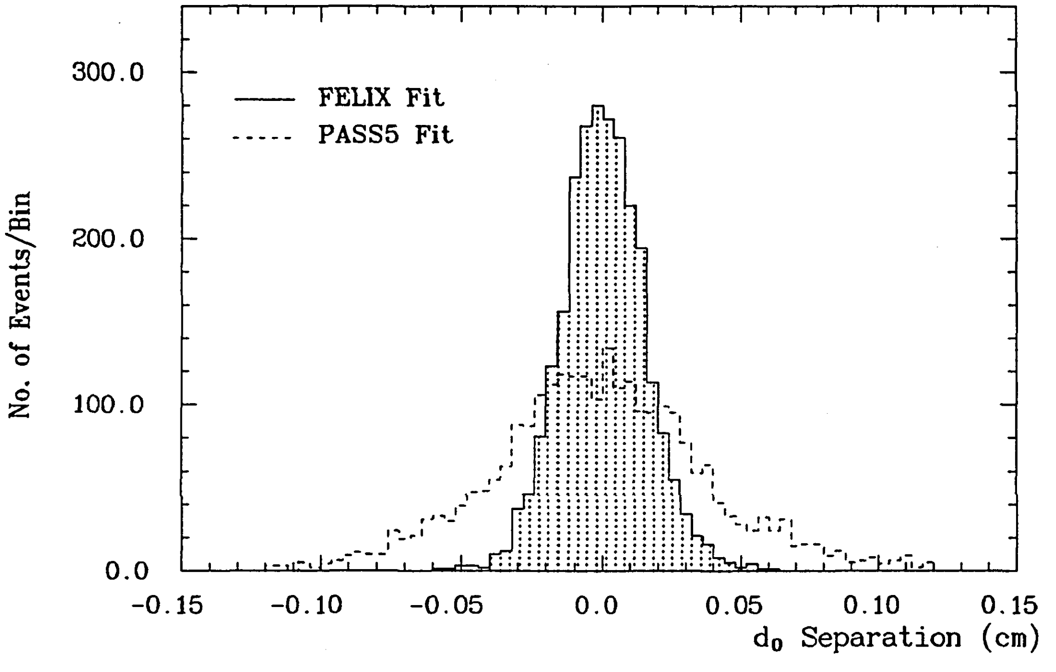

Figure 3.21: Comparison of 2-Prong d_0 Separations with Different Fits.

position within the beam envelope. The track fit used was the FELIX fit with a complete circle to all DC, CPC and VXD hits together but with different resolutions for the 3 different detector components. The Gaussian fit result of 143μm for the d_0 separation spread σ corresponded to an individual track impact parameter resolution of $143/\sqrt{2}$ $\sim$101 μm.

Monte Carlo Bhabha scattering events were generated with the knowledge of spatial resolutions obtained from the previous section and passed through the same fitting procedure as for the data. The Monte Carlo gave a d_0 separation width of 138μm, in good agreement with data. This gave an extra check on the offline calibration results, especially the VXD alignment. It excluded the possibility of large instabilities in VXD positions not detectable from a long term average.

The link between the main drift chamber tracks with VXD hits was found to be crucial for the required impact parameter resolution. The momentum reconstructed from the drift chamber track curvature gave the handle to reject low momentum tracks to avoid pattern confusions due to heavily scattered tracks. The long lever arm of the main drift chamber compensated the deficiency of the rather small radial span of the VXD. The effect can be seen directly from two different methods of fitting tracks. The FELIX fit gave a complete circle fit to all hits while the PASS5 fit took the track curvature from the main DC MILL track and then fitted to the VXD hits only to obtain the crucial $r - \phi$ geometry parameter d_0 near the beam position. Too much free leverage allowed by the mere $\sim$ 8cm radial span of VXD hits resulted in a rather wide impact parameter spread for the PASS5 fit as seen from Fig. 3.21.

The standard track fit used for the analysis improved further from the FELIX fit to allow a scattering kink at r = 16 cm as discussed previously in section 2.5. This mainly gave better impact parameter resolutions for the low momentum tracks.

Fitting	Track Momentum (GeV/c)				
Procedure	< 0.3	0.3–0.5	0.5–0.8	0.8–1.2	>1.2
A	896	549	431	324	222
B	724	464	389	346	338
C	777	476	386	304	217
D	716	451	359	286	196

Table 3.14: Impact Parameter Resolution Gaussian fit σ (μm).

The actual impact parameter resolutions for hadrons with various momenta were studied using the standard Monte Carlo for this analysis. A rather pessimistic mid-cell spatial resolution of 120μm was generated together with a cell variation scale also somewhat larger than the result obtained from the previous section. This was mainly due an early tuning of the detector simulation to the old data. However, it was found to be a reasonable approximation since the effect of multiple scattering overshadowed the importance of spatial resolution for the large population of low momentum particles. The impact parameter of a track in this case was simply the distance of the track to its actual Monte Carlo generating point. The results for various track finding and fitting procedures are shown in Table 3.14

The various track finding/fitting procedures referred in Table 3.14 were defined as follow:

A) The track finder FELIX was used to find hits and a single circle fit was performed through all hits in DC,CPC and VXD but with variable resolutions for different chambers.

B) The track finder PASS5 was used and the track curvature was fixed with fits to DC and CPC hits only. The final fit used VXD hits only to get the track ϕ_0, d_0.

C) The hits were taken from that found by FELIX and then the tracks were refitted allowing for a scattering kink between the main DC and VXD which entered as an extra χ^2 term. It also allowed a maximum rejection of 2 bad hits on a whole track.

D) The track hits were taken as the 'true' generated ones and the track fitting followed the same procedure as in **C)**. The comparison of this to **C)** should give an estimation of the relative importance of track finder mis-assigning hits.

Comparing **A)** and **B)**, it can be seen that the effective use of the long lever-arm from the DC hits in the case of **A)** lead to a much better impact parameter resolution for the important high momentum tracks. However, the PASS5 fit as in **B)** did a better job for low momentum particles which could be understood as it avoided the heavy scattering problem after the VXD.

The standard fitting procedure **C)** allowing a scattering kink, maintained the good resolution for the high momentum tracks as in the FELIX fit but also gave an important improvement for the low momentum FELIX tracks.

There was also a variation of the impact parameter resolution with the number of VXD hits assigned to a track. This corresponded to a $\sim\ \pm 20\%$ spread if tracks with 3 - 8 hits were treated separately. However this was found to be less important compared to the large variation with track momentum.

3.8 Determination of Beam Position

The beam positions relative to the detectors have been extensively used in many e^+e^- measurements in lifetime measurements. Because of the direct involvement with the lifetimes of short lived particles in this analysis, the beam positions were also partially used with the detailed discussion given in chapter 5.

Only an outline of the method used will be given here while the detail can be seen from [75]. Because there were possible beam orbit changes after each filling of new beams, the determination procedure was applied for each run separately or a few runs grouped together when event statistics was insufficient. The events which survived the PASS3 cuts (see section 2.4) were used taking advantage of the larger statistics since these included not only the e^+e^- interaction events but also some beam gas events.

Events with tracks intersecting each other in $r - \phi$ plane at >5 cm from detector centre or any track had $|z_0| > 15$ cm were rejected. This was to reduce the events occured along the beam line, such as beam pipe interactions. The tracks used were those found by PASS5 (see section 2.5) with track geometry parameters fitted using VXD hits only. After some fairly loose track quality cuts, the number of tracks used for each determination was typically 50 to 100.

Assume the unknown beam centre position was (x_b, y_b) and that a track i was in an event with event vertex (x_i, y_i) somewhere inside the beam envelope. A χ^2 for the track can be defined as

$$\chi_i^2 = \frac{d_i^2}{\sigma_t^2} + \frac{(x_i - x_b)^2}{\sigma_x^2} + \frac{(y_i - y_b)^2}{\sigma_y^2} \tag{3.21}$$

where

$$\begin{aligned} d_i &= \textit{Track distance to the event vertex } (x_i, y_i) \\ \sigma_t &= \textit{Track impact parameter resolution} \\ \sigma_x, \sigma_y &= \textit{R.M.S. beam widths in horizontal and vertical directions} \end{aligned}$$

The parameters $\sigma_t, \sigma_x, \sigma_y$ were fixed constants and were chosen to be

$$\begin{aligned} \sigma_t &= \sqrt{250^2 + \frac{200^2}{P^2}}\ (\mu m) \\ \sigma_x &= 500\mu m \\ \sigma_y &= 60\mu m \end{aligned}$$

where P was the track momentum in GeV/c. It can be noted that the scale and momentum dependence of σ_t was similar to the result in Table 3.14 for PASS5 as in case B).

The distance d_i was then expressed as a function of the standard track parameters d_0, ϕ_0 and x_i, y_i so that the conditions

$$\frac{\partial \chi_i^2}{\partial x_i} = 0 \qquad \& \qquad \frac{\partial \chi_i^2}{\partial y_i} = 0$$

would give the most probable (x_i, y_i) for each track. Subsequently, the χ^2 for each track could be expressed analytically with just x_b, y_b as unknowns while d_0, ϕ_0 were constants for each track and $\sigma_t, \sigma_x, \sigma_y$ were fixed global constants.

By taking the sum of χ_i^2 for all tracks in each determination, a grand sum could then be arrived at as

$$F(x_b, y_b) = \sum_i^{Tracks} \chi_i^2(x_b, y_b)$$

The conditions for minimising F

$$\frac{\partial F}{\partial x_b} = 0 \qquad \& \qquad \frac{\partial F}{\partial y_b} = 0$$

lead to the initial solution for (x_b, y_b). The χ_i^2 for each track was then evaluated using the initially obtained (x_b, y_b) and tracks with χ_i^2 >25 were rejected so that only the remaining tracks were summed to get the final result for (x_b, y_b).

The result of the beam position determinations for all the runs in 1985 are shown in Fig. 3.22 for x and y coordinates separately. It should be noted that the plot scale for x was twice as large as for y. The estimated statistical errors for the beam centre coordinates were typically 50–100 μm. But the inexact assumptions about the values of $\sigma_t, \sigma_x, \sigma_y$ and the effects of remaining tracks from weakly decayed particles or γ conversions in the sample could contribute some systematic errors. Although there were clearly large movements in the beam x coordinates which could be expected from beam orbit adjustments,

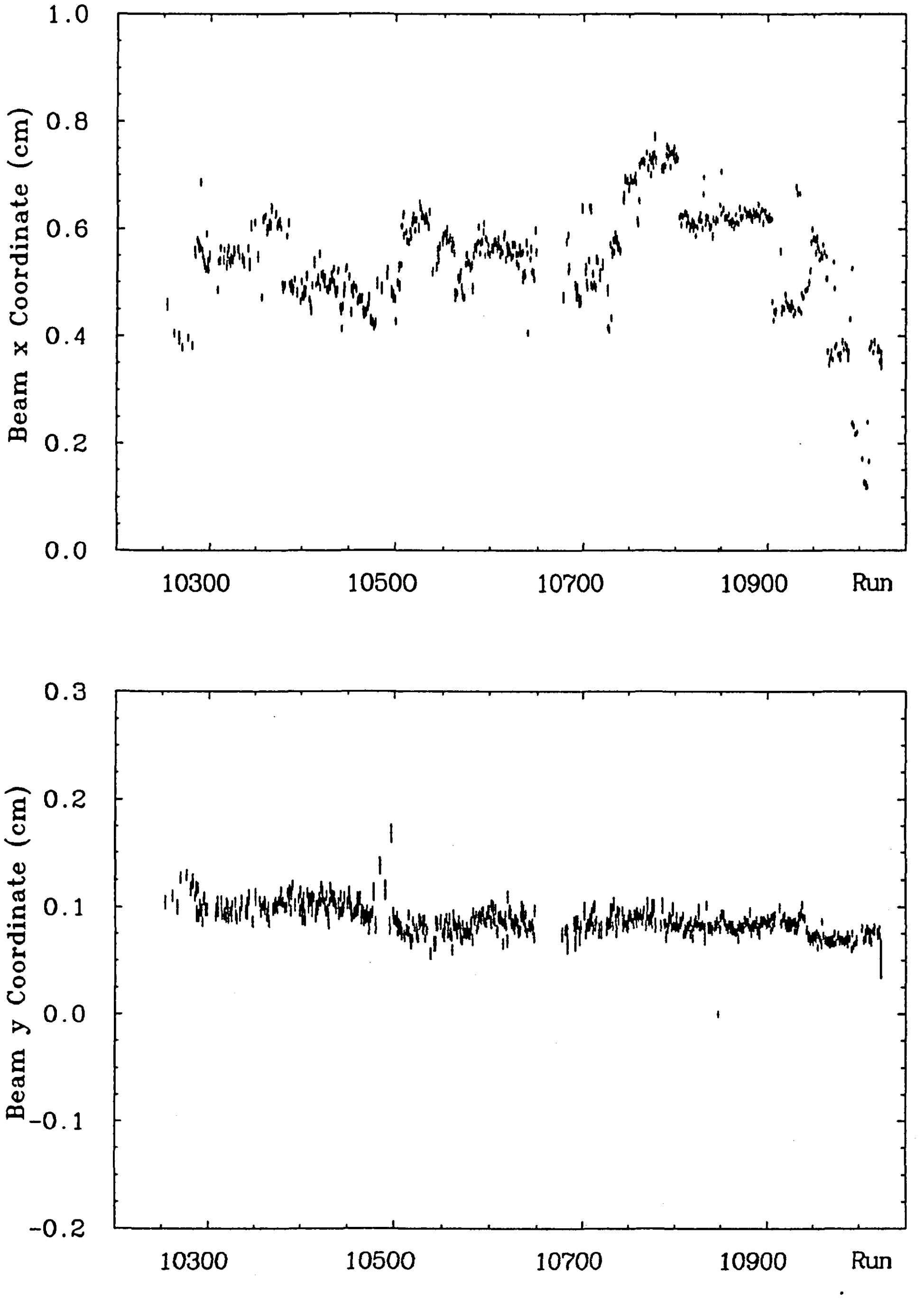

Figure 3.22: Determined Beam Positions for All Runs in 1985 (Note the Different Scales for x and y).

the beam y position was very stable. Even allowing the systematic movements between runs to be included, a large group of runs together would still give an absolute spread of the determined y position $<200\mu m$. This seemed to justify the estimated errors within a factor of 2 or less.

Recall the discussion in section 2.1, where the beam width in x was expected to be typically $500\mu m$ while the beam width in y was expected to be as narrow as $<20\mu m$. This should be compared with the track impact parameter resolutions discussed in the previous section and the estimated errors in the determination of the beam positions. The track resolution clearly gave the major contribution to the error in the beam y position determination while the error in the beam centre x coordinate did not really matter since the beam envelope was much larger.

To test the assumptions about the beam envelope sizes, an interesting method [75] is to plot track impact parameters with respect to the determined beam centre positions for tracks at different ϕ angles separately. To reduce the smearing due to track impact resolutions, only the high momentum back to back 2-prong events were used with tight track quality cuts. The track parameters were from the FELIX fit (as indicated in the previous section) which was the best choice for impact parameter resolution for high momentum tracks. The r.m.s. spread of the impact parameter distrib-utions at different ϕ angles were used to give the σ's in Fig. 3.23.

The fit to the ϕ variation with the function

$$< \sigma_{imp}(\phi) > = \sqrt{\sigma_t^2 + \sigma_x^2 sin^2\phi + \sigma_y^2 cos^2\phi} \qquad (3.22)$$

and fixing σ_t at $100\mu m$ according to the study from the previous section gave the curve in Fig. 3.23. The fitted value for σ_x was 419μ and for σ_y was $93\mu m$. It can be seen clearly that neither σ_t nor σ_y could be larger than $150\mu m$, bound by the lowest point in the plot. The rather large value of σ_x was not very

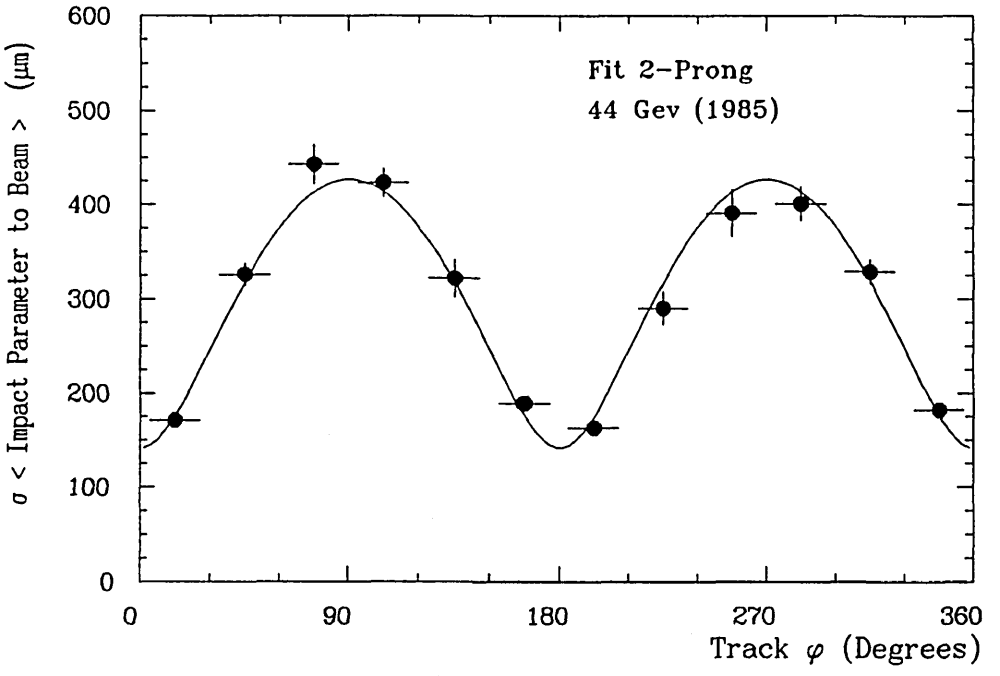

Figure 3.23: Track Impact Parameter Spread w.r.t. Beam Centre for Various Track ϕ Angles.

sensitive to the uncertainties in σ_t or σ_y. Although σ_x was somewhat smaller than the assumed 500μm, it was still comparable. The small spread in beam y including the errors in the determination, indicated that the actual vertical beam size must be <100μm at least.

Chapter 4

Monte Carlo Modelling

The e^+e^- interactions at high energies seen through a large detector involve many aspects other than that of the primary production. Some of these intermediate processes are relatively well understood while others hold interesting physics yet to be studied by the experiments. In reality, besides the initial state *i.e.* the e^+e^- beams, only indirect information after many intermediate processes is available from the final states of stable particles. To enable the study of a specific intermediate physics process, a simulation of all relevant known processes involved between the initial and final states can help the extraction of the contribution due to the process in question from the complicated final states.

In the case of e^+e^- annihilations into hadrons, for example, the initial stage of various multi-parton production is followed by the fragmentation of partons into hadrons and the decay of unstable and short lived particles. The stable particles in the final state may still interact with materials in the detector or even escape detection due to the limited detector acceptance. The variable resolutions with which different properties of different particles can be measured, the event triggering ability, event selections and ways of analysing data all hold intertwining influences on the final physics results to various extents.

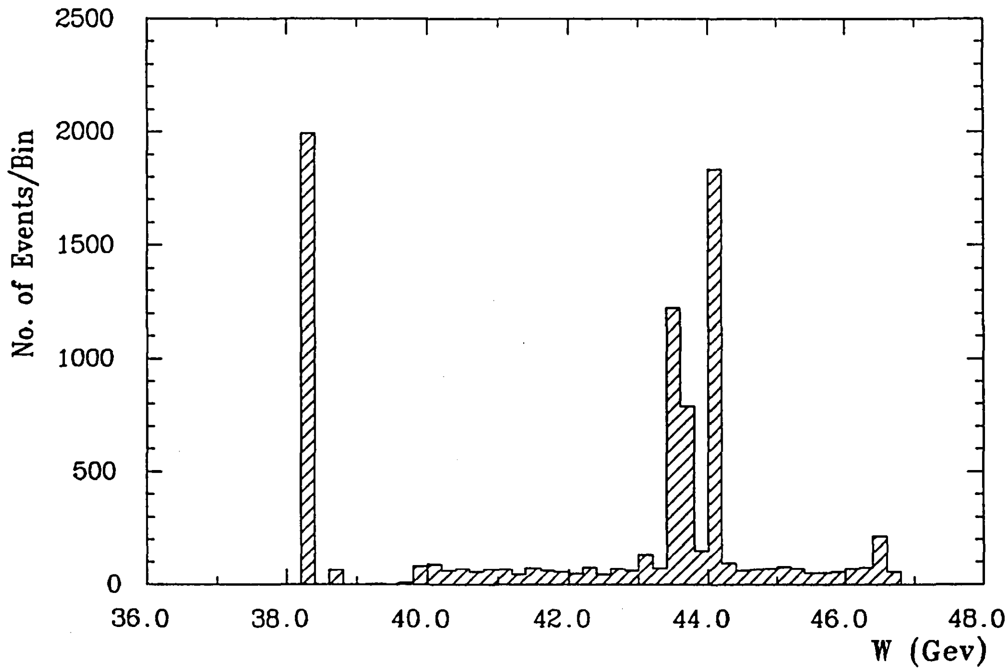

Figure 4.1: e^+e^- Centre of Mass Energy Spread of the Data Sample.

Thus Monte Carlo analysis was performed with theoretical or phenomenological inputs to generate events, and was followed by detector simulation. The final outcome could then be compared with data directly using the same analysis chain. This powerful tool significantly extends the sensitivity of the experiment.

The Monte Carlo used for this analysis was an independent jet fragmentation scheme together with a B decay simulation tuned to the experimental results of CLEO. The generated events after detector simulation were passed through the same event selection and track finding procedures as for the data. The Monte Carlo was generated at a fixed beam energy of 21.8 GeV/c while the whole data sample contained events with e^+e^- centre of mass energy W ranged from 38 GeV to over 46 GeV. The actual energy spread in the data is shown in Fig. 4.1. Most of the data were taken at two fixed energies of $\sim$44 GeV & $\sim$38 GeV respectively and the average W of all data events was 42.1 GeV.

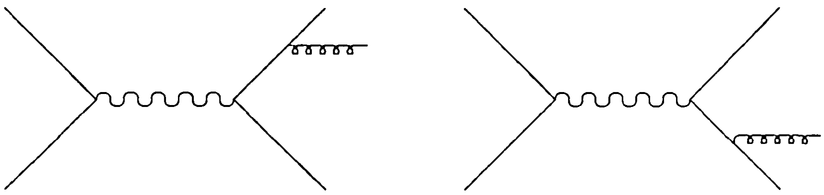

Figure 4.2: Feynman Diagrams of $e^+e^- \rightarrow q\bar{q}g$ to 1st order in α_s.

Because the Monte Carlo was mainly intended for heavy flavour lifetime measurements, the fragmentation parameters in the Monte Carlo were only roughly tuned to the early part of the data, so that the parameters might not be very accurately optimised. Nevertheless, the comparison between the resulting Monte Carlo and the whole data sample will be given in section 4.6 to enable an examination of the quality of the Monte Carlo.

4.1 Event Generation

The event generator incorporated a full 2nd order perturbative QCD calculations of FKSS [76] included 1st order contributions and second order virtual corrections for the $e^+e^- \rightarrow q\bar{q}g$ matrix elements and also second order matrix elements for $e^+e^- \rightarrow q\bar{q}q\bar{q}, q\bar{q}gg$ 4 parton final states. The original FKSS calculation used approximations related to the soft parton cut-off which neglected some terms of the order ϵ and δ^2 (to be defined later in this section). These terms were inserted in the event generator of this Monte Carlo (Extended FKSS) [77].

It is rather instructive to see the general features of the QCD prediction for the topology of $e^+e^- \rightarrow q\bar{q}g$ events with just the graphs to the 1st order in α_s as shown in Fig. 4.2.

The QCD differential cross section for the above 2 graphs with quarks taken to be massless gives

$$\frac{1}{\sigma_0}\frac{d\sigma}{dx_1 dx_2} = C_2(F)\frac{\alpha_s}{2\pi}\frac{x_1^2+x_2^2}{(1-x_1)(1-x_2)} \tag{4.1}$$

where

$$\sigma_0 = \frac{4\pi\alpha^2}{3s}\sum_i^{N_q} 3\,Q_i^2$$

is the lowest order QED cross section of $e^+e^-\rightarrow q\bar{q}$ abbreviated from Equation 1.20. $x_{1,2,3}$ are the energies of the 3 partons as a fraction of the half total C.M. energy *i.e.* $x_1 + x_2 + x_3 = 2$ and they are ordered such that $x_1 \geq x_2 \geq x_3$. The factor $C_2(F)$ is due to the colour summation for $q\rightarrow qg$ splitting and $C_2(F) = \frac{4}{3}$ for SU(3). The conservation of four momentum also constrains the topology to follow:

$$x_1 = \frac{2sin\theta_{23}}{sin\theta_{12} + sin\theta_{23} + sin\theta_{31}} \tag{4.2}$$

and cyclic permutations for x_2, x_3. Here θ_{ij} is the angle between momentum vectors of partons i and j.

It can be seen that there are singularities in the $e^+e^-\rightarrow q\bar{q}g$ differential cross section when x_1 and/or x_2 approaches 1. These correspond to the cases in which the gluon is very soft and/or collinear with q or $\bar{q}$, as is easily deducible from the simple kinematic constraints. However, these are exactly the cases when the 3 parton final states become non-distinguishable from $q\bar{q}$ final states. Theoretically, the infinities cancel out when contributions from virtual corrections to the $q\bar{q}$ final states are included. Experimentally, only the hard gluon emissions resulting in clear 3-jet events give observable differences from the 2-jet topology of the $q\bar{q}$ final states.

For the Monte Carlo generation, Sterman-Weinberg cuts were used to accept only hard non-collinear 3 or 4 jet events. A multi-parton final state was accepted only when each parton had at least a fraction ϵ=0.2 of the beam energy and the minimum angular separation δ between any pair of partons was required to be at least 40°. In the case of a 4-parton final state with only one parton failing the cuts, it was combined with the nearest neighbouring parton and the event was subsequently treated as a 3-jet event. The cross sections for 3 and 4 parton final states were integrated within the acceptance region and subtracted from the total cross section $\sigma(e^+e^- \rightarrow \text{Hadrons})$ to give the remaining cross section to 2 jet events.

Corrections were also made for QED initial state photon radiation according to Behrends & Kleiss [78]. The cut-off used was to require the radiative photon energy to be less than 0.98 of the beam energy. The effect of this reduction in C.M. energy is shown in Fig.4.3 for Monte Carlo with e^+e^- beam energies of 22 GeV each. $\Sigma\, E_{parton}$ was the sum of energies of all outgoing parton jets in an event and thus excluded the radiative photon energies. It can be seen that $\sim$ 87% of the events still had more than 90% of the original total beam energy.

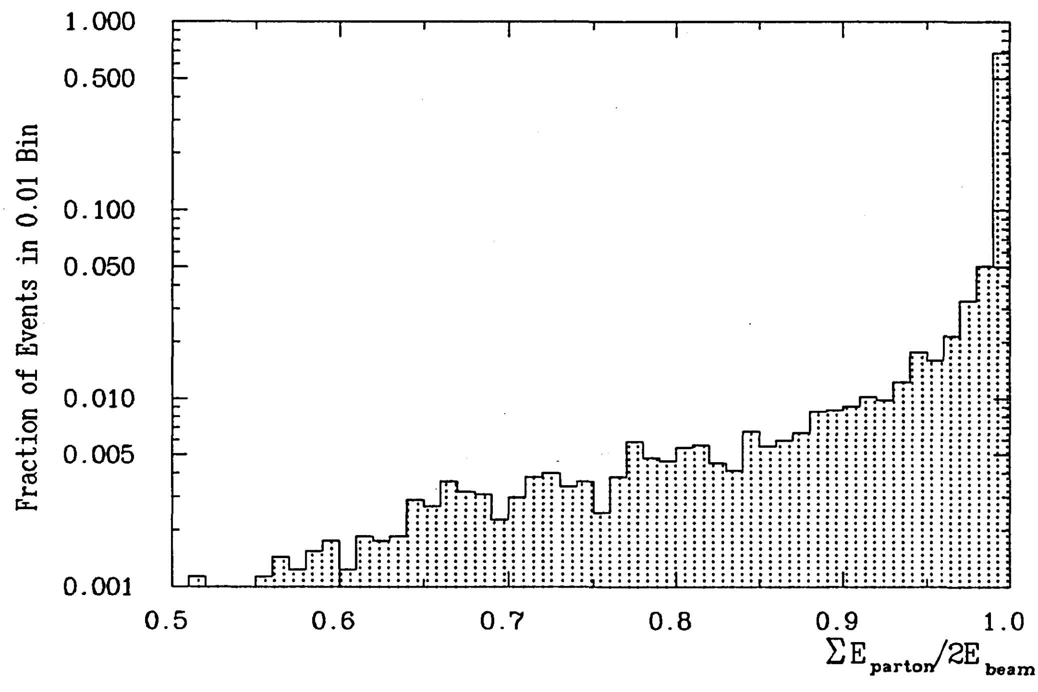

Figure 4.3: C.M. Energy Reduction Ratio due to QED Radiative Corrections.

The simple flavour production ratio $d : u : s : c : b$ of 1:4:1:4:1 was also mod-

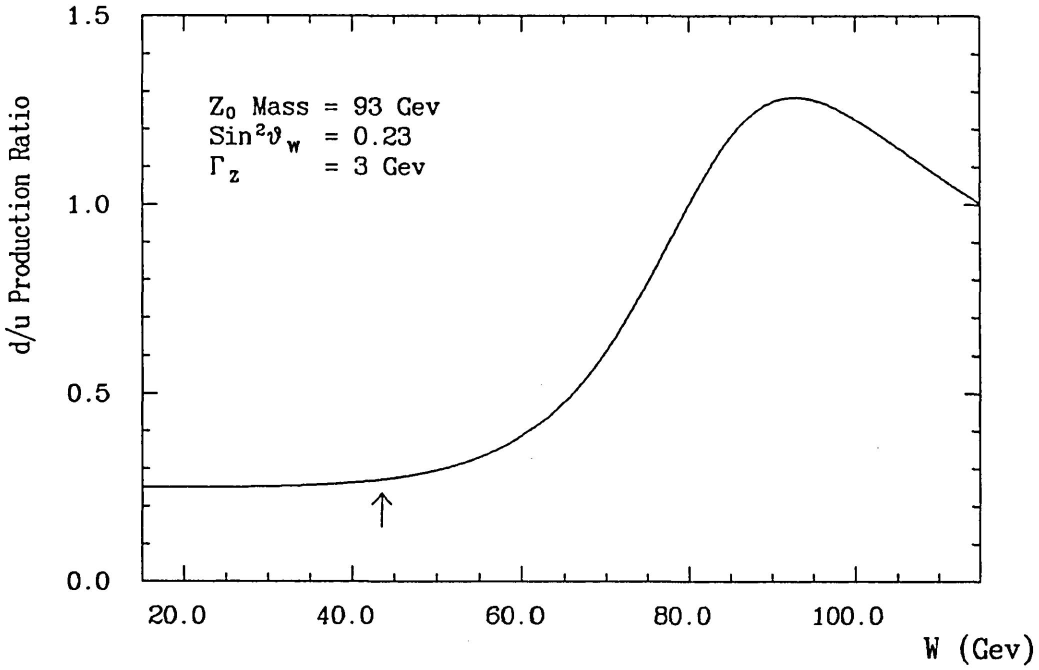

Figure 4.4: Lowest Order Electroweak $Q_{\frac{1}{3}}/Q_{\frac{2}{3}}$ Production Ratio.

ified by including the contribution of the $e^+e^- \rightarrow Z^0 \rightarrow q\bar{q}$ channel. The magnitude of this correction to the production ratio of charge 1/3 and 2/3 $q\bar{q}$ pairs at different e^+e^- centre of mass energies is shown in Fig.4.4 for the lowest order standard model electroweak calculation assuming massless quarks. The correction to $Q_{\frac{1}{3}}/Q_{\frac{2}{3}}$ production ratio at W=44 GeV corresponded to ~9% increase.

4.2 General Scheme of Fragmentation

The fragmentation process of quarks and gluons turning into jets of hadrons cannot be described by perturbative QCD satisfactorily due to the large α_s at low Q^2. Thus phenomenological models with semi-theoretical inputs have to be employed to simulate such processes. The Monte Carlo events used in the analysis of this thesis were generated with an independent jet fragmentation scheme developed from the original Field-Feynman algorithm [79].

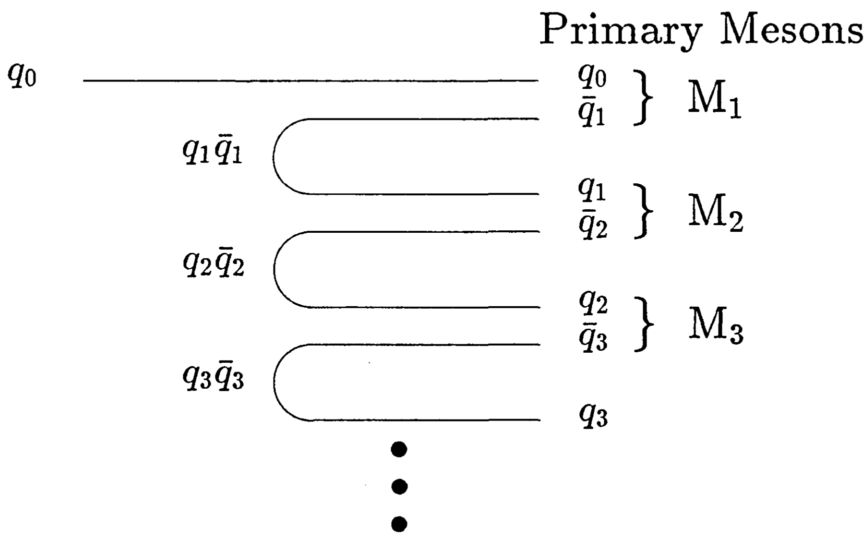

Figure 4.5: Illustration of Independent Jet Fragmentation Chain.

Once the partons were generated with known flavour, energy and momentum, the fragmentation chains were followed for each parton independently. Firstly, consider a quark q_0 moving away from the interaction point. The energy deposited in the colour field enabled a new quark-antiquark pair, $q_1\bar{q}_1$ say, to be produced. The antiquark $\bar{q}_1$ could combine with q_0 to form a primary meson while q_1 carried on in a similar way as the starting q_0. This chain process is illustrated in Fig.4.5. The chain would terminate when the energy which remained was insufficient to produce more hadrons.

The model also allowed diquark-antidiquark pairs to be produced in the same way as the $q\bar{q}$ pair to account for the baryon production. The implementation was based on the scheme described by T.Meyer in [83]. The Monte Carlo probability ratio was set to

$$\frac{Prob(qq\bar{q}q)}{Prob(q\bar{q}) \ + \ Prob(qq\bar{q}q)} = 0.10 \tag{4.3}$$

No charm or bottom baryons were produced by this Monte Carlo.

The gluons were dealt with by splitting them into a $q\bar{q}$ pair immediately after the generator phase and the energy of a gluon was given entirely to either q or $\bar{q}$ randomly. The fragmentation chain could then be carried out exactly, as the quark jets and the last quark (antiquark) of the chain would finally pick up the antiquark (quark) which was at rest from the initial splitting to form the last hadron in the gluon jet.

However this independent jet fragmentation scheme lead to the consequence that charge and flavour were not conserved separately for each quark jet due to the rounding of the last hadron. The quantum numbers were only made to be conserved for a whole event by forcing the last hadron of the last jet to match the required quantum numbers.

The flavour assignment to the $q\bar{q}$ pairs produced in the fragmentation chain assumed the same probability for $u\bar{u}$ and $d\bar{d}$ pairs. The probability of producing an $s\bar{s}$ pair was set to

$$\frac{Prob(s\bar{s})}{Prob(u\bar{u})} = \frac{Prob(s\bar{s})}{Prob(d\bar{d})} = 0.4 \tag{4.4}$$

but no $c\bar{c}$ and $b\bar{b}$ pairs were produced in the fragmentation chain. The probabilty ratios of various types of diquarks were set to the products of the flavour probability ratios of the 2 single quarks.

The assignment of particle types for the primary mesons of the same quark contents were arranged to give 42% pseudoscalar mesons and 58% vector mesons *i.e.*

$$\frac{P}{P + V} = 0.42 \tag{4.5}$$

No higher spin state mesons were produced. Similarly, only the lowest lying octet and decuplet baryons were produced with the ratio O/D equal to P/V for the mesons.

The decays of particles were modelled to follow the relevant branching ratios as well as the corresponding decay widths for unstable hadrons and the corresponding lifetimes for the short lived hadrons. This also included decays of the relatively long lived K^0, Λ, $K^{\pm}$, $\pi^{\pm}$.

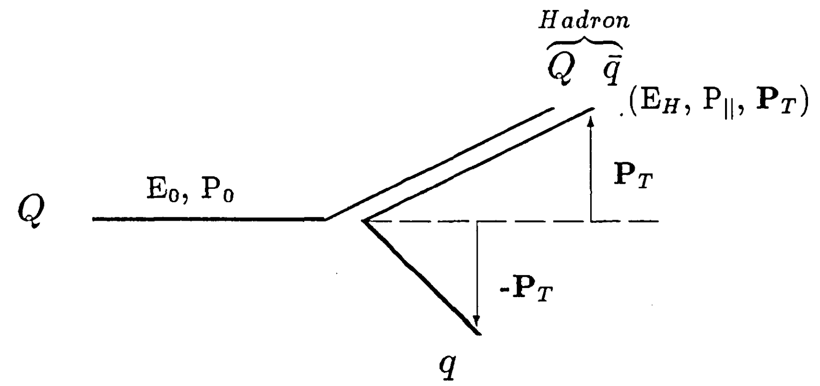

Figure 4.6: Kinematic Splitting of Fragmentation Chain.

4.3 Fragmentation Functions

The detailed energy momentum sharing at each fragmentation stage was controlled by fragmentation functions. The relevant kinematic variables are illustrated in Fig.4.6 for a $q\bar{q}$ production. The transverse momentum P_T was generated with a Gaussian probability function:

$$f(P_T)dP_T \sim e^{-\frac{P_T^2}{2\sigma_q^2}} dP_T$$

The parameter σ_q was set to 0.371 GeV/c for this Monte Carlo. The overall P_T was conserved by always giving the hadron and the next generation quark opposite sign P_T as indicated in Fig. 4.6.

The longitudinal energy momentum sharing was defined through a fragmentation function $f(z)$ where

$$z = \frac{(E + P_{||})_H}{(E_0 + P_0)_Q}$$

and $P_{||}$ was the longitudinal momentum of the newly formed hadron parallel to the incoming quark Q. At each fragmentation splitting (with the incoming quark or antiquark having energy E_0 and momentum P_0), a value z was generated according to the probability density function $f(z)$ whereby $z \cdot (E_0 + P_0)$ was given to $(E + P_{||})_{Hadron}$ and $(1-z) \cdot (E_0 + P_0)$ was given to $(E + P_{||})_q$. It can be noted that the independent jet nature of this scheme only ensured the conservation of the quantity $E + P_{||}$ but not E and $P_{||}$ separately. This was necessary to make the production of a new $q\bar{q}$ pair kinematically possible. Energy and momentum conservation were only reimposed after the fragmentation of the whole event was completed, *à la* Ali *et al.* [81], by means of a Lorentz boost to the new C.M. frame and then rescaling the energies of all final state particles.

Two different types of fragmentation functions were used depending on the flavour of the initial quark Q. In the case of light quarks u, d, s the fragmentation function was

$$f(z) \propto (1 - z)^{a_L} \tag{4.6}$$

as proposed by the LUND group [80]. The parameter a_L was set to 0.751 for the 44 GeV Monte Carlo. This Monte Carlo was only tuned to the rather small sample of old high energy data taken in 1983-84 with α_s, σ_q, a_L as free parameters. Besides the values of σ_q and a_L mentioned previously, the value of α_s was set to 0.188.

In case of heavy flavours c and b, the fragmentation used was of the form proposed by Peterson *et al.* [82]

$$f(z) \propto \frac{1}{z(1 - \frac{1}{z} - \frac{\epsilon}{1-z})^2} \tag{4.7}$$

This gave a reasonable description of the rather hard charm fragmentation function as seen from the D^* momentum spectrum observed by many e^+e^- experiments [84].

The form of the Peterson function was based on an argument based on first order perturbation theory which expected the amplitude of the splitting process in Fig. 4.6 to be

$$amplitude \propto (E_H + E_q - E_Q)^{-1} \tag{4.8}$$

The formula in Equation 4.7 was then obtained using an expansion about the transverse masses m_Q/P_0 and m_q/P_0 multiplied by a longitudinal phase space factor $1/z$. The derivation also gave the parameter ϵ as

$$\epsilon \; = \; (\frac{m_q}{m_Q})^2 \tag{4.9}$$

The resulting hard fragmentation of the heavy quarks can be naïvely understood as the attachment of a light antiquark to a heavy quark in the fragmentation process, with relatively small energy transfer, which should only decelerate the heavy quark slightly.

Fragmentation functions can conveniently be considered in terms of their mean values $< z >$. To extract $< z >$, corrections have to be made on the original experimental results mainly due to the different definitions of variables. The directly observed $< x_E >$ or $< x_p >$ where

$$\begin{aligned} X_E &= \frac{E_{D^*}}{E_{beam}} \\ X_p &= \frac{P_{D^*}}{\sqrt{E_{beam}^2 - m_{D^*}^2}} \end{aligned}$$

are not the same as the more intrinsic Lorentz invariant variable z needed by Monte Carlo.

A major factor comes from the effect of gluon radiation which often results in heavy quarks having significantly less energy than E_{beam} before fragmenting to make heavy mesons. The initial state photon radiation also gives the same effect but is smaller in magnitude. The corrections to these effects are energy dependent. To see the relative importance of this correction, the Monte Carlo x_E spectrum for leading D^* production is plotted together with the input charm fragmentation function f(z) as seen in Fig.4.7 for W=44 GeV. The solid line histogram was obtained by recalculating z from the generated final state D^* momentum and the stored charm quark momentum 4-vector. The slight discrepancy between this re-extracted z spectrum and that of the curve of the

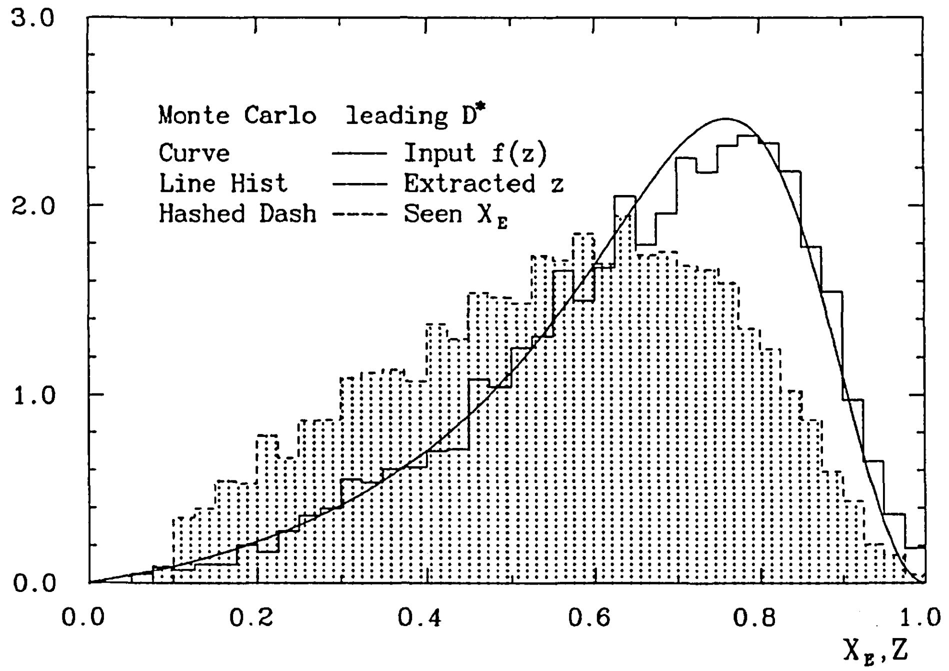

Figure 4.7: Monte Carlo Leading D^* X_E and z spectrum.

generated $f(z)$ represents the effect of reimposing global energy momentum conservation at the end of the fragmentation chain in this independent jet model.

The efficiencies of reconstructing D^* at different x and the effect of secondary D^*'s from B decays also varied from experiment to experiment. The compilation by S.Bethke [88] with different corrections to various experiments gave a world average of

$$< z_c > = \ 0.704 \ \pm \ 0.010 \ \pm \ 0.030$$

as listed in Table. 4.1. This corresponded to an ϵ_c value of $\sim 0.04 \pm 0.02$ for the Peterson function.

The fragmentation function of the bottom quark was studied by various experiments [89] with fits to the inclusive lepton momentum and jet P_T spectra allowing variations of assumed Monte Carlo fragmentation parameters. The experiments with Peterson function as input and resultant $< z >$ for Monte Carlo $f(z)$ are listed in Table 4.2 as compiled by S.Bethke.

Experiment	Observable	$< x >$	$< z_c >$
CLEO	$x_p > 0.35$	0.675 ± 0.015	0.73 ± 0.02
ARGUS	$x_p > 0.10$	0.589 ± 0.017	0.695 ± 0.020
DELCO	$x_p > 0.35$	0.585 ± 0.023	0.665 ± 0.035
TPC	$x_E > 0.30$	0.585 ± 0.038	0.695 ± 0.050
MARK II	$x_E > 0.30$	0.604 ± 0.040	0.66 ± 0.06
HRS	$x_E > 0.20$	0.525 ± 0.017	0.700 ± 0.025
JADE (D^{*+})	$x_E > 0.40$	0.635 ± 0.025	0.71 ± 0.03
JADE (D^{*0})	$x_E > 0.50$	0.660 ± 0.025	0.68 ± 0.04
TASSO	$x_E > 0.40$	0.647 ± 0.028	0.73 ± 0.04
Combined	–	–	$\mathbf{0.704 \pm 0.010}$

Table 4.1: Measurements of Charm Fragmentation Function from D^* Momentum Spectrum.

Experiment	Lepton	$< z_c >$	$< z_b >$
MAC	μ	$0.2 - 0.7$	0.8 ± 0.1
MARK II	e	(Fixed $\epsilon_c = 0.25$)	$0.75 \pm 0.05 \pm 0.04$
MARK J	μ	$0.46 \pm 0.02 \pm 0.05$	$0.75 \pm 0.03 \pm 0.06$
TASSO	e	$0.57 \pm {}^{0.10}_{0.09} \pm {}^{0.06}_{0.05}$	$0.84 \pm {}^{0.15}_{0.10} \pm {}^{0.15}_{0.11}$
TASSO	μ	$0.77 \pm {}^{0.05}_{0.07} \pm {}^{0.03}_{0.11}$	$0.85 \pm {}^{0.10}_{0.12} \pm {}^{0.02}_{0.07}$
JADE	μ	$0.77 \pm 0.03 \pm {}^{0.02}_{0.10}$	$0.88 \pm {}^{0.11}_{0.07} \pm {}^{0.05}_{0.03}$
Combined		$\mathbf{0.632 \pm 0.034}$	$\mathbf{0.778 \pm 0.038}$

Table 4.2: Measurements of Heavy Flavour Fragmentation Functions from Lepton Momentum Spectrum.

Most of the experiments also allowed the B semi-leptonic branching ratio and the charm fragmentation function parameter ϵ_c to vary as free parameters to be fitted together with ϵ_b. The result for $< z_c >$ was compatible with the value from D^*'s while the measured B decay semi-leptonic branching ratios from these experiments all yielded values ~12% in agreement with the $\Upsilon(4S)$ experiments [92]. The average values of z were

$$< z_b > = 0.778 \pm 0.038 \longrightarrow \epsilon_b \sim 0.014$$

$$< z_c > = 0.632 \pm 0.034 \longrightarrow \epsilon_c \sim 0.090$$

Notice that from expression 4.9 and the ϵ_c value from D^*'s, an effective mass $m_{u,d} \sim 300$ Mev/c^2 $\sim \Lambda_{QCD}$ is implied if m_c is taken to be 1.5 GeV/c^2. If an assumption of $m_b = 5.0$ GeV/c^2 is taken, this also gives an expectation of $\epsilon_b \sim 0.004 \rightarrow < z_b > \sim 0.85$, independent of the uncertainty in $m_{u,d}$. However, the effect of s quark mass related to D_s, D_s^*, B_s production is still not clear. Considering the uncertainties in the assumption of the quark masses and the still rather large measurement errors the general picture is quite consistent.

For the Monte Carlo used in the analysis, $\epsilon_c = 0.075$ and $\epsilon_b = 0.005$ were used corresponding to $< z_c > = 0.65$ and $< z_b > = 0.85$. The effect of the uncertainties in ϵ on the fragmentation function $f(z)$ can be seen from Fig. 4.8.

4.4 Production and Decay of Heavy Flavours

The production ratios of various heavy mesons from heavy quarks were modelled to respect the same $u : d : s$ ratio and pseudoscalar to vector meson production ratio as in Equations 4.4 and 4.5 for the general fragmentation processes. The ratio $u : d : s$ of 1:1:0.4 resulted directly in the primary production ratios:

$$(D^+ + D^{*+}) : (D^0 + D^{*0}) : (D_s + D_s^*) = 1 : 1 : 0.4 \qquad (4.10)$$

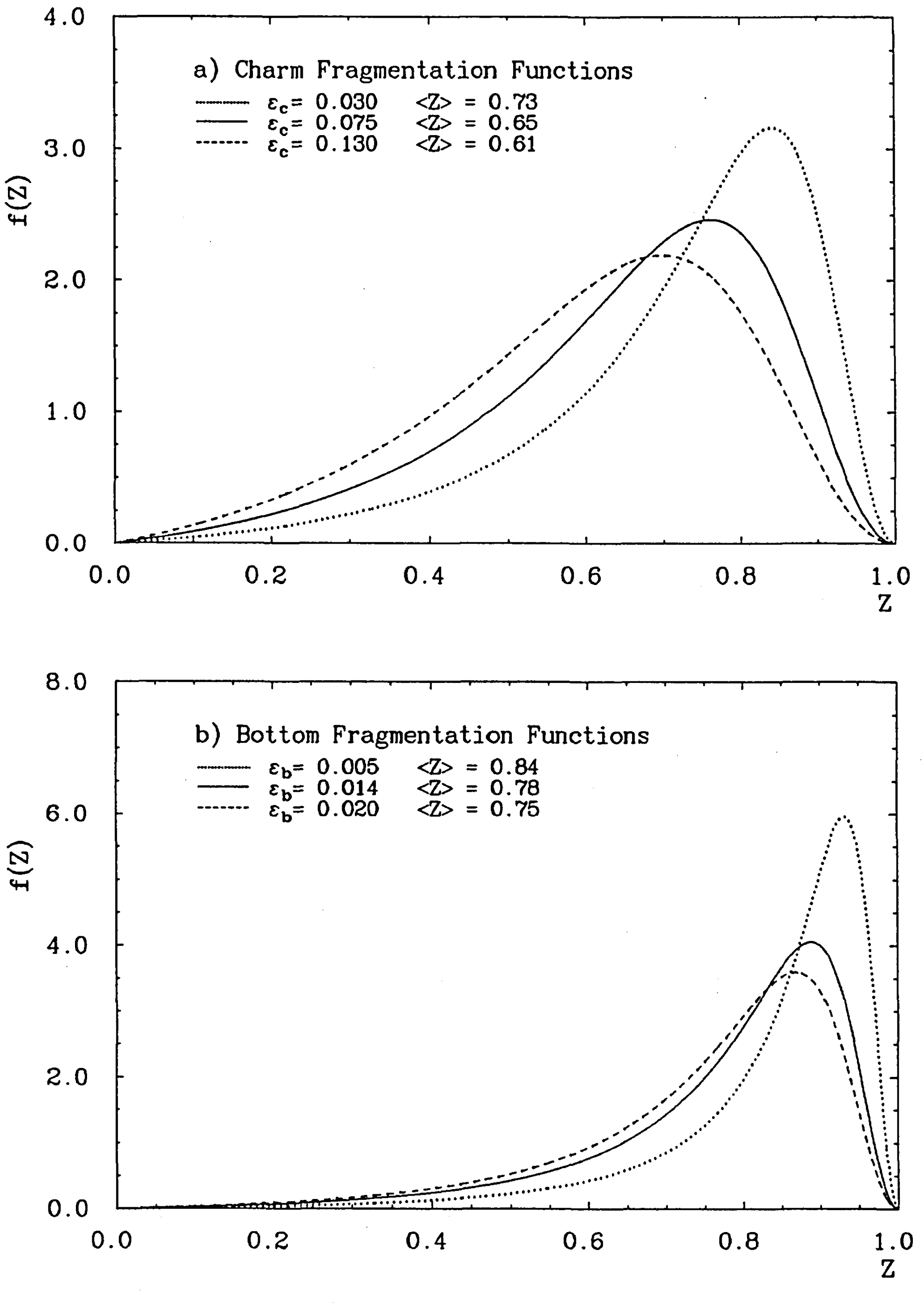

Figure 4.8: Heavy Flavour Peterson Fragmentation Functions.

Leading Charm Mesons (%)		Leading Bottom Mesons (%)	
D^0, $\bar{D}^0$	17.5	B^0, $\bar{B}^0$	41.7
$D^{\pm}$	17.5	$B^{\pm}$	41.7
$D_s^{\pm}$	7.0	$B_s^{\pm}$	16.6
D^{*0}, $\bar{D}^{*0}$	24.2	—	
$D^{*\pm}$	24.2	—	
$D_s^{*\pm}$	9.6	—	

Table 4.3: Monte Carlo Heavy Flavour Leading Meson Production Fractions.

and

$$B^+ \; : \; B^0 \; : \; B_s \; = \; 1:1:0.4 \tag{4.11}$$

The P/(P+V) ratio of 0.42 was also applied to the primary charm meson production ratio to give $D/(D^* + D) = 0.42$. No charm or bottom baryons were produced and no B^*, D^{**} or even higher spin state mesons were produced due to the insufficient experimental information. The resultant fractions of leading heavy flavour mesons are listed in Table. 4.3.

The important quantity in the primary charm production which can affect this analysis is the D^0/D^+ production ratio since their lifetimes are different by more than a factor of 2. This is in turn strongly influenced by the direct D to D^* production ratio due to the fact that D^{*0} decays entirely to D^0. If the primary charm production is dominated by D^* production, an important difference between the D^0 and D^+ production is expected.

Although many experiments claimed rather large D* production cross-sections in favour of the D* dominance, they reduced the numbers, after accepting the revised D decay branching ratios from Mark III. This direct evaluation of cross-section suffered from further uncertainty in Br($D^{*+} \to D^0\pi^+$), with the actual values used by different experiments ranged from 44% to 65%. The lower end of this branching ratio was obtained together with other D* decay branching ratios, by the Mark II experiment at SPEAR [87] using a global fit to the recoiling mass spectrum in charm production. They obtained

$$\begin{aligned} Br(D^{*+} \to D^0\pi^+) &= 44 \pm 10\% \\ Br(D^{*+} \to D^+\pi^0) &= 34 \pm 7\% \\ Br(D^{*+} \to D^+\gamma) &= 22 \pm 12\% \end{aligned} \tag{4.12}$$

without the constraint on isospin conservation. The branching ratio Br($D^{*+} \to D^0\pi^+$) used by this Monte Carlo was 64%. This was not in serious disagreement with the measurement result in Equation 4.13 since the measuremental error was large due to a simultaneous fit with many parameters.

It is more interesting to check with the direct measurement of inclusive D^0 and D^+ production together with D^* production. If a branching ratio of Br($D^{*+} \to D^0\pi^+$) = 60% was assumed, both the measurements of CLEO[85] and HRS[86] came fairly close to the expected $D/(D^* + D)$ ~1/4 from spin statistics. But HRS also made the unique simultaneous measurement of inclusive D^+ and D^0 production giving a ratio of D^+/D^0=0.7±0.3 which suffered less from uncertainties in branching ratios and other extra uncertainties in comparing different experiments. This, however, seemed to prefer substantially larger direct D production. Therefore the Monte Carlo input of $D/(D^* + D)$=0.42 was a compromise between the preference of the high D^* cross section and the rather large D^+/D^0 production ratio.

The D decay branching ratios were originally based on the the measurements by Mark I [21] and were subsequently updated according to the new Mark III results [22]. The non-2-body modes were modelled by phase space decay except the semi-leptonic modes where the V-A matrix elements were also included.

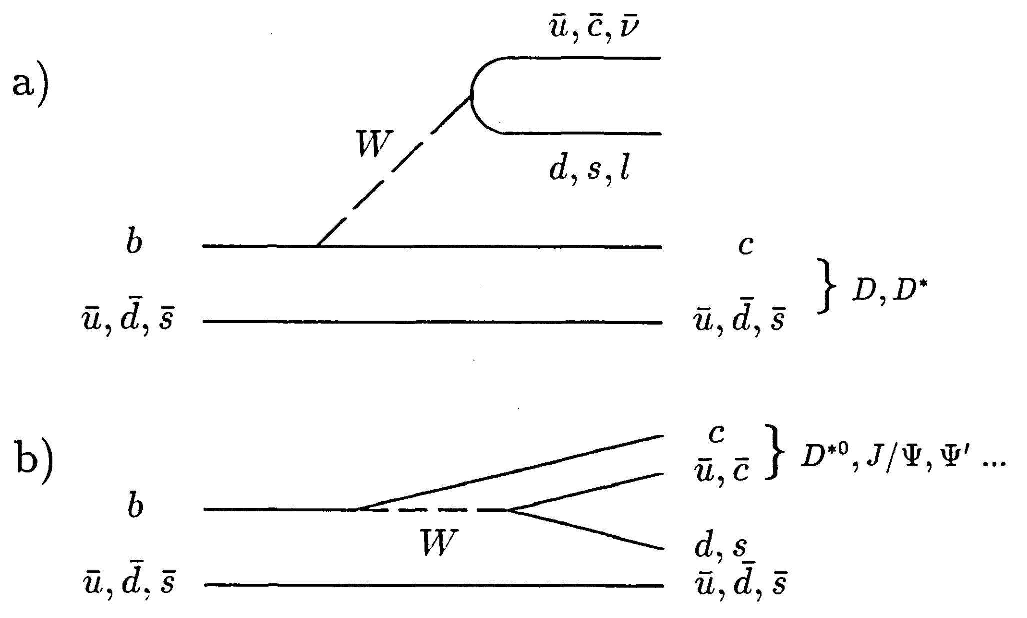

Figure 4.9: Illustration of spectator B decays: a) Charm-Spectator system and virtual W independent mode (no colour suppression); b) Colour suppressed mode.

A major feature of this independent jet model was the incorporation of a B decay Monte Carlo [90] based on various experimental results of CLEO. The major assumptions included:

1) The decays were purely spectator type as shown in Fig. 4.9a. The spectator light quark and the quark remaining after the b threw off the virtual W was assumed not to interfer with the fragments from the virtual W. This was based on the study of inclusive D^0 and $D^{*\pm}$ momentum spectrum from B decays done by CLEO [91]. The conclusion was drawn from the similarity between the D^0, D^* momentum spectra and the momentum of the c quark from $b \rightarrow cW$ where the c and W were assumed not to be interacting with each other. The type of decay as seen in Fig. 4.9b can occur as indicated by the recent measurements of B $\rightarrow$ J/Ψ + X [93] which cannot take place in process a). However this is believed to be suppressed compared to process a) due to the fact that the quarks from the W have to have the right colour to match up with the charm-spectator system to form colour neutral mesons. Because of the uncertainty in the magnitude of process b) before the measurements of $B \to J/\Psi + X$, it was not included in the Monte Carlo.

2) The coupling of $b \to cW$ was assumed to be 100% implying no $b \to uW$ mode. This was based on a strong limit of

$$\frac{\Gamma(b \rightarrow u)}{\Gamma(b \rightarrow c)} <\sim 5\%$$

at 90% confidence level set by the CESR experiments [92]. It was obtained by analysing the momentum spectrum of the leptons from B decays with especial emphasis on the high momentum end point beyond the $b \to cl\bar{\nu}$ phase space limit. Although there has been some discussion indicating that the limit should be relaxed [14], due to the dependence of the result on varying the previously fixed model parameter related to the assumed Fermi motion between the b quark and the light spectator in the B meson, most models still gave limits safely below 10%.

3) No further fragmentation in the charm-spectator system so that the charm quark and the light spectator quark would combine immediately to form a D or D^* meson (including D_s). This was consistent with the B decay charge multiplicity measurement [94] of 3.8 ± 0.4 for semileptonic modes. The measurement result of D meson decay charge multiplicity was $\sim$2.4 [21] and there was also the occasional transition $\pi^{\pm}$ from $D^{*\pm}$ in B decays. After subtracting these contributions and the lepton itself, the remaining charge multiplicity was consistent with zero. The rather hard D and D^* momentum spectra [91] also excluded the possibility of extensive fragmentation in the charm-spectator system which would significantly soften the D and D^* momenta.

The virtual W could either turn into $e\bar{\nu}_e$ or $\mu\bar{\nu}_\mu$ according to the specified 12% semileptonic branching ratio or fragment into hadrons after firstly turning the W into Cabbibo-favoured $\bar{u}d$ or $\bar{c}s$ pairs. The probability ratio of $\bar{u}d : \bar{c}s$ was set to 9:1 based on the expectation of phase space calculations. The V-A matrix elements were used together with the phase space factors to determine the B decay topology except in the case when only 1 meson was made from the W leading to a 2 body decay. Since the branching $W \to \tau\bar{\nu}_\tau$ suffered a phase space suppression similar to $W \to \bar{c}s$ with regard to the semi-electronic and semi-muonic modes, it was considered to be small enough to be neglected.

The most crucial parameter relevant to the analysis of this thesis is the B decay charge multiplicity. The Monte Carlo outcome can be compared to the CLEO measurements [94]

	$< n_{ch} >$	R.M.S $< n_{ch} >$
CLEO Data	$5.50 \pm 0.03 \pm 0.15$	$2.18 \pm 0.02 \pm 0.13$
Monte Carlo	5.57	2.11

The momentum spectra of the D and D^* from B decay in the B rest frame also agreed well with the measurement of CLEO. The inclusive D^0 momentum spectrum of B decay modelled by the Monte Carlo is shown in Fig. 4.10 together with the CLEO measurements corrected with the new Mark III D decay branching ratios and normalised to the same number of B^0,$B^{\pm}$ decays. The Monte Carlo can be seen to be consistent with the data within the rather large errors. The assumption of the spectator model can be examined by noticing the agreement in shape while the fraction of D^0 yield in B decay is reflected from the overall normalisation. The Monte Carlo used different decay lifetimes for different charm mesons and the same lifetime for all B mesons since no separate measurements of lifetimes for different species of B mesons exist up to date. The Monte Carlo input lifetime values together with the present world average values are shown in Table 4.4 as reviewed by Gilchriese [18].

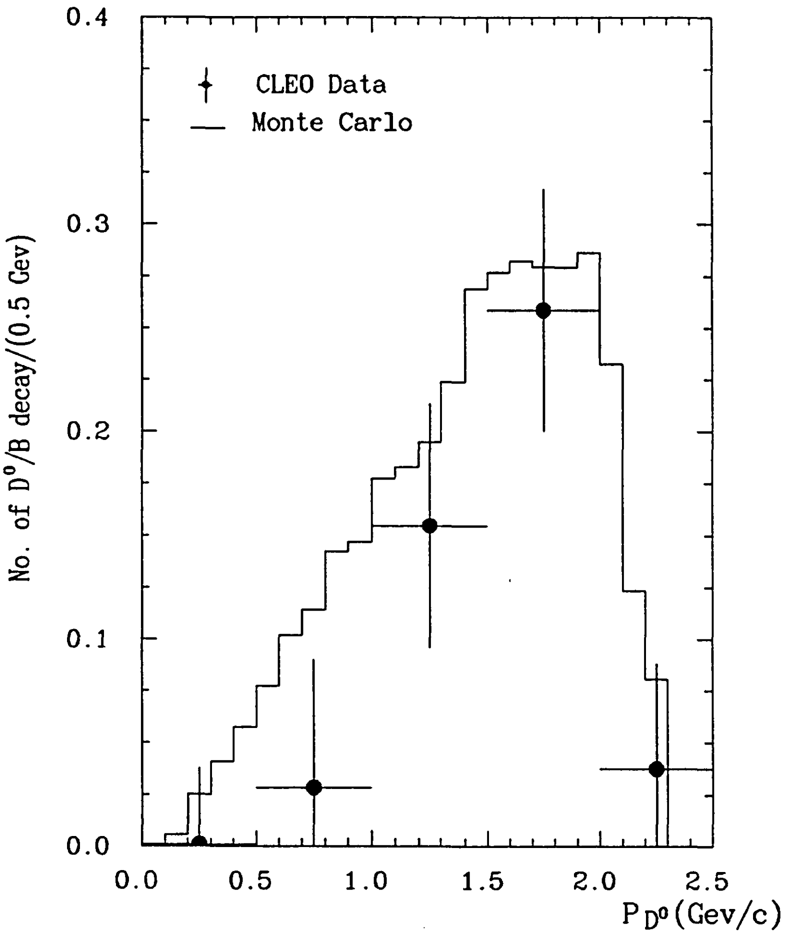

Figure 4.10: Momentum Spectrum of D^0 from B decays in B Rest Frame.

Particle	World Average of Measurements (10^{-13} sec)	Monte Carlo Input (10^{-13} sec)
$D^0, \bar{D}^0$	$4.30 \pm {}^{0.30}_{0.19}$	4.00
$D^{\pm}$	$10.31 \pm {}^{0.52}_{0.44}$	9.33
$D_s^{\pm}$	$3.5 \pm {}^{0.6}_{0.5}$	3.33
$< B\ hadron >$	$11.1 \pm {}^{1.4}_{1.3}$	10.00

Table 4.4: Monte Carlo Heavy Flavour Particle Lifetime Input.

4.5 Detector Simulation

The detector simulation code SIMPLE [95] was applied to the TASSO detector environment. The spatial starting points of the events were simulated to spread within a specified beam envelope. The starting point of each particle was generated with the decay distance included if the particle decayed weakly.

Each particle from the event generator was traced through the detector layer by layer from its generation point. For each layer of material, the possible γ conversions, elastic and inelastic nuclear scatterings, charged particle multiple Coulomb scatterings and electron bremsstrahlung were simulated. The hits due to charged particles traversing through the wire chambers were created according to the wire chamber efficiencies and spatial resolutions. The time of flight of each particle was also traced to the position corresponding to the inner time of flight counters and the time of flight measurements were simulated.

Both the main drift chamber and vertex detector simulations included variations of spatial resolutions at different parts of a wire cell. The hit efficiencies were allowed to vary from layer to layer according to the study of hadronic data and cosmics. The vertex detector spatial resolution was generated with the rather pessimistic value of 120μm in the middle of the wire cells due to the fact that the Monte Carlo was originally tuned to the old 1983-84 data only.

Random noise hits were also generated based on the study of extra hits in hadronic events and hits in random beam crossing events. This was done by generating hits randomly in ϕ with the hit multiplicities per event following a Poisson distribution and the mean hit multiplicity was similar to that described in chapter 3 for clean random beam crossings. No attempt was made to simulate large showering noise hit clusters in this Monte Carlo. A 2% probability of crosstalk within the same layer was also added for both the drift chamber and the vertex detector.

The hit banks were created by taking only the earliest hit on each wire irrespective as to whether it was a track hit or a noise hit to simulate the effect of normal TDC readout. The track finder FELIX (see section 2.5) was then performed on the hit bank in the same way as for the data. The scattering fit (also described in section 2.5) was then the performed on each track. The main hadronic event trigger was also simulated from the chamber and ITOF hits to reject events which would fail the trigger. Further rejections were made by passing events through the offline processing chain and hadronic selection program.

4.6 Data – Monte Carlo Comparison

After detector simulation of the Monte Carlo events including the offline passes and hadronic selection as well as the track finder processing, the general features of the data and Monte Carlo can be compared directly using the final form of the charged tracks. For the following comparisons only good tracks reconstructed in 3-D were used.

4.6.1 Event Shape

The event shape comparisons in figures 4.11 - 4.17 were all normalised to the same number of events as the entries were divided by the number of input events.

The inclusive charged particle momentum spectra are plotted in Fig. 4.11. The event charge particle multiplicities are plotted in Fig. 4.12 for both data and Monte Carlo. As stated at the beginning of this chapter, the Monte Carlo was at a fixed energy and only briefly tuned to part of the data. The slight excess of charge multiplicity in the Monte Carlo showed up mainly in the high momentum tail of the inclusive momentum spectrum. This excess will later on be included as a part of the systematic error in the tagging flavour content estimation. However, this was rather surprising since the most important parameter a_L which controlled the momentum spectrum already had a sizable increase from 0.630 for the 35 GeV Monte Carlo [96] up to 0.751. This was supposed to soften the momentum spectrum as naïvely expected from Equation 4.6.

The event thrust axis is defined as the direction along which

$$T = \sum_{j}^{N_{track}} \frac{\left|P_{j\|}\right|}{|P_j|} \tag{4.13}$$

is maximum, where the sum is over all tracks in the event and $P_{\|}$ is the momentum component of a track parallel to the thrust axis. The thrust axis is normally a good description of the original direction of the most energetic parton in the event. The maximum value of T is the *event thrust*. In the case of an event with 2 extremely narrow back to back jets, the thrust T approaches 1; in the case of a very spherical event, the thrust T tends to 0.5. Thus this is a useful parameter to distinguish 2-jet events and 3 or 4 jet events with the latter two bearing lower thrust values.

Further event shape parameters are defined by the normalised momentum tensors

$$T^{(\gamma)}_{\alpha\beta} = \frac{\sum_j p_{j\alpha} p_{j\beta} / |p_j|^{2-\gamma}}{\sum_j |p_j|^{\gamma}} \qquad \gamma = 1,2 \tag{4.14}$$

Diagonalising tensor $T^{(2)}$ gives eigenvectors $\hat{n}_1, \hat{n}_2, \hat{n}_3$ and the corresponding eigenvalues

$$Q_k = \frac{\sum_j (\mathbf{p_j} \cdot \hat{n}_k)^2}{\sum_j |p_j|^2} \tag{4.15}$$

Similarly the tensor $T^{(1)}$ gives eigenvectors $\hat{m}_1, \hat{m}_2, \hat{m}_3$ and the corresponding eigenvalues

$$L_k = \frac{\sum_j (\mathbf{p_j} \cdot \hat{m}_k)^2 / |p_j|}{\sum_j |p_j|} \tag{4.16}$$

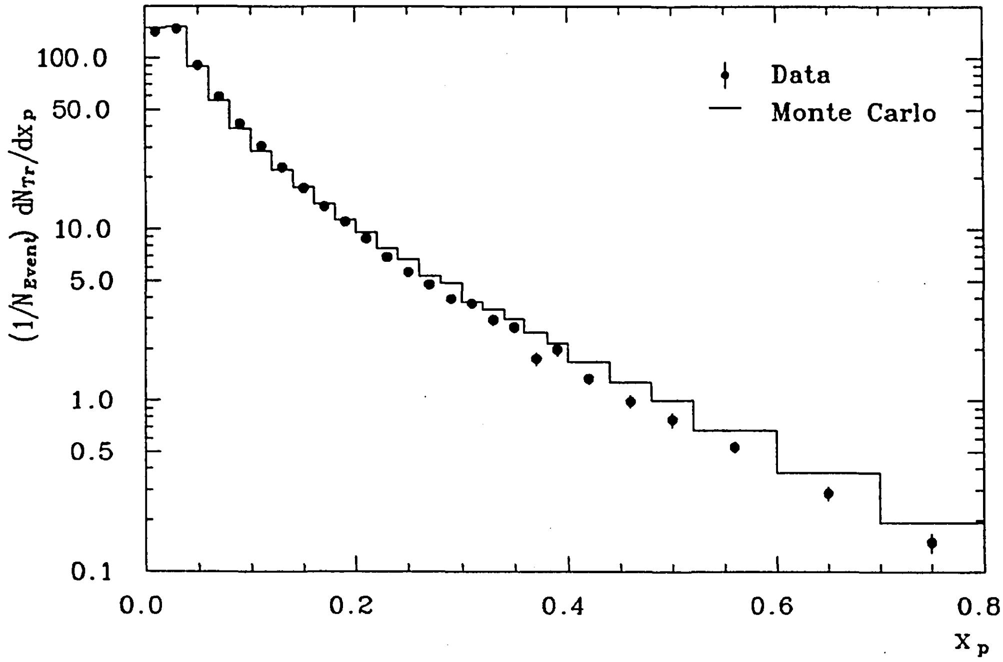

Figure 4.11: Inclusive Charged Particle Momentum Distribution.

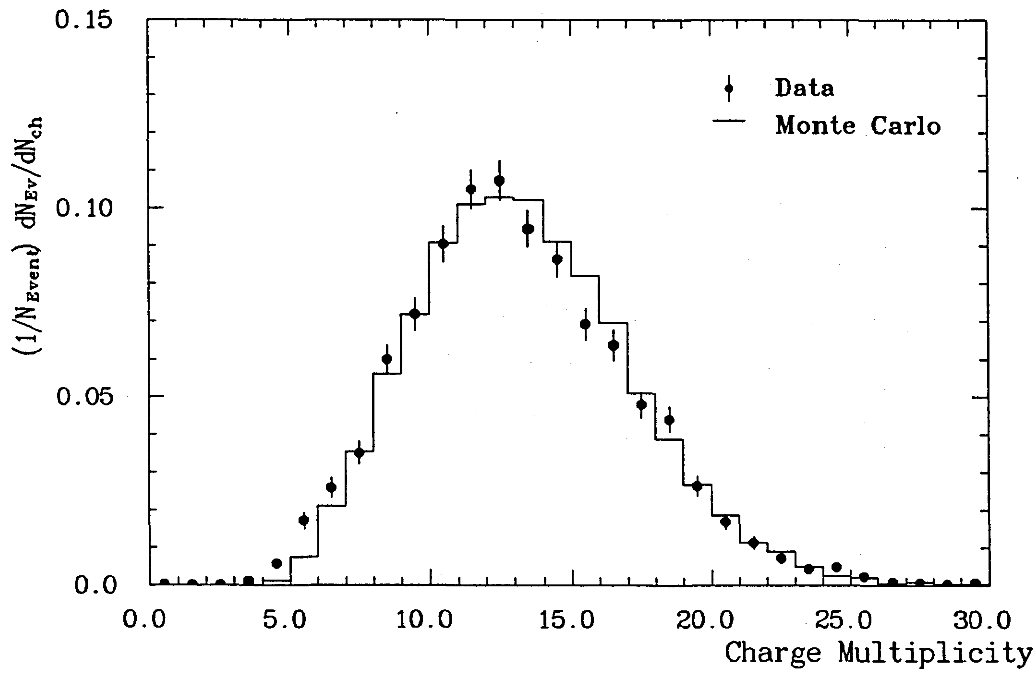

Figure 4.12: Event Charged Particle Multiplicity.

After ordering the eigenvectors such that $Q_1 \geq Q_2 \geq Q_3$ and $L_1 \geq L_2 \geq L_3$, the axes $\hat{n}_1, \hat{m}_1$ give directions close to that of the thrust axis. The direction of $\hat{n}_1$ is the sphericity axis and the event sphericity is defined as

$$S = \frac{3}{2}(1 - Q_1) \tag{4.17}$$

The variable S is close to 0 in case of an event with 2 narrow back to back jets and has larger values for more spherical events. It has a sensitivity comparable to that of T for 3 or 4 jet events due to hard gluon radiation. However, T is more easily related to QCD as it is linear in track momentum. The T and S distributions for data and Monte Carlo events, calculated using all charged tracks in the events, are shown in Fig. 4.13 and Fig. 4.14 respectively.

The characteristics of momenta of particles in transverse and longitudinal directions to the event thrust axis can be seen from the distributions of P_T^2 and rapidity η respectively. The rapidity of a particle is defined as

$$\eta = \frac{1}{2} ln \left(\frac{E + P_{\parallel}}{E - P_{\parallel}} \right) \tag{4.18}$$

where P_T and $P_{\parallel}$ are momentum components of a particle transverse and parallel to the event thrust axis respectively. The P_T^2 and η distributions of charged tracks are shown in Fig. 4.15 and Fig. 4.16. In calculating the energy E of the particles, a $\pi^{\pm}$ mass was assigned to all particles. The rather flat rapidity distribution of the Monte Carlo was a known problem [96] of the independent jet model which was not adjustable to produce the mid-plateau enhancement.

Since the axes $\hat{n}_3, \hat{m}_3$ are generally perpendicular to the event plane defined by acollinear jets, the P_T of particles with respect to axes $\hat{n}_3, \hat{m}_3$ ($P_{T\ out}$) characterises the flatness of an event. The P_T of particles with respect to the axes $\hat{n}_2, \hat{m}_2$ ($P_{T\ in}$) shows the spread of particle directions within the event plane. Thus the $P_{T_{out}}$ distribution is sensitive to the jet widths while $P_{T_{in}}$

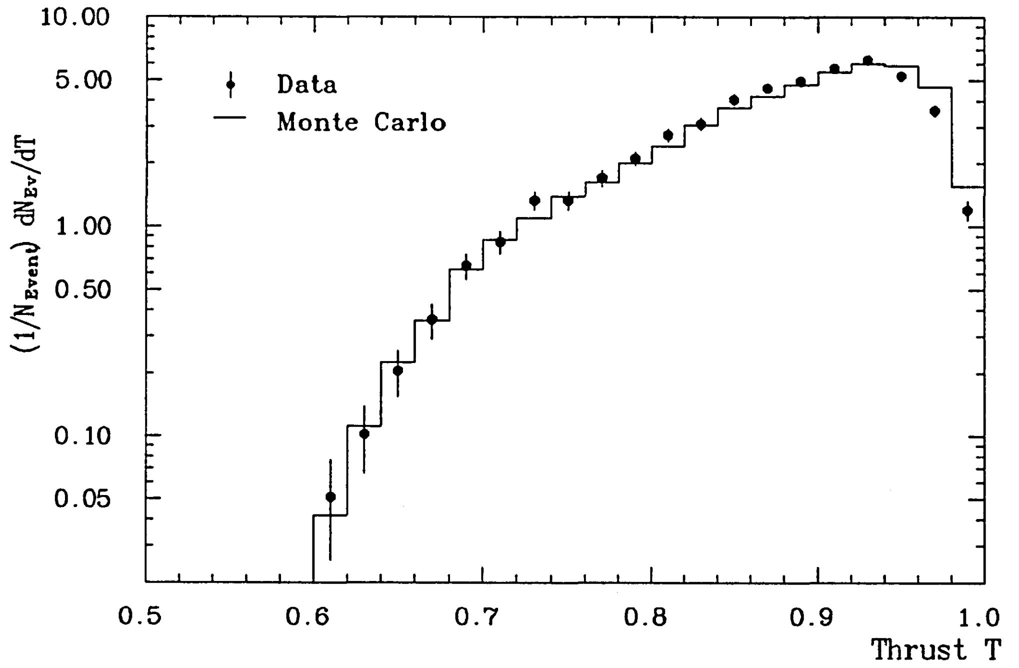

Figure 4.13: Event Thrust Distribution.

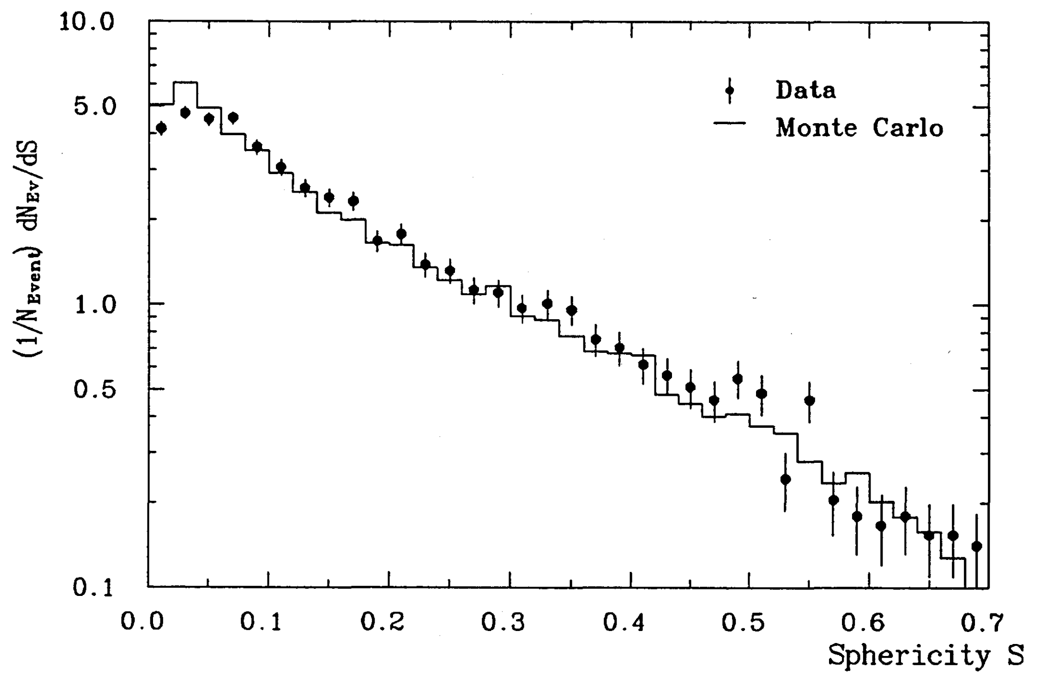

Figure 4.14: Event Sphericity Distribution.

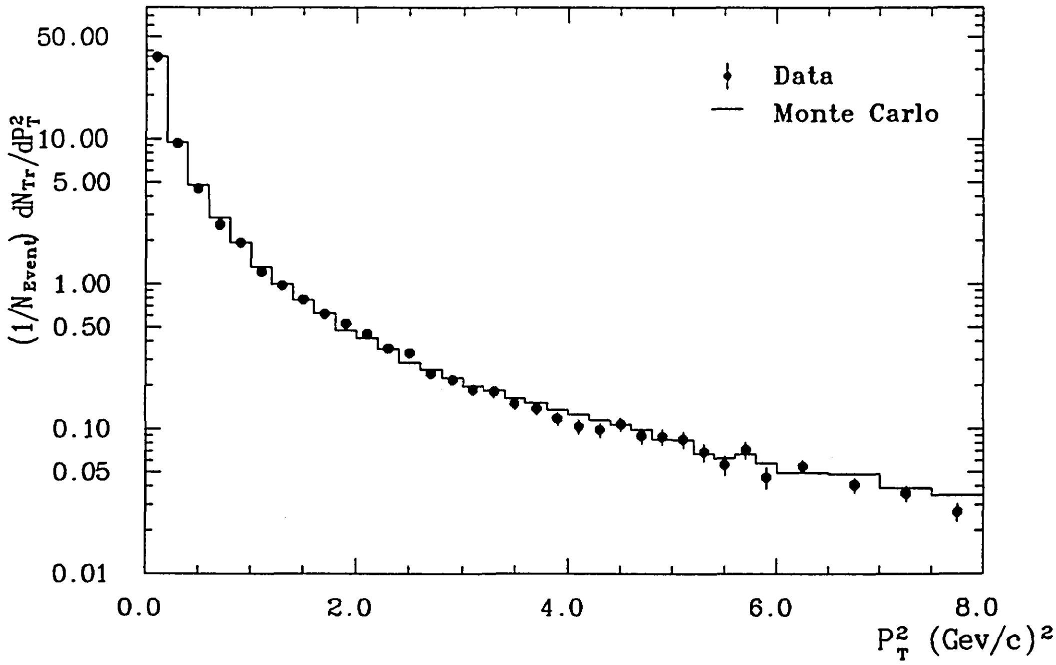

Figure 4.15: P_T^2 Distribution of Charged Tracks.

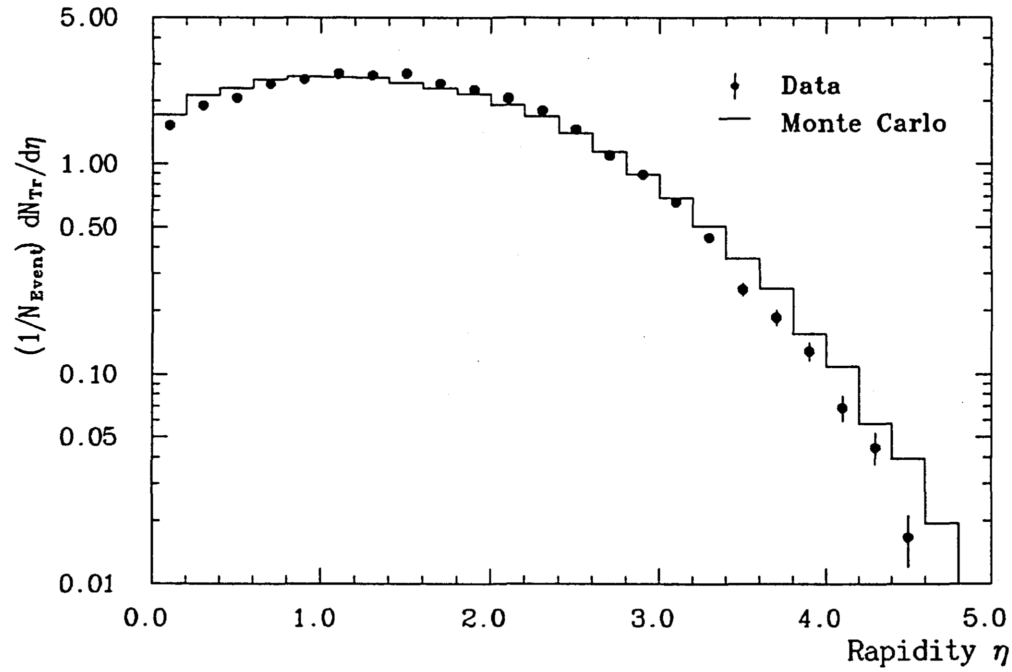

Figure 4.16: Rapidity Distribution of Charged Tracks.

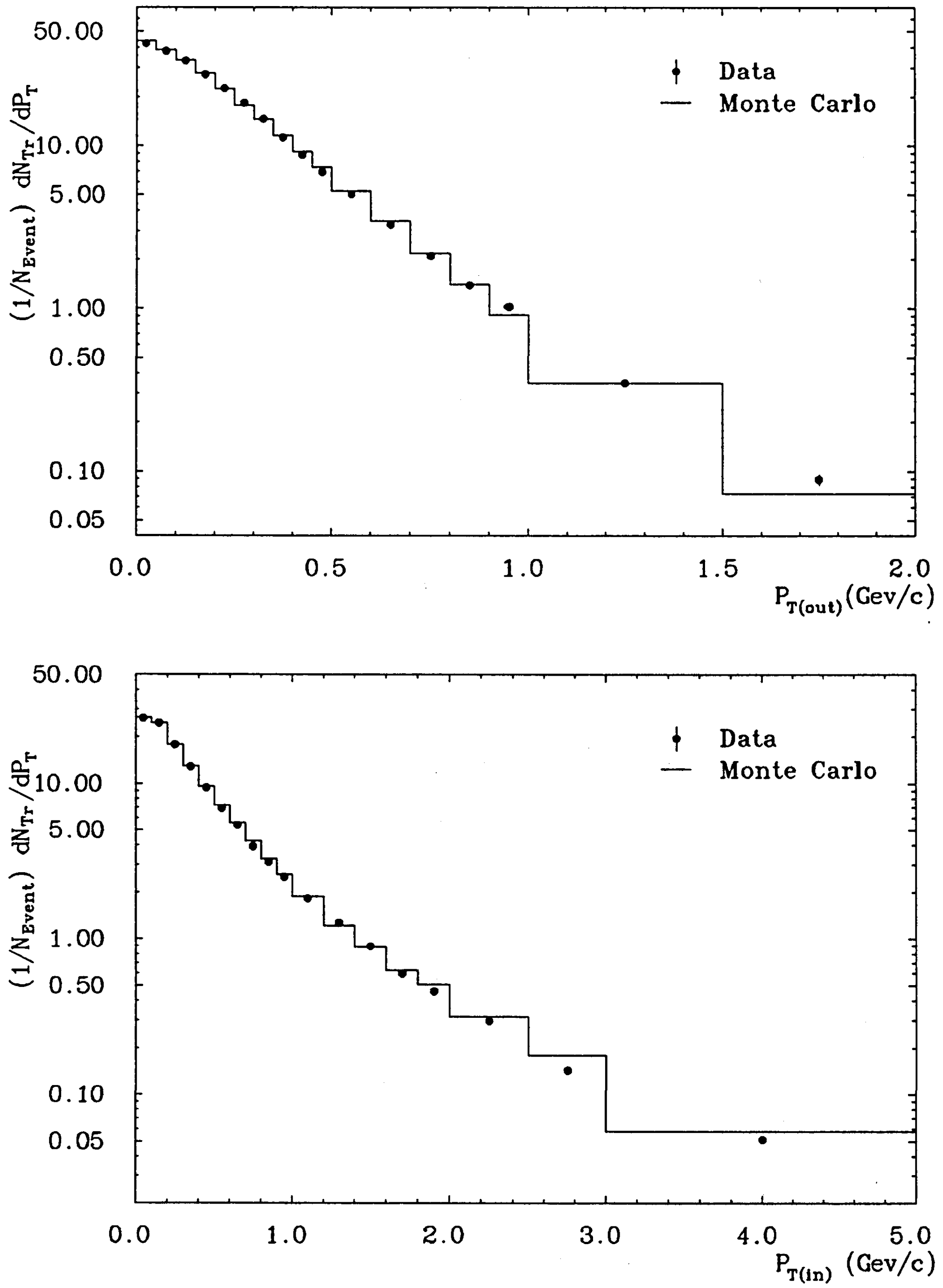

Figure 4.17: $P_{T_{out}}$ and $P_{T_{in}}$ Distributions of Charged Tracks.

distribution is more sensitive to the rate and hardness of gluon radiation which is proportional to the strong interaction coupling constant α_s. The $P_{T_{out}}$ and $P_{T_{in}}$ distributions are plotted with respect to the event $\hat{m}_3, \hat{m}_2$ axes determined from $T^{(1)}$ tensor in Fig. 4.17.

4.6.2 Tracking Resolution

To examine the quality of the detector simulation, the hit association with tracks were checked with data. The hits associated with tracks should reflect both the hit efficiency and effect of tracks sharing the same wire cells. The impact parameter resolution would worsen when the track had fewer VXD hits. Large discrepancies would also affect the number of tracks passing the cut on the minimum number of VXD hits. The percentages of tracks having hits associated with each of the 21 wire chamber layers of the TASSO inner detectors are shown in Fig. 4.18 for both data and Monte Carlo simulation. The distribution of the total number of VXD hits associated with tracks are plotted in Fig. 4.19.

The most important factor of the detector performance which would directly influence the various lifetime measurements and the plausibility of the decay vertex tagging is the track impact parameter resolution. The impact parameter resolution was checked for tracks in hadronic events passing the normal track cuts of P $>$ 0.4 GeV/c and VXD hits $\geq$ 3. The variable plotted in Fig. 4.20 is the impact parameter of tracks in hadronic events, to the event spot found for each event. The definition of the sign of impact parameters and the method of determining event spot will be discussed in chapter 5.

The generally reasonable agreement between data and Monte Carlo in both the event shape and detector performance provided the essential basis for establishing and estimating the effectiveness of fine decay structure tagging.

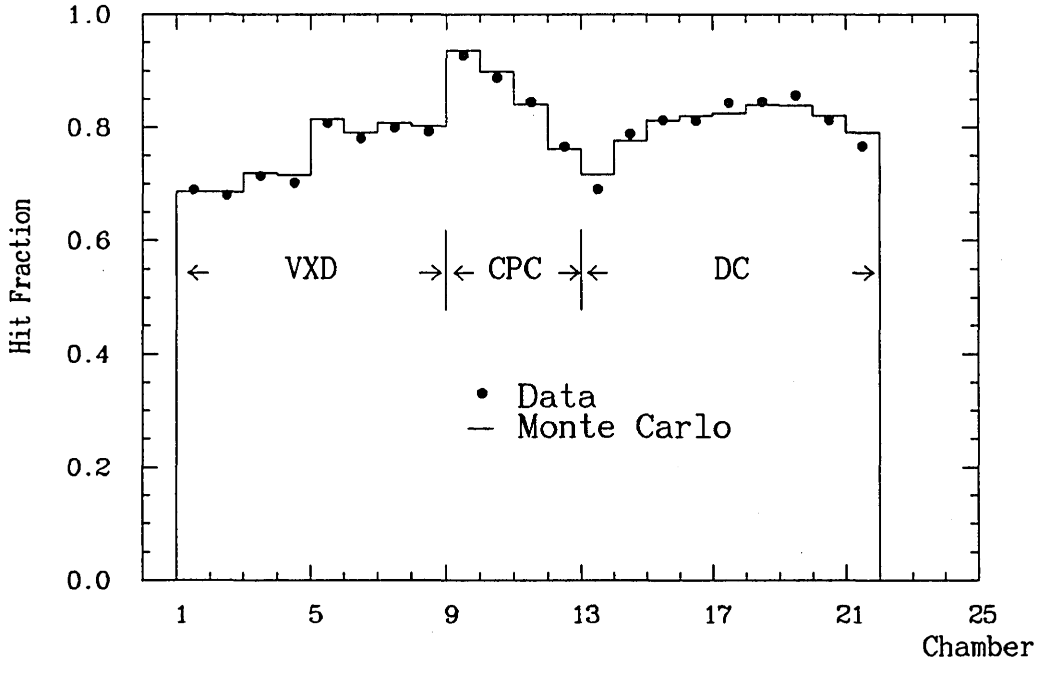

Figure 4.18: Hit-Track Association Percentages for All Wire Chamber Layers.

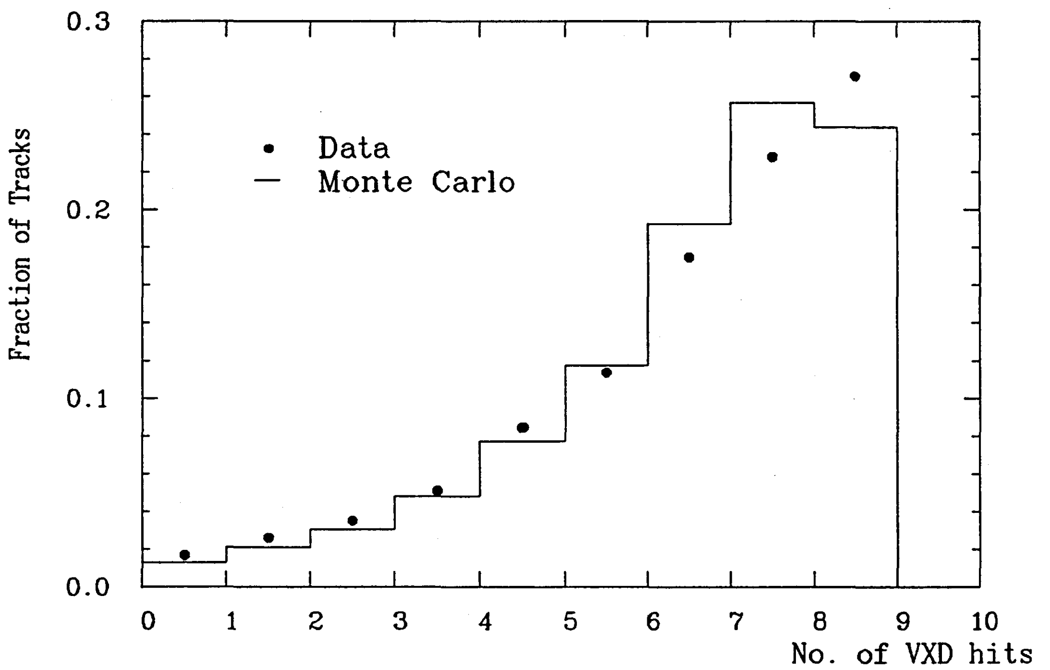

Figure 4.19: No. of VXD Hits Associated with Tracks.

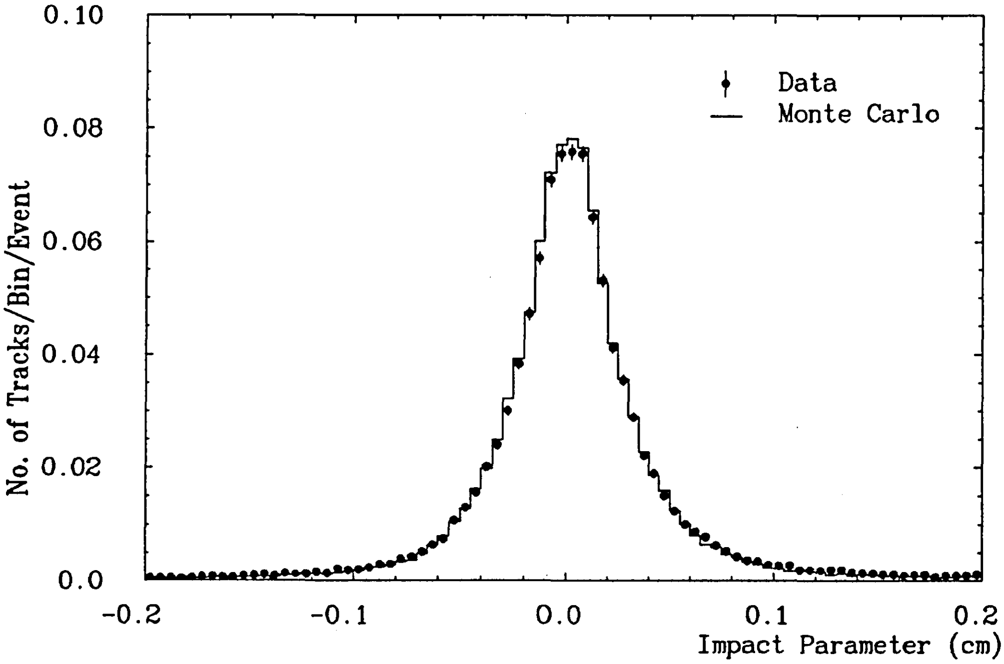

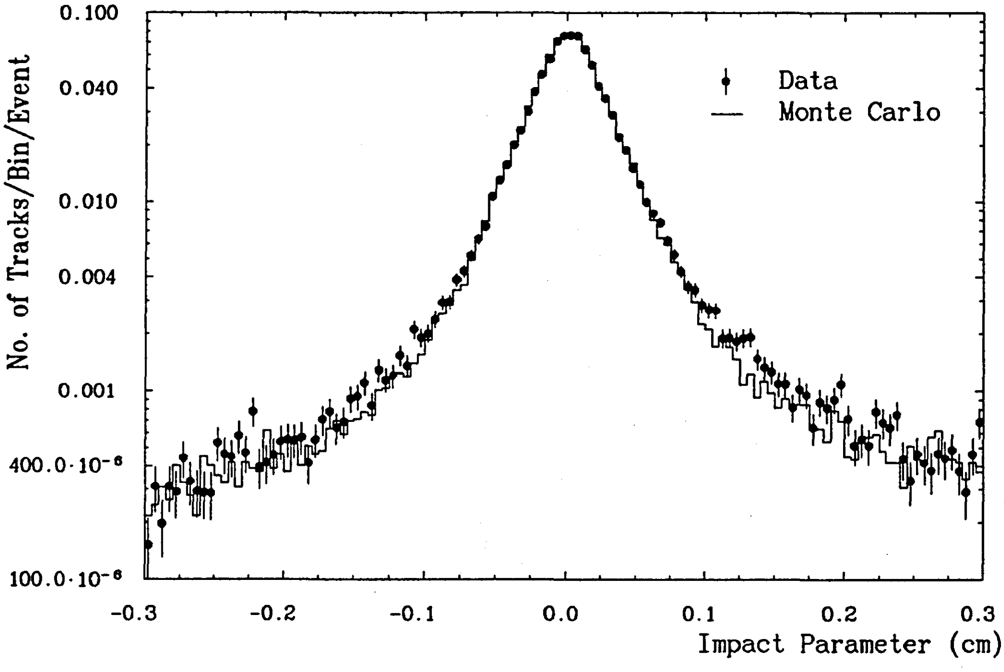

Figure 4.20: Track Impact Parameter to Event Spot in Hadronic Events.

Chapter 5

Analysis of b Enrichment Method

5.1 General Study of Requirements

The aim of this analysis is to use the long decay lifetimes of B mesons to separate the primary $b\bar{b}$ events in e^+e^- annihilations from the more abundant light flavours and charm events, so that the various properties of the b quark can be studied with less background from other flavours.

In the instrumentation of the TASSO detector, only charged particles can be detected with both momentum and spatial trajectory measurements to a high accuracy. For most e^+e^- experiments presently running, the accuracy of measuring charged track hits in the $r-\phi$ plane is normally an order of magnitude better than in z. The demand of recognising decay signatures in a region of a few mm in size limits the tagging method to one based on the geometry of charged tracks in the $r-\phi$ plane only. Therefore reference to tracks will exclusively mean charged tracks and the distance variables will mean the projected distances in the $r-\phi$ plane unless stated otherwise explicitly.

The event geometric configurations can be firstly considered in an idealised manner. A primary light flavour event is expected to consist of tracks all coming from the e^+e^- annihilation point apart from a few tracks from K^0_s or Λ

decays. A $c\bar{c}$ event should have most of the tracks coming from the primary event spot together with a few tracks from 2 separate decay vertices due to short lived charm hadrons. Ignoring the possible small fraction of B baryon production, the general feature of a $b\bar{b}$ event can be expected to contain two B mesons travelling opposite to each other with very high energy due to the rather hard heavy quark fragmentation function, together with a few primary fragmentation particles. Each B meson decays after some distance and almost always yields a charm meson with a few other particles at the decay point. The charm meson travels further and decays to form another vertex. This naïve idealisation can be seen from Fig. 5.1.

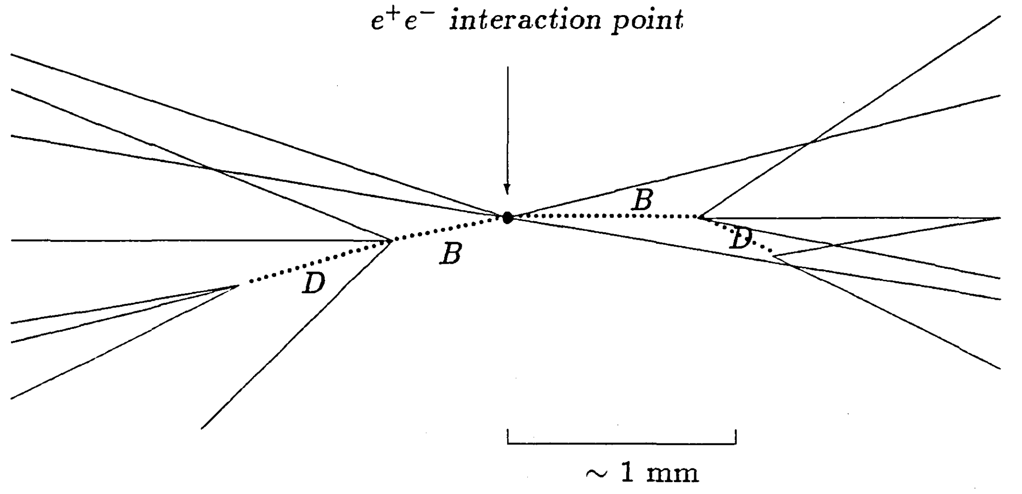

Figure 5.1: Illustration of an Idealised $b\bar{b}$ Event.

However this simple decay structure is normally smeared to a much more confusing picture due to the finite detector resolution which is comparable to the decay distances which are only of the order of 1 mm in general. The enrichment of $b\bar{b}$ events using these short distance decay structures is only possible when the decay distances are sufficiently long compared to the impact parameter resolution of average tracks.

Another concern is whether the $b\bar{b}$ events are separable from $c\bar{c}$ events since the charm hadrons also have comparable lifetimes. The expected decay

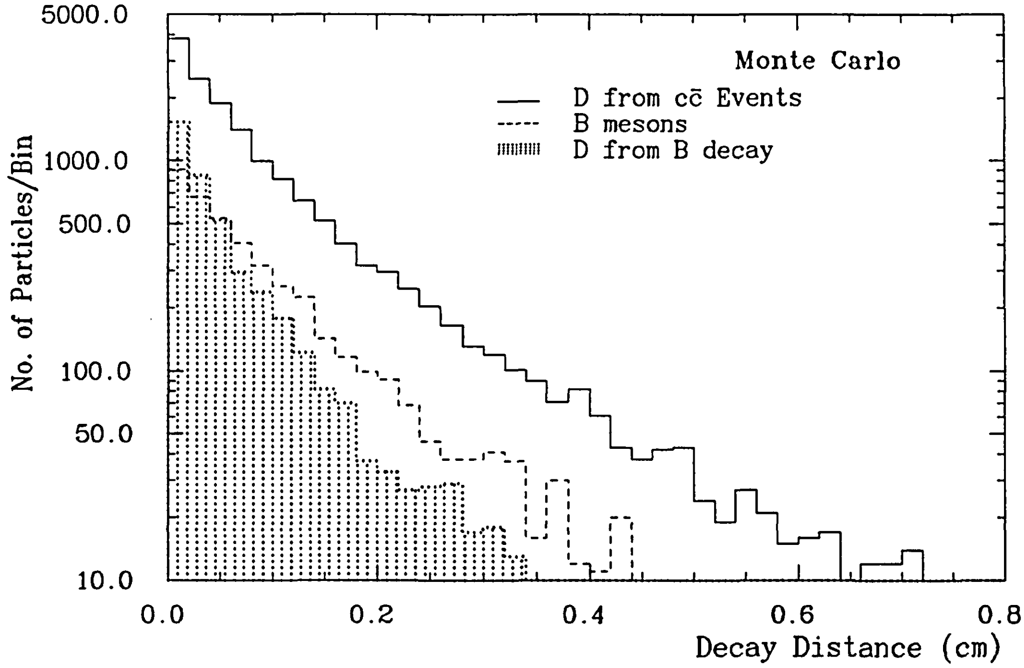

Figure 5.2: Monte Carlo Heavy Meson Decay Distances.

flight distances away from the event e^+e^- interaction point for heavy mesons of various origins are plotted in Fig.5.2. The problem seems rather serious at the first sight as charm mesons from $c\bar{c}$ events are not only very common, but their decay lengths are no shorter than those of the B mesons either. This is due to the fact the charm mesons normally have larger Lorentz boosts compared to B mesons which compensates for their slightly shorter lifetimes. The $D^{\pm}$, in fact, even has nearly the same lifetime as the average B hadrons which results in the large decay length tail. The charm mesons from B decays extend the B decay structure somewhat further but the distances are limited by the small Lorentz boost in this case.

To overcome this difficulty, the properties of the decay track impact parameters can be brought in to help. The impact parameter is defined as the distance of closest approach of a final reconstructed track to a reference point which can be the starting point of the particle or the e^+e^- interaction point. The definition of the sign of the impact parameter can be seen from Fig. 5.3 where the track with a positive impact parameter crosses the positive half of

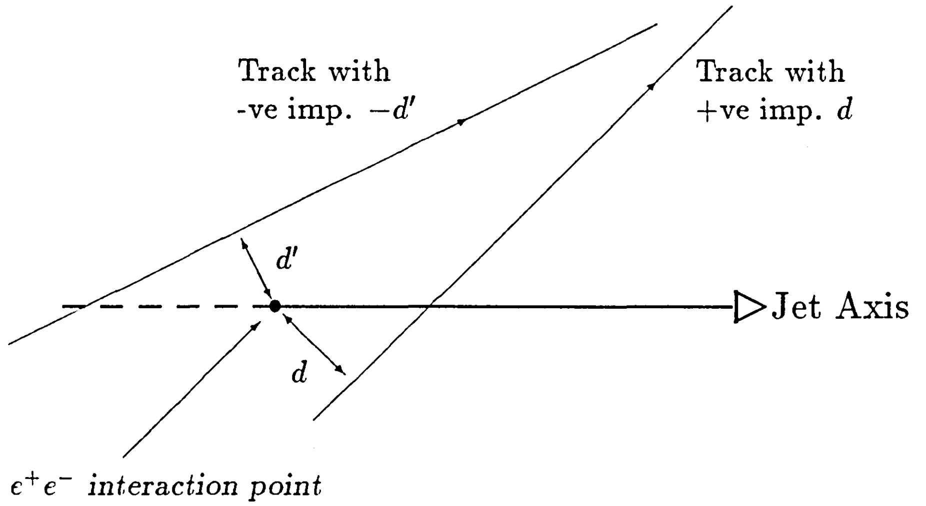

Figure 5.3: Sign Definition of Impact Parameters.

the axis of the jet to which it belongs. Consider a heavy meson travelling along the jet axis with various possible Lorentz boost factors. The longer decay distances resulting from larger Lorentz boosts are also accompanied by narrower opening angles of the decay tracks with respect to the heavy meson flight path for the same centre of mass frame decay configuration. These two effects tend to cancel each other with the interesting consequence that the decay track impact parameters are approximately independent of the heavy meson's Lorentz boost factor.

Since most of the annihilation events in PETRA energies are 2 jet-like, the events can simply be divided into two halves using the plane perpendicular to the event thrust axis. The outgoing vector along the thrust axis serves as a good approximation to the jet axis for each half. For this analysis, the thrust axis is calculated with the charged tracks in the event only. The angles of all generated Monte Carlo B meson flight directions with respect to the calculated thrust axes are shown in Fig. 5.4. The entries beyond 90° represent tracks in the extremely hard 3 or 4 jet events which cause two B mesons to end up in the same hemisphere. The Monte Carlo indicates that there are $\sim 3\%$ of $b\bar{b}$ events belonging to this class.

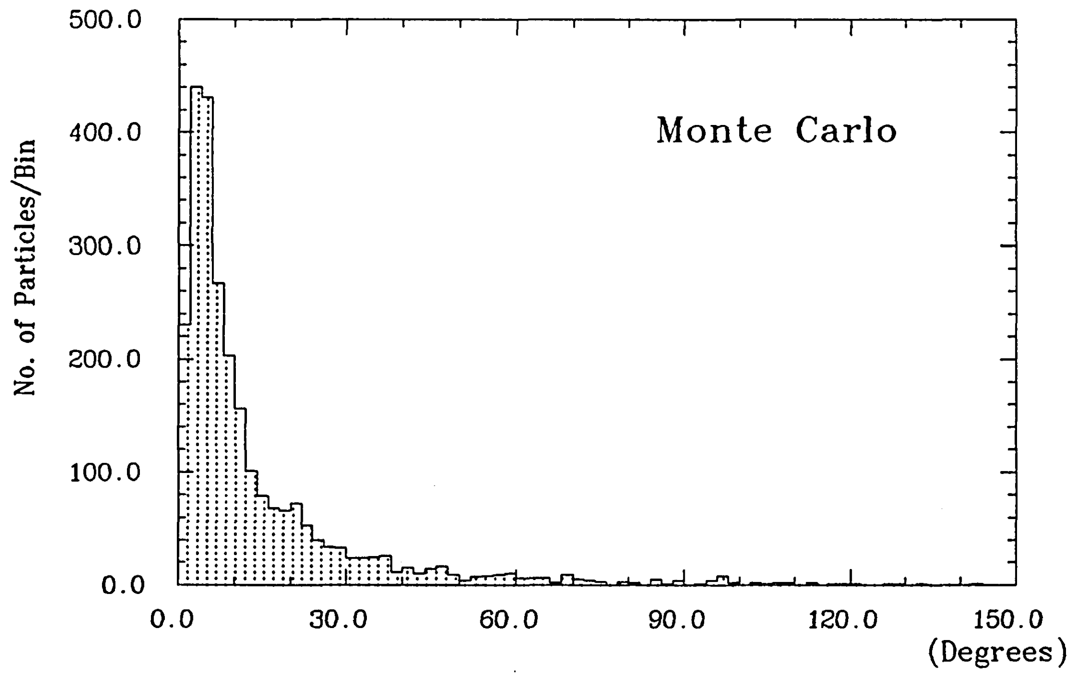

Figure 5.4: Monte Carlo B Flight Direction w.r.t Event Thrust Axis.

Following this definition of axes, the expected behaviour of different types of tracks can be studied from the Monte Carlo. The impact parameters of various types of Monte Carlo tracks with respect to the generated event e^+e^- interaction points are plotted in Fig. 5.5. The finite decay distances and smear due to finite detector resolution after track finding and fitting were folded in the distributions. Following the study of multiple scattering effects as in section 3.7, only good tracks with P $>$ 0.4 Gev/c were used and the number of VXD hits on each track was required to be ≥ 3. No normalisation was made so the different scales show the relative abundances of various types of tracks averaged over all hadronic events.

Although the large abundance of the fragmentation tracks and charm meson decay tracks still dominate the whole range of impact parameter distances, the positive shift in the impact parameters of B decay tracks can be seen to be more obvious than in those of the D meson decay tracks in $c\bar{c}$ events. As there are $\sim$ 10 times more $udsc$ events than b events, the severe background still

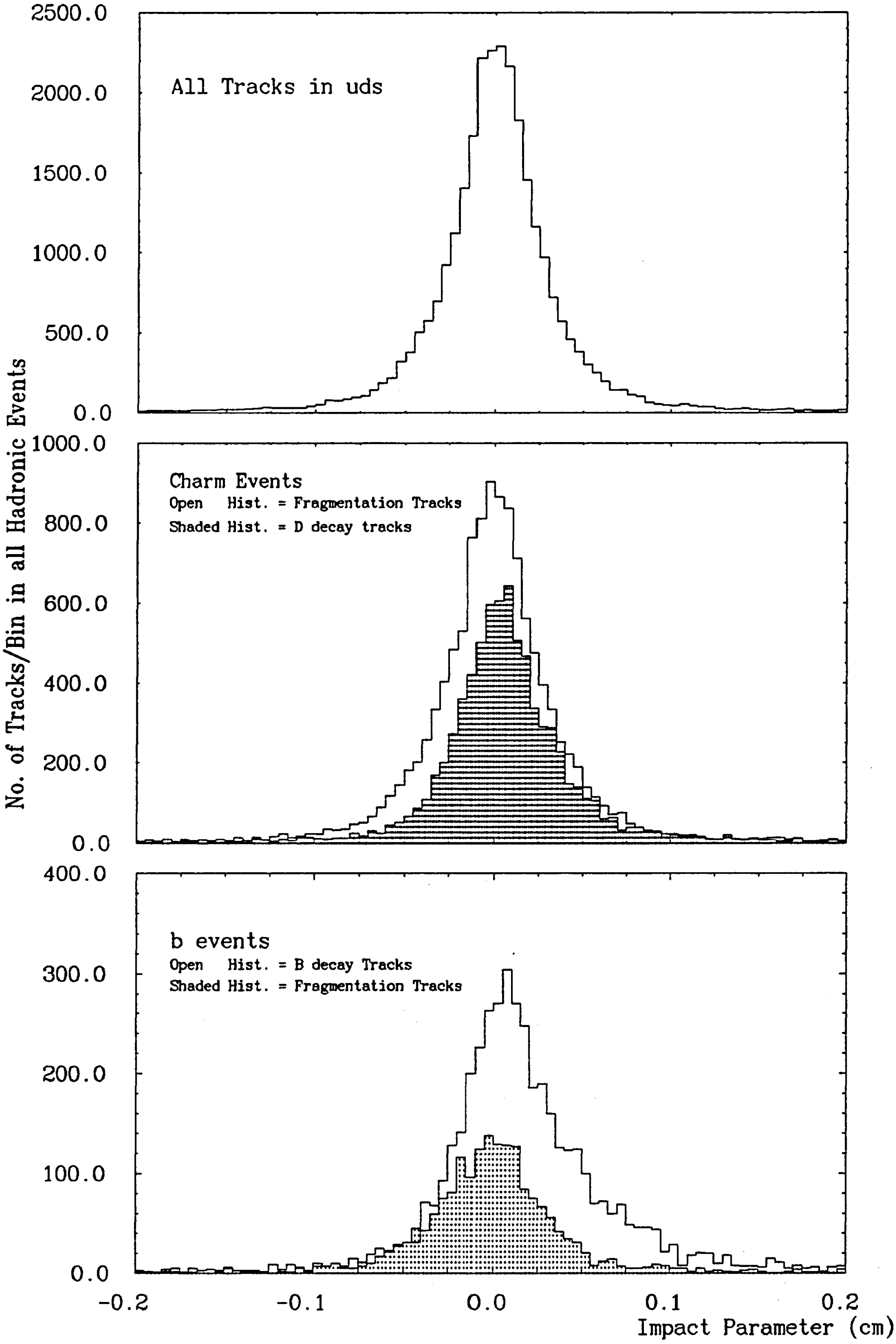

Figure 5.5: Monte Carlo Signed Impact Parameters of Different Types of Tracks.

presents a formidable difficulty even with very large positive impact parameter shifts. However, the fact that a B decay normally gives a large number of tracks in the same event holds the crucial key to the possible large suppression of both the uds and charm events.

5.2 Event Spot Finding

The distinction of a decay vertex could only be relevant when a reference point was given, ideally the event e^+e^- annihilation point. However, recalling the description in section 2.5, only an estimation of the centre of the beam envelope was available for each data-taking run. The spreads of individual event interaction points within the envelope were typically ~ 100 μm in y and ~ 500 μm in x. The track impact parameter resolutions, as studied in section 3.7, were in the range of 150μm – 300μm. This meant that the beam centre positions in y were already good estimations of the y coordinates of the event interaction points, since the event spread within the envelope was smaller than the track impact parameter resolution. However, the event spread in x was still fairly large compared to the track impact parameter resolution. Because this large spread was comparable to the expected B decay distances, a more accurate estimation of the event spot was required as a reference point.

To make the estimation of the event spot for each event, the procedure was simplified by fixing the event y coordinate to that of the beam centre since it was already known to a sufficient accuracy. The crossing points of all the tracks in the events with the horizontal line $y = y_{beam}$ were then found. With reference to Fig. 5.6, the x coordinate of the track crossing point for track i is denoted as x_i. A simple weight of $W_i = |sin\phi_i|$ was assigned to track i to emphasise the fact that the vertical tracks provided more accurate crossing points in x. Assuming the sum of the weights for all tracks was W_0, an ordered sum of track weights was then performed from left to right in the

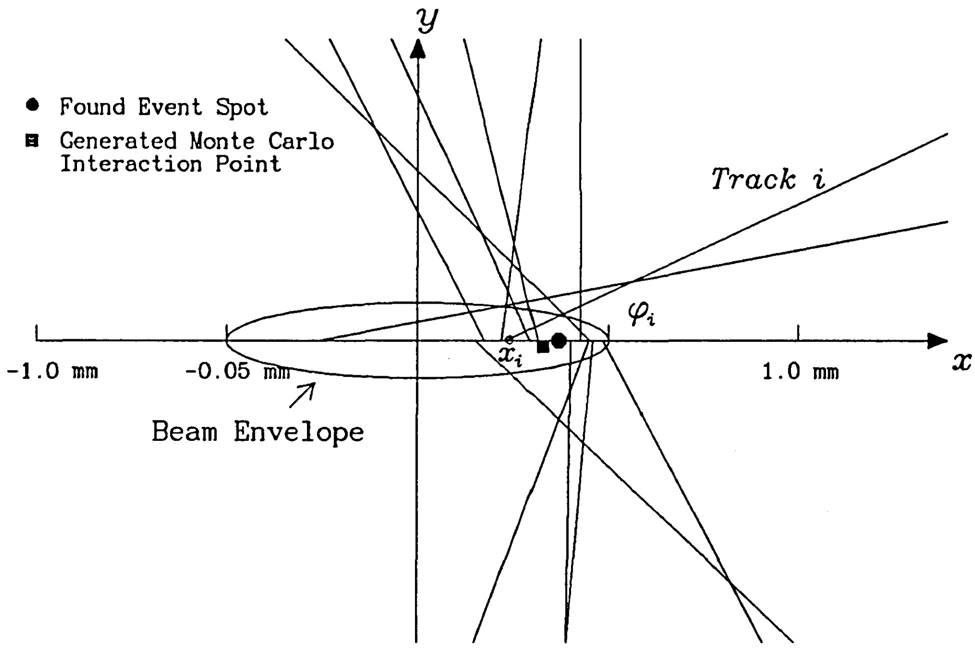

Figure 5.6: Illustration of Event Spot Finding Scheme.

order of increasing x_{cross}, until the sum reached the point closest to $W_0/2$. The weighted average of the two X_{cross} points just above and just below this half-sum was then assigned as the estimated event spot x. Fig. 5.6 is an example of the effect of this event spot finding scheme on a Monte Carlo event.

Notice that this scheme was just a simple counting of tracks without global distance averaging. Only the x_{cross} coordinates of two tracks in the middle had been used. This was to avoid a single track with large d_0 pulling the average. The effect due to tracks from decays at some distances away from the event interaction point should statistically cancel since each decay would tend to give equal number of tracks to the left and to the right. As long as the number of tracks on the left and right were balanced, the determination of x in the central part should be unaffected.

This method works on the basis of statistical convergence which was only valid for events with large enough number of tracks. So a quality cut required the total sum of weights $W_0 > 3$ was used. Most of the ~13% which failed this cut were horizontal with low charge multiplicity. The Monte Carlo also showed that the loss of $b\bar{b}$ events was slightly smaller than that of the other flavours.

The resulting improvement in the event spot x can be seen from Fig. 5.7 where the spread in x with respect to the generated Monte Carlo interaction point has been plotted both using the event spot given by this method and by using the simple beam envelope centre. The deviation from a true Gaussian for the event spot x spread was due to the fact this event spot resolution had some dependence on the event charge multiplicities and ϕ orientations.

To confirm the above resolution obtained from Monte Carlo, a direct comparison with data can be made by drawing a vertical line through the found x event spot to recalculate the y event spot in a similar way. The result is shown in Fig. 5.8 where ΔY is the spread of event spot y obtained by this method with respect to the beam centre y coordinate. The good agreement between the data and the Monte Carlo not only confirmed the resolution intrinsic to this method, but also verified the accuracy with which the beam centre y location was known. If either of them were significantly worse in accuracy, the histogram in Fig. 5.8 would be wider for the data.

5.3 The Tagging Method

The first step is to select the appropriate events and tracks for the tagging. The data used by this analysis were the TASSO high energy data collected after the installation of the VXD in 1983, up to the end of 1985. The e^+e^- centre of mass energy W ranged from ~38 Gev to ~46 Gev with most of the data accumulated at ~44 GeV and 38.3 GeV respectively as previously shown in Fig. 4.1. There were in total 7983 events in this sample with the VXD in normal operation.

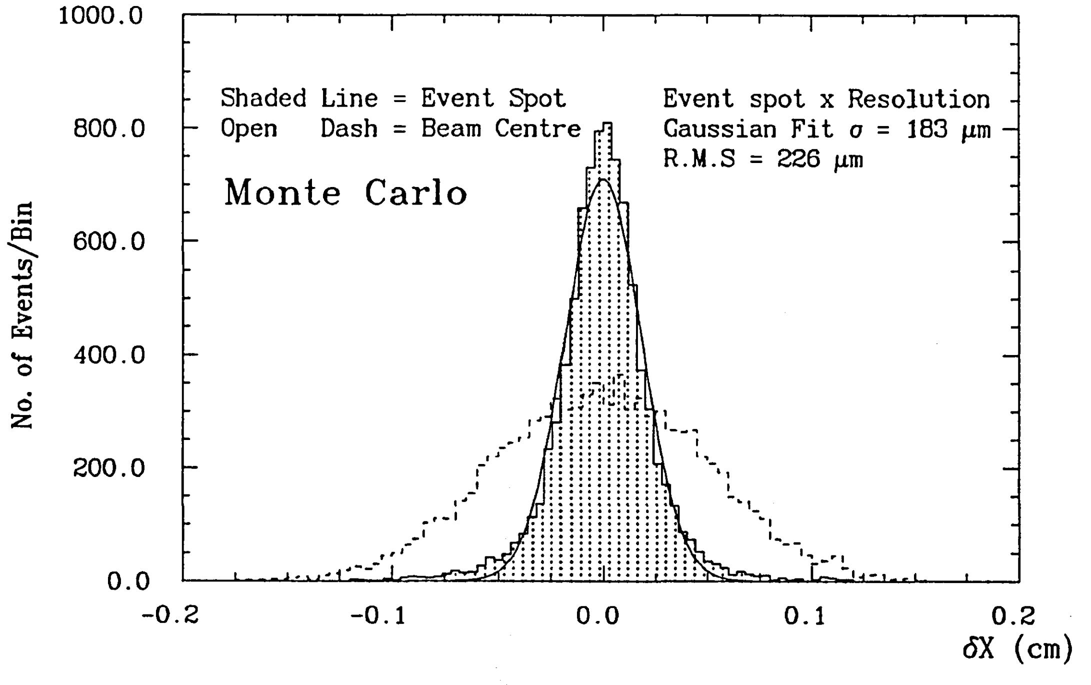

Figure 5.7: Monte Carlo Event Spot x Spread w.r.t Generated I.P.

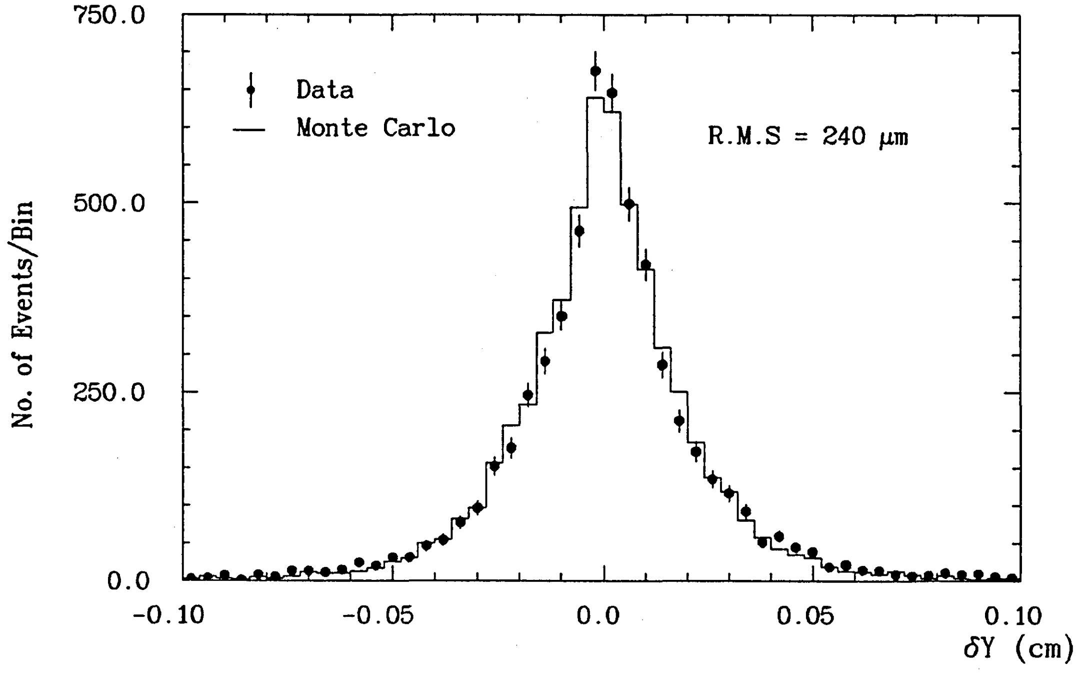

Figure 5.8: Spread of Re-traced Event Spot y w.r.t. Beam Centre.

To avoid large particle loss at lower θ angles due to the limited solid angle coverage of the tracking system, only events with thrust axis direction within $|cos\theta_{thrust}| < 0.75$ were used. About 13% of the events failed this cut. The event spot finding procedure, as described in the previous section, was then applied with the requirement of total track weight $W_0 > 3$.

A further rejection was made on events with large clusters of noise hits in the VXD. This was done by grouping VXD wires into 4×9 sectors and wires with hits assigned to tracks were masked out. A shower cluster sector was defined to be a sector with more than half of the remaining wires registering hits. An event was rejected if there were ≥ 2 shower clusters in the VXD. This resulted in a loss of 5.8% of the events in the data while only 0.02% of the Monte Carlo events accidentally fell in this category.

There were 5734 events surviving after all these event selection criteria and which were passed to the tagging program. The Monte Carlo events were passed through the same event selection procedure and 32568 events out of 40000 were left after all cuts.

The tracks used in this analysis were always the tracks found by the FELIX track finder, and followed by a scattering fit as described in section 2.5. The aim of the scattering fit was to improve the impact parameter resolution for low momentum particles. All event and track selection criteria were applied to the data and the Monte Carlo in the same way. The track selection requirements were

$\chi^2_{r\phi}$/NDF	< 3.0
$\|cos\theta\|$	< 0.87
$\|Z_0\|$	< 10.0 cm
$\|d_0\|$	< 0.25 cm
P	> 0.4 Gev/c
Track VXD Hits	≥ 3

The last 3 cuts were the most important. The term $|d_0|$ here referred to the closest approach of a track to the found event spot. The rather strong cut of 2.5 mm was used to reject K^0, Λ decays products, γ conversion electrons, badly tracked particles and particles deflected by inelastic scattering on detector materials. The momentum cut was a compromise between avoiding pattern recognition confusion due to serious multiple scattering problems for low momentum particles and maintaining as many B decay tracks as possible. The VXD hit cut was a further control of spurious tracks and also ensured reasonable impact parameter resolution for the track.

Since the main aim of the tagging for this analysis was to study the strong interaction and fragmentation aspects of the $b\bar{b}$ events, it was preferential not to use the event thrust or sphericity axes. Instead, tracks were paired to give reference to each other in a way similar to that used to define the signs of the impact parameters. Apart from certain assumptions described below, the good tracks in an event, which passed track selection cuts, were paired in all possible combinations to form simple vertices defined by their $r - \phi$ crossing points.

The following cuts were used to reject spurious vertices as being very unlikely to have been formed from a pair of B decay tracks:

$$\Psi_{3D} < 55^\circ$$

$$\Psi_{2D} > 5^\circ$$

$$|l_v| < 0.7 \text{ cm}$$

where Ψ_{3D} and Ψ_{2D} are the opening angles between the momentum vectors of the 2 tracks in 3-D and 2-D respectively. l_v is the distance in r-ϕ between a vertex and the found event spot. The cut on Ψ_{2D} was merely to reject vertices formed from a pair of tracks nearly parallel to each other in which case the uncertainty on crossing coordinates would be too large to be of any use. The

7 mm cut on the vertex distance l_v was a rather loose requirement with vertices due to the B decay track pairs being well contained inside yet it still rejected some crossing points due to slightly kinked K^0 decay tracks or tracks which interacted.

The Ψ_{3D} cut was based on the expectation of the decay kinematics of the B mesons. The Lorentz boost acquired by a B meson ensured that most of the decay tracks were in the forward cone centred around the original B flight direction. The Monte Carlo distribution of this opening angle for various types of track pairs are shown in Fig. 5.9 for tracks within the same hemisphere in an event defined by the plane perpendicular to the event thrust axis. The B and D decay pairs referred to vertices formed from pairs of tracks coming from the same heavy meson decay. The mixed types referred to pairs containing one track from heavy meson decay and one track from primary fragmentation.

The histograms plotted were normalised to the same number of events for the data and Monte Carlo. The different vertical scales of the three graphs should be compared as they indicate the absolute concentrations of different types of vertices in the total event sample. The excess of charged tracks in the Monte Carlo showed up here as clearly more vertices were formed per event in the Monte Carlo. The excess was mainly for pairs with large opening angles around Ψ_{3D} ~80°. A check on the absolute scales for the main sources of contributions in this region seemed to suggest this was most likely due to the excess of primary fragmentation tracks rather than due to the errors in simulation of the heavy meson production mechanism. The effect of the excess of wide angle tracks was significantly reduced when the 55° cut on Ψ_{3D} was imposed. However, because the exact cause of this excess was not investigated, systematic errors on flavour content of the tagged samples will be assigned (see section 5.5) to account for its effect.

As far as the B decay track pairs were concerned, the 55° cut was well into the distribution tail. This was to promote efficiency and avoid large

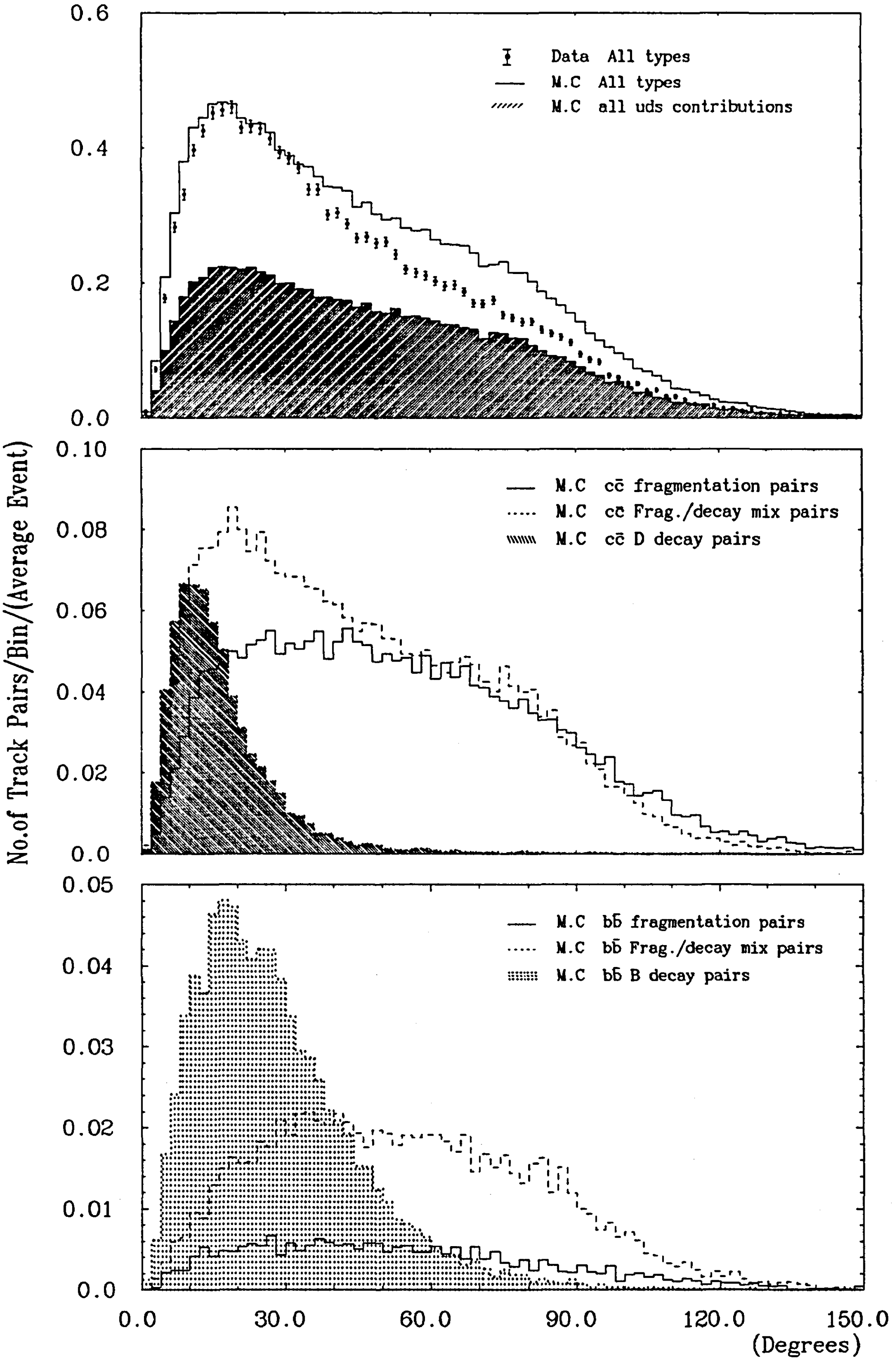

Figure 5.9: 3-D Opening Angles Ψ_{3D} of Various Types Track Pairs.

systematic errors due to *e.g.* uncertainty in the B momentum spectrum. On the other hand, this cut rejected a large fraction of vertices which were most likely involving primary fragmentation tracks.

For each vertex which passed the above cuts, a weighting factor was introduced to reflect how likely it was that it belonged to a real decay vertex. Put in more practical terms, this was to find how unlikely the vertex coincided with the event spot. Assume the $r - \phi$ projections of the momentum vectors of the 2 tracks forming a vertex were $\mathbf{P_1}$ and $\mathbf{P_2}$ respectively. The vertex $r - \phi$ momentum direction was simply defined by the vector sum of $\mathbf{P_1}$ and $\mathbf{P_2}$

$$\mathbf{P_v} = \mathbf{P_1} + \mathbf{P_2}$$

The apparent vertex flight distance l_v was defined by the displacement vector from the event spot to the 2 track crossing vertex as illustrated in Fig. 5.10. The $r - \phi$ collinear angle α referred to the angle between the vertex momentum and flight distance vectors $\mathbf{P_v}$ and $\mathbf{l_v}$. The vertex weight was then empirically chosen to be

$$W = (1 - e^{-\frac{(|\mathbf{l_v}| cos\alpha)^2}{2\sigma_v^2}}) \cdot cos\alpha \tag{5.1}$$

where the vertex distance resolution parameter σ_v depends on the momenta of the 2 tracks. This was based on a study of the effect of multiple scattering on track impact parameter resolutions.

The assumed track impact parameter resolutions listed in Table 5.1 were the same values extracted from the Monte Carlo study in section 3.7. The track impact parameter resolution was then modified by adding the above resolution values in quadrature to the event spot resolution *i.e.*

$$\sigma_{track} = \sqrt{\sigma'^2_{track} + \sigma^2_{ev-spot}} \tag{5.2}$$

The event spot resolution was simply chosen to be $\sigma_{ev-spot} = 200\ \mu$m based on the study in section 5.2.

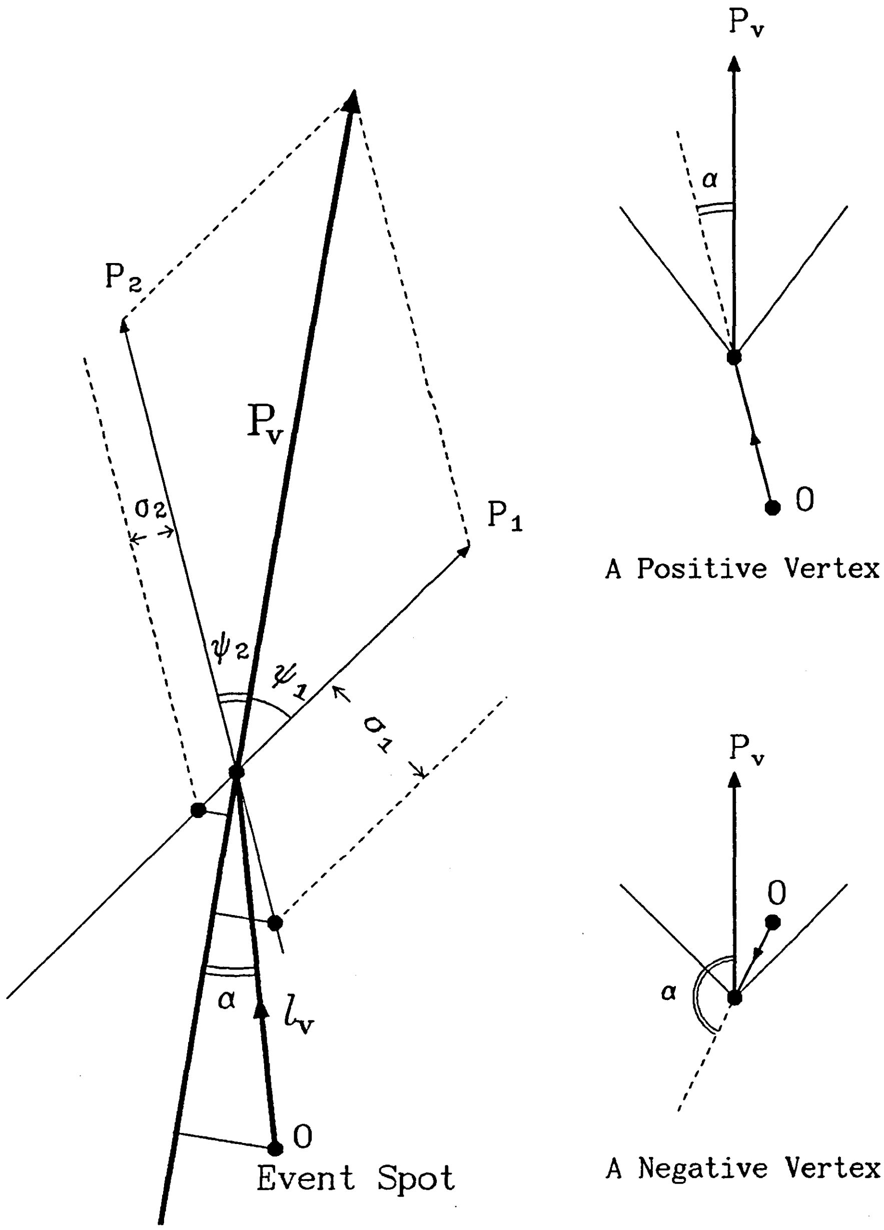

Figure 5.10: Illustration of Variables used in Vertex Weight Definitions.

Momentum (Gev/c)	Impact Parameter Resolution σ'_{track} (μm)
< 0.3	896
0.3 – 0.5	549
0.5 – 0.8	431
0.8 – 1.2	324
> 1.2	217

Table 5.1: Assumed Track Impact Parameter Resolution Variation with Momentum.

The vertex distance resolution was related to track impact parameter resolution by making a parallel shift of 1 σ_{track} for each track in turn and adding the resulting shifts in vertex coordinates along the $\mathbf{P_v}$ direction in quadrature. The detailed variable definitions are illustrated in Fig. 5.10. This translates mathematically to

$$\sigma_v \ = \ \frac{1}{sin(\psi_1 \ + \ \psi_2)}\sqrt{(\sigma_1 cos\psi_2)^2 \ + \ (\sigma_2 cos\psi_1)^2} \tag{5.3}$$

where σ_1,σ_2 are the modified impact parameter resolutions of track 1 and 2 respectively.

Notice that the vertex weight definition in Equation 5.1 involved the collinear angle α twice. This was intended to weigh down the rather spurious type of vertices with their momentum vector nearly perpendicular to the apparent decay paths. The $cos\alpha$ factor outside also defined the sign of the weight so that vertices with P_v and l_v pointing in opposite directions would acquire negative weights. The fact that uds events had tracks which nearly all came from the event spot would make vertex weights be equally positive and negative, so that the sum of weights in an event would be close to zero on average. The design of the weight also ensured that the maximum weight obtainable is 1. This saturation was needed to avoid a single long distance vertex carrying too much weight.

The actual distribution of the vertex weights is shown in Fig. 5.11 for all vertices which passed the selection cuts. These were again for pairs within the same hemisphere divided by the plane perpendicular to the event thrust axis. The data and Monte Carlo were normalised to the same number of entries. The variations of the weights are also shown for the Monte Carlo, by changing the original track impact parameter resolution σ'_{track} by $\pm$ 20%. The discrepancies between data and Monte Carlo can be seen to be larger with these alternative resolution values. The weight distributions for all pairs in Monte Carlo *uds* events and B decay pairs are also shown together normalised to the same number of entries.

Most of the vertices were distributed symmetrically around zero as expected from pure broadening due to detector resolution. Although a large fraction of B decay pairs were also in the region around zero or less, the clear positive shift was already exploitable. The main principle of tagging was to sum the weights of all the pairs in an event or a jet together to separate a fraction of $b\bar{b}$ events from the rest. The *uds* events were expected to have this sum peaked close to zero due the statistical cancelling for non-decay pairs while $c\bar{c}$ and $b\bar{b}$ events should have net positive shifts. The criteria required for the tagging signal were clearly long decay times and large decay charge multiplicities. As far as the background was concerned, the sum of a set of symmetrically distributed positive and negative weights should be relatively stable against normalisation problems e.g. excess of Monte Carlo tracks or small deficiencies in the decay model.

There were two possible modes of tagging. The *Jet-mode* tag was the conventional technique of dividing an event into 2 hemispheres using the plane

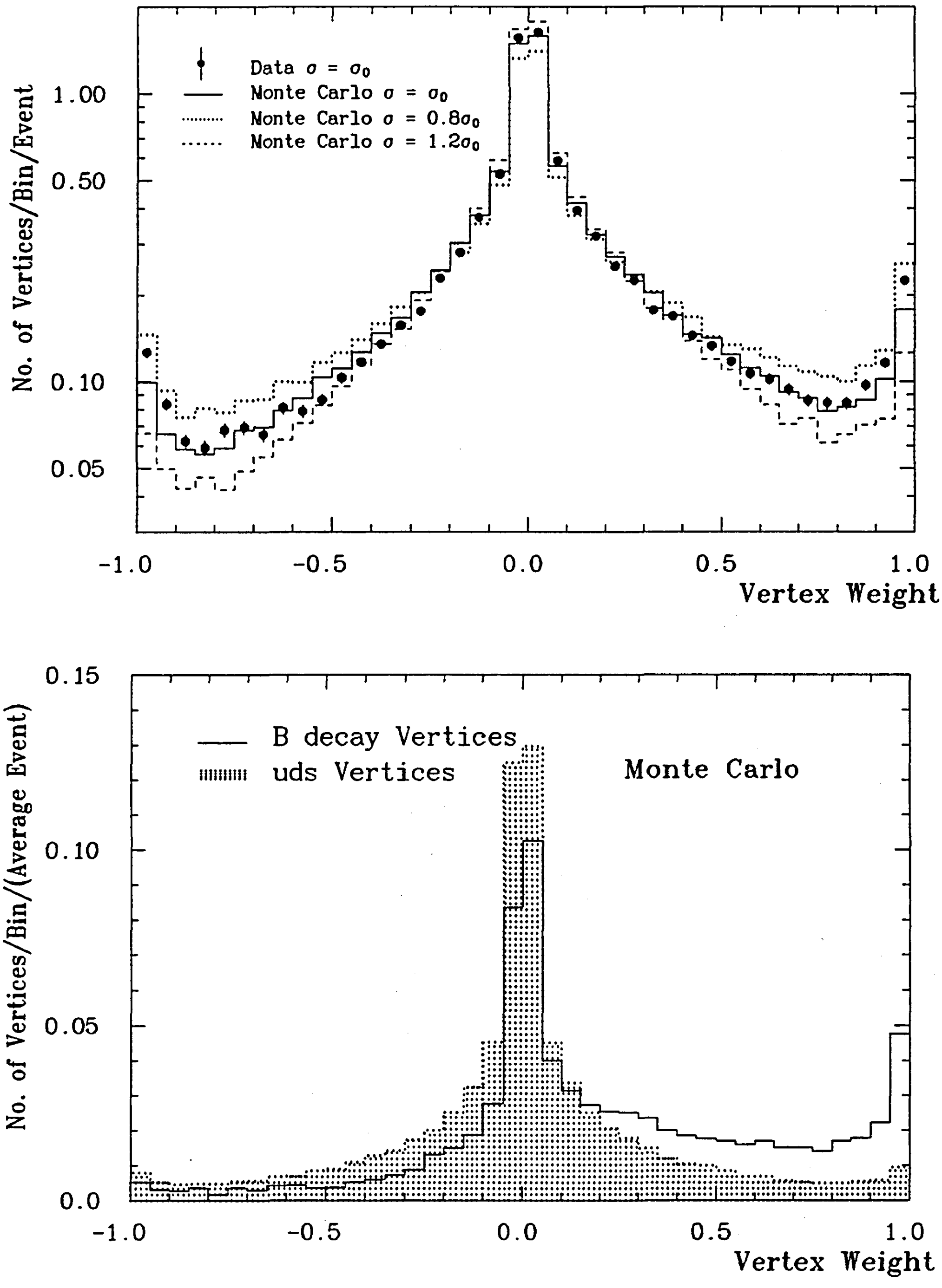

Figure 5.11: Distributions of Vertex Weights.

perpendicular to the event thrust axis so that tagging one side would leave the other half to be studied free of bias. The *Global-mode* tag was the method of taking all track pairs in an event together without dividing the event. This was done with exactly the same cuts as for the *jet-mode* except tracks from different hemispheres could also combine. However the 3-D opening angle cut of 55° strongly restricted the otherwise large number of spurious combinations. The availability of this easy switch was mainly due to the design of the vertex weight where the use of the thrust axis direction was deliberately avoided. The fact that the *Global-mode* did not need the thrust or sphericity axis at all, can be a useful tool for studying strong interaction aspects of the tagged $b\bar{b}$ events which would rely on the effects due to multi-jet events.

The half event weight sums for the *Jet-mode* tag are shown in Fig. 5.12 for data and Monte Carlo, normalised to the same number of input events. The flavour content at positive ΣW are also indicated for the Monte Carlo in the second view. A similar set of plots for the *Global-mode* tag can be found in Fig. 5.13.

The enrichment of $b\bar{b}$ events can be obtained by various cuts on the weight sum ΣW depending on the desired purity and acceptable efficiency. The preliminary estimation of the efficiency and purity of the tagged samples are listed in Table 5.2 for *Jet-mode* and in Table 5.3 for *Global-mode* separately. The input Monte Carlo events of 32566 were scaled down to normalise to the input data events of 5734 for these tables and also the remaining tables in this chapter. The errors on the efficiency and purity will be given in section 5.5 together with the inclusion of systematic effects. The efficiency values were estimated from tagged Monte Carlo b jets/events as a fraction of input b jets/events. The efficiency for *Jet-mode* was fairly low but there were two chances in each event.

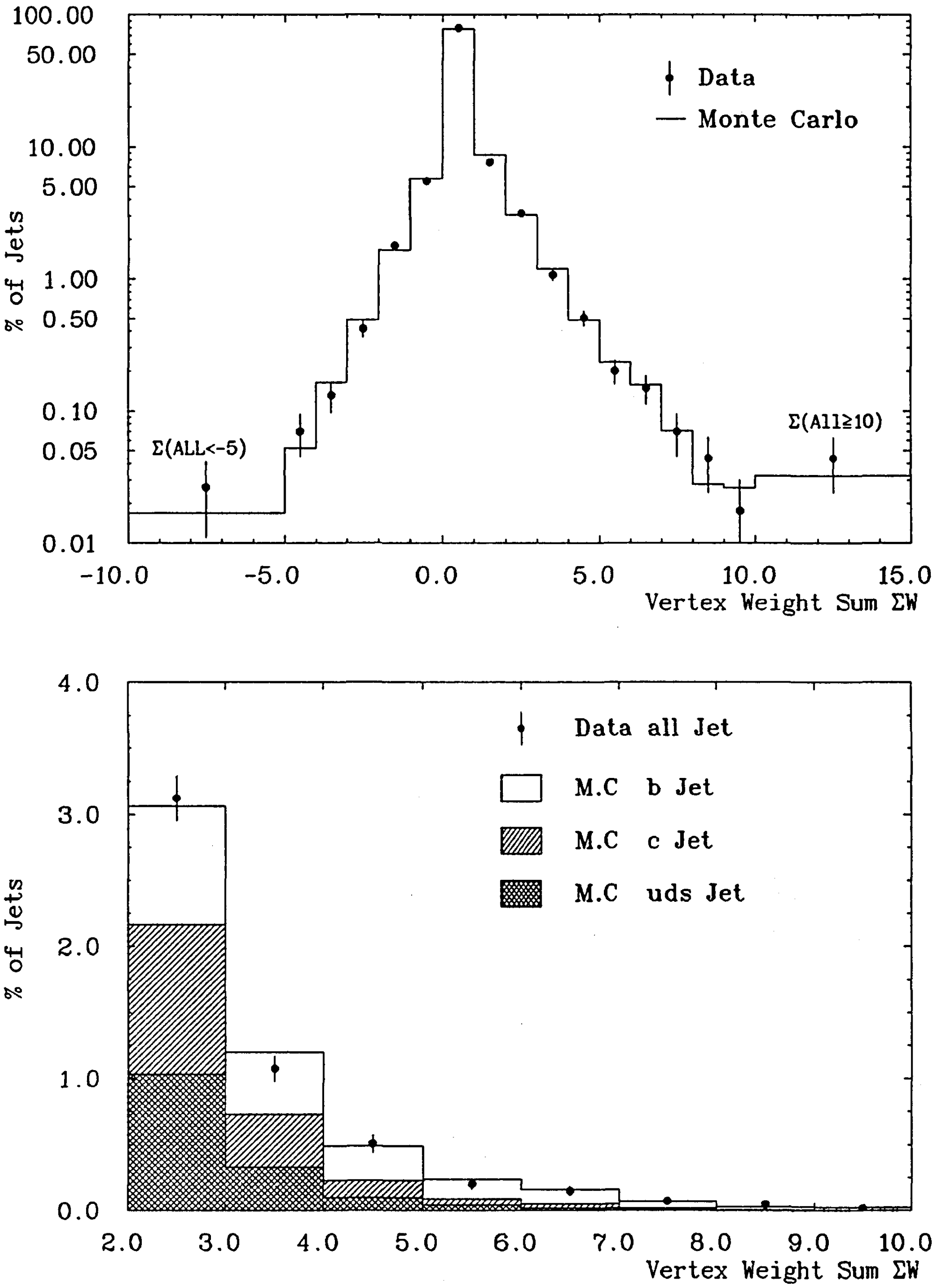

Figure 5.12: Half Event Weight Sums for *Jet-mode* Tag.

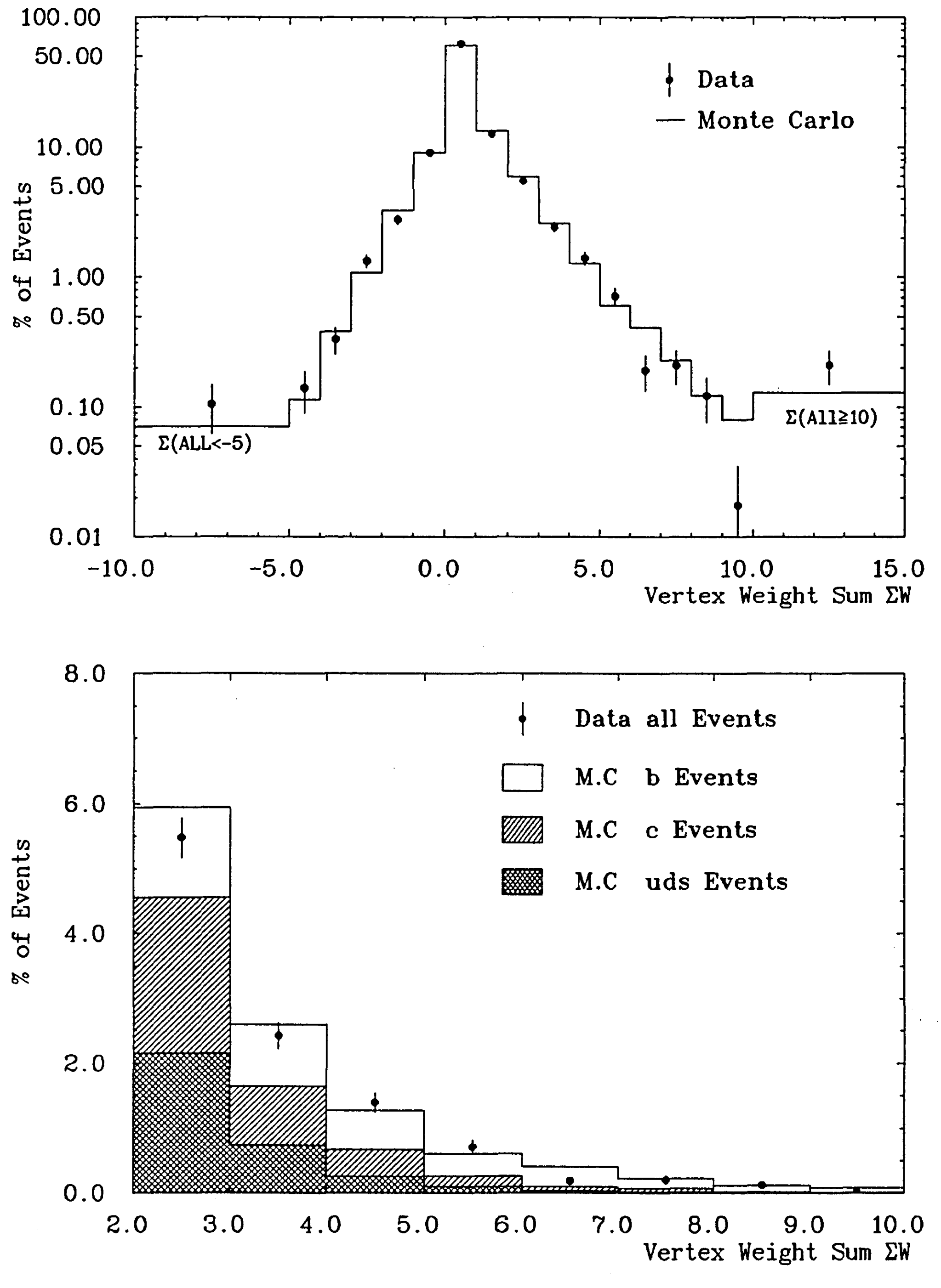

Figure 5.13: Whole Event Weight Sums for *Global-mode* Tag.

ΣW Cut	Tagged Data Jets	Tagged M.C. Jets	M.C. Flavours $b\bar{b}$	$c\bar{c}$	uds	M.C. b jet tag Efficiency (%)	M.C. b Purity (%)
≥ 2	599	607	230	203	174	19.1	38
≥ 3	241	255	126	71	58	10.5	49
≥ 4	118	119	73	26	20	6.0	61
≥ 5	60	63	42	11	10	3.5	67
≥ 6	37	36	26	6	4	2.2	73

Table 5.2: Initial Estimates of Tagging Efficiency and Purity in *Jet-mode*.

ΣW Cut	Tagged Data Events	Tagged M.C. Events	M.C. Flavours $b\bar{b}$	$c\bar{c}$	uds	M.C. b event tag Efficiency (%)	M.C. b Purity (%)
≥ 2	617	654	233	229	192	38.5	36
≥ 3	303	313	153	92	68	25.3	49
≥ 4	164	164	99	40	25	16.3	60
≥ 5	84	91	64	17	10	10.6	70
≥ 6	43	56	44	7	5	7.3	79

Table 5.3: Initial Estimates of Tagging Efficiency and Purity in *Global-mode*.

5.4 Verification of b Enrichment

Although the agreement between data and Monte Carlo on tagging statistics was fairly good, some independent means of verification is still very desirable to give better confidence in the b enrichment.

5.4.1 Internal Consistency Verification

One of the interesting ways of checking the tagging statistics was to count the single tag and double tag events for the *Jet-mode* tag. From the results in Table 5.2, it can be seen that the expected level of suppression on *udsc* events was already very large when a cut of $\Sigma\ W\ \geq 2$ was demanded. The fact that only a small fraction of the jets passed high $\Sigma\ W$ cuts, gave only a very small chance for both jets in an event to be tagged independently at the same time, if the tagging source was random. However if a coherent event source, *e.g.* $b\bar{b}$ events, provided a much higher probability for tagging, the overall double tag probability could be raised significantly even if this source was only a small fraction of the total event sample. The only external factor brought in by the analysis which might correlate the two halves of an event was the event spot obtained using all tracks in the event. However, if one side benefitted from a shifted event spot due to reconstruction error to get tagged, it would make the opposite side more unlikely to be tagged at the same time. Therefore, large numbers of double tagged events would be a strong support of b enrichment.

The actual tagging statistics for the data and Monte Carlo are shown in Table 5.4 together with a rough estimate for the case of random tagging source. The random probability was given by

$$Double\ Tag = All\ Events\ \times\ \left(\frac{Tagged\ Jets}{All\ Jets}\right)^2$$

$\Sigma\ W$ Cut	Tagged Data Events Single	Double	Tagged M.C Events Single	Double	Expected Random Double Tag
≥ 2	535	32	549	29	16
≥ 3	219	11	237	10	2.5
≥ 4	108	6	114	3	0.6
≥ 5	54	3	62	1	0.2
≥ 6	33	2	35	1	<0.1

Table 5.4: Statistics of Double Tag Events in *Jet-mode.*

Another similar approach of verification is to check the mean impact parameters with respect to event spot for tracks opposite a tagged jet, again using the *Jet-mode* tag. This was based on the idea that if the tagged event was a b event then the bias free jet opposite the tagged jet in the same event should also contain a B hadron often decaying to tracks with large positive impact parameters. Again, if events were tagged because event spots were shifted, the impact parameters of tracks in the opposite jet would more likely be negative than positive.

Average Jets		Opposite Tagged Jets	
Data	Monte Carlo	Data	Monte Carlo
$33 \pm 3\ \mu$m	$29 \pm 2\ \mu$m	$156 \pm 30\ \mu$m	$94 \pm 11\ \mu$m

Table 5.5: Mean of High Quality Track Impact Parameters in μm.

The tracks used in this case were high quality tracks with P $>$ 1 Gev/c and at least 5 VXD hits. The tagging requirement was $\Sigma\ W\ \geq 4$. The actual track

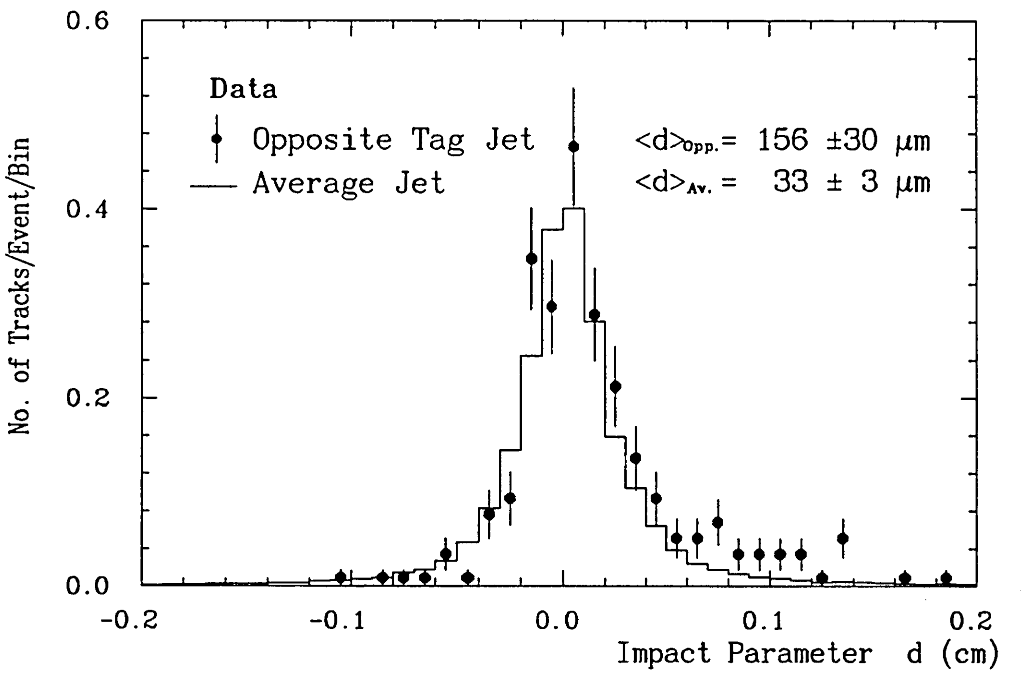

Figure 5.14: Impact Parameter Distributions of High Quality Tracks in Average jets and b Enriched Jets.

impact parameter distributions for tracks in average jets and tracks opposite tagged jets are shown for the data in Fig. 5.14. The mean impact parameter values obtained with cut $|d| < 3$ mm are listed in Table 5.5.

The expected mean of impact parameters for high quality tracks was 124 μm for pure $b\bar{b}$ events and 38 μm for pure $c\bar{c}$ events according to the Monte Carlo with B lifetime of exactly 1 ps. Both the high double tag statistics and the large positive value of the mean impact parameter in the data gave good confidence for this tagging scheme. The fact that the data even surpassed the Monte Carlo expectation somewhat was consistent with fact that the TASSO measurement of average B hadron lifetime [30,34] was longer than 1 ps by a similar ratio.

5.4.2 Test with Muon Candidates

Some independent evidence can also be obtained by comparing the vertex tagging method with existing enrichment schemes. Firstly, it can be compared to the so far most popular method of using high P_T leptons. Due to the problem that half of the TASSO liquid argon shower counter was not operational for a large fraction of the data taken in 1985, only muons will be considered here.

The detailed description of TASSO muon chambers can be found in [61]. The muon track selection cuts were:

At least 3 Hits from 4 chambers

Muon Momentum $>$ 2.0 Gev/c

Confidence level of DC track to μ-chamber hits association > 0.01

All ambiguous candidates sharing μ-chamber hits were rejected.

The resulting muon P_T spectrum with respect to the event thrust axis are shown together for data and Monte Carlo [97] in Fig. 5.15 normalised to the same number of events for the data and Monte Carlo. The relative fractions of contributions from various origins as estimated from Monte Carlo are shown in Table 5.6. The number of muon candidates in tagged samples at various $\Sigma\ W$ cuts are shown for the *Global-mode* tag in Table 5.7. The last column shows the expected number of muon candidates for the case that the tagged samples had no effect in flavour selection at all, so that the probabilities of getting muon candidates were equal to those for an average event. Unfortunately, the rather poor statistics and purity of the muon sample did not allow a convincing conclusion on the b enrichment.

μ Type	All P_T	P_T >1.0 Gev/c
$b \rightarrow \mu$	15%	24%
$b \rightarrow c \rightarrow \mu$	7%	5%
$c \rightarrow \mu$	28%	24%
Fakes	50%	47%

Table 5.6: Monte Carlo Estimate of Origins of Muon Candidates.

	Actual Tagged Data Events		Actual Tagged M.C Events		Expected Muons if ΣW Had No Flavour Selection	
	All	P_T >1.0	All	P_T >1.0	All	P_T >1.0
All Events	212	65	204	82	(212)	(65)
$\Sigma\, W \geq 4$	11	4	13	6	4	2

Table 5.7: Statistics of P>2 Gev/c Muon Candidates in All and Tagged Events for *Global-mode*.

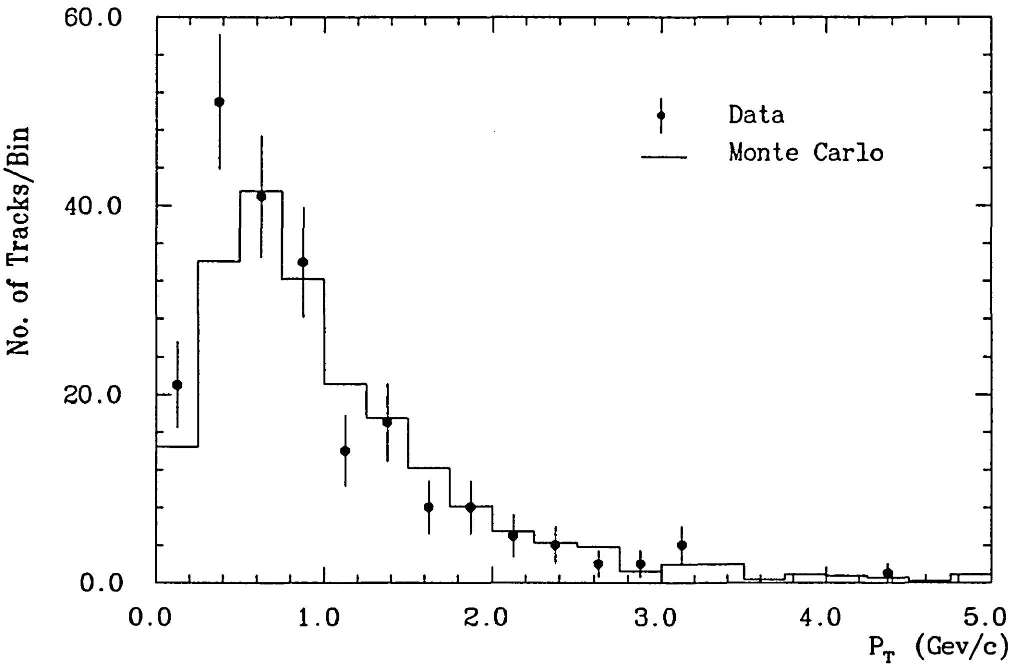

Figure 5.15: Muon Candidate P_T distribution.

5.4.3 Comparison with Sphericity Product Enrichment

Another approach is to compare with the b enrichment scheme using the event sphericity product [30]. Although this scheme depends quite heavily on the Monte Carlo simulation of strong interaction and fragmentation features which are to be studied with the lifetime tagging method, the main point here is that the information used by the two enrichment methods are independent.

The sphericity product method was based on the decay kinematics of the B meson in a $b\bar{b}$ event. An event was divided into two halves by the plane perpendicular to the event sphericity axis. Tracks within a 41° cone around the sphericity axis were taken for each side and a Lorentz transformation was performed on these selected tracks. The transform was made back toward the rest frame of a hypothetical particle travelling along the event sphericity axis with an empirically chosen β of 0.74. The sphericity in the new frame was then calculated using the selected tracks for each side separately. The

$\Sigma\ W$ Cuts	Tagged Data Events	Tagged M.C Events	Expected Events if ΣW Had No Flavour Selection
All Events	780	575	(780)
$2 \leq \Sigma\ W\ < 4$	90	79	60
$4 \leq \Sigma\ W\ < 6$	26	35	11
≥ 6	25	22	5

Table 5.8: *Global-Mode* Tagging Statistics at Various $\Sigma\ W$ Ranges after $S_1 \cdot S_2\ > 0.1$ Cut.

resultant product of the sphericity values on two sides, $S_1 \cdot S_2$, was the variable used for the b enrichment cut.

With a cut of $S_1 \cdot S_2$, a moderate purity of 31% was obtained with the fairly good efficiency of 34% for the $b\bar{b}$ events. However, increasing the cut further could not improve the sample purity significantly while the efficiency would drop quickly.

The comparison of tagging statistics between data and Monte Carlo with a cut of $S_1 \cdot S_2\ > 0.1$ for the sphericity product method and various ΣW regions for the *Global-mode* tag is shown in Table 5.8. The total number of input Monte Carlo events was normalised to be equal to the 5734 data events. The last column shows the effect that the quantity ΣW had no flavour selection power so that the expected number of events passing $S_1 \cdot S_2$ cut are listed for average events with same event statistics as in various $\Sigma\ W$ range.

There was a systematic normalisation problem in the Monte Carlo as far as the sphericity product method was concerned since the fraction of *all* events passing the $S_1 \cdot S_2\ > 0.1$ cut in the Monte Carlo was somewhat less than the data. However, the positive correlation between the two methods was still very significant.

Finally, two different views of a tagged event are shown in Fig. 5.16 as an example. In the close up view of the event, very low momentum tracks and obviously bad tracks with impact parameters of the order of a few cm from the beam spot were removed according the tagging selection track cuts.

5.5 Study of Systematic Effects

For simplicity, the results on systematic effects given here were mainly for the *Jet-mode* tag. This was because most of the systematic effects were similar for both methods and the *Jet-mode* dealt with one B meson at a time which allowed an clearer insight by weighting the generated Monte Carlo parameters.

5.5.1 Dependence on Quality of VXD Information

One of the major discrepancies between the data and Monte Carlo, as far as VXD simulation was concerned, was the extra $\sim$ 6% of events rejected from the real data which contained large clusters of noise hits. To investigate the possibility that rather large number of extra spurious events in the data were tagged due to the effect of noise hit clusters not being recognised, the events rejected purely because the noise hit pattern in VXD were recovered and the tagging procedure was applied to these events alone.

Among these previously rejected as 'noisy' data events, only 5 jets were tagged from 2$\times$329 input, with the cut of $\Sigma W \geq 4$. This corresponded to a fraction of 0.8$\pm$0.3% of the total as compared to the 1.0$\pm$0.1% with the normal data sample. This can be understood because the effect of wrong hit associations due to confusing hit information would mostly tend to give crazy

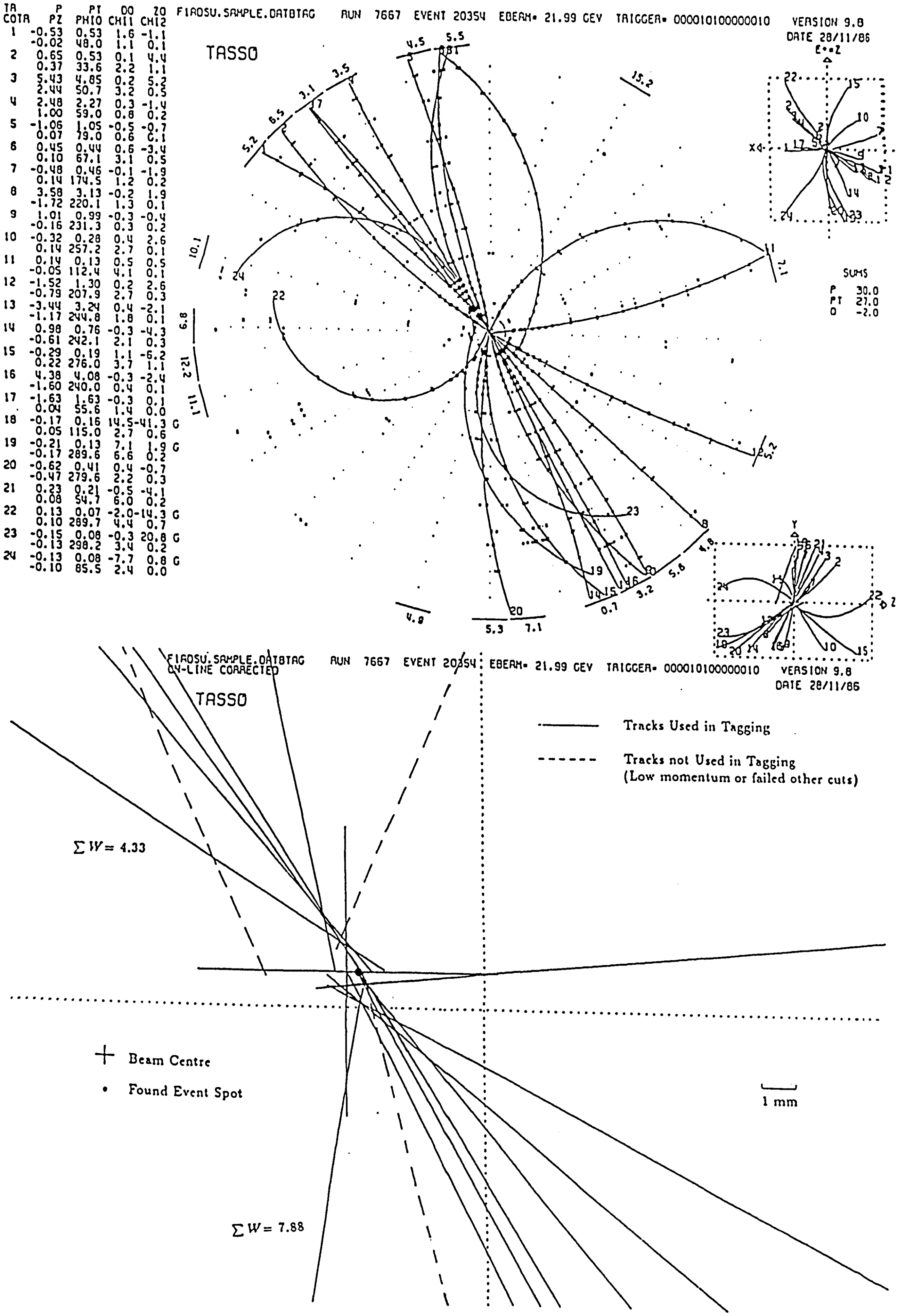

Figure 5.16: Two Views of a Tagged Event. The top picture shows the event in the main drift chamber and the bottom picture is an expanded view near the beam centre for the same event.

tracks which were obvious enough to fail the track quality cuts immediately. It was therefore unlikely that the hidden 'noisy' events could make a significant enhancement of the background in the tagged sample.

In the event spot finding procedure, the only input was the assumed y coordinate of the beam centre. The consistent stability in the determined beam centre y coordinates between different runs has previously been shown in section 3.8 and the good agreement between data and Monte Carlo on the retraced beam y position has also been shown in Fig. 5.8. Both indicated that the error in beam y position determination was very close to 100 μm.

To test the stability of the tagging method against possible uncertainties in event spot coordinates, the y beam centres were smeared further by artificially shifting the y coordinates within a $\sigma = 100$ μm Gaussian envelope for both data and Monte Carlo. The x event spots were found and the usual tagging procedure followed. The resultant change on jet $\Sigma\ W$ was a small symmetric spread with an RMS of 0.22. For the normal cut of $\Sigma\ W\ \geq 4$ in *Jet-mode*, this gave a gain of 16 candidates and a loss of 6 candidates from the original 118 in the data with comparable changes in the Monte Carlo. Since this was only a local smear for jets which had $\Sigma\ W$ very close to 4, the change of relative concentrations of different flavours was small. Since the beam y position was known to be better than in the case with an extra 100μm spread, no systematic errors will be assigned to flavour content from this source.

To check the effect of beam spot from another point of view, the fractions of tagged events in the *Jet-mode* are plotted in Fig. 5.17 for different event thrust axis ϕ angles. Because the way of determining the event spot was asymmetric in ϕ, the fraction of tagged events could well be very different at different ϕ angles if the beam spot resolution was an important factor. The result was very much consistent with a uniform efficiency in all ϕ angles although the significance is limited by statistics.

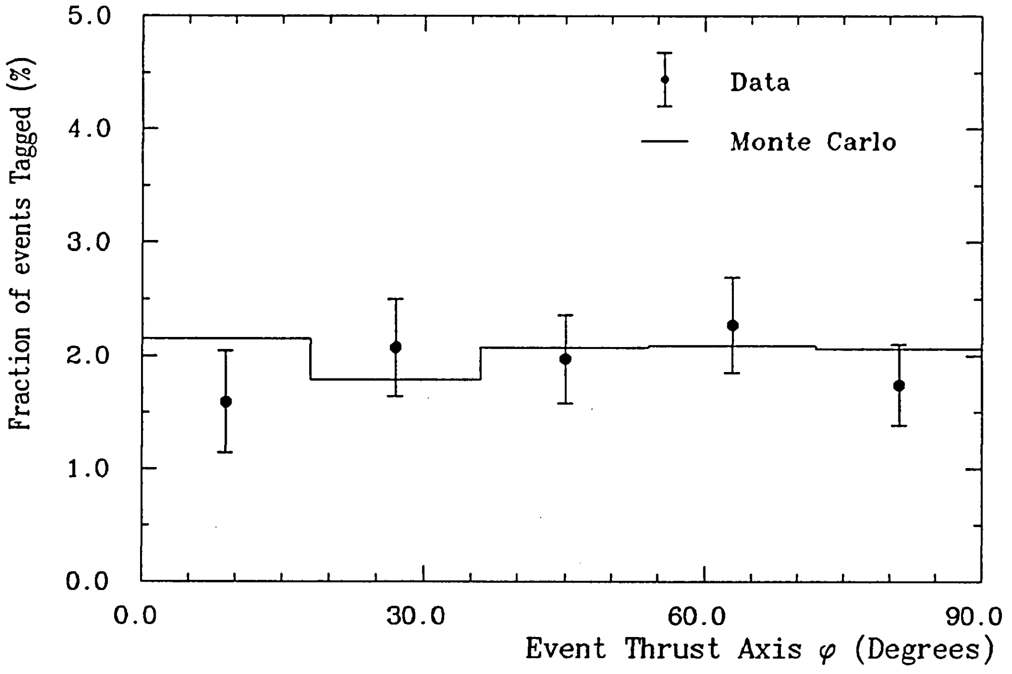

Figure 5.17: Thrust Axis ϕ Angle Distribution for *Jet-mode* Tagged Events.

The errors in the determinations of VXD position with respect to the main drift chamber could also make a systematic effect in principle. The errors in x, y coordinate shifts were of less importance since the beam centre coordinates were determined using PASS5 giving fixed result in the VXD coordinate. The relative track geometry pattern around the beam spot remained unchanged for shifts $\leq \sim 100$ μm as long as the same coordinates were used for track fitting and beam spot determination. However, the determination of the VXD rotation with respect to the main drift chamber was more important when tracks were fitted with hits in all chambers together to obtain the impact parameters. A rotation error would result in a distortion causing 2 tracks opposite in ϕ to be separated away from each other near the event spot.

The procedures of VXD position determination as described in section 3.2.2 gave very accurate values with different methods in agreement with each other. The VXD rotation angle was artificially changed by 0.1 mrad, and the tracks were then refitted with the new rotation for all data events. The result on the *Jet-mode* tag with a cut of $\Sigma\ W\ \geq 4$, was a loss of 4 jets and a gain of 6

	Tagged Data Jets			Tagged Monte Carlo Jets					
Used σ'	Gain	Stay	Loss	Gain	Stay	Loss	b	c	uds
σ'_0 (standard)	–	118	–	–	119	–	73	26	20
$0.8 \cdot \sigma'_0$	32	118	0	37	119	0	+13	+13	+11
$1.2 \cdot \sigma'_0$	0	91	27	0	89	30	–15	–8	–7

Table 5.9: *Jet-mode* Tagging Statistics with Different Impact Parameter Resolution Factors.

jets from the original 118 tagged jets in the data. Not only was the change in tagged candidates small, but the effect was also similar to the beam spot smear with changes only relevant to jets having ΣW close to 4. Therefore, the effect in this aspect will be neglected in the estimation of systematic errors in the relative flavour content of the tagged samples.

The effect due to uncertainties in VXD resolution can be studied by changing the assumed track impact parameter resolution values from those in Table 5.1. A rather large change of $\pm 20\%$ was made to see a clear effect. The resulting tagging statistics with the *Jet-mode* are listed in Table 5.9 for the standard cut of $\Sigma W \geq 4$. The gain and loss in the table refer to the changes of tagged candidates with the different resolution assumptions compared to the standard resolution.

It can be noticed that the magnitude of candidate changes were comparable for the data and Monte Carlo. However, the discrepancies between the data and Monte Carlo became larger when the alternative resolutions were used for the Monte Carlo only as seen from the distributions of vertex weights in Fig. 5.11. So the actual uncertainties in flavour content were conveniently taken as half of the changes in Table 5.9 and assigned independently to different flavours.

5.5.2 Tagging Stability Checks with Different Cuts

The variations of tagging statistics with cuts were checked for some of the cuts which might possibly have a large effect. Each cut was changed in turn while keeping the others at the standard values. The changes in tagged candidates and Monte Carlo flavour content are listed in Table 5.10 for *Jet-mode* tag with $\Sigma W \geq 4$.

It can be seen from Table 5.10 that most of the variations of cuts only produced small changes in the tagged candidates and yet Monte Carlo followed data closely. Because these cuts were not completely independent of each other, there was no need to evaluate related systematic errors for each in turn. The errors related to track impact parameter, vertex flight distance and VXD hit cuts should have been already included in the impact parameter resolution error. The vertex opening angle and track momentum cuts were more sensitive to the errors in Monte Carlo fragmentation modelling. The discrepancies from this aspect were most pronounced in the distribution of vertex 3-D opening angle Ψ_{3D} as previously shown in Fig. 5.9 as both the normalisation and distribution shape were different in the data and Monte Carlo. Therefore a collective systematic error on flavour content due to the fragmentation model was assigned to be equal to the variation of Ψ_{3D} cuts in Table 5.10.

5.5.3 Dependence on Heavy Flavour Properties

This was studied purely with the Monte Carlo by giving jets different weights depending on the generated Monte Carlo parameters. As an example, the

Used Cuts	Data Jets Gain	Data Jets Stay	Data Jets Loss	Monte Carlo Jets Gain	Monte Carlo Jets Stay	Monte Carlo Jets Loss	b	c	uds
All Standard	–	118	–	–	119	–	73	26	20
3-D Vertex Open Angle: Standard Cut $\Psi_{3D} < 55°$									
$\Psi_{3D} < 50°$	3	103	15	2	100	19	–8	–4	–5
$\Psi_{3D} < 60°$	17	115	3	17	117	2	+5	+4	+6
2-D Vertex Open Angle: Standard Cut $\Psi_{2D} > 5°$									
No cut	1	118	0	3	116	3	–1	+1	±0
$\Psi_{2D} > 10°$	4	105	13	5	98	21	–9	–6	–1
Track Momentum: Standard Cut $P > 0.4$ Gev/c									
$P > 0.3$	26	115	3	30	116	3	+13	+6	+8
$P > 0.5$	3	96	22	3	93	26	–11	–6	–6
Track Impact Parameter: Standard Cut $\|d\| < 0.25$ cm									
$\|d\| < 0.20$ cm	2	111	7	1	110	9	–4	–3	–1
$\|d\| < 0.30$ cm	8	118	0	7	118	1	+3	+2	+1
Vertex Flight Distance: Standard Cut $\|d_v\| < 0.70$ cm									
$\|d_v\| < 0.60$ cm	4	105	13	2	109	10	–5	–2	–1
$\|d_v\| < 0.80$ cm	4	118	0	8	119	0	+3	+3	+2
Track VXD Hits: Standard Cut $N_{Vhit} \geq 3$									
$N_{Vhit} \geq 4$	3	107	11	1	96	23	–12	–5	–5

Table 5.10: Variations of *Jet-mode* Tagging Statistics with Different Cuts.

effect of different B lifetimes were estimated by recovering the generated Monte Carlo B centre of mass decay time and the jet was weighted according to the probability ratio of this decay time in another exponential distribution with a different decay lifetime.

Only the three variables most likely to have significant effects were studied. The decay lifetimes of D^0,D^+ mesons and all B mesons were weighted with the exponential distributions of centre of mass decay times. The effect of the uncertainty in heavy flavour fragmentation functions were studied by weighting the generated heavy meson fragmentation z during the formation of a B meson, assuming different Peterson functions. The decay charge multiplicities of B mesons were weighted using Poisson distributions with different mean values.

The resultant weights from each variable were checked so that it was ensured that the average weights for all events were always equal to 1 within 1%. This was expected since the small changes in Monte Carlo parameters normally should not create large ratios between distributions in this context. The small changes also ensured that the exactness of modelling the distributions were not important.

The effect of various assumptions on Monte Carlo parameters are listed in Table 5.11. The effect of D_s lifetime was ignored because of the much smaller yield of D_s compared to D^0 or D^+ and its yet shorter lifetime. The effect of omitting the Λ_c should also be very small for the same reason.

Firstly, it can be seen from Table 5.11 that the lifetimes of charm mesons were known to a sufficient accuracy so that they could not affect the result significantly. The fact that both the b content and c content would increase together when the charm lifetimes increased, gave an extra stabilising factor in the b purity estimation.

However, the uncertainty in B meson lifetime had the largest effect of all as expected. To study this, the Monte Carlo jets were weighted with a broad

Monte Carlo Parameters	Tagged Monte Carlo Jets b	c	uds
All Standard	73	26	20
Generated average B lifetime τ_B =1.0 ps			
τ_B =0.9 ps	−7	–	–
τ_B =1.1 ps	+6	–	–
τ_B =1.3 ps	+19	–	–
Generated D^0 lifetime τ_{D^0} =0.40 ps			
τ_{D^0} =0.38 ps	−1	±0	–
τ_{D^0} =1.43 ps	+1	+1	–
τ_{D^0} =1.48 ps	+2	+2	–
Generated D^+ lifetime τ_{D^+} =0.93 ps			
τ_{D^+} =1.03 ps	+1	±0	–
τ_{D^+} =1.13 ps	+3	+1	–
Generated b fragmentation Peterson Function ϵ_b =0.005 ($< z_b >$=0.84)			
ϵ_b =0.013 ($< z_b >$=0.78)	+2	–	–
ϵ_b =0.020 ($< z_b >$=0.75)	+2	–	–
Generated c fragmentation Peterson Function ϵ_c =0.075 ($< z_c >$=0.65)			
ϵ_c =0.030 ($< z_c >$=0.73)	–	−7	–
ϵ_c =0.130 ($< z_c >$=0.60)	–	+4	–
Generated average B decay charge multiplicity $< n_B > = 5.57$			
$< n_B > = 5.34$	−5	–	–
$< n_B > = 5.80$	+4	–	–

Table 5.11: Variations in *Jet-mode* Tagging Statistics with Different Monte Carlo Heavy Flavour Parameters.

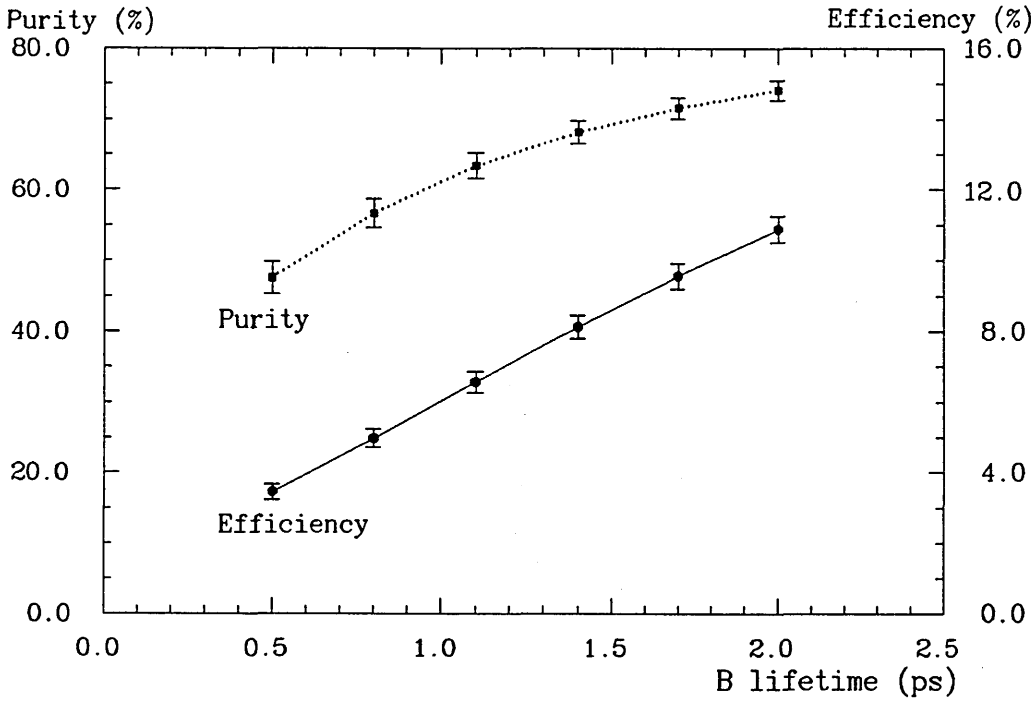

Figure 5.18: Monte Carlo *Jet-mode* Tag b Efficiency and Purity as Functions of Different B Lifetimes at a Fixed Cut of $\sum W \geq 4$.

range of B lifetime values and the resultant jet tagging efficiency and b purity values are plotted in Fig. 5.18 for a fixed cut of $\sum W \geq 4$. The errors were simply the statistical errors in the Monte Carlo. The systematic error on the b content in the tagged sample due to uncertainty in B lifetime was taken as the variation of B lifetime between 0.9 and 1.3 ps. It should be noted that this was asymmetric with respect to the generated value of 1 ps but was centred around the present world average measurement value of 1.1 ps (see Table 4.4). Although the present world average of B lifetime measurements already gave an error smaller than 0.2 ps, it was rather unrealistic to quote such a value since we had reached the level that possible different lifetimes of different B mesons might become important.

The fact that the tagging efficiency did not grow very rapidly as the assumed B lifetime increased was mainly because the rather hard ΣW cut of 4 for suppressing background. This essentially gave up on B's decayed with relatively low charge multiplicities even at very long decay distances. Thus the efficiency would saturate to much less than 100% if the same $\Sigma\ W$ cut was maintained for all possible B lifetimes as shown in the plot. If the B lifetime was really much longer than 1 ps, ΣW could of course be changed to optimise the efficiency for that B lifetime instead.

The smaller Peterson fragmentation ϵ values should give harder heavy meson momentum spectra thus longer heavy meson decay flight paths but less primary fragmentation particles. The vertex weight definition in the tagging method employed a vertex flight path resolution factor σ_v as seen in Equation 5.3, where longer decay lengths of high momentum heavy mesons were counterbalanced by the narrower vertex opening angles. This was intended to bring a similar property of a small Lorentz boost dependence to the vertices as for ordinary track impact parameters. This seemed to be a success as far as the b content was concerned since the rather large variations of ϵ_b were consistent with no effect. However, there was a somewhat surprising effect on charm jets in favour of tagging jets with low z primary D or D^* instead. This might be due to the extra combinations of wider opening angle D decay tracks and more primary fragmention tracks in the low z D, D^* jets.

To check the B momentum dependence in a more direct way, the tagging efficiencies for Monte Carlo b jets with different B momenta are listed in Table 5.12 for several B momentum ranges. The errors are purely due to Monte Carlo statistics. The result can be seen to be fairly stable in the high mometum range but the efficiency for B's with momenta <10 GeV/c were somewhat lower. These efficiency values should be interpreted in terms of absolute momentum rather than momentum scaled with respect to the beam energy since the multiple scatterings and the relative opening angles of B decay tracks were all directly related to the absolute B momentum.

The variations of b content due to B decay charge multiplicity weighting should also to taken as an independent source of systematic error. The effect

B Momentum (Gev/c)	b Jet Tagging Efficiency (%)
< 10	2.7 ± 0.6
$10 - 13$	4.0 ± 0.7
$13 - 15$	6.2 ± 0.8
$15 - 17$	7.3 ± 0.8
$17 - 19$	7.3 ± 0.7
> 19	7.1 ± 0.7

Table 5.12: Monte Carlo Dependence of b jet tagging Efficiency on B momentum in *Jet-mode* (E_{beam} = 22 Gev/c).

of D decay charge multiplicities were also briefly checked and was found to be negligible.

Finally, the effect of primary D^0/D^+ yield was checked. As discussed in section 4.4, there was still a large possible range of (Direct D)/D* production ratio in $c\bar{c}$ events and the decay branching ratio Br($D^{*+} \rightarrow D^0\pi^+$) was also very uncertain. It was checked for the tagged Monte Carlo $c\bar{c}$ jets with *Jet-mode* that the efficiency for D^+ was 0.82$\pm$0.09% while for D^0 it was 0.54$\pm$0.06%. Although D^+ had a larger probability to be tagged owing to its longer lifetime, the larger yield of D^0 was still a more important source. The Monte Carlo generated a net yield of $D^0 : D^+$ = 1.7:1 in $c\bar{c}$ events. Using the different Monte Carlo tagging probabilities and assuming the $D^0 : D^+$ production ratio to be 4:1 and then 1:1, the resultant changes in tagged primary charm jets would be $\pm$ 2 among the tagged 26 jets as normalised to the data.

Systematic Error Origins	**Tagged Monte Carlo Jets**		
	b	c	uds
Actual Contents	72	26	20
Impact parameter resolutions	+7 −7	+7 −4	+5 −4
Track Normalisation & Ψ_{3D} cut	+5 −8	+4 −4	+6 −5
B lifetime	+19 −7	– –	– –
B decay charge multiplicity	+4 −5	– –	– –
Charm fragmentation function	– –	+4 −7	– –
D^0/D^+ yield	– –	+2 −2	– –
Combined	+21 −14	+9 −9	+8 −6

Table 5.13: Systematic Error Contributions in *Jet-mode* Tag with $\Sigma W \geq 4$.

5.5.4 Summary

Summarising the above results on systematic effects, the magnitudes of various significant systematic errors of tagged flavour content are listed in Table 5.13 for *Jet-mode* tag.

For the *Global-mode* tag the first two types of contributions were obtained in a similar way as for *Jet-mode* while the errors due to heavy flavour properties were taken from the *Jet-mode* values scaled by the number of tagged events. The best estimate of flavour content in the tagged data sample includ-

Tagging Mode		Tagged Jets/Events b	c	uds
Jet-mode	No. of Jets	$72\ ^{+23}_{-14}$	26 ± 10	20 ± 8
	Flavour Fractions	61 ± 10 %	22 ± 8 %	17 ± 7 %
Global-mode	No. of Events	$99\ ^{+31}_{-18}$	40 ± 14	25 ± 10
	Flavour Fractions	60 ± 9 %	25 ± 8 %	15 ± 6 %

Table 5.14: Final Estimates of Flavour Content in Tagged Data Samples with Statistical and Systematic Errors All Included. Tagging Cut Was $\Sigma W \geq 4$ for Both Modes.

ing systematic errors and statistical errors together are listed in Table 5.14 with tagging cut of $\Sigma W \geq 4$ for both modes. Taking the systematic errors as proportional to the number of events, the Monte Carlo estimates of b tagging efficiency and purity are plotted for the *Global-mode* in Fig. 5.19 with different ΣW cuts.

5.6 Conclusions on Tagging Method

The analysis has shown that b enrichment can be obtained by exploiting the B decay track geometry in a region a few mm around the e^+e^- event interaction point. A reasonable b purity of $\sim$ 60% has been obtained with an efficiency of $\sim$15% under the actual detector geometry of TASSO.

The method is very flexible as it is capable of performing in both the usual *Jet-mode* to tag half an event leaving the other half to be studied bias free, and also in the *Global-mode* with no need of any event axes. There is a large range of available combinations of efficiencies and purities obtainable by simply

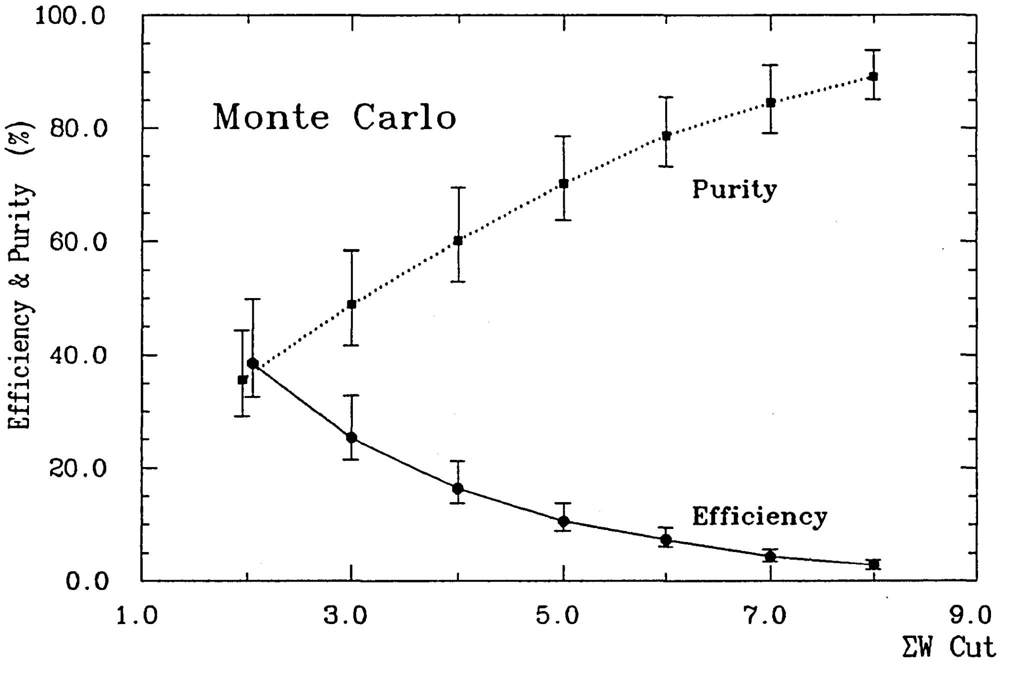

Figure 5.19: Monte Carlo Estimates of b tagging Efficiency and Purity in *Global-mode* with Various ΣW Cuts.

moving the ΣW cut depending on the specific purpose of an analysis. The verification of b enrichment with both internal checks and external comparisons to other enrichment schemes yielded consistent results.

The method has natural biases in favour of b events with long B decay times and large B decay charge multiplicities. However, it has a relatively uniform acceptance of B's with momenta >10 GeV/c. The most sensitive systematic uncertainty is the B lifetime. As far as the background events from light flavours are concerned, some systematic uncertainties may be removed with an improved detector simulation and possibly better Monte Carlo fragmentation parameters.

The resultant enrichment achieved using this scheme can be compared to the existing experimental studies of b event properties with high P_T leptons as shown in Table 5.15. The event selections are somewhat different between different experiments. For simplicity, the b tag efficiencies listed are calculated

Experiment	Method	Total Input Events	Estimated $b\bar{b}$ Tagged	b Purity	b tag Efficiency
DELCO [100]	High P_T e	~ 67000	121	83%	2.0%
MARK II[101]	High P_T e, μ	> 60000	440	64%	8.1%
TASSO	*Jet-mode*	~ 8000	72	61%	9.9%
(This Analysis)	*Glolal-mode*	~ 8000	99	60%	13.6%

Table 5.15: Comparison with Existing Measurements used b Enrichment Data Samples. The Tagging Cut Quoted for Both Modes in This Analysis was $\Sigma\ W\ \geq 4$.

from 1/11 of the total data sample rather than the events actually passed into the tagging programs. To avoid confusion of tagged jets and events, a tagged jet is counted as one event.

The main problem for this analysis is the lack of data statistics. However, the situation should be much improved with the 33000 hadronic events taken by TASSO in 1986. The quality of the new data is also expected to be with improved VXD resolution and less noise compared to the high energy running. This should lead to improved efficiency and purity with this method. A slight narrowing in background ΣW spread may bring the possibility of lowering the $\Sigma\ W$ cut to give better efficiency. However, the problem of multiple scattering may become slightly worse due to the lowering of track momenta. The generally lower B momenta may also need some changes of cuts.

This type of b enrichment may have a much more important role in the future e^+e^- experiments at SLC/LEP. The large amount of data available at the Z^0 energy will open up more interesting topics to be studied with the b quark which are limited by statistics for the existing experiments.

Besides the large statistics, another very important advantage at the Z^0 peak is that the $b\bar{b}$ events will be produced nearly equally with other flavours compared to the 1/11 at lower energies which already reduces the need for enrichment by a factor of 2. Another advantage is that the average B decay track momentum will increase so that the multiple scattering problem will be less serious than at lower energies. The main disadvantage is that the average charge multiplicity in the events will increase while the B signal tracks remain the same as at lower energies. Therefore the task of controlling the background may be more difficult. The fact that jets will also get narrower should be well compensated by the superior designs of the new generation of drift chambers with Flash ADC readout capable of good 2-track resolutions.

The tagging strategy developed in this analysis is optimised to the case that the detector resolution is comparable to B decay distances. The planning of possible installations of silicon vertex detectors in some of the SLC/LEP experiments may require the tagging strategy to be changed completely for even better efficiency and purity if the impact parameter resolution can be improved dramatically. For detectors without silicon vertex detectors or where the beam pipe is not narrow enough to limit the effect of multiple scattering, this type of strategy may still be applicable.

Chapter 6

Applications of b Enrichment Method

6.1 Review of Existing Measurements

The various flavour tagging methods used in e^+e^- experiments were important tools in studying both the electroweak and strong interaction properties of different flavours. In the electroweak domain, the direct reconstructions of the D^* mesons provided the basic platform for measurements of charm meson lifetimes [34] and the $c\bar{c}$ forward-backward asymmetry [98]. The uses of high P_T leptons or event shape variables gave the more demanding b enrichment for average B hadron lifetime measurements [34]. The combinations of both were also used to measure the $b\bar{b}$ forward-backward asymmetry [99].

The measurements to be presented in the next two sections are applications of the b enrichment method described in the last chapter. Since they are studies of the strong interaction properties of the b quark, the existing measurements for both charm and bottom flavours are to be discussed in some detail in the next few paragraphs.

TASSO made the first measurement in this direction by tagging the $c\bar{c}$ events with fully reconstructed charged D^*'s and subsequently observed the general properties of the charm 'jets' defined as all particles in half-hemispheres opposite the tagged D^* jets [102]. No significant difference in event shape was observed between the charm jets and average jets. The geometry of the remaining particles in the tagged D^* jets, after removing the particles from D^* decays, were very similar to the events at an equivalent lower centre of mass energy of 14 GeV. The only difference came from the higher charge multiplicity of the charm jets:

$$\begin{aligned} Average\ Jets: \ < n_{ch} > &= \ 6.7 \pm 0.02 \pm 0.3 \\ Charm\ Jets: \ < n_{ch} > &= \ 7.5 \pm 0.5 \ \pm 0.3 \end{aligned} \tag{6.1}$$

The same technique was also used by TASSO to test the flavour independence of α_s using the track P_{Tin} and P_{Tout} distributions [103]. Benefitting from the partial cancellations of systematic errors, a ratio of the α_s values was obtained as:

$$\frac{\alpha_s(charm)}{\alpha_s(Average)} = 1.00 \pm 0.20 \pm 0.20 \tag{6.2}$$

The HRS collaboration [104] also used D^* to tag the $c\bar{c}$ events but compared the charm jets with light flavour jets enriched with a high momentum leading particle tag. The differences in most of the event shape variables were found to be small, but some significant differences were observed in . charge multiplicity and inclusive momentum spectrum. Although this measurement also used jets opposite to trigger jets as bias free samples, an additional cut on jet mass was made to remove events with gluon emissions. Therefore when comparing with other experiments for quantities such as mean sphericity and jet P_T^2, the effect of this cut should be treated with caution. Their results on charged multiplicity and average charge particle momentum were:

$$\begin{aligned} Light\ Jets: \ < n_{ch} > &= 5.8 \pm 0.1 \\ Charm\ Jets: \ < n_{ch} > &= 6.6 \pm 0.2 \end{aligned} \tag{6.3}$$

$$\begin{aligned} Light\ Jets: \ < P > &= 1.52 \pm 0.04 \\ Charm\ Jets: \ < P > &= 1.38 \pm 0.06 \end{aligned} \tag{6.4}$$

Experiments	DELCO [100]	Mark II [101]	HRS [104]
Variables	$< n_{ch} >$ (Jets)	$< n_{ch} >$ (Events)	$< n_{ch} >$ (Jets)
Average	6.16 ± 0.01	$12.9 \pm 0.1 \pm 0.6$	6.55 ± 0.30
uds	–	$12.2 \pm 0.4 \pm 1.3$	5.8 ± 0.1
c	–	$13.2 \pm 0.5 \pm 0.9$	6.6 ± 0.2
b	7.16 ± 0.16	$16.1 \pm 0.5 \pm 1.0$	–

Table 6.1: Charge Multiplicity Measurements of different Flavours from PEP experiments at W=29 GeV.

The popular technique of tagging the $b\bar{b}$ events with high P_T leptons was used by DELCO [100] to tag the $b\bar{b}$ events and the properties of b jets in comparison with the average jets which were dominated by large populations of $udsc$ flavours. In this case, significant differences were observed as the b jets were seen to be softer and more spherical. Their results on scaled momentum distributions were

$$\begin{aligned} Average\ Jets: & \quad < x_p > = \ 0.0892 \quad \pm 0.0001 \\ Bottom\ Jets: & \quad < x_p > = \ 0.073 \quad \pm 0.003 \end{aligned} \tag{6.5}$$

The MARK II collaboration [101] also used the same method to mainly study the b jets charged multiplicities. Since the PEP experiments all operated at the same e^+e^- centre of mass energy of 29 GeV, the various charged multiplicity measurement results are listed together in Table 6.1.

The b enrichment by lifetime tagging as presented in the last chapter clearly has different systematics compared to the high P_T lepton tagging. The lifetime tagging used a limited amount of kinematic variables related to event shape in the enrichment phase which is a desirable feature for event shape studies. However, the tagging cut on the sum of vertex weights ΣW has a bias for high charge multiplicities. The track opening angle cut of 55° results in some inefficiency for B's with of very low momenta which is similar to the cases of high x D^* and high x single particle tags.

6.2 Properties of b Jets

The b enriched sample using the *Jet mode* tag method was employed for the study of b jets. Each event was divided into two hemispheres by the plane perpendicular to the event thrust axis calculated using charged tracks. Each hemisphere will subsequently be referred to as a 'jet'. This sample contained 102 events with 108 tagged jets, thus also giving 108 jets opposite the tagged jets, which will subsequently be referred to as 'b enriched jets', with relatively small bias. The term 'average jet' will be used for jets in all hadronic events.

The raw distributions were calculated using charged tracks reconstructed in 3 dimensions with rather loose track selection cuts as conventionally used in TASSO fragmentation studies:

$$
\begin{array}{ll}
|cos\theta| & < 0.87 \\
|Z_0| & < 20.0 \text{ cm} \\
|d_0| & < 5 \text{ cm} \\
P_{r\phi} & > 0.1 \text{ GeV/c}
\end{array}
$$

and only events with $|cos\theta_{thrust}| < 0.75$ were used.

To enable comparison with other experiments, a corrective procedure was taken to modify the raw distributions calculated from the observed charged tracks. This was to remove the detector bias due to acceptance, tracking inefficiency, approximations of event axes and QED radiative effects. The Monte Carlo program described in chapter 4 was used to obtain these correction factors. A Monte Carlo sample without detector simulation or QED radiative corrections was generated at a fixed e^+e^- centre of mass energy of 43.6 GeV. The 'true' event thrust and sphericity axes were calculated using both charged and neutral tracks in an event and then the 'true' distributions were calculated using charged tracks only. The Monte Carlo events were then generated at the same e^+e^- centre of mass energy but with QED radiative corrections and passed through detector simulation, trigger simulation, track finding and hadronic selection procedure. The actual observed charged tracks in this later Monte Carlo sample were used to obtain the 'observed' raw distributions. All particles with lifetimes shorter than 3×10^{-10}s were decayed which included K_s^0's and Λ's while K_L^0's, for example, were kept stable. The correction factors were obtained by dividing the 'true' distributions by the 'observed' distributions.

6.2.1 Jet Sphericity and Thrust

The initial observed jet thrust and sphericity distributions were calculated using the charged tracks in a hemisphere but each track's P_T and $P_{||}$ were defined with respect to the corresponding axes determined from charged tracks in a whole event. The same correction factors were applied to the observed distributions of average jets and jets in tagged events. No background subtraction was performed here.

The jet thrust and sphericity distributions for b enriched jets as compared to average jets and Monte Carlo are shown in Fig. 6.1. Because the events were broken into two halves and only charged tracks were used in the calculations, these distributions were broader than the corresponding distributions calculated using all tracks in an event. No significant difference between the b enriched jets and average jets was observed within the statistical errors. The behaviour of b jets as predicted by the Monte Carlo also agreed reasonably with the data.

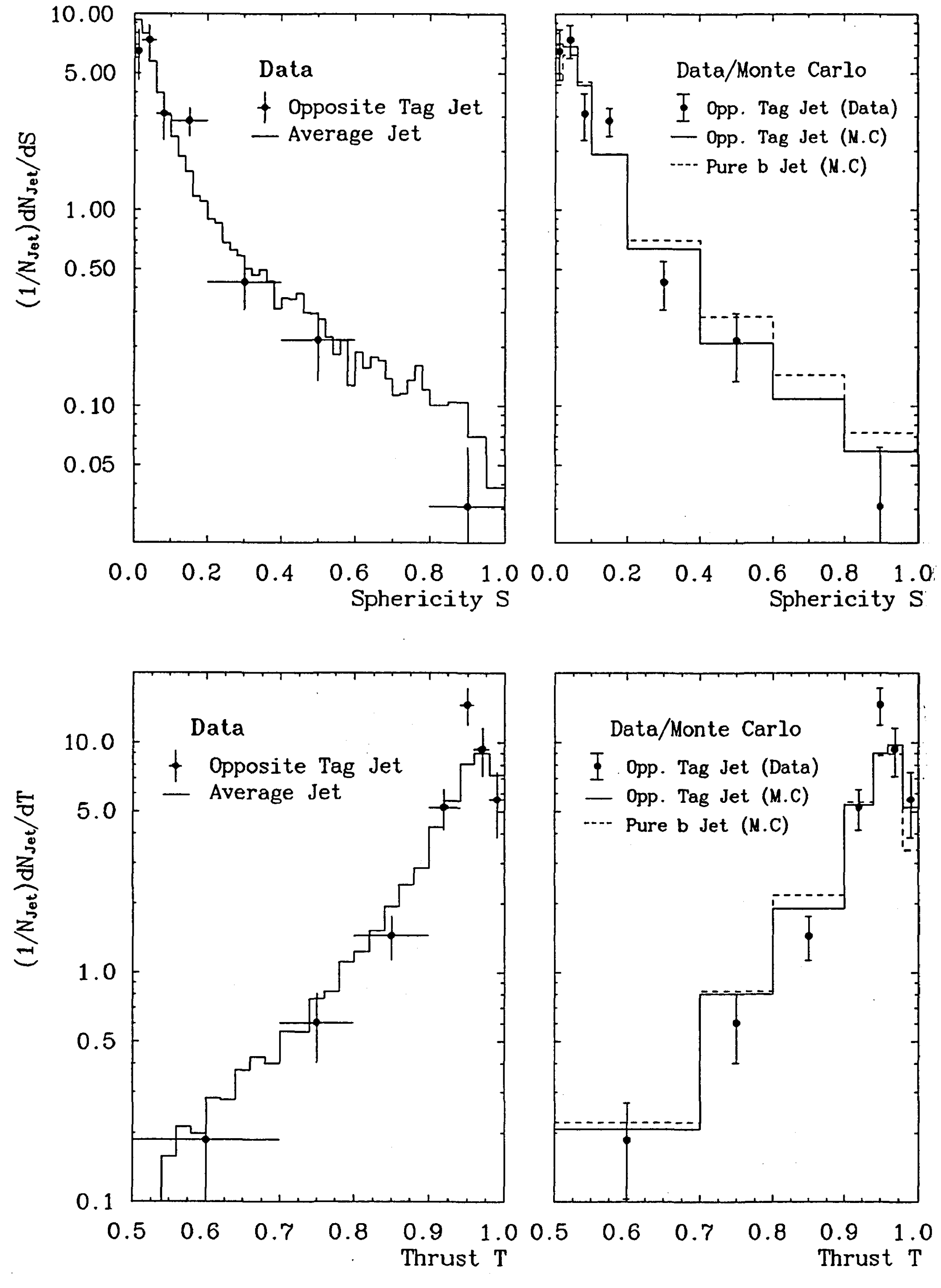

Figure 6.1: Jet Sphericity and Thrust of b Enriched Samples.

The broadening of sphericity and thrust distributions due to heavier b quark mass is only expected to contribute moderately, especially at high energies. The very high sphericity and very low thrust events should still be mainly due to hard gluon emissions. Although these distributions may be used as evidence for the presence of gluon emission in $b\bar{b}$ events, a more detailed examination of its significance will be deferred until section 6.3.

6.2.2 Transverse and Longitudinal Momenta

The squared transverse momentum P_T^2 distributions and rapidity distributions for charged tracks in the b enriched jets are shown in Fig. 6.2 after correction for detector effect, in comparison to average jets and Monte Carlo. The P_T was defined with respect to the event sphericity axis and the $P_{||}$ used for calculating rapidity was with respect to the event thrust axis. All particles were assigned the pion mass.

The P_T^2 distributions were similar in b enriched jets and average jets. The apparent dip just beyond the naive kinematic limit of B decay track P_T of $\sim$2 GeV/c was consistent with a statistical fluctuation.

However, the difference between the b enriched jets and average jets in rapidity distribution was very much more statistically significant. This can be seen to be mainly an enhancement the in mid-plateau region of η $\sim$1–2. To examine the origin of this enhancement, the rapidity distribution for the tagged jets were also plotted in Fig. 6.2 which was known to be biased by having a large number of b decay tracks due to the tagging Σ W cut. The even more pronounced enhancement seemed to indicate that this was just due to the kinematics of B decays as the Monte Carlo also produced a similar enhancement without extra assumptions. This enhancement seemed to be accompanied by a dip in the low rapidity region as it appeared for both the

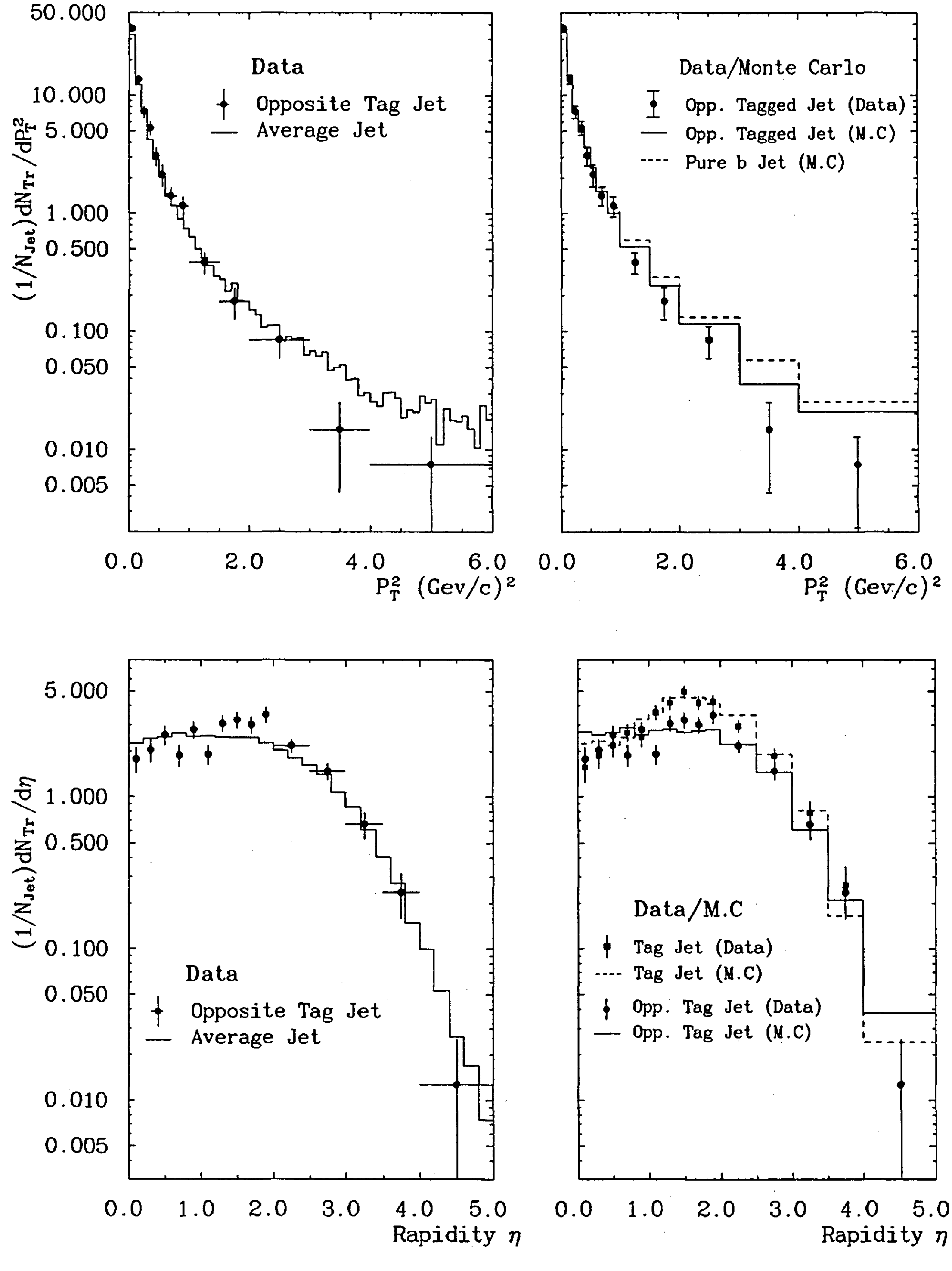

Figure 6.2: Track Jet P_T^2 and Rapidity in b Enriched Samples.

tagged jets and the b enriched jets which were only followed to a lesser extent by the Monte Carlo. This might have a correlation with the fact that the independent jet Monte Carlo was not able to produce the low rapidity dip for the average hadronic sample as previously shown in Fig. 4.16.

6.2.3 Inclusive Momentum Spectrum

The inclusive momenta of charged particles are shown in Fig. 6.3 for b enriched jets opposite tagged jets compared to the momentum spectra of average jets for data and Monte Carlo separately. The distributions were corrected for detector effects. The softer momentum spectrum for the b jets can be seen from the excess of tracks in the low x region of just below 0.1 for the b enriched jets. However, the fact that Monte Carlo also reproduced this softening to a comparable amount seemed to indicate again that it was merely a kinematic effect due to the heavier b quark mass.

The average scaled momentum $< x_p >$ for charged tracks in the all hadronic data, with an average centre of mass energy of 42.1 GeV, was found to be

$$< x_p > = \ 0.0823 \ \pm \ 0.0004 \ (\textit{statistical only}) \tag{6.6}$$

after correction for detector effect. Since this was only used for comparison with the values deduced from b enriched sample where much of systematics were similar, the systematic errors were not estimated specially. However, a comparison can be made with the values previously published by TASSO at lower energies [96]. To enable a more well defined check, only part of the data was selected in a narrow energy bin around $W = 43.6$ GeV, the same energy as the Monte Carlo events used to obtain the correction factors. The result was:

$$< x_p > = \ 0.0820 \ \pm \ 0.0005 \ (\textit{statistical only})$$

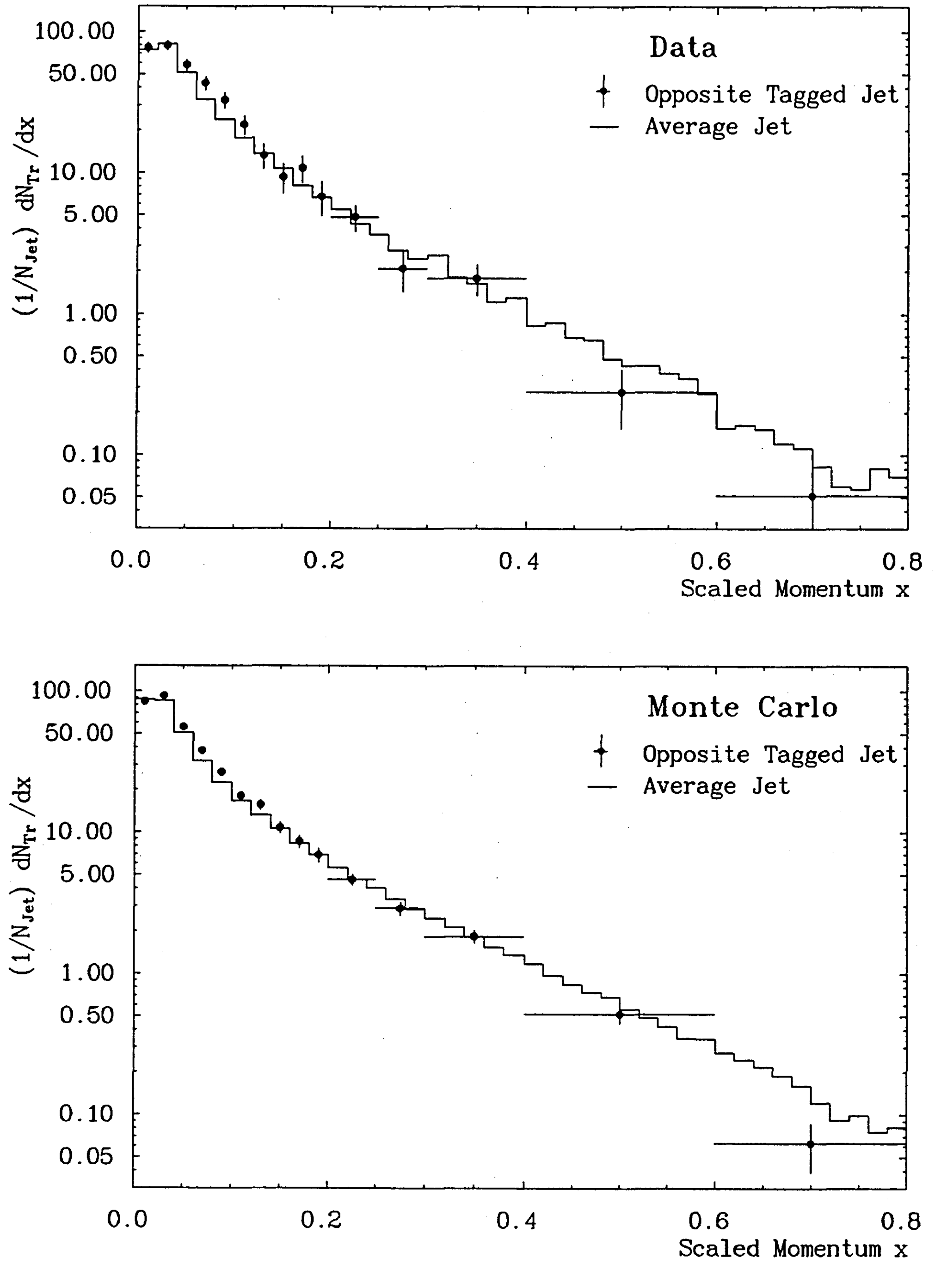

Figure 6.3: Momentum Spectra of Charged Tracks in b Enriched Samples.

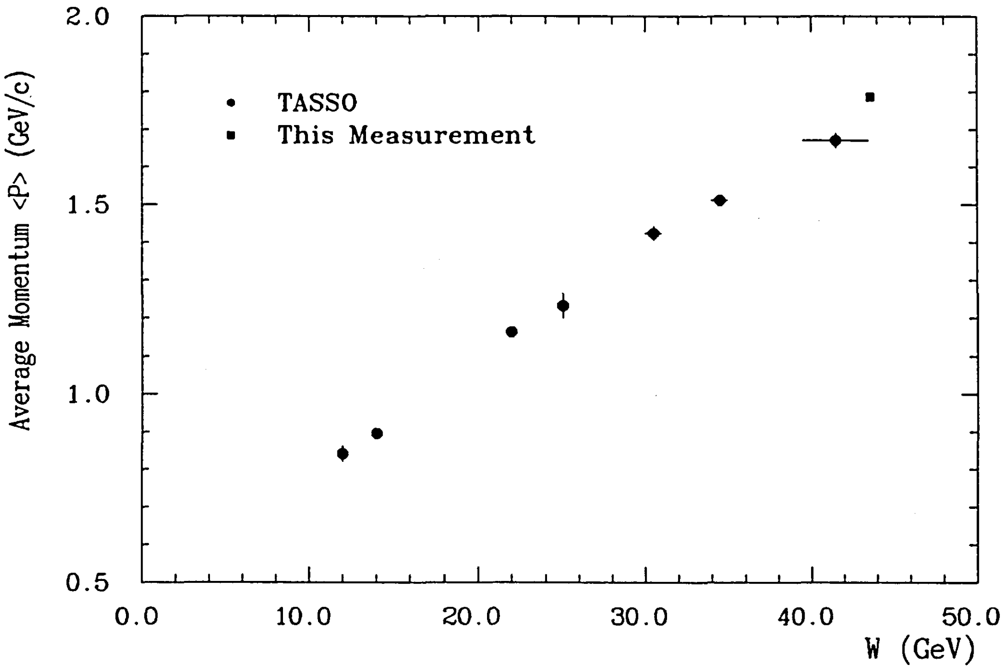

Figure 6.4: Average Momentum of Charged Particles at Different Energies.

or

$$< p > = \ 1.787 \ \pm \ 0.011 \ GeV/c \ (statistical \ only)$$

The value of $< P >$ is plotted in Fig. 6.4 in comparison to the published TASSO values at lower energies. This higher energy value seems to follow the trend of lower energy points.

To quantify the difference between b jets and average jets in average momentum, the same detector effect correction factors applied to the b enriched jets gave

$$< x_p > = \ 0.0775 \ \pm \ 0.0030 \ (statistical \ only) \tag{6.7}$$

without background subtraction. By checking the values of $< x_p >$ for different flavours in the Monte Carlo separately before and after tagging, no significant bias was found in this respect for the tracks opposite the tagged jets. Assuming the ratio of 10:1 for $udsc : b$ in all hadronic events and 61:39 in the tagged sample as determined in the last chapter, the unfolded result using the values in Equations 6.6 and 6.7 gave

$$< x_p > \ (b \ jets) \ = \ 0.074 \ \pm \ 0.005 \ \pm \ 0.003 \tag{6.8}$$

where the systematic error of 0.003 came from the 10% uncertainty in b purity and a possible 10% difference in $< x_p >$ between uds and c flavours according to the HRS result in Equation 6.4. It should be noted that this result was for $W \sim 42$ GeV and the data had a rather large spread in W. Also because some of the systematic errors, common to the results for the whole hadronic sample and the tagged sample, were not included, this result should always be treated in comparison to the result in Equation 6.6.

6.2.4 Charge Multiplicity

Since the charge multiplicity distributions were rather sensitive to the detector biases, two distinct steps were taken to unfold the charge multiplicity distributions with the assistance of Monte Carlo.

The first step was to correct the tracking inefficiency and the losses due to limited detector acceptance. This was done by checking the number of observed tracks N_T against the actually generated number of tracks for each Monte Carlo event after detector simulation and track finding. An unfolding matrix was then formed to predict the probability that the true produced charge multiplicity of an event was n_P when n_O tracks were observed. Therefore an intermediate stage unfolded charge multiplicity distribution could be obtained as

$$f(n_P) \; = \; \frac{1}{N_{ev}} \sum^{N_{ev}} \sum_{n_O}^{tracks} \epsilon(n_P, n_O) \; n_O \tag{6.9}$$

where

$$\epsilon(n_P, n_O) = \frac{No.\ of\ events\ with\ n_P\ tracks\ produced\ when\ n_O\ tracks\ were\ observed}{No.\ of\ events\ with\ n_O\ tracks\ observed} \tag{6.10}$$

This procedure typically gave 2.4 tracks more per event at W=44 GeV after unfolding compared to the observed tracks. It should be noted that all unfolding schemes including the above method rely on an approximate knowledge of how many tracks actually produced using Monte Carlo estimation or assuming certain model for the multiplicity distribution. Of course, no unfolding scheme could account for the possibility that there was some occasional yet coherent source giving a dramatically large density of tracks in the detector unless it assumed such an effect *a priori*. However, when neglecting such a possibility and knowing that the number of observed tracks in the data and Monte Carlo agreed reasonably well and the tracking efficiency was reasonably high, the different unfolding methods should have small effects.

The effect of QED initial state radiation could result in a reduction of effective centre of mass energy, thus also a reduction in charge multiplicity. This was estimated to be −1.0 at W=44 GeV using the QED radiative correction caculations of Behrends & Kleiss [78] with a maximum radiative photon energy cut-off of $0.98 \cdot E_{beam}$. However, the detector trigger and hadronic selections gave a bias of +1.2 toward higher multiplicity. Therefore a set of correction factors for the second step were obtained by dividing the multiplicity distribution of the fixed W Monte Carlo without detector simulation, by the unfolded multiplicity distribution of the fully simulated Monte Carlo. The correction factors here were generally small compared to the first stage except at the very low multiplicity region.

To test the correction procedure, the fraction of data in the range W=43.3-44.3 GeV with average W of 43.6 GeV were used. The systematic errors due to detector simulations and the correction procedure were monitored by applying the same analysis for two rather different track finding programs MILL and FELIX (see section 2.5) separately with different unfolding matrices ϵ. The result obtained for average event charge multiplicity with full corrections was

$$< n_{ch} > = \ 15.08 \ \pm \ 0.08 \ (statistical) \ \pm \ 0.37 \ (systematic) \qquad (6.11)$$

where the main contribution to the systematic error was due to the difference between the two track finders MILL and FELIX. After averaging the results, the systematic error was ± 0.32. The result was after a correction for the 0.5% τ pair and 1.0% $\gamma\gamma$ background events as estimated in [62], assuming their average charge multiplicity was 6. This resulted in a +0.13 shift of the $< n_{ch} >$ together with a 100% error associated with it. Since the entries for charge multiplicity ≤ 4 were mostly determined from Monte Carlo, a 100% error on the entries gave ± 0.14 in the systematic error of $< n_{ch} >$.

This result can be compared with the average charge multiplicity values of TASSO [96] at lower energies as seen in Fig. 6.5. The multiplicity distribution for the MILL tracks after all corrections except the background subtraction is plotted in Fig. 6.6. The simple 'single' Poisson

$$f(n) \;=\; \frac{2\, e^{-<n>}(< n >)^n}{n!} \tag{6.12}$$

looked too narrow compared to data while the 'pair' Poisson

$$f(n) \;=\; \frac{e^{-<n>/2}(< n > /2)^{n/2}}{\Gamma(\frac{n}{2}+1)} \tag{6.13}$$

looked too wide as was previously observed by TASSO [96] as an increasingly clear feature as e^+e^- beam energy increased. However, as noted in [105,106], the negative binomial distribution

$$f(n) \;=\; \frac{\Gamma(n+k)}{\Gamma(k)\,\Gamma(n+1)} \left(\frac{\frac{<n>}{k}}{1\,+\,\frac{<n>}{k}}\right)^n \left(\frac{1}{1\,+\,\frac{<n>}{k}}\right)^k \tag{6.14}$$

where

$$\begin{aligned} \frac{1}{k} \;&=\; \frac{1}{< n >} - \frac{D^2}{< n >^2} \qquad \mathit{and} \\ D \;&=\; \mathit{RMS\ Dispersion}\ \sqrt{< n^2 > - < n >^2} \end{aligned}$$

described all charge multiplicity distributions rather well. This seemed also to be true for the distribution in Fig. 6.6 at the highest e^+e^- centre of mass energy range of PETRA.

The above procedure was then modified to unfold multiplicity distributions of two hemispheres of an event separately. Each hemisphere was considered as

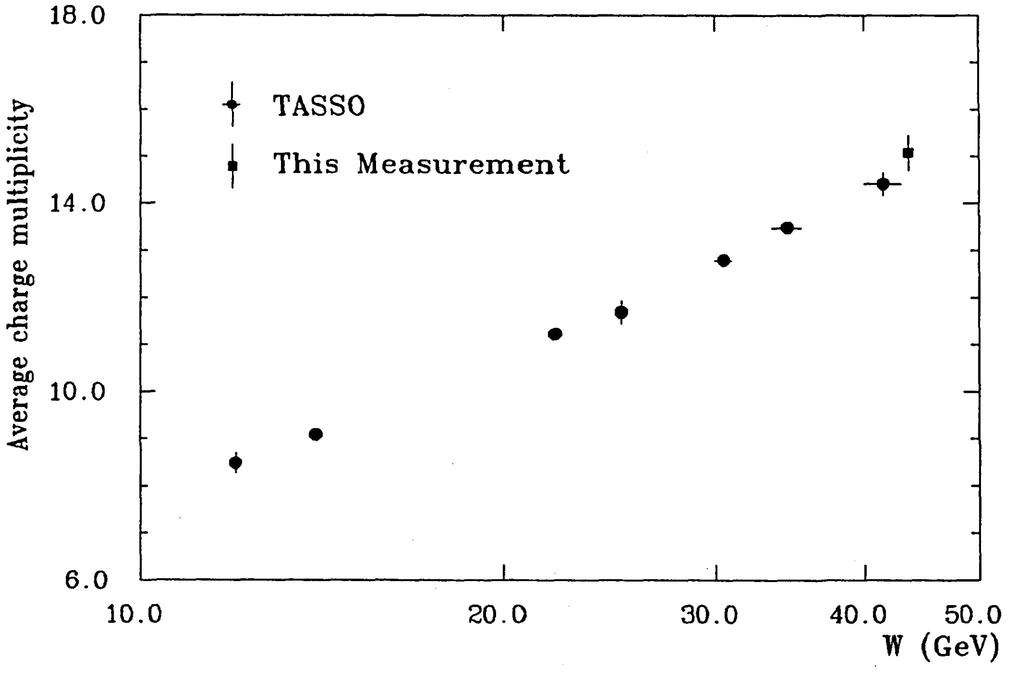

Figure 6.5: Average Charge Multiplicity Compared to lower W TASSO Values.

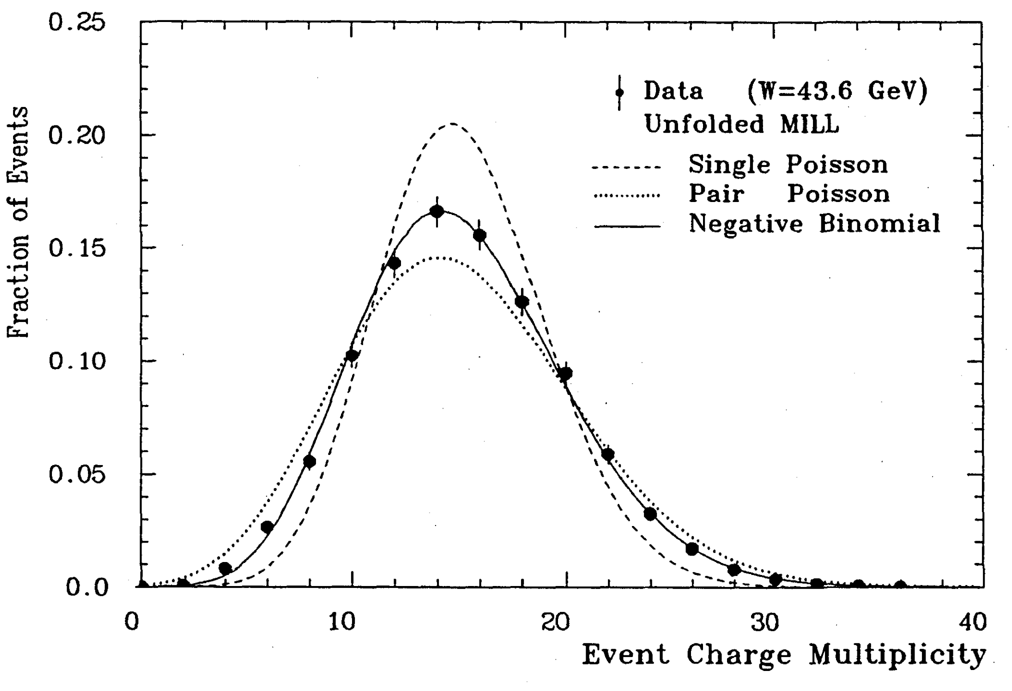

Figure 6.6: Event Charge Multiplicity Distribution at W =43.6 GeV.

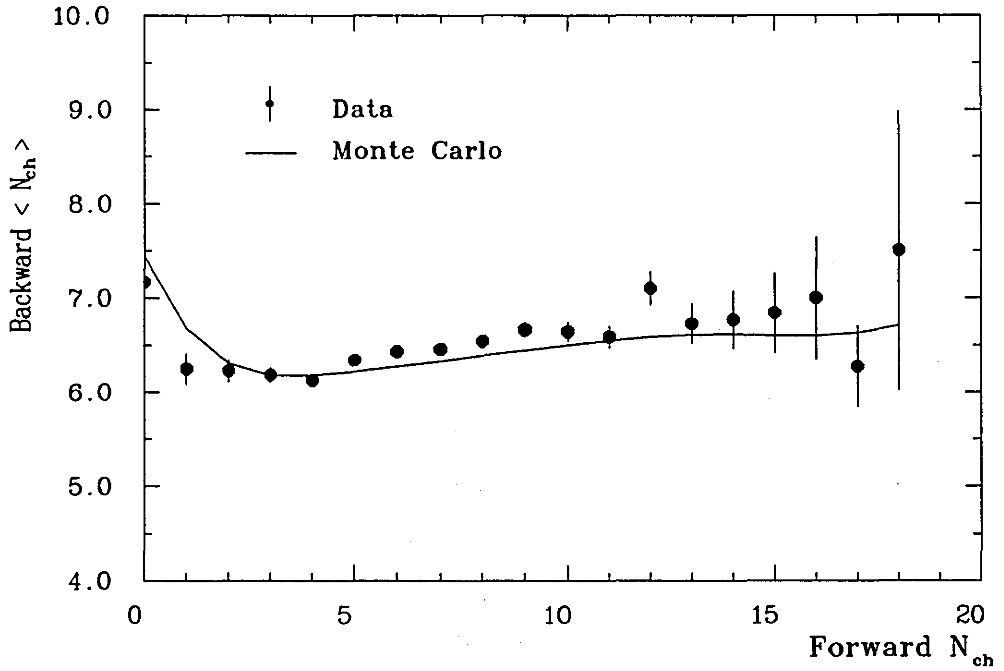

Figure 6.7: Forward-Backward Charge Multiplicity Correlation.

the backward and then the forward hemisphere in turn. Because of the event trigger bias in multiplicity, the multiplicity in the backward hemisphere, had some dependence on the forward hemisphere multiplicity. This was mainly for the case when the forward multiplicity was very low, and the backward multiplicity had to be large enough to pass the trigger. The actual dependence of the mean 'jet' charge multiplicity of backward jets as a function of the forward multiplicity is shown in Fig. 6.7 for observed MILL tracks in the data and Monte Carlo. This bias can be seen to be followed by the Monte Carlo detector simulation reasonably. As the bias diminished as the forward multiplicity increased, the multiplicity unfolding matrices constructed for counting backward multiplicities were different for different forward multiplicity n_f up to n_f=5. The cases n_f $\geq$6 shared a single matrix.

Since the procedure of unfolding the jet charge multiplicity was to compare the average jets with the small b enriched sample, all data without a W range cut were used. The average e^+e^- centre of mass energy was 42.1 GeV with the energy spread as shown previously in Fig. 4.1. Following a similar procedure as for the case of whole event charge multiplicity, the result for average jets was

$$< n_{ch} > \ (Average\ Jets) \ = \ 7.44 \ \pm \ 0.03\ (statistical) \ \pm \ 0.19\ (systematic) \tag{6.15}$$

after all corrections including the background subtraction. It was checked that when the *event* unfolding procedure was applied to the same data sample, the result was very close to be twice the average jet multiplicity. It was also checked using only the backward jets with corresponding forward jet charge multiplicity $\geq$6 which suffered less from uncertainties in background and very low multiplicity contributions, and the result was also consistent with the whole sample.

Owing to the intrinsic bias towards high multiplicity in the tagged jets, the τ pair and $\gamma\gamma$ background and uncertainties due to very low multiplicity events were negligible in the case of the b enriched jets. The average charge multiplicity of b enriched jets was found to be

$$< n_{ch} > \ (b\ Enriched\ Jets) \ = \ 8.09 \pm 0.29\ (statistical) \pm 0.16\ (systematic) \tag{6.16}$$

with the systematic error attributed to the difference of MILL and FELIX only. The 'observed' and the unfolded jet charge multiplicity distributions are shown for the b enriched jet (without subtracting the *udsc* content) together with that of the average jets in Fig. 6.8.

To ensure that the b enriched jets were independent of the tagging jets as far as the charge multiplicity was concerned, the generated charge multiplicities of different flavours in the Monte Carlo b enriched jets opposite tagged jets can be compared with the same flavours in all accepted Monte Carlo events. This is shown in Table 6.2. The result confirmed that there was no obvious

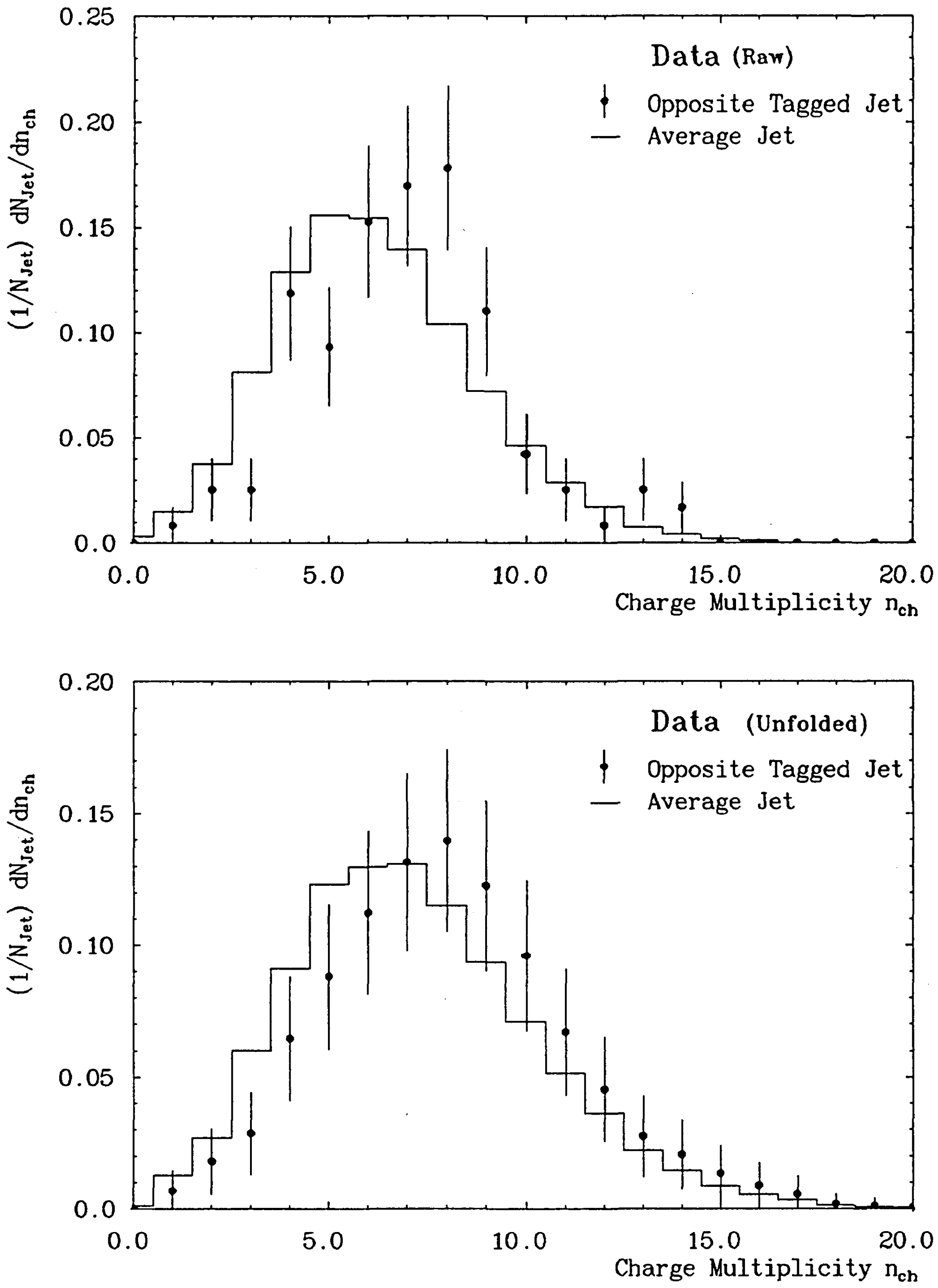

Figure 6.8: Jet Charge Multiplicity Distributions of b Enriched Jets and Average Jets.

Flavours	All Jets	b enriched Jets
uds	7.45±0.01	7.43±0.28
c	7.68±0.02	7.51±0.26
b	8.42±0.03	8.40±0.15

Table 6.2: Monte Carlo Jet Charge Multiplicity in All and Tagged Samples.

bias within Monte Carlo statistics.

To extract the average charge multiplicity for b jets only, the following equations were used

$$\begin{aligned} F_{uds}N_{uds} \ + \ F_cN_c \ + \ F_bN_b \ &= \ <n> \ (all\ jets) \\ f_{uds}N_{uds} \ + \ f_cN_c \ + \ f_bN_b \ &= \ <n> \ (b\ enriched\ jets) \end{aligned} \quad (6.17)$$

where N's were unknown average charge multiplicities of different flavours and F and f were the fractions of different flavours in all jets and b enriched jets respectively. Because the b purity was reasonably high in the tagged sample, a guessed difference of $N_c - N_{uds} = 0.5 \pm 0.5$ using results in Equation 6.1 and Table 6.1 was sufficient to reduce the number of unknowns to two without seriously affecting the result of N_b.

The electroweak effect modified the simple flavour ratio of $F_{uds} : F_c : F_b$ of 6:4:1 slightly to 55:35:10 in the nominal mixture of hadronic events at W=44 GeV. The fractions of different flavours $f_{uds} : f_c : f_b$ in the b enriched sample were $61 \pm 10 : 22 \pm 8 : 17 \pm 7$ as determined previously in chapter 5. Solving the equations 6.17 for MILL and FELIX results separately to avoid double counting systematic errors, the final combined result gave:

$$< n_{ch} > \ (b\ Jets) \ = \ 8.51 \ \pm \ 0.50\ (statistical) \ \pm \ 0.35\ (systematic) \quad (6.18)$$

The uncertainty in the b purity of $\pm 10\%$ made the major contribution of ± 0.27 to the systematic error. The difference between MILL and FELIX again gave ± 0.19. The uncertainty in $< n >$ of average jets gave ± 0.06. The uncertainty in the fraction of charm events in the tagged sample and the assumed difference between charm jets and light flavours gave ± 0.09.

The result of the b jet charge multiplicity can be compared to that of the average jets in Equation 6.15. The excess of ~ 1 track per jet was also predicted by the Monte Carlo. When considering there were ~ 5.5 charged tracks per B decay as measured by CLEO [94], it meant that the average ratio of B decay tracks to fragmentation tracks in $b\bar{b}$ events at $W \sim 42$ GeV was still as large as 11:6. It was therefore not surprising that some of the jet properties were rather different from those of light flavours.

6.3 Test of Flavour Independence of α_s

6.3.1 introduction

The flavour independence of the strong interaction strength is an important assumption in QCD. The large momentum transfer Q^2 involved in hard QCD processes like 3 jet events in $e^+e^- \rightarrow$Hadrons, makes the perturbative QCD calculations possible so that the QCD predictions can be compared with experiments. Various event shape variables sensitive to hard gluon bremsstrahlung have been used by high energy e^+e^- experiments [107,108,109,77], to measure the strong coupling constant α_s, incoporating various QCD matrix element calculations up to $O(\alpha_s^2)$ and fragmentation models.

There were many systematic uncertainties in the measurement results. The α_s values at $Q^2 \sim 35^2(\text{GeV})^2$, obtained among the PETRA experiments varied in a rather large range from 0.1 to 0.2. However, it was found that as long as the same QCD matrix element calculation and the same fragmentation model were used, fairly consistent values of α_s could be obtained from various different distributions [77].

When pursuing the task of testing the flavour independence of α_s, the possible differences can be quantified by the ratios of the measured α_s values of different flavours. Since most of the biases resulted from different QCD calculations and fragmentations which were imposed without distinction of flavours in the Monte Carlo, the ratios of the α_s values of different flavours should be relatively insensitive to these biases compared to the absolute α_s values.

The result of TASSO (Equation 6.2) gave the first indication that the strong interaction coupling of charm was consistent being the same as the average of all flavours in $e^+e^- \rightarrow$Hadrons events. This result benefitted from the partial systematic cancellation when taking the ratio of α_s values as previously discussed.

It is even more important to obtain the ratio between the α_s value of the b flavour and the average of all flavours since the average α_s is mainly governed by the large populations of $udsc$ flavours with very small influence due to b flavour in the original Monte Carlo tuning.

Owing to the rather large spread of e^+e^- centre of mass energy in the data sample, the use of many event shape distributions such as thrust and sphericity became rather undesirable as they were known to have clear energy dependences. Track P_{Tin} and P_{Tout} distributions also had the additional problem of track normalisation while the tagging method was intrinsically biased toward accepting high multiplicity events.

The energy-energy correlation (EEC) has been proposed [110] as an event shape variable sensitive to gluon bremsstrahlung in the high energy e^+e^- environment where partons fragment into narrow jets. The normalised EEC is defined as

$$\frac{1}{\sigma_0}\frac{d\Sigma(cos\chi)}{d\,cos\chi} = f(cos\chi) = \frac{1}{N}\sum_{Events}^{N}\sum_{i,j}\frac{E_i\cdot E_j}{W_{vis}^2}\,\delta(cos\chi - cos\chi_{ij}) \quad (6.19)$$

where χ_{ij} is the angle between two particles i and j with energies E_i and E_j in a event. W_{vis} is the total visible energy in an event. The summation is extended over all pairs i, j of particles in an event including the case $i = j$, and over all events N. The normalisation is therefore

$$\int f(cos\chi)\,d\,cos\chi = 1 \quad (6.20)$$

An idealised view case of 2 narrow back to back jets would only give entries near $|cos\chi| \sim 1$, but acollinear configurations of multiparton events can give entries in the small $|cos\chi|$ regions. While the EEC distribution itself is still affected by the fragmentation of $e^+e^-\rightarrow q\bar{q}$ events, these effects are suppressed if the asymmetry of EEC

$$A(cos\chi) = f(cos(\pi - \chi)) - f(cos\chi)) \quad (6.21)$$

is considered instead. This gives the enhanced sensitivity to $e^+e^-\rightarrow q\bar{q}g$ events as required to measure α_s.

The remaining effects due to fragmentation of 2 jet events near $|cos\chi| \sim 1$ can be further removed by constraining the fits to obtain α_s from the central region $|cos\chi| < 0.7$ of EEC asymmetry. This procedure gave good agreement between data and QCD calculations at the parton level [111]. Both the QCD calculations [111] and experimental measurements [107,108,109,77] have shown that results obtained from this scheme have very small dependences on QCD soft parton cut-off, *i.e.* different (ϵ, δ) cuts or different minimum mass combination cuts y_{min}. Although the shape of EEC itself was energy dependent, the asymmetry of EEC was found to be fairly stable at different e^+e^- centre of mass energies [112].

Based on the above discussion, the procedure for the determinations of α_s values was chosen to be the fits to the asymmetry of energy-energy correlation distributions in the range $|cos\chi| < 0.7$.

6.3.2 Determination of $\alpha_s(b)/\alpha_s(Average)$

Data Samples

For the procedure of the determination of the α_s ratio, the b enriched sample using the *Global-mode* tag was chosen. This tagging mode allowed free combinations of tracks only constrained by the angle between each other, but did not forbid the combinations of tracks from different hemispheres defined using the event thrust axis in contrast to the case of the *Jet-mode*. This was to avoid the problem that the plane perpendicular to the thrust axis was less meaningful in the case of hard 3 jet events, which could more often result in tracks from the same B decay ending up in different hemispheres.

The tagged data sample contained 164 events with an average e^+e^- centre of mass energy of W ~42.1 GeV and the estimated fraction of $b\bar{b}$ events to be 60±9% as previously shown in Table 5.14. The corresponding Monte Carlo sample contained 931 events with a fixed W of 43.6 GEV. The efficiencies of accepting 2 jet events and 3 or 4 jets events as defined in the Monte Carlo were studied for the *Global-mode* tagging procedure with the standard cuts. The results are listed in Table 6.3. There was some inefficiency in accepting multiparton $b\bar{b}$ events as compared to 2 jet $b\bar{b}$ events. This was mainly due to the effect of a 55° opening angle cut between pairs of tracks for reducing the combinatorial background. This resulted in more track pairs from low momentum B's with $P <\sim 10$ GeV/c, failing the opening angle cut, which could be thought to have more influence on multijet events. The reduction of sensitivity to gluon bremsstrahlung events due to this inefficiency was traded for a better b purity.

Monte Carlo Flavours	Tagging Efficiency 2 jets	3 or 4 jets
$b\bar{b}$	19.8±0.9%	11.4±0.9%
$c\bar{c}$	2.2±0.2%	1.7±0.3%
uds	0.8±0.1%	0.9±0.2%

Table 6.3: *Global-mode* Tagging Efficiencies of Different Flavours and Different Final State Parton Multiplicities.

The average flavour data sample contained all 4798 hadronic events in the W range of 42.0 to 45.0 GeV at an average W of 43.8 GeV while the corresponding Monte Carlo sample contained ~40000 events at a fixed energy of 43.6 GeV.

Event Weighting Procedure

Because of the rather complicated mixture of different flavours and some bias in the tagging procedure, no corrective procedures were taken for detector effects in the data, but it was chosen always to compare data with Monte Carlo passed through full detector simulations. Only charged particles were used in the calculations, therefore the quantity W_{vis} in Equation 6.19 was the sum of energies of all charged particles in an event assuming pion mass for all.

To avoid generating and processing many different samples of Monte Carlo events considering the rather small data sample, an event weighting procedure was devised to follow the effect of generating different Monte Carlo events. The Monte Carlo events were weighted according to their generator phase parton multiplicity:

$$
\begin{aligned}
r &= \frac{\alpha_s(To\ be\ simulated)}{\alpha_s(Generated)} \\
3\ parton\ events:\ weight &= r + T_{21}\, r^2 \\
4\ parton\ events:\ weight &= r^2 \\
2\ parton\ events:\ weight &= 2\ jet\ cross\ section,\ after\ subtraction \\
&\quad of\ weighted\ 3,4\ parton\ cross\ sections \\
&\quad as\ a\ fraction\ of\ total\ cross\ section.
\end{aligned}
$$

where the constant T_{21} was the ratio of average 2nd and 1st order contributions to 3 parton final states. Two differences remained when compared to actually generating the events were: (a) T_{21} was a fixed constant rather than varying from event to event. (b) The running of α_s in the case of reduced W due to QED radiative effect was ignored. However, the effects due to these approximations were found to be small as far as the distributions of EEC and its asymmetry were concerned.

To test this event weighting scheme, Monte Carlo events were generated at α_s=0.15 and events were weighted toward different α_s values as compared to actually generating those events at the corresponding α_s values. The results for both the EEC and the EEC asymmetry distributions are shown in Fig. 6.9. When fits were performed on the asymmetry distributions, the discrepancy between the weighted events and generated events in α_s values remained < 0.01 in the range of α_s from 0.0 to 0.2.

Measurement Results

The event weighting procedure was first applied to the average hadronic sample using the Monte Carlo generated with α_s=0.188. The EEC asymmetry distribution was fitted in the region $|cos\chi| < 0.7$, giving the result

$$\alpha_s(Average\ Hadrons) = 0.132 \pm 0.012\ (statistical\ only) \tag{6.22}$$

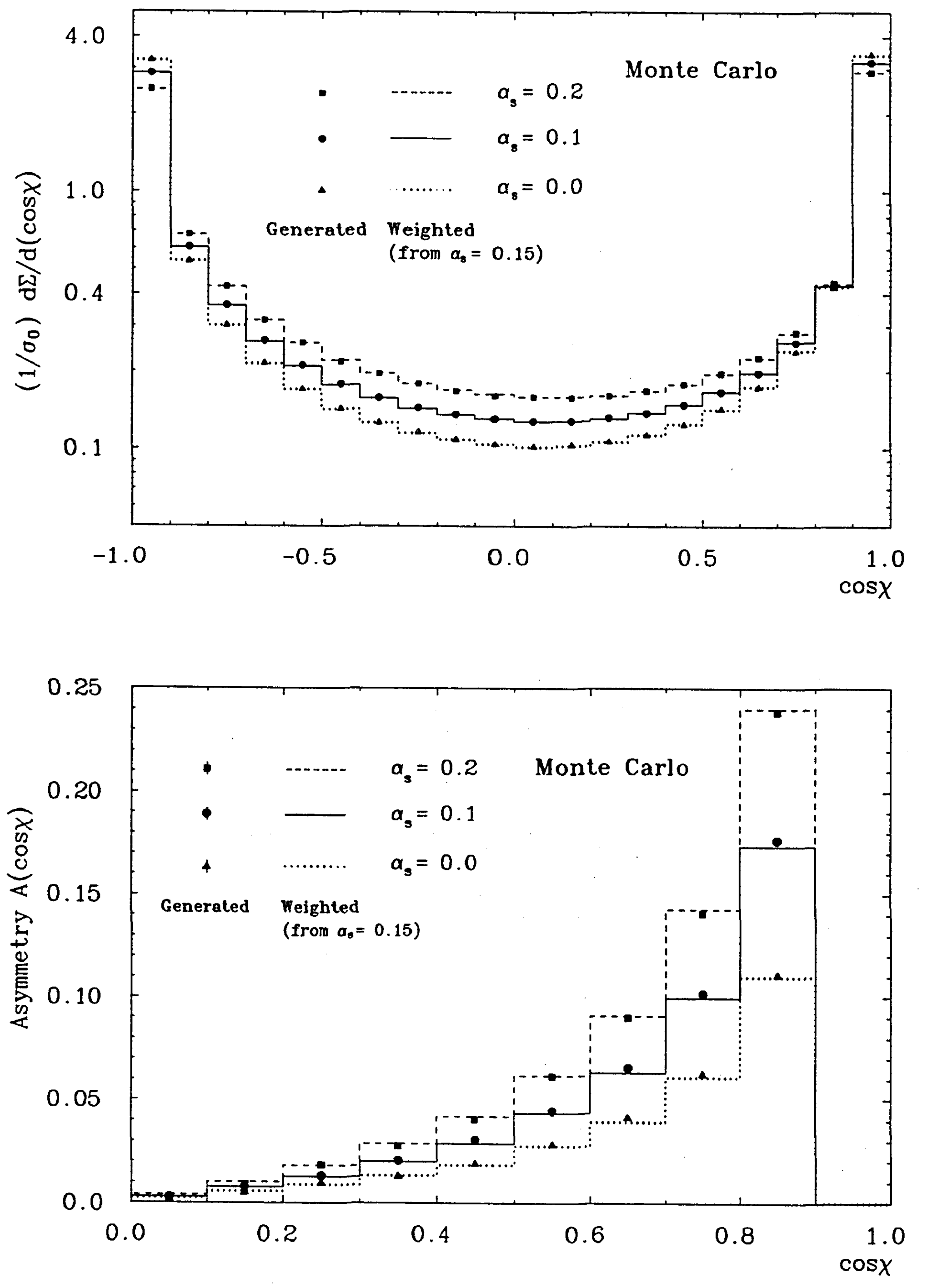

Figure 6.9: Test of Monte Carlo Event Weighting for EEC and EEC Asymmetry Distributions.

with a $\chi^2/d.o.f$ of 3.7/6. The Monte Carlo weighted according to this fit result for both the EEC and the EEC asymmetry distributions can be compared to data as seen in Fig. 6.10 together with some Monte Carlo variations near the fitted value.

Following the previous discussions on systematic effects of α_s determinations, it should be stressed that this result was based on an extended FKSS 2nd order QCD matrix elements (see section 4.1) together with an independent jet fragmentation scheme where gluons were fragmented in the same way as quarks and the energy-momentum conservation scheme was according to the Monte Carlo of Ali *et al.* [81].

When the upper limit of the fitting region was varied from $cos\chi$ of 0.6 to 0.9, the effect on the fit result was a small reduction of -0.01. Although the fit of the EEC asymmetry distribution was good as seen in Fig. 6.10, the Monte Carlo preference of α_s as seen from EEC distribution itself was however a higher value of $\sim$0.16. There was also some discrepancy in the Monte Carlo in the region of $cos\chi$ from 0.7 to 0.9 which seemed to be not adjustable by just varying α_s. Although these discrepancies might well be the fragmentation effects which are supposed to cancel when the EEC asymmetry was taken, a systematic error of +0.03 was nevertheless assigned to the result, giving:

$$\alpha_s(Average\ Hadrons) \;=\; 0.132 \;\pm\; 0.012 \;\pm^{0.03}_{0.01} \tag{6.23}$$

It should be noted that the systematic error was still partial as the effects of different QCD calculations and different fragmentation schemes were not included. However, this was considered to be adequate as the aim was to pursue a ratio of two α_s values and the same procedure would be used for the b enriched sample.

When the same fitting procedure was used using the tagged data and Monte Carlo samples by fixing the α_s value of $udsc$ background events to that of the

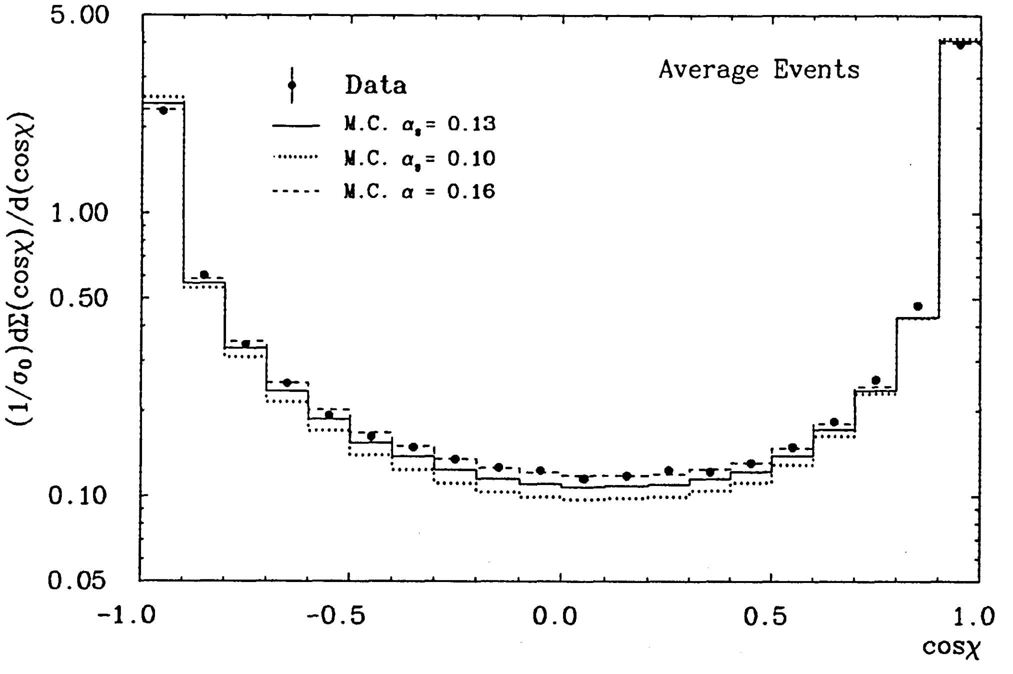

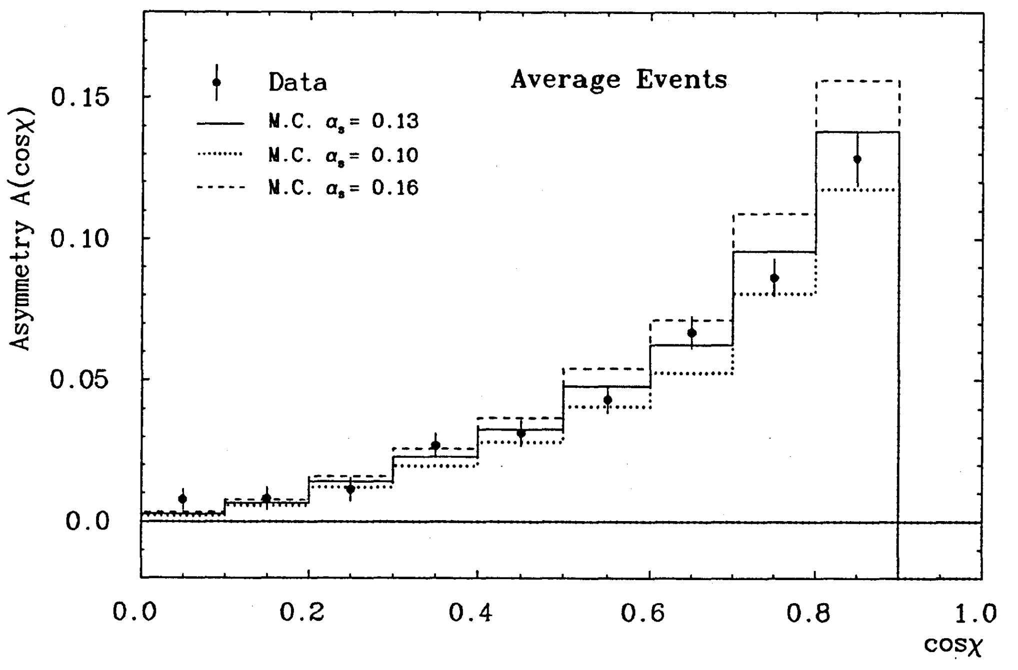

Figure 6.10: EEC and EEC Asymmetry Distributions of Average Hadrons Together with Fitted Result of Monte Carlo.

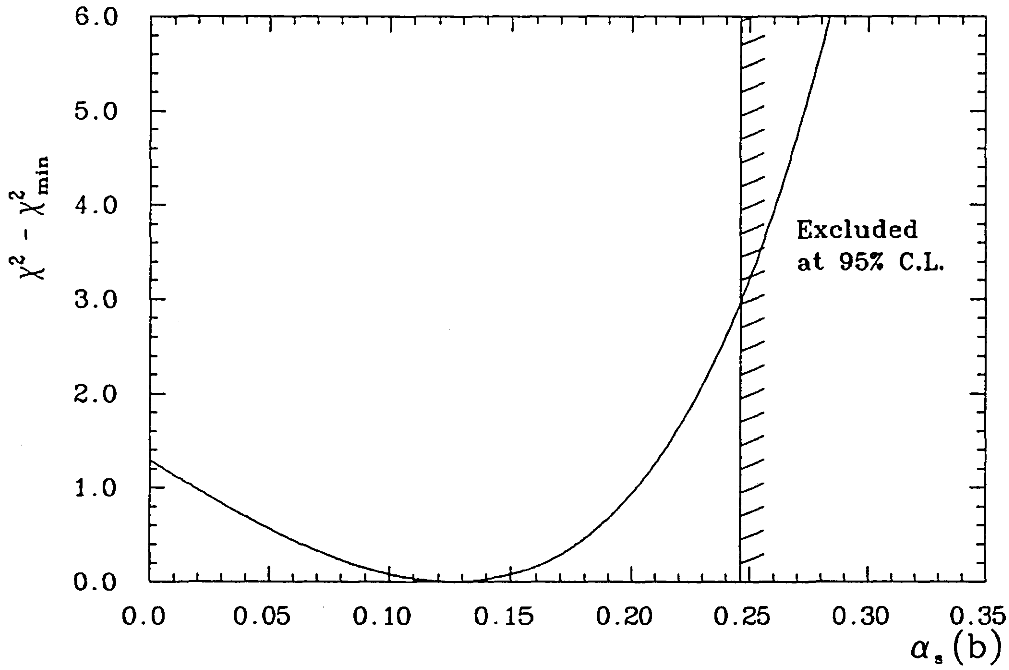

Figure 6.11: $\alpha_s(b)$ Fit χ^2 as a Function of $\alpha_s(b)$.

average hadrons as obtained in Equation 6.23 and only allowing $\alpha_s(b)$ as a free parameter, the result was

$$\alpha_s(b) \quad = \quad 0.127 \ \pm \ {}^{0.076}_{0.102} \ (statistical \ only) \tag{6.24}$$

with a $\chi^2/d.o.f$ of 1.5/6. The χ^2 as a function of $\alpha_s(b)$ is shown in Fig. 6.11. The estimated errors were taken at the points where $\chi^2 - \chi^2_{min} = 1$. This can be seen to be statistically insufficient to exclude the case $\alpha_s(b) = 0$, however the sensitivity to larger $\alpha_s(b)$ was somewhat better. The statistical errors were found by plotting the mean values of EEC asymmetries of each bin for every 200 events in a large data sample. These mean values were found to be distributed as Gaussians and their RMS spreads were equal to the average estimated errors. By integrating the probability space from $\alpha_s(b)$=0 up to a total of 95%, assuming the error came from a Gaussian with $\pm\sigma$ at $\chi^2 - \chi^2_{min}$=1 and $\pm 2\sigma$ at $\chi^2 - \chi^2_{min}$=4 *etc.*, the upper limit of $\alpha_s(b)$ was

$$\alpha_s(b) \ < \ 0.246 \ at \ 95\% \ confidence \ level \tag{6.25}$$

only considering the statistical error from the fit.

The data compared to the Monte Carlo according to this result are shown in Fig 6.12 for both the EEC and the EEC asymmetry distributions. The problem can be seen to be mainly due to the lack of statistics. The result was further degraded by the background contamination and the somewhat lower efficiency for multiparton b events compared to 2 jet b events in the tagging procedure.

The effect of changing the fixed value of α_s by ± 0.03 for the background events had negligible influence on the result for α_s of b. The effect due to the uncertainty in b purity of $\pm 10\%$ in the tagged sample was also negligible.

However, the inclusion of the points at $cos\chi$ between 0.7 and 0.9 would pull the result to zero for $\alpha_s(b)$. From the observed non-negligible influence of b quark mass on the properties of b jets as discussed in the previous section, the effect on the EEC and the asymmetry of EEC was also checked. Monte Carlo events were generated including QED radiative effects with α_s=0.13 for all flavours and also for b flavour only. Since the full second order QCD matrix element calculations treated all quarks as massless, some partial second order Monte Carlo events with b flavour only were also generated without the 2nd order virtual corrections to the 3-parton final states, but which used a 1st order 3-parton final state matrix element calculation of Ioffe [113] which included the quark masses. The resultant comparison can be seen in Fig. 6.13.

It can be seen that the effects of b quark mass on both the shape of EEC and EEC asymmetry were not negligible. However, the effect of including the b quark mass in QCD matrix element was relatively small. The broadening of the peaks near $|cos\chi| \sim 1$ can also be seen in the tagged data sample as shown in Fig. 6.12 compared to the average hadron sample. The dip in the central region of EEC distribution for the tagged sample was mainly due to the tagging bias which was followed by Monte Carlo closely, and to a smaller extent the phase space effect of b quark mass. With marginal statistics, the

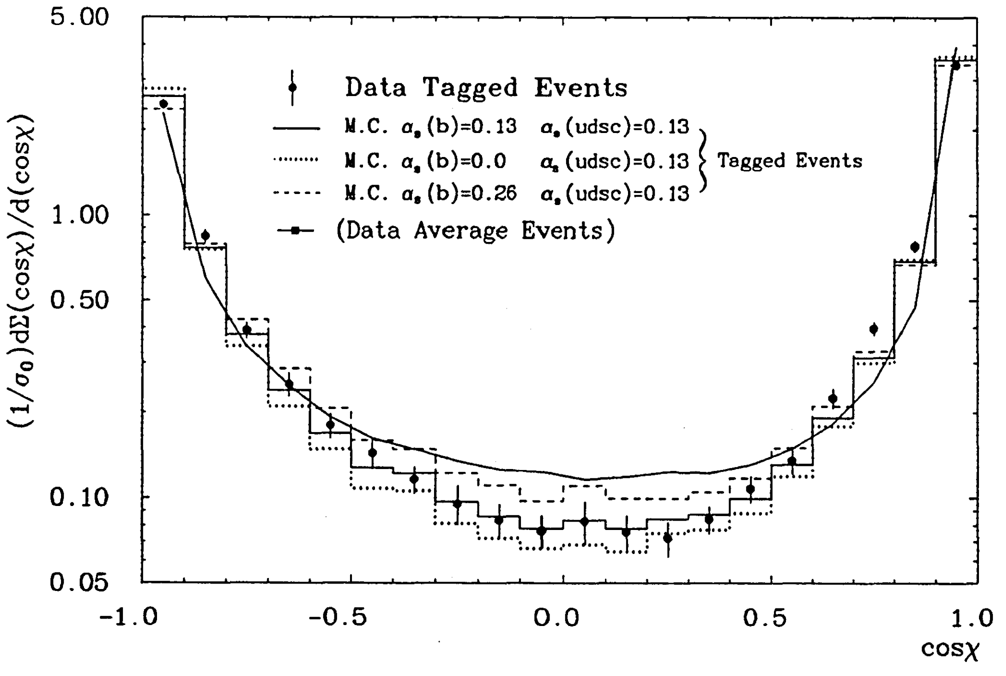

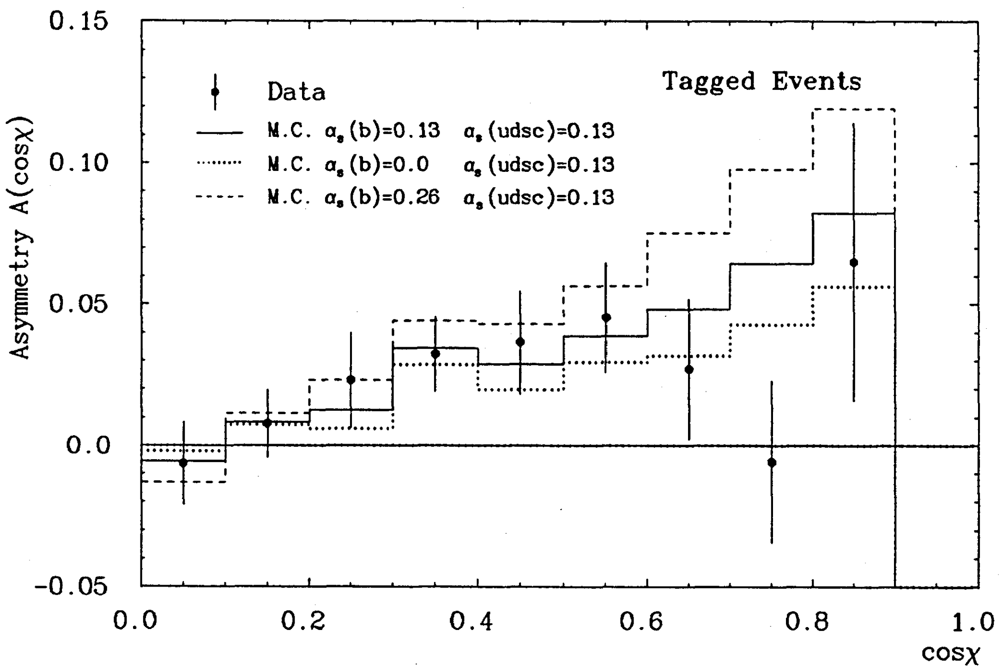

Figure 6.12: EEC and EEC Asymmetry Distributions for Fitted $\alpha_s(b)$ Result.

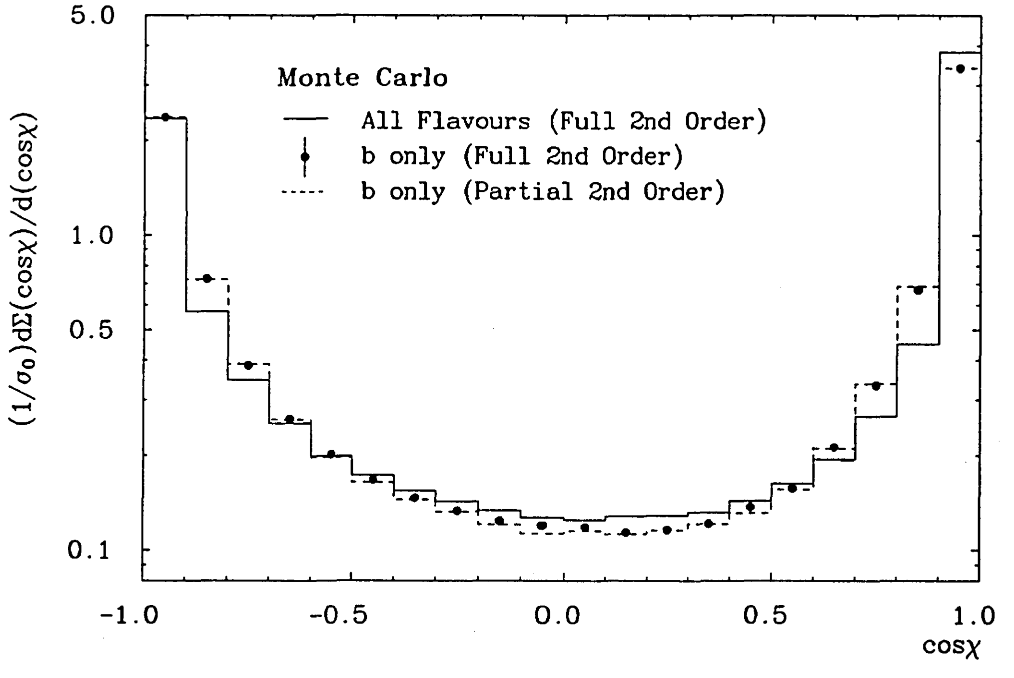

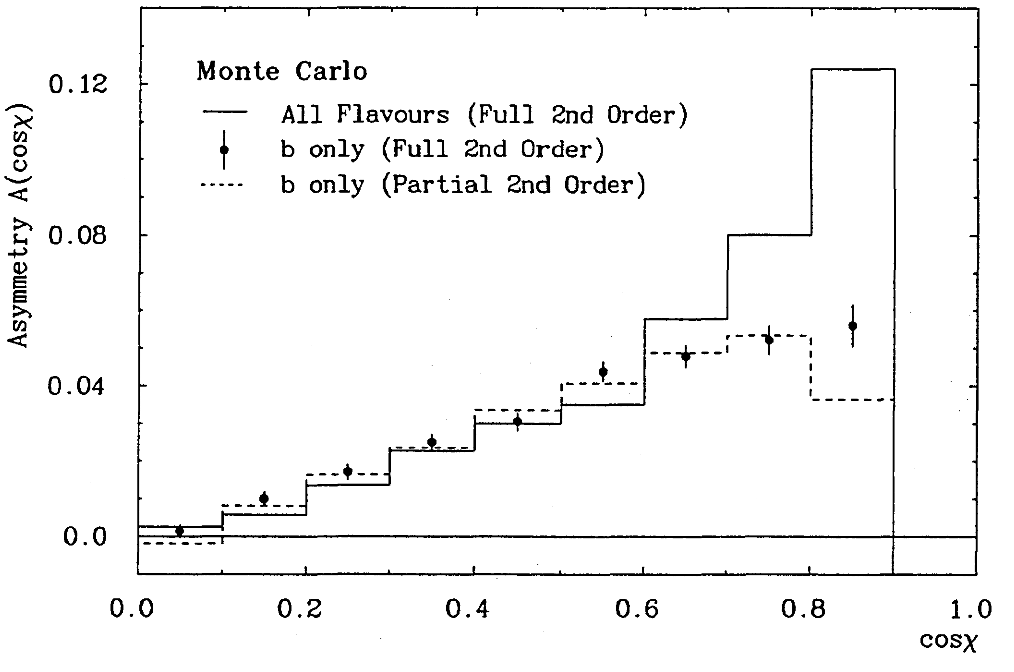

Figure 6.13: Monte Carlo Expectations of EEC and EEC asymmetry for b Flavour Only.

expected lowering of EEC asymmetry in the region $cos\chi$ ~0.7-0.9 compared to average hadronic events was present in the tagged data sample.

Based on the discussion that only the region $|cos\chi| < 0.7$ in the EEC asymmetry should be trusted for reliable information, the final result was therefore taken as the ratio of Equations 6.24 and 6.23 to give

$$\frac{\alpha_s(b)}{\alpha_s(Average\ Flavours)} = 0.96 \pm {}^{0.59}_{0.80} \tag{6.26}$$

where the statistical error and systematic error were combined in quadrature, with the statistical error in determining $\alpha_s(b)$ from the b enriched sample giving the dominant contribution. The systematic uncertainties in the EEC distribution of average hadronic events and in the EEC asymmetry distribution of the tagged events could only lower the ratio $\alpha_s(b)/\alpha_s(Average\ Flavours)$. Therefore a safe upper limit on this ratio can be drawn from Equations 6.25 and 6.23 as

$$\frac{\alpha_s(b)}{\alpha_s(Average\ Flavours)} < 2.1\ at\ 95\%\ confidence\ level \tag{6.27}$$

6.4 Conclusions

Both the *Jet-mode* and *Global-mode* b enrichment methods were applied to the TASSO high energy data to study different aspects of strong interaction properties of b quark.

Some differences were seen between the b jets and average jets, characterised by higher charge multiplicity and softer charged particle momentum in the b jets. It was also found that the b jet charged particle rapidity distribution had a clear excess over the case of the average jets in the mid plateau region. The results on average charged particle scaled momentum after corrections for detector effects were

$$\begin{aligned} Average\ Jets\quad < x_p > &= 0.0823 \quad \pm 0.0004\ (statistical\ only) \\ b\ jets\quad < x_p > &= 0.074 \quad \pm 0.005 \pm 0.003 \end{aligned} \tag{6.28}$$

where the systematic errors for the b jet result was only partial which came from the uncertainty in background subtraction from b enriched sample. The results on average charged multiplicity, also after corrections for detector effects, were

$$\begin{aligned} Average\ Jets \quad < n_{ch} > &= \ 7.44 \ \pm 0.03 \ \pm \ 0.19 \\ b\ jets \quad < n_{ch} > &= \ 8.51 \ \pm 0.50 \ \pm \ 0.35 \end{aligned} \tag{6.29}$$

The distributions of energy-energy correlation asymmetry were used to measure the strong coupling constant α_s for average flavours and b flavour only. Only results from the fit to the region $|cos\chi| \ < 0.7$ were used. When the ratio between the two α_s values were taken, most of the model dependent systematic uncertainties should cancel. This gave the result

$$\frac{\alpha_s(b)}{\alpha_s(Average\ Flavours)} \ = \ 0.96 \ \pm \ ^{0.59}_{0.80} \tag{6.30}$$

where the statistical and systematic errors were combined in quadrature but still dominated by the statistical error. This result alone was insufficient to exclude the possibility of this ratio being zero. However, with a better sensitivity, an upper limit on this ratio was obtained as

$$\frac{\alpha_s(b)}{\alpha_s(Average\ Flavours)} \ < \ 2.1 \ at\ 95\% \ confidence\ level \tag{6.31}$$

Although some differences were observed in event shape distributions including the energy-energy correlation distribution between the b enriched samples and average hadronic events, the fact that they were also reproduced by the Monte Carlo to various extents without exotic assumptions indicated that they were just effects due to heavier b quark mass. The explicit test on the strong coupling constant α_s also showed no significant difference between b quark and light flavours, although with limited accuracy.

We are now in a position to access the implication and potential of this technique of b enrichment. Although the data in this thesis was of limited statistics and in some ways poor quality, it has been demonstrated that good tagging efficiency and purity can be achieved. Work is currently underway to apply this tagging method on the 110 pb^{-1} of data took by TASSO during 1986, at a fixed W of 35 GeV. Making reasonable assumptions about efficiencies, we expect to have one of the largest samples of b events with comparable purities among the PETRA/PEP experiments. This will allow b jet fragmentation studies at a different energy and a more precise measurement $\alpha_s(b)/\alpha_s(Average)$.

Owing to the sufficiently long B decay lifetime, this analysis has shown that the vertex resolution required is not particularly demanding as the impact parameter resolutions for a large fraction of tracks involved in this analysis were only 200-300μm. This strongly encourages the applications of this type of b enrichment scheme with the LEP experiments. Further developments of equally realistic but more sophisticated methods under the narrow beam environment of SLC should provide an even more powerful tool for heavy flavour physics.

Appendix A

TASSO Coordinate Conventions

The standard TASSO coordinate system is shown in Fig. A.1. The origin was defined to be the centre of the main drift chamber. The z axis was along the positron beam direction, the y axis was in vertically upwards direction and the x axis was in the horizontal direction pointing toward the accelerator ring centre. The plane perpendicular to the beam was called the $r - \phi$ plane. The $r - \phi$ projection of the initial direction of a track was defined as the s axis for that track, starting from the track $r - \phi$ point closest to the $r - \phi$ origin.

The definitions of the main track parameters were:

$\boxed{R_0}$ Track radius in the $r - \phi$ plane.

$\boxed{x_0, y_0}$ $r - \phi$ Coordinates of the point where track $r - \phi$ projection was closest to the $r - \phi$ origin.

$\boxed{\phi_0}$ Track direction angle in $r - \phi$ plane at (x_0, y_0).

$\boxed{d_0}$ Track closest approach distance to the origin in the $r - \phi$ plane.

$\boxed{z_0}$ z coordinate of the track point where $r - \phi$ projection was (x_0, y_0).

$\boxed{\theta}$ Angle between track and $+z$ axis at the point (x_0, y_0, z_0).

$\boxed{P_{r\phi}}$ Track momentum in the $r - \phi$ plane.

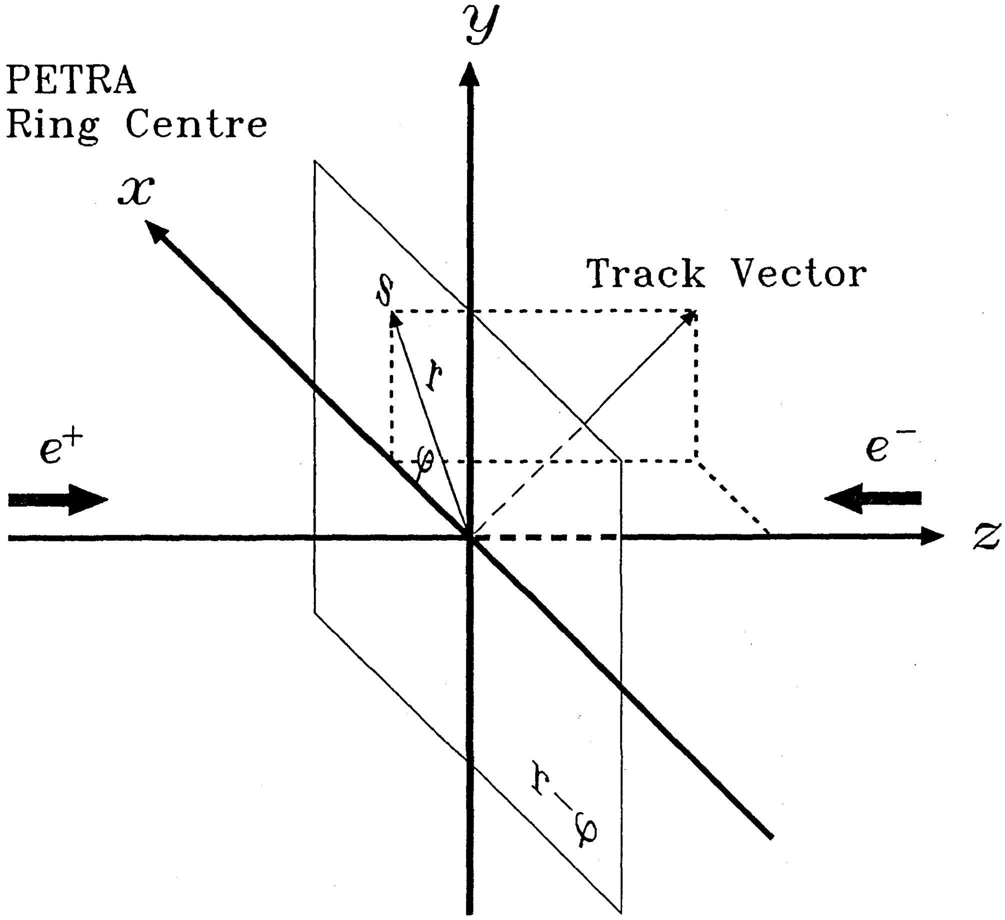

Figure A.1: TASSO Coordinate System Definitions

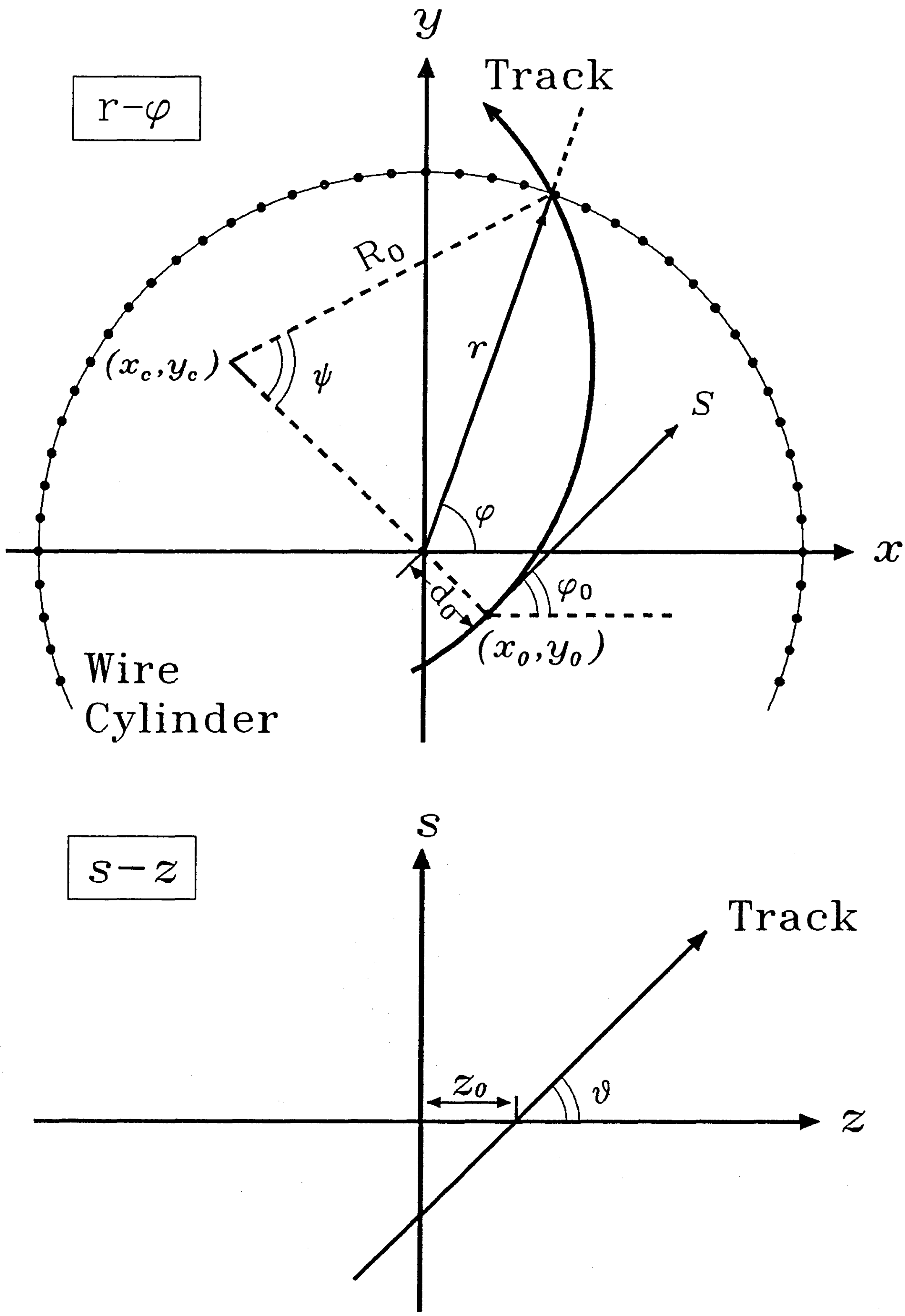

Figure A.2: TASSO Track Parameter Definitions

Coordinate Transformation from VXD to DC

The transformation from VXD coodinates to DC coordinates was defined as the *Backward* Euler transformation in TASSO. The 3 Euler angles were denoted as $\alpha_1, \alpha_2, \alpha_3$. The translation of the VXD with respect to the DC was denoted by x_v, y_v, z_v.

$$\begin{pmatrix} X' \\ Y' \\ Z' \end{pmatrix}_{DC} = A^{-1} \begin{pmatrix} X \\ Y \\ Z \end{pmatrix}_{VXD} + \begin{pmatrix} x_v \\ y_v \\ z_v \end{pmatrix}_{VXD}$$

where

$$A^{-1} = \begin{pmatrix} cos\alpha_3 cos\alpha_1 - cos\alpha_2 sin\alpha_1 sin\alpha_3 & -sin\alpha_3 cos\alpha_1 - cos\alpha_2 sin\alpha_1 cos\alpha_3 & sin\alpha_2 sin\alpha_1 \\ cos\alpha_3 sin\alpha_1 + cos\alpha_2 cos\alpha_1 sin\alpha_3 & -sin\alpha_3 sin\alpha_1 + cos\alpha_2 cos\alpha_1 cos\alpha_3 & -sin\alpha_2 cos\alpha_1 \\ sin\alpha_2 sin\alpha_3 & sin\alpha_2 cos\alpha_3 & cos\alpha_2 \end{pmatrix}$$

References

[1] H. Yukawa: *Proc. Phys. Maths. Soc. Japan* **<u>17</u>** *(1935) 48*

[2] D. H. Perkins: *Introduction to High Energy Physics* 2nd ed. (1982) Addison-Wesley

[3] C. N. Yang, R. L. Mills: *Phys. Rev.* **<u>96</u>** *(1954) 191*

[4] S. L. Glashow: *Nucl. Phys.* **<u>22</u>** *(1961) 579*

[5] A. Salam, J. C. Ward: *Phys. lett.* **<u>13</u>** *(1964) 168*

[6] P. W. Higgs: *Phys. Rev. Lett.* **<u>30</u>** *(1964) 1343*;
P. W. Higgs: *Phys. Rev.* **<u>145</u>** *(1966) 1156*;
T. W. B. Kibble: *Phys. Rev.* **<u>155</u>** *(1967) 1554*

[7] S. Weinberg: *Phys. Rev. Lett.* **<u>19</u>** *(1967) 1264*;
A. Salam: *Elementary Particle Theory* ed. N. Svartholm (Stockholm,Almquist 1968) P369

[8] Gargamelle Collab.: F. J. Hasert *et al.*: *Nucl. Phys.* **<u>B73</u>** *(1974) 1*

[9] UA1 Collab.: G. Arnison *et al.*: *Phys. lett.* **<u>122B</u>** *(1983) 103*;
UA2 Collab.: M. Banner *et al.*: *Phys. lett.* **<u>122B</u>** *(1983) 476*;
UA1 Collab.: G. Arnison *et al.*: *Phys. lett.* **<u>126B</u>** *(1983) 398*;
UA2 Collab.: P. Bagnaia *et al.*: *Phys. lett.* **<u>129B</u>** *(1983) 130*

[10] H. D. Politzer: *Phys. Reports.* **<u>14C</u>** *(1974) 129*

[11] D. J. Gross, F. Wilczek: *Phys. Rev. lett.* **<u>30</u>** *(1973) 1343*;
H. D. Politzer: *Phys. Rev. lett.* **<u>30</u>** *(1973) 1346*

[12] J. Gasser, H. Leutwyler: *Phys. Rep.* **<u>87</u>** *(1982) 77*

[13] Particle Data Group: *Phys. Lett.* **<u>170B</u>** *(1986)*

[14] E. H. Thorndike: **UR-935** Talk given at International Symposium on Lepton and Photon Interactions, Kyoto, Aug 1985;
E. H. Thorndike: **UR-938** *Ann. Rev. Nucl. Part. Sci.* **35** *(1985) 195-243*

[15] M. Kobayashi, K. Maskawa: *Prog. Th. Phys.* **49** *(1973) 652*

[16] S. Wojcicki: **SLAC-PUB-3431** Lectures presented at at the 12th Summer Institute on Particle Physics, Stanford, July-Aug 1984

[17] S. L. Glashow, J. Iliopoulos, L. Maiani: *Phys. Rev.* **D2** *(1970) 1285*

[18] M. G. D. Gilchriese: CLNS-86/754 & Rapporteur talk given at XXIIIrd International Conference on High Energy Physics, Berkley, July 1986

[19] D. E. Klem, Ph.D thesis, Stanford Linear Acceleration Center, SLAC-300, UC-34D

[20] A. Ali, E. Pietarinen: *Nucl. Phys.* **B154** *(1979) 519*

[21] Mark I Collab.:, R. Schindler *et al.*: *Phys. Rev.* **D24** *(1981) 78*

[22] R. H. Schindler: **SLAC-PUB-3799** Talk given at SLAC Summer School on Physics of the High Energy Accelerators, Stanford, July 1985

[23] D. Hitlin: **CALT-68-1230**

[24] B. Guberina, S. Nussinov, R. D. Peccei, R. Rückl:
Phys. Lett. **89B** *(1979) 111*

[25] M. Bander, D. Silverman, A. Soni: *Phys. Rev. Lett.* **44** *(1980) 7*

[26] H. Fritzsch, P. Minkowski: *Phys. Lett.* **90B** *(1980) 455*

[27] MAC Collab.: E. Fernandez *et al.*: *Phys. Rev. Lett.* **51** *(1983) 1022*

[28] Mark II Collab.: N. S. Lockyer *et al.*: *Phys. Rev. Lett.* **51** *(1983) 1316*

[29] DELCO Collab.: D. E. Klem *et al.*: *Phys. Rev. Lett.* **53** *(1984) 1873*

[30] TASSO Collab.: M. Althoff *et al.*: *Phys. Lett.* **149B** *(1984) 524*

[31] JADE Collab.: W. Bartel *et al.*: *Z. Phys.* **C31** *(1986) 349*

[32] MAC Collab.: W. W. Ash *et al.*: **SLAC-PUB-4123 (1986)**

[33] W. T. Ford: **COLO-HEP-87** Talk given at the Aspen Winter Physics Conference 1985.

[34] G. E. Forden: **RAL-85-076** Talk given at the 13th Summer Institute on Particle Physics, Stanford, July-Aug 1985

[35] CLEO Collab.: A. Bean *et al.*: *Phys. Rev. Lett.* **58** *(1987) 183*

[36] J. P. Leveille: **UM-HE-81-18** & *Proceedings of a CLEO Collaboration Workshop* **CLNS-81/505** July 1981

[37] M. Dine, S. Sapirstein: *Phys. Rev. lett.* **43** *(1979) 668*;
K. G. Chetyrkin, A. L. Kataev, F. V. Tkachov: *Phys. lett.* **85B** *(1979) 277*;
W. Celmaster, R. J. Gonsalves: *Phys. Rev. lett.* **44** *(1980) 560*

[38] R. Marshall **RAL-85-078** Talk given at XVI International Symposium on Multiparticle Dynamics, Kiryat Anavim, Israel, June 1985

[39] D. H. Saxon **RAL-86-073** Talk given at IX Warsaw Symposium on Elementary Particle Physics, Kazimierz, May 1986

[40] S. L. Wu: *Phys. Reports* **107** *(1984) 59*

[41] S. Komamiya: **HD-PY-86/01** & Talk give at International Symposium on Lepton and Photon Interactions, Kyoto, Aug 1985

[42] "Updated version of PETRA proposal (1976)"

[43] PETRA Storage Ring Group: *IEEE Trans.V.NS-28,No.3 (1981) 2025*;
K. Steffen: DESY Internal Report M-79/23 (1979);
J. Roßbach: DESY Internal Report M-81/01 (1981)

[44] A. Piwinski: *IEEE Trans.V.NS-30,No.4 (1983) 2378*

[45] TASSO Collab.: R. Brandelik *et al.*: *Phys. Lett.* **83B** *(1979) 261*

[46] H. M. Fischer, N. Wermes: DESY Internal Report F12-80/01 (1980)

[47] H. Boerner *et al.*: *Nucl. Instr. & Meth.* **176** *(1980) 151*

[48] H. Boerner: Ph.D thesis, Univ. Bonn (1981)

[49] J. K. Sedgbeer: Ph.D thesis, Imperial College, London (1983)

[50] C. Youngman: Ph.D thesis, Imperial College, London (1980)

[51] A. J. Campbell: Ph.D thesis, Imperial College, London (1983)

[52] S. Jarowslavski: *Nucl. Instr. & Meth.* **176** *(1980) 263*

[53] TASSO Collab.: R. Brandelik *et al.*: *Phys. Lett.* **94B** *(1980) 444*

[54] TASSO Collab.: R. Brandelik *et al.*: *Phys. Lett.* **113B** *(1982) 98*

[55] TASSO Collab.: R. Brandelik *et al.*: *Phys. Lett.* **108B** *(1982) 67*

[56] TASSO Collab.: M. Althoff *et al.*: *Phys. Lett.* **146B** *(1984) 443*

[57] V. Kadansky *et al.*: *Physical Scripta* **23** *(1981) 337*

[58] H. Burkhardt *et al.*: *Nucl. Instr. & Meth.* **184** *(1980) 319*

[59] K. W. Bell *et al.*: *Nucl. Instr. & Meth.* **179** *(1981) 27*

[60] T. Wyatt: Ph.D thesis, Univ. Oxford (1983)

[61] TASSO Collab.: R. Brandelik *et al.*: *Phys. Lett.* **92B** *(1980) 199*;
TASSO Collab.: M. Althoff *et al.*: *Z. Phys.* **C22** *(1984) 219*

[62] TASSO Collab.: M. Althoff *et al.*: *Phys. Lett.* **138B** *(1983) 441*

[63] TASSO Collab.: R. Brandelik *et al.*: *Phys. Lett.* **113B** *(1982) 499*

[64] D. G. Cassel, H. Kowalski: *Nucl. Instr. & Meth.* **185** *(1981) 235*

[65] W. Schütte: TASSO Note 243 (1982), Unpublished.

[66] Nijenhuis and Wilf: "Cominatorical Algorithms", Academic Press (1978)

[67] W. A. T. Wan Abdullah: Ph.D thesis, Imperial College, London (1985)

[68] D. H. Saxon: *Nucl. Instr. & Meth.* **A234** *(1985) 258*

[69] D. M. Binnie *et al.*: *Nucl. Instr. & Meth.* **228** *(1985) 267*

[70] A. Peisert, F. Sauli: *CERN Yellow Report* **84-04**

[71] F. Sauli: *CERN Yellow Report* **77-09**

[72] D. M. Binnie: *Nucl. Instr. & Meth.* **A234** *(1985) 54*

[73] D. M. Binnie: Private Communication

[74] J. Va'vra: *Nucl. Instr. & Meth.* **A244** *(1986) 391*

[75] D. M. Strom: Ph.D thesis, Univ. Wisconsin (1986)

[76] K. Fabricius, G. Kramer, G. Schierholz, I. Schmitt:
Phys. Lett. **97B** *(1980) 431*; *Z. Phys.* **C11** *(1982) 315*

[77] TASSO Collab.:, M. Althoff *et al.*: *Z. Phys.* **C26** *(1984) 157*

[78] F. A. Behrends, R. Kleiss: *Nucl. Phys.* **B177** *(1981) 237*;
Nucl. Phys. **B178** *(1981) 141*

[79] R. Field, R. Feynman: *Nucl. Phys.* **B136** *(1978) 1*

[80] B. Anderson, G. Gustafson, T. Sjöstrand:
Phys. Lett. **94B** *(1980) 211*; *Z. Phys.* **C6** *(1980) 235*;
Nucl. Phys. **B197** *(1982) 45*

[81] A. Ali *et al.*: *Phys. Lett.* **93B** *(1980) 155*

[82] C. Peterson *et al.*: *Phys. Rev.* **D27** *(1983) 105*

[83] T.Meyer: *Z. Phys.* **C12** *(1982) 77*

[84] MARK II Collab.: J. M. Yelton *et al.*: *Phys. Rev. Lett.* **49** *(1982) 430*;
TASSO Collab.: M. Althoff *et al.*: *Phys. Lett.* **126B** *(1983) 493*;
HRS Collab.: S. Ahlen *et al.*: *Phys. Rev. Lett.* **51** *(1983) 1147*;
JADE Collab.: W. Bartel *et al.*: *Phys. Lett.* **146B** *(1984) 121*;
ARGUS Collab.: H. Albrecht *et al.*: *Phys. Lett.* **150B** *(1985) 235*;
JADE Collab.: W. Bartel *et al.*: *Phys. Lett.* **161B** *(1985) 197*

[85] CLEO Collab.: P. Avery *et al.*: *Phys. Rev. Lett.* **51** *(1983) 1139*

[86] HRS Collab.: M. Derrick *et al.*: *Phys. Rev. Lett.* **53** *(1984) 1971*

[87] MARK II Collab.: M. Coles *et al.*: *Phys. Rev.* **D26** *(1982) 2190*

[88] S. Bethke: *Z. Phys.* **C29** *(1985) 175*;
& Talk given at International Symposium on Production and Decay of Heavy Flavour, Heidelberg, May 1986

[89] MARK II Collab.: M. E. Nelson *et al.*: *Phys. Rev. Lett.* **50** *(1983) 1542*;
MAC Collab.: E. Fernandez *et al.*: *Phys. Rev. Lett.* **50** *(1983) 2054*;
MARK J Collab.: B. Aveda *et al.*: *Phys. Rev. Lett.* **51** *(1983) 443*;
TASSO Collab.: M. Althoff *et al.*: *Z. Phys.* **C22** *(1984) 219*;
TASSO Collab.: M. Althoff *et al.*: *Phys. Lett.* **146B** *(1984) 443*;
JADE Collab.: W. Bartel *et al.*: *Phys. Lett.* **163B** *(1985) 277*;
JADE Collab.: W. Bartel *et al.*: **DESY 86-129**

[90] P. Avery: CLNS-84/608
J. Izen: TASSO Note 322, Unpublished.

[91] CLEO Collab.:, J. Green *et al.*: *Phys. Rev. Lett.* **51** *(1983) 347*;
CLEO Collab.:, S. E. Csorna *et al.*: *Phys. Rev. Lett.* **54** *(1985) 1894*

[92] CUSB Collab.:, C. Klopfenstein *et al.*: *Phys. Lett.* **130B** *(1983) 444*;
CLEO Collab.:, A. Chen *et al.*: *Phys. Rev. Lett.* **52** *(1984) 1084*

[93] CLEO Collab.:, M. Alam *et al.*: **CLNS-86/739**

[94] CLEO Collab.:, M. Alam *et al.*: *Phys. Rev. Lett.* **49** *(1982) 357*;
CLEO Collab.:, R. Giles *et al.*: *Phys. Rev.* **D30** *(1984) 2279*

[95] S. L. Lloyd, B. Foster, SIMPLE writeup, unpublished.

[96] TASSO Collab.: M. Althoff *et al.*: *Z. Phys.* **C22** *(1984) 307*

[97] D. J. Mellor, Private communication.

[98] TASSO Collab.: M. Althoff *et al.*: *Phys. Lett.* **126B** *(1983) 493*

[99] JADE Collab.: W. Bartel *et al.*: *Phys. Lett.* **146B** *(1984) 437*

[100] DELCO Collab.: M. Sakuda *et al.*: *Phys. Lett.* **152B** *(1985) 399*

[101] MARK II Collab.: P. C. Rowson *et al.*: *Phys. Rev. Lett.* **54** *(1985) 2580*

[102] TASSO Collab.: M. Althoff *et al.*: *Phys. Lett.* **135B** *(1984) 243*

[103] TASSO Collab.: M. Althoff *et al.*: *Phys. Lett.* **138B** *(1984) 317*

[104] HRS Collab.: P. Kesten *et al.*: *Phys. Lett.* **161B** *(1985) 412*

[105] HRS Collab.: M. Derrick *et al.*: *Phys. Lett.* **168B** *(1986) 299*

[106] UA5 Collab.: G. J. Alner *et al.*: *Phys. Lett.* **167B** *(1986) 476*

[107] MARK J Collab.: B. Adeva *et al.*: *Phys. Rev. Lett.* **50** *(1983) 2051*

[108] CELLO Collab.: H. J. Behrend *et al.*: *Phys. Lett.* **138B** *(1984) 311*

[109] JADE Collab.: W. Bartel *et al.*: *Z. Phys.* **C25** *(1984) 321*

[110] C. L. Basham *et al.*: *Phys. Rev. Lett.* **41** *(1978) 1585*

[111] A.Ali, F. Barreiro: *Nucl. Phys* **B236** *(1984) 269*

[112] F. Barreiro, G. Kreutz, L. Labarga: TASSO Note 338 (Publication in preparation).

[113] B. L. Ioffe: *Phys. Lett.* **78B** *(1978) 277*